The charge transport mechanism in cable bacteria

van der Veen, J.R.

DOI
10.4233/uuid:eedc76eb-6970-425b-98f6-8593cd1f5b7d

Publication date
2024

Document Version
Final published version

Citation (APA)
van der Veen, J. R. (2024). *The charge transport mechanism in cable bacteria*. [Dissertation (TU Delft), Delft University of Technology]. https://doi.org/10.4233/uuid:eedc76eb-6970-425b-98f6-8593cd1f5b7d

The Charge Transport Mechanism in Cable Bacteria

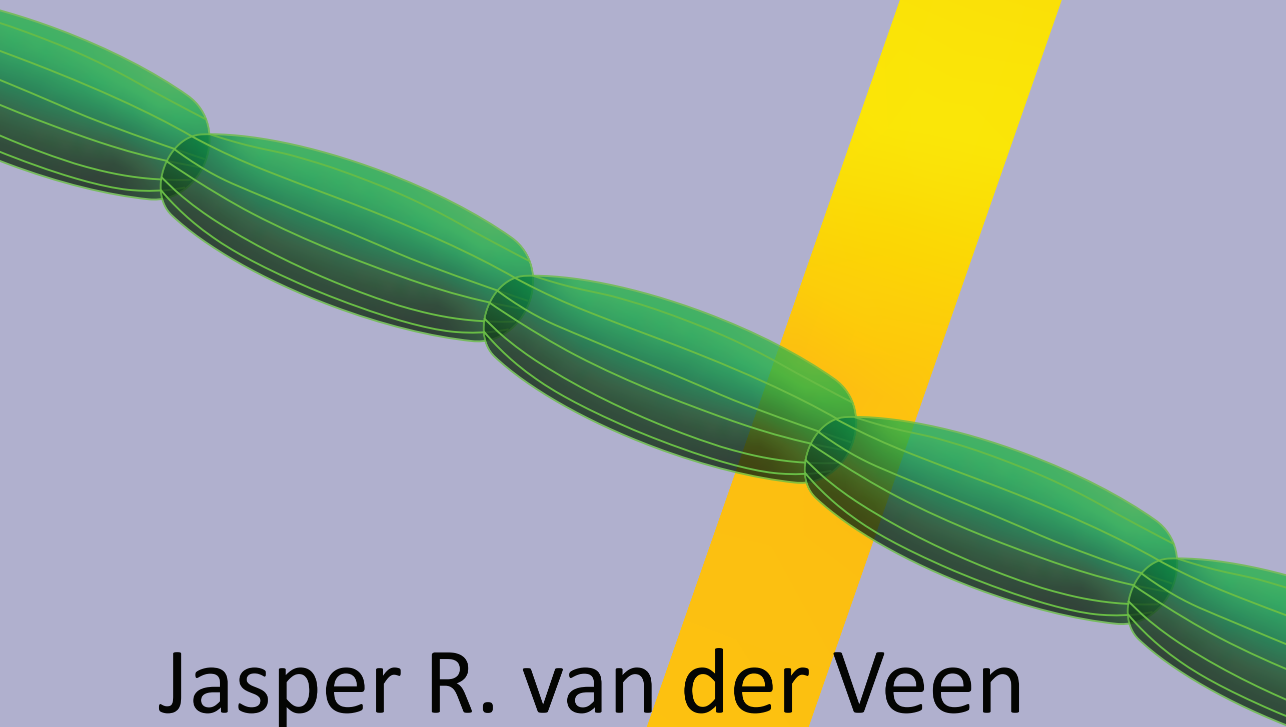

Jasper R. van der Veen

THE CHARGE TRANSPORT MECHANISM IN CABLE BACTERIA

THE CHARGE TRANSPORT MECHANISM IN CABLE BACTERIA

Proefschrift

ter verkrijging van de graad van doctor
aan de Technische Universiteit Delft,
op gezag van de Rector Magnificus prof.dr.ir. T.H.J.J. van der Hagen,
voorzitter van het College voor Promoties,
in het openbaar te verdedigen op donderdag 2 mei 2024 om 15:00 uur

door

Jasper Ruud VAN DER VEEN

Master of Science in Applied Physics,
Technische Universiteit Delft, Nederland,
geboren te Den Haag, Nederland.

Dit proefschrift is goedgekeurd door de

promotor: Prof. dr. ir. F.J.R. Meysman
promotor: Prof. dr. ir. H.S.J. Van der Zant

Samenstelling promotiecommissie:

Rector Magnificus prof.dr.ir. T.H.J.J. van der Hagen	voorzitter
Prof. dr. ir. H.S.J. Van der Zant	Technische Universiteit Delft
Prof. dr. ir. F.J.R. Meysman	Technische Universiteit Delft Universiteit Antwerpen

Onafhankelijke leden:

Dr. L. Jourdin	Technische Universiteit Delft
Prof. dr. Y.M. Blanter	Technische Universiteit Delft
Prof. dr. S.S. Skourtis	University of Cyprus
Prof. dr. J. Blumberger	University College London
Prof. dr. F. Hollman	Technische Universiteit Delft, reservelid

Delft University of Technology, Faculty of Applied Sciences,
Department of Quantum Nanoscience, van der Zant lab
Department of Biotechnology, Filip Meysman group

Front & Back: J.R. van der Veen

CONTENTS

SUMMARY

In this dissertation, the charge transport mechanism in the conductive fibres of cable bacteria is investigated. In Chapter 1, the research field of bacterial electricity is introduced. Three kinds of bacterial nanowires are discussed: Shewenella nanowires, Geobacter nanowires and the conductive fibres from cable bacteria. Even though the three types of protein wires are all conductive, the cable bacteria's protein wires stand out because their activation energy of conductance is much lower than that of the other nanowires and because they transport electrons over centimeter instead of micrometer distances. These differences suggest they have a distinct charge transport mechanism. To put different transport mechanisms in more context, metallic conduction, semiconduction, and hopping conduction are treated side by side and emphasis is placed on the temperature dependence of conductivity.

In Chapter 2, temperature dependent measurements of the conductivity are presented, that were done in a wide temperature range (4-300 K). To execute these measurements, gold electrode patterns were fabricated on a silicon chip with an insulating silicon dioxide layer on top. Bacterial cables were placed across the electrodes, such that for many segments of cable bacteria, the current-voltage curves, could be measured. As the temperature is decreased, so is the conductance, with an activation energy of 42 meV, averaged over 53 segments. When lowering the temperature below 75 K, the conductivity decreases less rapidly than expected from the activation energy. The combination of this low- and of the high-temperature dependence of conductance fits well with a quantum-corrected hopping model, in which, upon cooling below 75 K, the energy in vibrational modes remains higher than classically predicted due to the quantum vibrational energy. In accordance with this model, the low-temperature conductance follows a power law in temperature and electric field. The experimental data fits the accompanying, predicted universal scaling curve, which estimates that the distances between hopping sites exceed 10 nm.

In Chapter 3, the hopping model proposed in Chapter 2 is treated in more detail, to be able to estimate whether the 100 S/cm conductivity levels observed in cable bacteria, are reasonable. Cable bacteria are modelled here as a collection of many parallel one-dimensional hopping chains, each with a diameter of 2 nm, such that per 26 nm fibre 125 conduction channels fit in, for a total of 7500 conduction channels in 60 parallel fibres. Taking into account that each hopping site has an energy and occupation probability, the electrical current through the hopping chains can be calculated. When there is no voltage drop in the hopping chain, but over the electrodes, the occupation probabilities of the hopping chain follow a linear profile and the current is in a concentration-driven regime. In this case, the current-voltage curve saturates above 0.1 V at room temperature, which is never experimentally seen. When all voltage drops in the hopping chain, the occupation probabilities are all equal. This is the field-driven regime, which is the optimal case for conductivity. There is also an in-between scenario, in which the occupation probability follows a tangent shape. If an injection barrier would be present, the current-voltage curve would consist of two distinct regimes, which is not experimentally observed. The question remains whether 100 S/cm conductivity levels are attainable within the proposed model. The constraint is used, that for the observed reorganisation energy of roughly 0.2 eV, the electronic coupling between hopping sites should not exceed one tenth of that (0.02 eV), to avoid a breakdown of hopping theory. Even with this maximum hopping rate, large distances between hopping sites are required to obtain a 100 S/cm conducitivity level, similar to 10 nm.

In Chapter 4, gate voltage dependent measurements of the conductivity are presented in a wide temperature range (10 - 300 K). To execute these measurements, gold electrode patterns were fabricated on a doped silicon substraat with an 285 nm thick insulating silicon dioxide layer on top. A gate voltage is applied between the doped silicon and the ground electrode. At room temperature, the gate voltage has little effect on the conductance (< 2 %). At lower temperatures (< 150 K), the conductance increases for both positive and negative gate voltages. The gate effect becomes stronger with decreasing temperature, but the gate never doubles the conductivity. The gate response saturates for high gate voltage, which suggests this method cannot improve the charge carrier density in cable bacteria by much, which would be possible in a semiconductor. A model proposition is done, in which there is an small energy gap of the order of ~ 1 meV, outside which there are multiple electronic states contributing to transport.

In Chapter 5, magneto-resistance measurements at temperatures below 10 K are presented. At 1.8 K, a relative magneto-resistance of up to 50 % can be observed in cable bacteria at a magnetic field of 8 T. As the temperature is increased, the magneto-resistance diminishes, such that at 10 K it is only a few percent. Also, as a function of the applied bias voltage, the magneto-resistance disappears. By measuring segments with a different electrode seperation (4 micrometer and 40 micrometer), it was seen that the applied voltage per length, i.e., the electric field, has the reducing effect on the magneto-resistance. The behaviour observed fits a wave function shrinkage model. The hopping distance, that can be estimated from this model, is of the order of 10 nm, just as seen in Chapters 2 and 3.

SAMENVATTING

In dit proefschrift, wordt het ladingstransportmechanisme van de geleidende vezels in kabelbacteriën onderzocht. In Hoofdstuk 1, wordt het onderzoeksveld ’bacteriële elektriciteit’ geintroduceerd. Drie types bacteriële nanodraden worden behandeld: Shewanella nanodraden, Geobacter nanodraden en the geleidende vezels in kabelbacteriën. Hoewel de drie soorten allen geleidend zijn, zijn de kabelbacterievezels uitzonderlijk, omdat hun activeringsenergie veel lager is dan die van de andere nanodraden en omdat ze elektronen transporteren over centimeterlange afstanden in plaats van micrometers. Deze verschillen suggereren dat hun transportmechanisme wezenlijk anders is. Om verschillende transportmechanismes in context te plaatsen, worden metallische geleiding, halfgeleding en hopgeileiding één voor één behandeld, met nadruk op de temperatuursafhankelijkheid van de geleiding.

In hoofdstuk 2, worden temperatuursafhankelijke metingen van de geleiding gepresenteerd, die gedaan zijn in een groot temperatuursbereik (4 K - 300 K). Om deze metingen uit te kunnen voeren, zijn gouden elektrodepatronen geplaatst op een siliciumsubstraat met een isolerende bovenlaag van siliciumdioxide. Bacteriële kabels werden dwars over de elektrodes gelegd, zodat voor veel verschillende kabelbacteriesegmenten het verband tussen stroom en spanning kon worden vastgelegd. Als de temperatuur verlaagt wordt, vermindert de geleiding, met een activeringsenergie van 42 meV, wat het gemiddelde is van 53 gemeten segmenten. Voor temperaturen onder de 75 K, neemt de geleiding minder snel af dan verwacht wordt aan de hand van de activeringsenergie. De combinatie van dit lage en het hoge temperatuursgedrag, passen goed bij een kwantum-gecorrigeerd hopmodel, waarin onder de 75 K de trillingsenergieën hoger blijven dan voorspeld in de klassieke mechanica, dankzij de kwantumtrillingsenergie. In overeenstemming met dit model, volgt de geleiding een machtsrelatie in temperatuur en elektrisch veld voor lage temperaturen. De experimentele data past op de voorspelde universele schalingskromme, die voorspelt dat de hopafstanden groter dan 10 nm zijn.

In hoofdstuk 3, wordt het hopmodel dat wordt voorgesteld in hoofdstuk 2 in meer detail uitgewerkt, om in te kunnen schatten of het geobserveerde, maximale geleidingsniveau van 100 S/cm wel redelijk is. Kabelbacteriën worden hier gemodelleerd als een verzameling parallelle, een-dimensionale hopketens, elk met een diameter van 2 nm, zodat er 125 geleidingskanalen passen in één 26 nm wijde vezel, voor een totaal van 7500 kanalen voor 60 vezels. In acht nemend dat elke hopplek een energie en bezettingsgraad heeft, kan de elektrische stroom door de hopketens worden uitgerekend. Waneer er geen spanningsval in de hopketen is, maar wel over de elektrodes, volgt de bezettingsgraad een lineair profiel and dan is de stroom concentratie-gedreven. In dit geval, verzadigt de stroom boven een spanning van 0.1 V, wat nooit in het experiment gezien wordt. Waneer alle spanning valt binnen de hopketen, heeft elke hopplaats dezelfde bezettingsgraad. Dit is het veld-gedreven geval, dat optimaal is voor de geleiding. Er is ook een tussengebied, waarbij het bezettingsprofiel een tangentiële vorm heeft. Als er een injectiebarrière voor transport zou zijn, zou de stroom-spanningskromme uiteenvallen in twee aparte gebieden, wat niet overeenkomt met het experiment. De vraag blijft dan of 100 S/cm haalbaar is binnen het voorgestelde model. De randvoorwaarde wordt gebruikt, dat bij een reorganisatie-energie van 0.2 eV, de elektronische koppeling tussen hopplaatsen niet meer mag bedragen dan een tiende daarvan (0.02 eV), om uiteenvallen van het hopmodel te voorkomen. Zelfs met deze maximale hopfrequentie, zijn hopafstanden van ongeveer 10 nm nodig om 100 S/cm te bereiken.

In hoofdstuk 4, worden poortspanningsafhankelijke metingen van de geleiding gepresenteerd in een groot temperatuursbereik (10 - 300 K). Om deze metingen uit te voeren, werden gouden elektrodepatronen gemaakt op een gedoteerd siliciumsubstraat met een bovenlaag van isolerend siliciumdioxide van 285 nm dik. De poortspanning wordt aangelegd tussen het gedoteerde silicium en de geaarde elektrode. Bij kamertemperatuur, heeft de poortspanning weinig effect op de geleiding (<2 %). Bij lagere temperaturen (< 150 K), neemt de geleiding toe bij zowel positieve als negatieve poortspanningen. Het poorteffect wordt met het verlagen van de temperatuur, maar verdubbelt nooit de geleiding. De poortrespons verzadigt voor hoge poortspanning, wat suggereert dat de ladingsdichtheid in kabelbacteriën niet veel verbeterd kan worden met deze methode, wat wel mogelijk zou zijn in een halfgeleider. Een modelvoorstel wordt gedaan, waarbij er een kleine energiekloof is van 1 meV, waarbuiten er meerdere elektronische standen meedoen aan transport.

In hoofdstuk 5, worden magnetoweerstandsmetingen bij temperaturen onder de 10 K gepresenteerd. Bij 1.8 K, wordt een relatieve magnetoweerstand van wel 50 % geobserveerd in kabelbacteriën, bij een magnetisch veld van 8 T. Met het verhogen van de temperatuur, vermindert de magnetoweerstand snel, zodat er nog maar een paar procent over is. Ook neemt de magnetoweerstand snel af met de toegepaste spanning. Door segmenten van verschillende lengte te meten (4 micrometer en 40 micrometer), is het vastgesteld dat de spanning per lengte-eenheid, ofwel het elektrisch veld, hiervoor verantwoordelijk is. Het geobserveerde gedrag past goed bij een model, waarbij de golffunctie krimpt met het magnetisch veld. Dit model voorspelt dat de hopafstand ongeveer 10 nm is, net zoals in hoofdstuk 2 en 3.

1

INTRODUCTION

It is a relatively new discovery that bacteria can grow structures that efficiently conduct electricity over long distances. In this, the term "long" is critically important and refers to macroscale conduction, i.e., charge transport over micrometer to centimeter scale distances, much longer than the nanometer size of the individual proteins that guide these currents. However, the mechanisms of charge transport in these biological conductors remain poorly understood. Biological protein structures are generally thought to be poorly conductive, and so it is enigmatic how microorganisms can efficiently guide electrical currents over such long distances.

For now, cable bacteria hold the "world record" in terms of long-range conduction: they are able to channel currents over centimeter distances [1–3]. The objective of this work is to shed light on this intriguing centimeter-scale charge transport in cable bacteria. As a background to the work presented in this thesis, I will first provide a general introduction to conduction mechanisms in materials (irrespective of whether the material is biotic or abiotic). Subsequently, I will briefly review the current knowledge on the conduction mechanism in three of the most studied groups of microbes that display long-range conduction: Shewanella, Geobacter and cable bacteria..

1.1. CONDUCTION MECHANISMS

The conductance in microbial structures can be theoretically approached with concepts that generically apply to any conducting material. Foremost, the electrical conductivity, σ, can be expressed as a combination of two factors, the charge carrier density, n, and the charge carrier mobility, μ, via the relation:

$$\sigma = ne\mu, \tag{1.1}$$

In this, $e = 1.6 \cdot 10^{-19}$ C represents the elementary charge. The term 'charge transport mechanism' puts the focus on the mobility, μ, since it describes how fluently individual charges are moving through the conductor. In contrast, the charge carrier density describes how many charges are effectively moving. Both terms are of equal importance to understand electrical conductivity: it is crucial to treat n and μ on equal footing. In the sections below, metallic conductors, semiconductors and biological conductors are compared. For each of these categories, the charge carrier concentration, n, and the mobility, μ, are different in character.

1.1.1. METALLIC CONDUCTORS

In metals, each atom contributes one or more free electrons that can participate in the conduction. Metallic conduction is hence characterised by a high charge carrier concentration, n, which is on the order of the concentration of the atoms per unit volume ($\sim 10^{23}$ cm^{-3} in magnitude). The charge carrier mobility, however, is not extraordinarily high in metals, with an order of magnitude: $\mu \approx 10$ cm^2/Vs. The combination of charge carrier concentration and mobility provides a conductivity of:

$$\sigma = ne\mu \approx 10^{23}\ \mathrm{cm}^{-3} \cdot 10^{-19}\ \mathrm{C} \cdot 10^{1}\ \mathrm{cm}^2/\mathrm{Vs} \approx 10^{5}\ \mathrm{S/cm}. \tag{1.2}$$

In metals, the charge carrier concentration, n, does not vary with temperature, and as a result, the temperature dependence of the conductivity, $\sigma(T)$, is solely determined by the temperature dependence of the mobility, $\mu(T)$. In metals, electrons will frequently undergo collisions (scatter) with the crystal lattice, in which electrons are deflected and loose energy (Fig. 1.1a). Because of this scattering, the drift speed of the electron in a 1 cm long metal bar under an applied bias voltage of 1 V, $v_d = \mu V/L \approx 10$ cm/s, is much lower than the absolute speed of the electron ($v_F \approx 10^8$ cm/s, the Fermi velocity). As the temperature of the metal increases, the atoms in its crystal lattice will vibrate with greater amplitude, thus increasing the chances of a collision with the electron. Therefore, a higher temperature decreases the mobility of the electron and thus the conductivity of the metal. In summary, metallic conduction is characterised by two features: a high, temperature insensitive charge carrier density, n, and a moderate mobility, μ that decreases with increasing temperature.

1.1.2. SEMICONDUCTORS

In semiconductors and insulators, there are no free electrons due to the nature of the chemical bonds between atoms. For example, in silicon crystals, atoms are covalently bonded. There are four electrons in the outer shell of the silicon atom, that each form a covalent bond with a neighbouring atom. The electrons participating in these bonds cannot move around. The electrons are all residing in a valence band, which is separated from the conduction band by the band gap energy U_g. Still, a freely moving electron-hole pair can be created (Fig. 1.1b), but this requires an external energy input that equals the band gap energy, U_g, related to the covalent bond [4]. At zero temperature, thermal fluctuations are absent and the required energy is not available, but at a fine temperature, there is a chance that free charge carriers are created. As a consequence, when the temperature of a semiconductor is increased, the conductivity increases, in contrast to metals. The charge carrier concentration for semiconductors is not constant but varies as [5, 6]:

$$n = n_0 \exp\left(\frac{-U_g}{2k_B T}\right), \tag{1.3}$$

where k_B is Boltzmann's constant and T is the temperature. Here, n_0 would be the charge carrier concentration, if silicon would be metallic in nature. Using $U_g = 1.1$ eV as for silicon, the exponential dependence on the band gap energy suppresses the conductivity at room temperature by a factor of 10^{-10}. So all other things being equal, a conductivity on the order of 10^{-5} S/cm is expected for silicon (downscaled from the metallic conductivity 10^5 S/cm derived above). At the same time, the mobility in silicon is an order of magnitude higher than in metals ($\mu \approx 100$ cm^2/Vs). As a result, the intrinsic conductivity of silicon is $\sigma \sim 10^{-4}$ S/cm. In summary, semiconducting transport is characterised by a low charge carrier density that is very sensitiveto temperature, n, and a relatively high mobility, μ, which is comparable or even higher than in the metallic case.

1.1.3. DOPED SEMICONDUCTORS AND HOPPING CONDUCTION

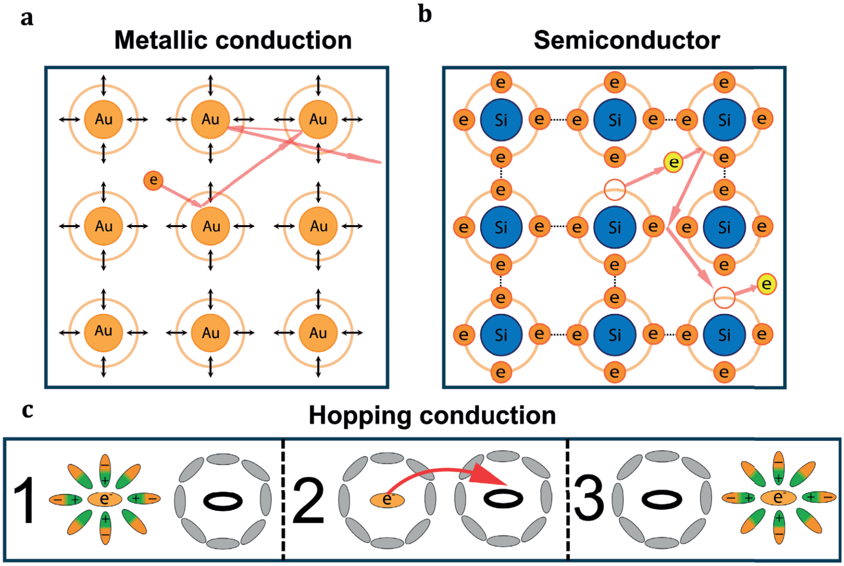

Figure 1.1: **Different types of bacteria producing electrically conducting nanowires**. **a**, Metallic conduction, with gold atoms depicted in yellow. A free electron e^{-1} is freely moving in the lattice, but its path changes often due to collisions (red arrows). **b**, Semiconductor, with silicon atoms depicted in grey blue. Four electrons (orange) are drawn in the outer shell of silicon. These electrons form covalent bonds (dashed lines). Free electrons (yellow) can exist if these bonds are broken, after which they can move through the lattice (red arrows). **c**, Hopping conduction, where thee states are important (1,2 and 3). In state 1, the electron is the initial state, and the charge distribution around creates an attractive force (green for positive charge, orange for negative). The ovals represent matter surrounding the electron. In state 2, the electron is in the transition state, in which the attractive force is compensated by thermal motion. In this state, there is no preference for the initial or final position. In state 3, the electron has moved to the final position and the surrounding matter has reorganised around the electron.

Therefore, the way to increase the conductivity of semiconductors is by increasing n. This can be done by adding impurities in the crystal lattice of the semiconductor (e.g., a phosphorus or boron atom in the place of silicon, thus introducing an extra electron or hole to the silicon crystal). In principle, these charge donors, with concentration n_D, want to stay at the impurity. Yet, when there is an external input that exceeds the donor activation energy, U_D, a free charge carrier is created. As long as the thermal energy is higher than this activation energy ($k_B T > U_D$), the charges are free and the charge carrier concentration is n_D. Because the donor activation energies are small with respect to the band gap ($U_D < U_g$), the charge carrier density is boosted with respect to the undoped semiconductor. The mobility μ is again limited by collisions in the lattice. This conductivity in a highly doped semiconductor is in principle equivalent to metallic conductivity, but with a lower charge carrier concentration and thus lower conductivity.

However, for low enough temperatures ($U_D > k_B T$), the creation of free charges becomes again a thermally activated process, and the number of charge carriers in the conduction band again drops exponentially as in Eq. 1.3. When lowering the temperature enough, it becomes faster to directly move from impurity to impurity, without creating a free electron, in what is known as a 'hopping event' [7]. Miller and Abrahams proposed that electrons move in a network of hopping sites with disorder in site energy and distance. Each site has a random energy, U_i, and there are random distances, r_{ij}, between the sites i and j. The transition rates between site i and j are of the form [7], if $U_j > U_i$:

$$\Gamma_{i,j} = \Gamma_0 \exp\left(-\frac{r_{ij}}{\xi}\right) \exp\left(-\frac{U_j - U_i}{k_B T}\right), \tag{1.4}$$

where Γ_0 is a constant pre-factor. In the situation where $U_i < U_j$, the transition rate becomes:

$$\Gamma_{i,j} = \Gamma_0 \exp\left(-\frac{r_{ij}}{\xi}\right). \tag{1.5}$$

In this regime, the electron mobility μ is entirely determined by the hopping rate. Instead of a free particle colliding in a lattice, there are now trapped particles tunneling between localised states. The mobility, μ, is thermally activated and the charge carrier concentration is still the dopant concentration, n_D. The Miller-Abrahams rates are at the basis of the Variable Range Hopping (VRH) model, which explains the conductive behaviour in many doped semiconductors at lower temperatures [8]. In summary, doped semiconductor conduction is characterised by a charge carrier density determined by the dopant concentration, n_D, and a mobility that is 'metallic-like' at high temperatures and 'hopping-like' at low temperatures (VRH). Doping in silicon is effective up until $n_D \approx 10^{19}$ cm^{-3}, such that the conductivity can be increased to the ~ 10 S/cm order of magnitude [9]. The doped semiconductor, polyactelyene, can reach conductivity levels close to that of metals (10^4 S/cm) [10].

1.1.4. BIOLOGICAL CONDUCTORS

In biological systems, electrical conductivity is generally thought to occur via hopping mechanism, referred to as multi-step hopping. The prime example is the electron transport that occurs between adjacent heme centres in multi-heme cytochromes [11]. Without these heme centres, the protein structures are insulators with large band gaps (~ 8 eV) [12]. The heme centres, iron groups that can have a Fe(II) or Fe(III) oxidation state, are hopping sites, with electrons transitioning from one site to the other. In biological proteins and other organic, flexible materials, the reorganisation effect plays a major role. This effect is not included in the Miller-Abrahams rate (Eq. 1.4), which is more suitable for inorganic semiconductors, which are inflexible. The reorganisation energy, λ, is the difference in the electron's potential energy between the charged and uncharged molecular state [13, 14], resulting from dipoles rearranging when an extra electron is loaded onto the hopping site (Fig. 1.1c). The combination of electron and dipoles is called the 'polaron'. The transition rate when accounting for this effect is the Marcus hopping rate [15]:

$$\Gamma_{\mathrm{R}} = \frac{2\pi}{\hbar}\frac{H^2}{\sqrt{4\pi\lambda k_{\mathrm{B}}T}}\exp\left(-\frac{(\lambda-(U_j-U_i))^2}{4\lambda k_{\mathrm{B}}T}\right). \tag{1.6}$$

Here, H is the electronic coupling, which comes from the electrostatic interaction between hopping sites, which is commonly described in the formulation by Mulliken and Hush [16, 17].

1.2. ELECTRICAL CONDUCTION IN MICROBIAL STRUCTURES

Now, the three most studied groups of microbial conductors will be introduced: *Shewanella* membrane extensions, *Geobacter* nanowires, and the conductive fibres of cable bacteria. The latter are the subject of this thesis.

1.2.1. SHEWANELLA

The history of the field of microbial electricity starts at lake Oneida, state of New York (USA), when the bacterium *Shewanella oneidensis MR-1* was isolated from sediments in this lake (discovery published in 1988 [18]). These bacteria live in anaerobic conditions, so they cannot rely on oxygen as an electron acceptor for their metabolism. Instead, it was found that these bacteria use external solid electron acceptors that are abundant in anoxic sediments. Specifically, it was discovered that *Shewanella* performs this extracellular electron transport by discarding its electrons onto manganese oxides (MnO_2) [18]. These minerals then dissolve to form Mn^{+2} ions, according to the redox half-reaction:

$$\mathrm{MnO_2} + 2\mathrm{e}^- + 2\mathrm{H}^+ \rightarrow \mathrm{Mn}^{2+} + 2\mathrm{OH}^-. \tag{1.7}$$

To channel electrons to these external metal oxides, *Shewanella* grows so-called nanowires, which are extracellular appendages that can be several micrometers long and several nanometers wide [19, 20] (Fig. 1.2a). These nanowires were found to be electrically conductive [19], thus explaining the capability to perform extracellular electron transport. A first estimate for the conductivity of these nanowires at room temperature was obtained from conductive Atomic Force Microscopy (c-AFM) measurements of single nanowires, and suggested a high conductivity of ~ 1 S/cm [20]. In *Shewanella* nanowires, non-linear current-voltage ($I(V)$) curves were already before, in 2008. After filtering, peaks were seen the derivative of $I(V)$ curves, which were attributed to a non-trivial density of charge carrying states, n [21]. The non-linearity itself was explained by a multi-step hopping mechanism [11]. Later, the activation energy of biofilms of *Shewanella* was measured: $U_A = 0.3$ eV [22], indicating $\lambda = 4U_A \approx 1.2$ eV, which is a typical value for cytochromes [23]. A multi-step hopping mechanism with heme cytochromes seems to be responsible for electrical conductivity in *Shewanella*.

The nanowires of *Shewanella* are extensions of the outer membrane of the bacterial cell that are richly embedded with specific type of proteins named 'cytochromes' [24]. Cytochromes are proteins that contain hemes as cofactors, which consist of iron centre coordinated by a surrounding conjugated porphyrin ring structure (also present in hemoglobin in red blood cells). The heme iron can attain multiple oxidation states (for example, Fe^{2+} and Fe^{3+}) and hence has the ability to temporally store an electron [25]). As the electrons travel from one heme centre to the other, the oxidation state of the hemes alternates between Fe^{2+} and Fe^{3+}. In *Shewanella* nanowires, multi-heme cytochromes are placed close together in the cell membrane, thus enabling an electron transport pathway [24, 26]. The electron transport mechanism hence involves a combination of direct electron hopping within the multiheme cytochromes, as well diffusion and interaction of multi-heme electron carriers themselves.

1.2.2. GEOBACTER

Similar metal-reducing bacteria exist within the *Geobacter* genus and their capacity for external electron transfer was discovered around the same time as *Shewanella*. In 1987, it was found that *Geobacter metallireducens* species perform reduction of iron minerals, thus producing magnetite in sediments of the Potamac River, Chesapeake bay (USA) [27]. To this end, these bacteria are channeling electrons freed up from organic matter oxidation to ferric (hydr)oxides in the sediment [27] (Fig. 1.2b). This process can be represented by the redox half-reaction:

$$3Fe_2O_3 + 2e^- + 2H^+ \rightarrow 2Fe_3O_4 + H_2O. \tag{1.8}$$

In 1994, a closely related species, *Geobacter sulfurreducens*, was found in a ditch contaminated with hydrocarbons, and it was able to use both iron and sulfur compounds as an electron acceptor [28]. Later on, *Geobacter sulfurreducens* was found to produce nanowires that directly contact iron oxides in order to reduce them [29]. With c-AFM measurements, these nanowires were shown to be electrically conductive [29]. Initially, it was hypothesized that *Geobacter* nanowires were made of metal-free pilin proteins [29, 30]. Yet, recently, this hypothesis has been invalidated, and detailed Cryo-Electron microscopy investigations have demonstrated that Geobacter nanowires are essentially thin protein filaments consisting of polymerized multi-heme cytochromes [31]. Different types of nanowires, containing different types of multiheme cytochrome (OmcS and OmcZ) have been reported [32]. Recently, the molecular structure of the OmcZ nanowire was resolved [33], which shows a closely packed, linearly arranged array of heme through the nanowire fiber.

Reported values for the conductivity of Geobacter nanowires show a range of conductivities. From conductive AFM measurements, conductivity levels of 1 - 4 S/cm were found [34]. In another study, two types of Geobacter nanowires were measured. It was found that the conductivity is on average is 30 S/cm for OmcZ nanowires [32], while nanowires made from OmcS cytochromes display a lower conductivity (~ 0.02 S/cm). The latter value is consistent with earlier reports on the conductivity of wild-type Geobacter nanowires [35]. When the protein pilA from *Geobacter metallireducens* is expressed in *Geobacter Sulfurreducens*, conductivity levels of in the hundreds of S/cm can be reached [36]. However, these measurements are puzzling, since the protein pilA is no longer thought to be involved in pili conduction.

In biofilms of *Geobacter* nanowires, the temperature dependence of conductivity was measured in 2011 [37]. A conductivity level at room temperature of ~ 5 mS/cm was reported. Because the conductance decreased between $T = 260$ K and $T = 300$ K, the mechanism was reported to be 'metallic-like' (in a metal, the conductivity decreases upon heating due to electron-lattice scattering). However, for lower temperatures, the conductivity showed a thermally activated behaviour with $U_A \approx 0.6$ eV [37]. The conductivity was highly tunable with a gate voltage, indicating that there is an energy gap and thus a sub-optimal charge carrier density, as in a semiconductor [37]. The increase in conductivity between room temperature and $T = 260$ K has been attributed to a restructuring of hydrogen bonds [38], which can increase conductance by a factor 300 [39]. It was suggested that this makes the structure more planar and decreases the reorganisation energy [39]. The charge transport, therefore, seems to be governed by a hopping mechanism.

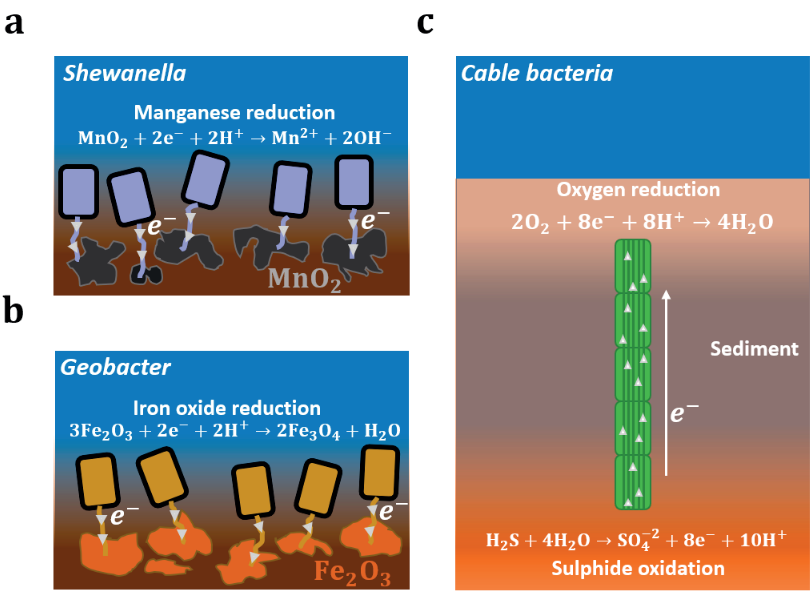

Figure 1.2: **Different types of electrogenic bacteria produce wire structures that are electrically conductive.** **a**, *Shewanella* bacteria and their nanowires (gray blue). Rocks containing manganese oxide are drawn in dark grey (water in blue, sediment in brown). For electrons (e^{-1}) the direction of flow is indicated with an arrow (they are channeled to the rocks). Only the reduction half reaction is depicted (the other half reaction involves organic matter oxidation). **b**, *Geobacter* bacteria and their nanowires, depicted in dark yellow. Rocks containing iron (hydr)oxide are drawn in orange (water in blue, sediment in brown). Only the reduction half reaction is given in the plot. **c**, Cable bacteria (green), with their internal conductive network of periplasmic fibres (dark green). Further down in the sediment, the sulphide concentration is higher (orange colour), and near the water the oxygen concentration is higher. Electron (e^{-1}), freed up by sulphide oxidation, are transported over the cable to reduce oxygen (half reactions indicated in the figure).

1.2.3. CABLE BACTERIA

Cable bacteria are multi-cellular, filamentous bacteria in the *Desulfobulbaceae* family (Desulfobacterota phylum) that have the capacity for extremely long-range transport (on the scale of the centimeters). These bacteria are relatively recently discovered (first publication in 2012 [1]), and as their name suggests, they grow to form non-branched, centimeter-long "cable" filaments that comprise > 1.000's of cells. Cable bacteria were originally discovered in marine sediments, after it was noticed that electrical currents were flowing from 1 cm down in the sediment towards the sediment-water interface [40] (Fig. 1.2c). This electrical current was accompanied by the consumption of oxygen in the top layer and a consumption of hydrogen sulphide deeper in the sediment [40]. It turned out that cable bacteria were inducing these currents by mediating an internal transport of electrons through their filaments [1]. By means of long-range electron transport, cable bacteria are coupling two redox half-reactions in the sediment that are physically separated. Deep in the sediment, hydrogen sulphide is oxidized according to the half-reaction:

$$\mathrm{H_2S + 4H_2O \rightarrow SO_4^{2-} + 10H^+ + 8e^-}. \tag{1.9}$$

Subsequently, the cable bacteria transport the electrons upwards along an internal conductor system over centimeters distance. Close to the sediment-water interface, the electrons are used to reduce oxygen (Fig. 1.2c):

$$2O_2 + 8\mathrm{H}^+ + 8\mathrm{e}^- \rightarrow 4\mathrm{H_2O}. \tag{1.10}$$

The electron transport induced by cable bacteria stretches a 10.000 times further than in the micrometer long nanowires of *Shewanella* and *Geobacter*.

The discovery of long-range electron transport by cable bacteria immediately brought up the question of how electrons were transported through the filaments. It was found that cable bacteria harbour a set of fibres in their cell envelope [41]. These fibres are located in the periplasm, which is the space between the inner membrane (which defines individual cells) and the outer membrane (which provides a "wrapping" around the filament, common to all cells). The fibers extend along the whole filament, are continuous across cell/cell interfaces, and were found to be ~ 50 nm in diameter [41]. Thick cable bacteria contain more fibers than thinner filaments, but the fiber structure appears highy similar between between different types of cable bacteria. The thick strain Ca. Electrothrix gigas (~ $5\mu m$ diameter) is examined in detail in this thesis and contains approximately 60 parallel fibres located cell envelope [42]. Based on electrode investigations and [2] and c-AFM measurements [43] it was confirmed that these perisplasmic fibers are indeed the conductive structures in cable bacteria.

A second important question pertains to the molecular structure and composition of the conductive fibers in cable bacteria. Using Raman spectroscopy, it was found that the fibres contain a sulfur-ligated nickel cofactor and do not contain cytochrome heme groups [44]. The presence of nickel-based cofactors rather than iron-based cofactors sets the conduction mechanism in cable bacteria apart from *Shewanella* and *Geobacter* nanowires. From Time-Of-Flight Secondary Ion Mass Spectroscopy (ToF-SIMS) measurements, it was furthermore deduced that the fibres are made out of protein, and contain a conductive core with a diameter of 26 nm [44].

The conductance of the fiber network in cable bacteria was measured by depositing a so-called 'fiber sheath' onto a silicon chip with pre-patterned gold electrodes [2]. A fiber sheath is obtained by chemical extraction of native cable bacterium filaments, so that only the regular network of conductive fibers remains on top of a connecting polysaccharide sheath. The long length of the fibre sheaths (up to millimeters) allows for macroscale investigation with electrode contacts, rather than conductive AFM, which reduces the risk of measurement artifacts. This way, it was also shown that the conductance of the fiber sheaths remains stable through time under vacuum conditions [2]. This hence creates a stable experimental environment in which detailed electrical characterisation of conductive structures can be performed.

Intriguingly, the conductivity of the periplasmic fibres in cable bacteria was found to reach up to 300 S/cm, which provides a high conductivity for a biological material. Moreover, the contact resistances between the gold electrode and the fibre sheaths were found to be low [2]. As such, the obtained conductivities reflect the intrinsic conductivity of the protein fibre material. Also, it was demonstrated that the activation energy of the conductivity is much lower than *Geobacter* and *Shewanella* nanowires: between 0.04 and 0.05 eV [45]. This activation energy is very small with respect to semiconducting band gaps (1.1 eV in silicon), and the activation energies observed for *Shewanella* (0.3 eV) [22] and *Geobacter* (0.6 eV) [37]. The origin of the low activation energy and high conductivity hence need to be further explained. Therefore, in this thesis, the temperature range measured over which the conductance is measured, is expanded to lower temperatures, close to absolute zero ($T = 0.1 - 300$ K). Because the activation energy is so small, the conductance drops far less rapidly than in *Shewanella* and *Geobacter*. This, in combination with the stable experimental conditions for cable bacteria [2], provides a unique opportunity for experimental investigation of the charge transport mechanism in cable bacteria.

1.3. DISSERTATION OUTLINE

This thesis addresses a number of outstanding questions pertaining to the long-range transport in periplasmic fiber network of cable bacteria: [1] What are the electrical properties of periplasmic fibers at cryogeneic temperatures? [2] What is the mechanism of charge transport in these fibers? [3] Is the charge transport different than the microbial nanowire structures from Geobacter or Shewanella? [4] Is the charge transport different from "traditional" multi-step hopping as seen in the conductive membrane proteins that contain FeS clusters or hemes as cofactors? [5] How to explain the high conductivity and low activation energy? [6] Can we explain the shape of the I/V curves recorded?

As outlined above, the temperature dependence of conductivity has the ability to differentiate conductivity mechanisms. In Chapter 2, we present detailed electrical maesurements on cable bacterium filaments over a wide range of temperatures ($T = 4 - 300$ K). This provides a set of I/V curves, from the temperature dependence of the conductivity can be derived. In Chapter 3, we address the question whether a traditional one-dimensional hopping chain allows to explain the I/V curves recorded in Chapter 2 as well as the high conductivity levels observed in cable bacteria. In Chapter 4, we study the gate-dependence of the conductance to investigate whether the charge transport displays an energy gap. In Chapter 5, we investigate the effect of a magnetic field has on the conductivity. In combination, these investigations provide a deeper insight into the conduction mechanism in cable bacteria.

2

QUANTUM-ASSISTED ELECTRON TRANSPORT IN MICROBIAL PROTEIN WIRES ACROSS MACROSCOPIC DISTANCES

**Jasper VAN DER VEEN, Silvia Hidalgo Martinez,
Albert Wieland, Matteo De Pellegrin, Rick Verweij,
Yaroslav M. Blanter, Herre S.J. van der Zant and Filip J.R. Meysman**

ABSTRACT

Multicellular cable bacteria display an exceptional form of biological conduction, channeling electrical currents across centimeter distances through a regular network of protein fibers embedded in the cell envelope. The fiber conductivity is among the highest recorded for biomaterials, providing a promising outlook for new bio-electronic technologies, but the underlying mechanism of electron transport remains elusive. Here, we use detailed electrical characterization down to cryogenic temperatures, which reveals that long-range conduction in these bacterial protein wires is based on a unique type of quantum-assisted multistep hopping. The conductance near room temperature reveals thermally activated behavior, yet with a low activation energy, suggesting that

---

This chapter is a version of the article 'Quantum-assisted electron transport in microbial protein wires across macroscopic distances', published on Arxiv.

substantial delocalization across charge carrier sites contributes to high conductivity. At cryogenic temperatures, the conductance becomes virtually independent of temperature, thus indicating that quantum vibrations couple to the charge transport. Our results demonstrate that quantum effects can manifest themselves in biological systems over macroscopic length scales.

2.1. INTRODUCTION

Conventionally, the reference point for long-range biological charge transport are the protein complexes of the electron transport chain in mitochondria or the photosynthetic reaction centers in chloroplasts [46, 47]. These membrane-bound complexes enable sequential hopping of electrons between closely spaced cofactors (e.g. hemes or iron-sulphur clusters) over total distances covering ≤ 10 nm [48]. Recent studies, however, demonstrate that biological electron transport may greatly surpass this length scale. While metal-reducing bacteria such as Geobacter and Shewanella can mediate electron transport over micrometer distances through thin surface appendages [20, 29, 31], the discovery of cable bacteria extends the range of biological electron transport to the centimeter scale [1, 3, 49]. However, the question as to why biological protein structures can sustain conduction over these macroscopic distances remains fundamentally unresolved.

Cable bacteria harbor an internal conductive network, which consists of centimeter-long protein fibers that run in the cell envelope along the entire length of the filamentous bacteria [2, 41, 43, 44, 50]. Room-temperature characterisation [2, 44, 45] reveals that these protein fibers possess an electrical conductivity up to 300 S/cm^{-1}, which surpasses that of biomaterials by several orders of magnitude, and even exceeds the conductivity of most organic semiconductors [51]. To elucidate the transport mechanism underlying this extraordinary form of biological long-range conduction, we characterised the fiber conductance over a wide temperature range from room temperature down to liquid helium temperature. These measurements reveal that charges are transported through a unique type of multi-step hopping, involving low barriers due to delocalized charge carrier wave functions and quantum vibration effects at temperatures below 75 K.

2.2. TEMPERATURE DEPENDENCE OF CONDUCTANCE

Conductivity probing as a function of temperature is widely applied to elucidate the charge transport mechanism in electronic materials [52]. For biological materials, investigation of low-temperature conduction (< 10 K) is not physiologically relevant, but is instrumental to get insight into the mechanism of electron transport in proteins, as thermal excitation becomes suppressed. Up until now, cryogenic characterization of electron transfer has been primarily applied to photosynthetic reaction centers [53, 54], which are experimentally accessible through facile light activation and high electron transfer rates. For other protein systems, however, data on low-temperature conductance are critically missing, and consequently, it remains uncertain to what extent insights and parameters from photosynthetic reaction centers can be extrapolated [55]. In particular, low-temperature conduction studies are lacking for macroscale (≥ 1 μm) protein structures, as the increasing resistance with length prevents current detection at low temperatures. The high conductance sustained across millimetres in cable bacteria

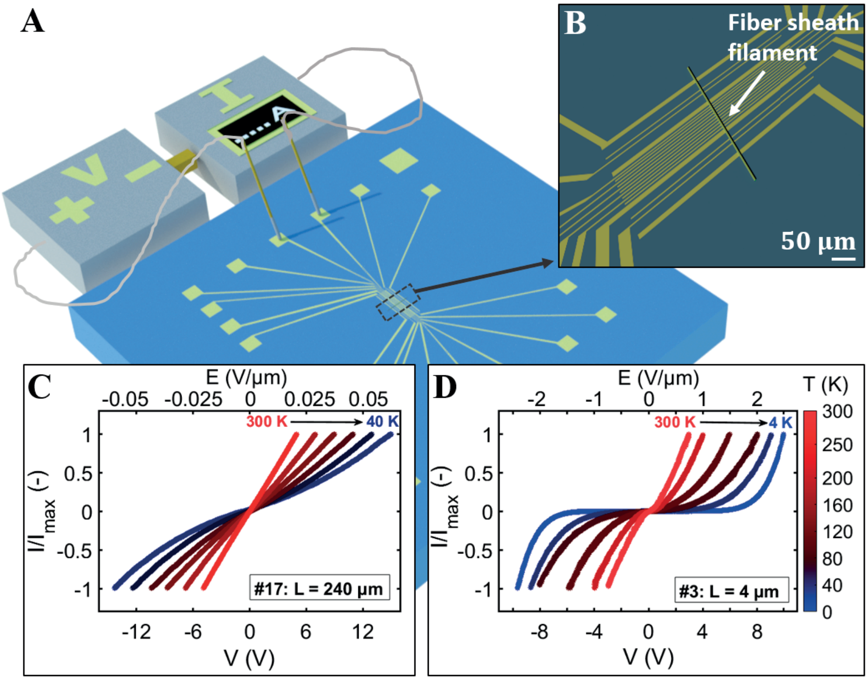

Figure 2.1: **Current as a function of temperature and electric field.** (**A**) Individual fiber sheaths are deposited on Si/SiO$_2$ substrate with prepatterned gold contacts. (**B**) A fiber sheath filament is stretched across a series of gold contacts. (**C** and **D**) Representative current (I) versus bias voltage (V) curves at different temperatures for two different segment lengths, L. The current is normalized to the maximum current of each $I(V)$ trace. Temperature is indicated by the color scale. The top axis displays the applied electric field, $E = V/L$. Shorter segments allow to investigate the conductance at lower temperatures and higher electrical fields. For the longer segment ($L = 240$ µm), the current fell below the detection limit below 40 K.

alleviates this experimental bottleneck.

To probe the conductance of the periplasmic fibers, long cable bacterium filaments (> 2 mm) were individually isolated from enrichment cultures. Subsequent extraction provides a so-called "fiber sheath" that retains the conductive fiber network lying on top of a connective carbohydrate sheath.[2] The number of parallel fibers embedded in one fiber sheath is determined by microscopy (fig. S1). Combined with the known [44] fiber diameter (26 nm), this enables the fiber conductivity to be calculated from the measured conductance (Eq. S1 in Supplementary Text). This procedure has been shown to provide reliable fiber conductivity data [2, 45], as native filaments and fibers sheaths provide similar fiber conductivities, indicating that the extraction procedure does not affect the electrical response [2].

fiber sheaths of variable length (diameter 4 µm; length up to several mm) were deposited onto insulating silicon substrates with pre-patterned gold electrodes (Fig. 2.1A) for electrical characterization under vacuum. The multiple electrical contacts per filament allow conduction to be evaluated over different segments of the fiber sheath (Fig. 2.1B). Room-temperature, four-probe measurements on single filaments show a linear dependence of the resistance R on the probed segment length L over a distance of millimeters (fig. S2). These measurements demonstrate that the fiber network possesses a uniform conductivity over mm-scale distances, which hence justifies the comparison of different segments.

Current-voltage characteristics ($I(V)$ curves) were recorded for 53 segments of varying length ($L = 4$ µm to 2 mm), of which 16 were also measured down to cryogenic temperatures (4.2 – 10 K). Measurements were highly consistent between filaments, revealing a similar response. Figure 2.1C and D display representative $I(V)$ data for both a long ($L = 240$ µm) and short segment ($L = 4$ µm) (fig. S3 provides data for all segments). The measured current shows a distinct response to the temperature, T, and to the imposed electric field, $E = V/L$. At high temperature and low electric field, the $I(V)$ curve is linear (Fig. 2.1B). Yet, when temperature decreases and the electric field strength increases, the $I(V)$ becomes increasingly more non-linear (Fig. 2.1C and D).

In a two-probe configuration, the measured resistance accounts for the intrinsic resistance of the probed filament segment as well as the contact resistance between the gold electrodes and filaments[2]. To verify our approach, two-probe and four-probe measurements were compared on the same segment, revealing that contact resistances do not influence the shape of the $I(V)$ profile, nor the temperature dependence of the conductance (fig. S5).

When replotting the $I(V)$ data in terms of the conductance, $G = I/V$, we consistently observe the same $G(T,E)$ response across all segments (Fig. 2.2A and B; fig. S3). At high temperatures ($T > 75$ K), the $G(T)$ data collected at different E-values converge (Fig. 2.2B), so conductance is not affected by the electric field. Moreover, the charge transport is thermally activated and follows a classical exponential Arrhenius-type dependence [45]. Below the cross-over temperature $T_C \backsim 75\ K$, the temperature dependence becomes noticeably weaker, and for T < 20 K, the conductance remains high and becomes virtually independent of temperature at moderate electric fields (Fig. 2.2B). At these low temperatures, the conductance is strongly affected by the electric field. For example, at 5 K, G increases by 3 orders of magnitude when E is increased from 1 to 2.5 V/µm (Fig. 2.2B).

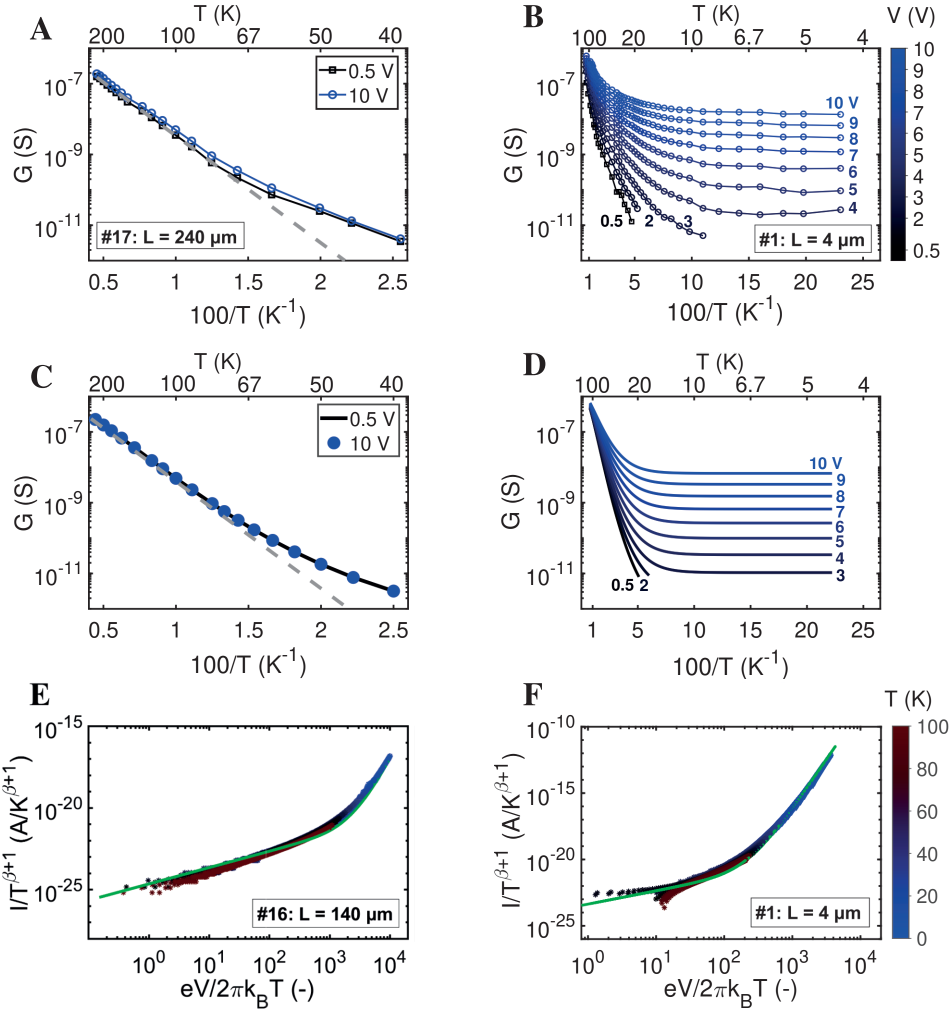

Figure 2.2: **Dependence of conductance on temperature and electrical field.** (**A** and **B**) Conductance data $G = I/V$ are plotted as a function of inverse temperature at a constant electric field strength (i.e. fixed bias voltage) for two segments of different length. Data are extracted from $I(V,T)$ curves as shown in Fig. 1. In panel (A), the Arrhenius fit to the high-temperature conductance data is included for reference (dashed grey line). (**C** and **D**) Model simulation of the conductance data in panels (A) and (B) via a 1D hopping chain model with one effective vibrational mode (Jortner model). Model parameters in panel (C): reorganization energy, $\lambda = 0.35$ eV and effective vibrational frequency, $\langle\omega\rangle = 122$ cm^{-1} (15 meV). The number of hopping sites, N_S, does not change the shape of the curve. Model parameters in panel (D): $\langle\omega\rangle = 58$ cm^{-1} (7.2 meV), $\lambda = 0.16$ eV, number of hopping sites, $N_S = 200$. (**E** and **F**) $I(V,T)$ data replotted as a universal scaling curve [56, 57]; T is temperature, e is the elementary charge, and k_B is Boltzmann's constant. The green solid line represents a model fit to the data that has two fitting parameters: the dimensionless exponent β and the number of hopping sites, N_S. For the longer segment, $N_S = 1400$ and $\beta = 6.0$; for the shorter segment, $N_S = 120$ and $\beta = 6.5$.

2.3. QUANTUM VIBRATIONS COUPLE TO THE ELECTRON TRANSPORT

The observation that the conductance remains elevated as the temperature decreases, and eventually becomes independent of temperature, is remarkable. The deviation from an exponential temperature dependence is at odds with the standard semi-classical Marcus theory of electron transfer [15], which assumes that transitions are thermally activated. The fact that the conductance remains high at low temperatures thus hints at an energy source other than thermal energy that assists the charge transfer. In seminal experiments on photosynthetic reaction centers in purple bacteria, DeVault and Chance observed a similar temperature dependence that could not be accounted for by Marcus theory. The charge separation reactions of photosynthesis continued at cryogenic temperature and the rate of these reactions became independent of temperature [53, 54].

This finding spurred a host of theoretical developments, which eventually extended electron transfer theory to a fully quantum-mechanical treatment [56, 58–60]. Quantum theory asserts that at absolute zero, molecular vibrations retain a finite zero-point energy. At low temperatures, thermal motion is frozen out, but quantised vibrational modes can assist the electron tunnelling, in a process referred to as nuclear tunneling [58, 59]. Marcus theory[15] accounts for electron tunneling, but uses a classical harmonic approximation of the nuclear motion, so it neglects the impact of nuclear tunneling and therefore underestimates the electron transfer rate at low temperatures.

To verify whether nuclear tunnelling could explain our observations, we modelled electron transport subject to quantum vibrational coupling in a one-dimensional hopping chain that mimics the conduction path in the fiber sheaths (Supplementary Text). In metalloproteins, vibrational coupling can involve both high-frequency intramolecular vibrations of the charge carrying cofactor as well as lower-frequency vibrations of the surrounding protein matrix and solvent molecules. This vibrational coupling can be described with models of increasing complexity. As a first step, we applied a model where only one effective high-frequency mode $\langle\omega\rangle$ stimulates the hopping process (Jortner model [59], Supplementary Text). These model calculations adequately capture the essence of our experimental data: the conductance displays two regimes with a transition at the cross-over temperature $T_\mathrm{C} = \hbar\langle\omega\rangle/k_\mathrm{B}$, where k_B is the Boltzmann constant and $\hbar$ the reduced Planck constant. For $T > T_\mathrm{C}$, the vibrational mode remains thermally excited, and the conductance adopts a classical Arrhenius-type dependence (Fig. 2.2C). Below T_C, the vibrational mode is no longer thermally excited, but due to the quantum vibrational energy, the conductance remains higher than predicted by the Arrhenius relation. Upon further cooling below $T_\mathrm{C}/5 \approx 25$ K, the conductance becomes virtually independent of temperature (Fig. 2.2D).

Across all sixteen segments investigated, we find a mean cross-over temperature $T_C = 75 \pm 14$ K, which corresponds to a characteristic frequency $\langle\omega\rangle = k_\mathrm{B} T_C/\hbar = 52 \pm 10\ \mathrm{cm}^{-1}$ for the single effective vibrational mode that couples to the electron hopping (vibrational energy $\hbar\langle\omega\rangle = 6.4 \pm 1.2$ meV). The experimental verification of vibronic coupling is highly challenging in biological systems, and has only been done for photosynthetic reaction centers, which yields substantially higher characteristic frequencies $\hbar\langle\omega\rangle \approx 60$ meV [61]. Previously, it has been speculated that the 60 meV frequency could be a general feature of electron tunneling reactions in natural proteins [55]. Our results invalidate this hypothesis, and instead, suggest a substantial variability in vibrational coupling, where the characteristic frequency is likely dependent on the specific molecular configuration of the cofactor and metalloprotein involved in the electron transport. To illustrate this, fig. S9 compares the data fit for a cable bacterium to that of the photosynthetic reaction center in *Allochromatium vinosum*.

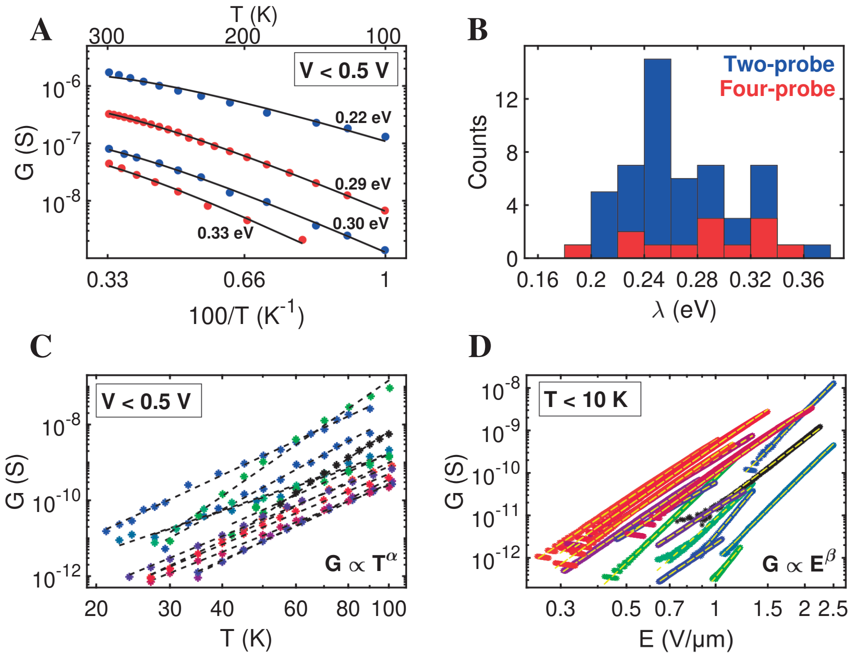

Figure 2.3: **Empirical fits to conductance data.** (**A**) Low-bias conductance, G, as a function of inverse temperature for $T > 100$ K. Data for 4 segments. Two- and four-probe measurements are shown in blue and red markers respectively. Solid black lines are fits by the non-linear least squares method to the Marcus equation $G = g_0 (k_B T)^{-3/2} \exp(\frac{\lambda}{4 k_B T})$, where g_0 is a pre-factor and λ the reorganization energy, of which the value is given next to the data. (**B**) Histogram with reorganization energies for $n = 53$ samples (blue: two-probe measurements; red: four-probe measurements). (**C**) Low-bias conductance against temperature in the region 20 – 100 K for 16 segments. Black dashed lines represent power law fits (determining α). (**D**) Conductance versus applied electric field at the lowest temperature achieved ($T < 10$ K), for the same 16 segments. Yellow dashed lines represent power law fits (determining β).

2.4. CONDUCTANCE FOLLOWS A UNIVERSAL SCALING RELATION

The single-mode vibrational model predicts that the zero-bias conductance should become constant at the lowest temperatures. Yet closer data inspection reveals that the conductance continues to decrease as a power law ($G \propto T^{\alpha}$; Fig. 2.3C), which suggests that vibrational modes lower than $\omega = k_B T_C / \hbar$ are additionally coupling to the electron transport. To accommodate for this, we integrated a multi-mode description of vibrational coupling in our one-dimensional hopping model (Egger model [56], Supplementary Text). There are several predictions that can be tested. At high temperatures, all vibrational modes must remain thermally excited, and hence, one should retrieve the results of Marcus theory. This is indeed the case. For $T > 100$ K, the conductance follows a Marcus-type dependence on temperature, $G \backsim T^{-3/2}\exp(-\lambda/4k_BT)$, where λ is the reorganization energy (Fig. 2.3A; Supplementary Text). Also, at high temperatures, the conductance should remain independent of E, which provides linear $I(V)$ curves, as observed (Fig. 2.1B). The reorganization energy is low and shows limited variation (Fig. 2.3B), $\lambda = 270 \pm 40$ meV ($n = 53$ segments). The corresponding activation energy, $U_A = \lambda/4 = 42 \pm 8$ meV (fig. S6), aligns well with earlier high-temperature electrical measurements on both intact cable bacteria and fiber sheaths [45].

The multi-mode model predicts that the conductance should follow a power-law dependence on temperature at low electric fields, $G \propto T^{\alpha}$, and a power-law dependence on the electric field at low temperatures, $G \propto E^{\beta}$. The fiber network conductance indeed shows such a power law behaviour with exponents $\alpha \approx 3.7 - 7.7$ and $\beta \approx 4.0 - 8.3$ (Fig. 2.3C and D; table S2). Moreover, the multi-mode model asserts that in the low-temperature regime, the $I(V, T)$ data for a given segment can be suitably reduced to a single universal scaling curve [57] (see Supplementary Text), which features the normalized current $I/T^{1+\beta}$ as a function of a normalized bias $\overline{V} = eV/(2\pi k_BT)$. The rescaled I/V data closely follow this universal scaling curve for all 16 segments investigated (Fig. 2.2E and F; fig. S4). This universal scaling behavior has not been seen before for a biological material, but is characteristic for various synthetic one-dimensional conductors, such as networks of graphene nanoribbons[62] and carbonized polymer nanofibers[63], which display similarly high conductivities as the periplasmic fibers in cable bacteria. Moreover, the power law exponent β, which designates the degree of vibronic coupling, is on par with these synthetic conductors, thus suggesting that cable bacteria may have evolved a similar electron relay system.

2.5. A UNIQUE FORM OF MULTISTEP HOPPING

Our results provide several insights into the mechanism that sustains long-range conduction in the periplasmic fiber network of cable bacteria. Foremost, the observed temperature dependence of conduction displays the hallmark of quantum-mechanical electron tunneling [55]. At high temperatures, electron transport is assisted by thermal fluctuations, thus providing an Arrhenius dependence, while at low temperatures, quantized molecular vibrations couple to the electron transfer, thus resulting in higher conductance than classically expected. Nuclear tunneling has been previously observed in photosynthetic reactions centers [54], but not in macroscale electron transfer.

Electron tunneling shows a strong exponential dependence of the electron transfer rate on distance, which limits individual electron transfer events to distances ≤ 1.5 nm [55]. Still, it is well known that protein structures can support electron transport over much longer distances, of which the cm-scale conduction in cable bacteria represents the most extreme example. Biology has resolved this problem by arranging cofactors in chains at close spacings (typically 10–15 Å). This enables multi-step electron hopping, in which electrons are moving through the protein matrix by consecutive tunneling steps, as for example, documented for multiheme cytochromes involved in extracellular respiration [48] and FeS clusters aligned in the complexes of the respiratory chain [64]. While our data support this multi-step hopping picture, there are several unique features in which the electron transport in cable bacteria is distinct from the currently known forms of long-range electron transport in proteins.

Foremost, the length scale over which hopping takes place in cable bacteria is extraordinary, as it covers distances of millimetres to centimeters. Raman spectroscopy has shown that the periplasmic fiber network does not contain FeS clusters nor cytochromes [2, 44], thus excluding a heme-based conduction mechanism as found in the surface appendages of metal-reducing bacteria [24, 31, 65]. Instead, recent work suggests that the periplasmic fibers in cable bacteria contain a nickel-sulfur cofactor that mediates the electron transport [44]. The involvement of nickel is remarkable, as all currently known metalloproteins involved in electron transport rely on either iron- or copper-containing cofactors, but never nickel [66]. It is thus reasonable to suggest a model in which the quantized vibrational modes of this nickel-sulfur cofactor are strongly coupled to the electron transport. If such vibronic coupling is due to a single mode, this mode would have characteristic frequency of $\omega \approx 50$ cm^{-1}. The corresponding Huang-Rhys factor, which provides a dimensionless measure for the coupling strength, is high ($S = \lambda/\hbar\langle\omega\rangle = 42$), thus indicating strong vibronic coupling. While the molecular structure of nickel cofactor remains unresolved, the appearance of distinct Ni-associated Raman peaks in the spectra of fiber sheaths near this frequency [44] suggests that cofactor modes could be indeed involved in the reorganization process [67]. Most likely, multiple modes are coupling to the electron transport, which then provides the observed universal scaling response (Fig. 2.2E and F) as also seen in abiotic one-dimensional conductors [57, 63, 68].

A second notable feature is that the reorganization energy at room temperature (0.27 eV) is markedly lower than observed for other forms of biological electron transport. Typical values for single electron transfer steps in enzymes are in the range $0.7 < \lambda < 1.4$ eV, while multi-step electron transport in the surface appendages of the metal-reducing bacteria also exhibits similarly high reorganization energies [22, 37]. Within the thermally activated regime, and assuming a negligible driving force (as the voltage bias is distributed over very many transitions in the hopping chain), the rate of electron transfer scales with $\sim \exp(\lambda/4k_B T)$, and so, a low reorganization energy helps explaining the extraordinary high fiber conductivity observed in cable bacteria. Moreover, the reorganization energy is known to inversely scale with the localisation length of the charge carriers [69]. Therefore, high reorganization energies imply that electrons are strongly localized on the charge carrier site, while low reorganization energies, as seen here, suggest substantial delocalization of the charge carrier wave function. Heme-localised electronic states are examples of the former: they form low energy states (“traps”) that are separated by sizable activation barriers of 0.2 −0.3 eV, which are large compared to thermal activation barrier ($\approx 10\ k_B T$ at 300 K) [48]. In contrast, the electronic states on the cable bacterium fibers appear to be far more delocalized, thus enabling fast transitions. Comparably low reorganization energies have been reported for highly-mobility organic semiconductors, such as rubrene and naphtalene[70], in which the charge carrier sites display sizeable conjugation and delocalization.

2.6. THE CHALLENGE OF HIGH CONDUCTIVITY

Overall, the observed temperature dependence is consistent with multistep hopping, which forms the cornerstone of the existing theories of long-range biological electron transfer [48]. Still, the high fiber conductivity recorded (up to ∽ 100 S cm^{-1}; fig. S2) poses a profound challenge to this hopping model. The key problem is the magnitude of the electron transfer rate Γ_R, which is related to the fiber conductivity σ via the relation

$$\Gamma_{\mathrm{R}} = \sigma \frac{k_{\mathrm{B}} T}{e^2} \frac{\pi N_{\mathrm{S}} d_{\mathrm{F}}^2}{L N_{\mathrm{C}}}, \tag{2.1}$$

In nearly all electron transfer reactions in biology, the center-to-center spacing between charge carriers falls within the range of $a = 0.5 - 2$ nm. Consequently, one needs N_{S} = 5-20 x 10^6 sequential charge carriers to cover the typical L = 1 cm length scale of a cable bacterium filament. Even if we assume massive parallelization of conduction channels (each fiber consists of $N_{\mathrm{C}} = 125$ parallel channels of 2 nm diameter; Supplementary Text), the required transition frequency for nearest neighbor hopping exceeds 10^{13} s^{-1} (see details in Supplementary Text). This < 0.1 picosecond electron transfer rate is orders of magnitude faster than currently observed for non-light driven electron transfer, which maximally reaches nanoseconds for inter-heme transfer in cytochrome c oxidase, but is more typically on the scale of microseconds [48]. Effectively, the 10^{13} s^{-1} hopping rate exceeds the speed limit of non-adiabatic electron transfer, where relaxation times of vibrational modes are slower than the hopping rate itself [55, 71].

Our data hint at a possible resolution to this problem. A larger center-to-center distance would allow for the same conductivity with a smaller hopping rate, thus bringing the electron transport back in the non-adiatabic regime. The universal scaling curve displays a cross-over point between high and low temperature regimes, which enables a direct estimate for the number of hopping sites ($N_{\mathrm{S}} = eV/(2\pi k_{\mathrm{B}} T)$). We find that N_{S} linearly scales with the segment length L (table S2; fig. S8), thus providing a center-to-center distance between hopping sites in excess of 10 nm. Clearly, this distance is far too large to enable through-space tunneling of electrons [72, 73], and largely exceeds the known heme-to-heme distances in cytochromes (< 1 nm) [23, 74]. Still, in doped organic semiconducting nanowires, like polyacetylene, the universal scaling curves provides similar center-to-center distances (~ 10 nm) [57, 63, 68]. A potential model that can accommodate these large center-to-center distance consists of hopping chains embedding stacks of tightly spaced cofactors (> 10 nm). Electron tunneling then occurs across low-potential barriers between the cofactor stacks, while in the internal part of the stacks, electrons are delocalized and electron transport occurs largely unobstructed (fig. S7). This speculative model provides a potential explanation of how the high electrical conductivity in the periplasmic fibers in cable bacteria can be reconciled with the multistepping mechanism that emerges from data obtained here, but requires further experimental validation. Ultimately, such a better understanding of the charge carrier transport in cable bacteria may enable the design and construction of new bio-mimetic materials for electronics and energy conversion [75–77].

2.7. METHODS

CONDUCTIVE FIBER NETWORKS FROM CABLE BACTERIA

Cable bacterium filaments were harvested from enrichment cultures that were set up using natural sediment collected in the creek bed of a salt marsh (Rattekaai, The Netherlands). Upon collection, sediment was sieved and repacked into PVC core liner tubes (diameter 40 mm). The cores were incubated in aerated artificial seawater at *in situ* salinity, and the development of cable bacteria was tracked by microsensor profiling and microscopy (procedure as in Ref. 11). Under a stereo microscope, individual filaments were gently pulled out from the top layer of the sediment with custom-made glass hooks.

Through sequential extraction, the conductive fiber network is isolated from the cell envelope of individual filaments. This extraction removes the membranes and cytoplasm, but retains the parallel conductive fibers embedded in a basal sheath (procedure as in Ref. 8). These so-called "fiber sheaths" form the starting material for all investigations performed here. To produce these fiber sheaths, freshly isolated cable bacterium filaments were cleaned by transferring them at least six times between droplets ($\sim$20 µl) of MilliQ water on a microscope cover slip. Subsequently, filaments were extracted in a droplet of 1 (w/w) sodium dodecyl sulfate (SDS) for 10 minutes, followed by six MilliQ washes. Filaments were then incubated for 10 minutes in a droplet of 1 mM sodium ethylene diamine tetra-acetate (EDTA), pH 8, and again six times washed in MilliQ.

ELECTRICAL CHARACTERIZATION DOWN TO CRYOGENIC TEMPERATURES

Gold electrode patterns (Fig. 2.1) were deposited onto p^{++}-doped silicon substrates with a surface layer of silicon dioxide (285 or 500 nm thickness) via optical lithography. A laser writer illuminates the desired pattern in a single light-sensitive resist layer (AZ ECI 3007 or 3012). The laser wave length (365 nm) limits the minimum feature size to approximately 1 µm. The gold thickness was 100 nm, with 5 nm of titanium underneath to promote adhesion of the gold layer to the SiO_2 surface. Fiber sheaths were positioned onto patterned substrates immediately after extraction and substrates were directly transferred to the vacuum chamber of the probe station. In this way, fiber sheaths retain a stable conductance for up to a period of weeks [2].

The conductance of fiber sheaths was measured down to liquid helium temperatures in two separate set-ups. The first setup is based around a dewar of helium, in which a stick containing a vacuum sample chamber can be inserted. In this setup, the patterned substrates were glued to a chip carrier, either with silver paint or epoxy glue. The electrode pads of the substrate were subsequently wire bonded to the electrodes of the chip carrier. For the lowest temperatures ($T < 20$ K) the sample chamber is not completely vacuum, because helium exchange gas is used to reach the desired temperature. The minimum temperature reached is near the helium condensation point (4.2 K). For higher temperatures ($T > 20$ K), this exchange gas was pumped out of the sample chamber. A resistor was used to heat up the device, while a thermometer is placed nearby the sample to measure the temperature. The second set-up used was a cryo-free LakeShore Cryogenic Probe Station (Type CRX 6.5 K). In this case, the electrode pads did not need to be wire bonded. Of the 16 segments for which the temperature dependence was measured down to the lowest temperatures ($T < 10$ K; fig. S3), segments 1 - 5 were measured in the first set-up and segments 6 - 16 were measured in the second.

To assess the impact of contact resistances, two-probe and four-probe measurements were conducted. In a two-probe measurement, a bias voltage, V_B, is applied across two electrodes, and the induced current, I_M, is measured. This yields the two-probe resistance, $R_{2P} = V_B / I_M = R_i + R_C$, which is composed the intrinsic resistance of the fiber sheath segment, R_i, and the two contact resistances between the fiber sheath and the electrodes, R_C. In the four-probe approach, the bias current, I_B, is injected over the two outer electrodes, while the voltage, V_M, is measured over the two inner electrodes. The four-probe resistance, $R_{4P} = V_M / I_B$, equals the intrinsic resistance of the conductive fiber sheath segment between the two inner pads. The contact resistance is hence determined as $R_C = R_{2P} - R_{4P}$.

2.8. FIGS. S1 TO S9

FIGURE S1

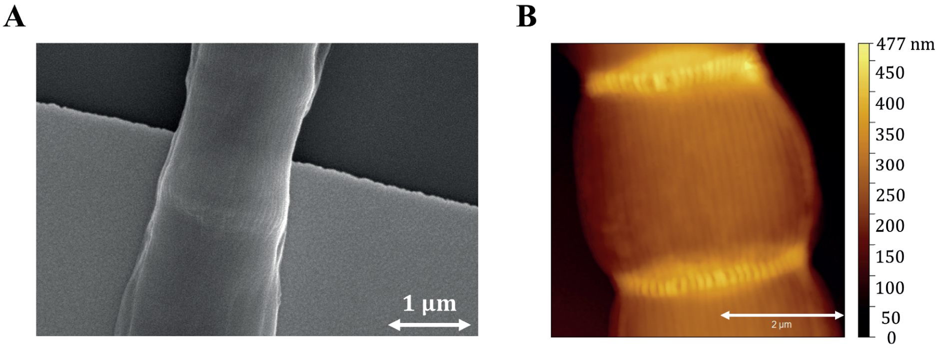

Figure S1: **Microscopic images of fiber sheaths from cable bacteria**. (**A**) Scanning electron micrograph (acceleration voltage 10 kV) of a fiber sheath deposited silicon-dioxide substrate with gold patterned electrodes. The scale bar is indicated in the bottom right corner of the image. The dark background is silicon dioxide, the lighter grey background is the gold electrode. (**B**) Atomic force microscopy image of a fiber sheath filament. The colour indicates the measured height profile (see colour bar). The fiber sheath displays the conductive fibers as a set of lines running in parallel to the bacterial filament.

FIGURE S2

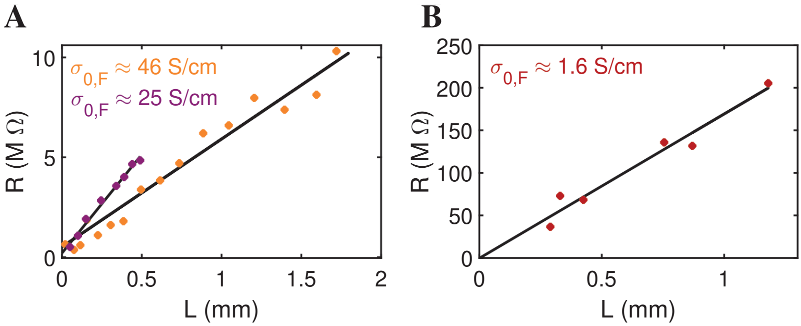

Figure S2: **Linear dependence of electrical resistance on probing length over mm distances.** (**A** and **B**) Four-probe measurements of the resistance, R, as a function of the electrode spacing, L, at 300 K for three separate fiber sheath filaments of cable bacteria. In these measurements, the two current-carrying electrodes and one voltage-sensing electrode were kept at a fixed position, while the second voltage-sensing electrode was varied along the filament, for increasing L. The resistance was calculated as $R = V/I$, where V is the voltage measured across the voltage-sensing electrodes and I is the applied current. The resistance increases linearly with the probing length L, thus demonstrating that the fiber network possesses a uniform conductivity. The black lines represent linear fits through the data, which provide an estimate of the fiber conductivity (inset values) derived as $\sigma_{0,F} = 4/(N_F \pi d_F{}^2 b)$, where b is the fitted slope, $N_F = 60$ is the number of fibers in a filament (as determined by microscopy), and $d_F = 26$ nm is the cross-sectional diameter of the conductive core of a fiber [2, 44].

FIGURE S3

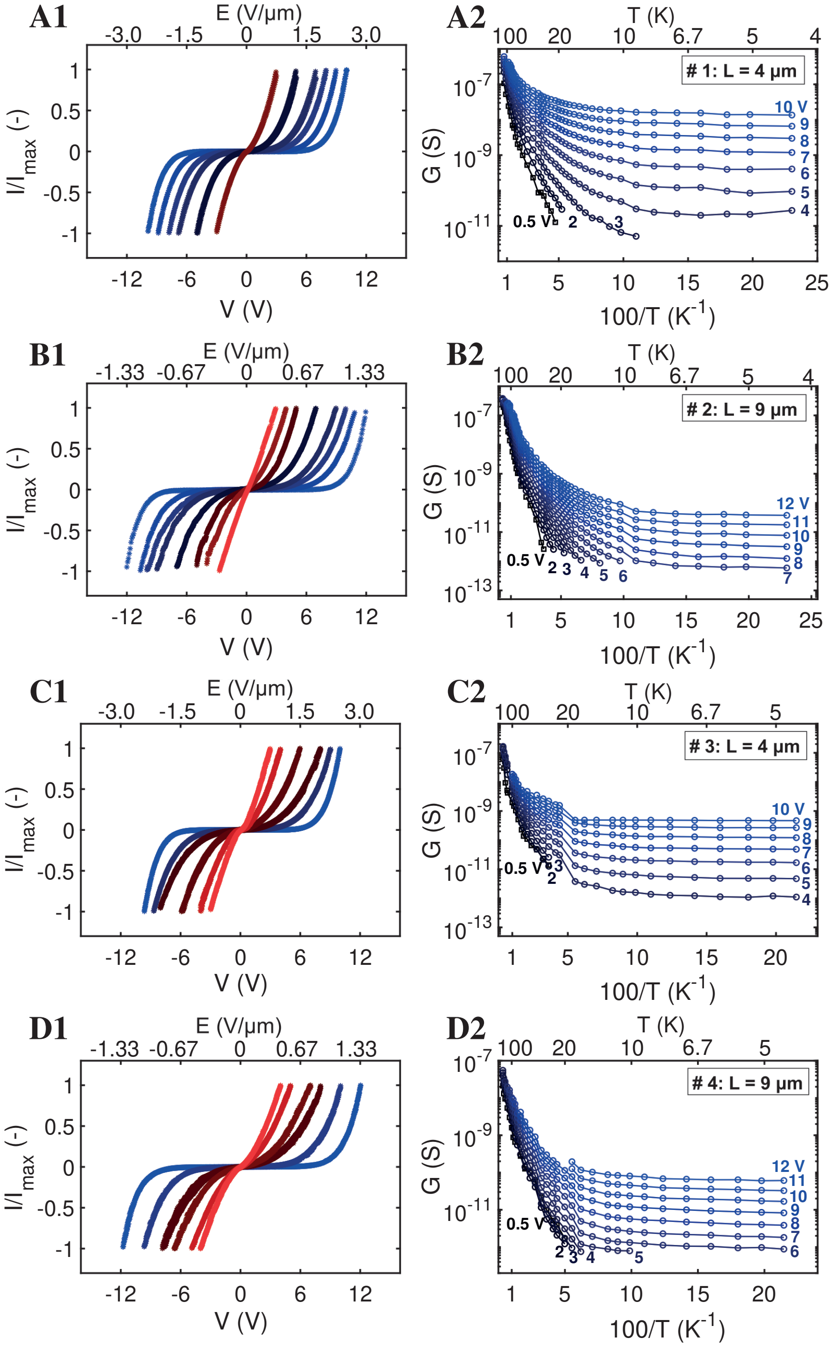
A1
E (V/μm)
-3.0 -1.5 0 1.5 3.0
I/I_max (-)
1 0.5 0 -0.5 -1
-12 -6 0 6 12
V (V)
A2
T (K)
100 20 10 6.7 5 4
1: L = 4 μm
G (S)
10^-7 10^-9 10^-11
10 V 9 8 7 6 5 4
0.5 V 2 3
1 5 10 15 20 25
100/T (K^-1)
B1
E (V/μm)
-1.33 -0.67 0 0.67 1.33
I/I_max (-)
1 0.5 0 -0.5 -1
-12 -6 0 6 12
V (V)
B2
T (K)
100 20 10 6.7 5 4
2: L = 9 μm
G (S)
10^-7 10^-9 10^-11 10^-13
12 V 11 10 9 8 7
0.5 V 2 3 4 5 6
1 5 10 15 20 25
100/T (K^-1)
C1
E (V/μm)
-3.0 -1.5 0 1.5 3.0
I/I_max (-)
1 0.5 0 -0.5 -1
-12 -6 0 6 12
V (V)
C2
T (K)
100 20 10 6.7 5
3: L = 4 μm
G (S)
10^-7 10^-9 10^-11 10^-13
10 V 9 8 7 6 5 4
0.5 V 3 2
1 5 10 15 20
100/T (K^-1)
D1
E (V/μm)
-1.33 -0.67 0 0.67 1.33
I/I_max (-)
1 0.5 0 -0.5 -1
-12 -6 0 6 12
V (V)
D2
T (K)
100 20 10 6.7 5
4: L = 9 μm
G (S)
10^-7 10^-9 10^-11
12 V 11 10 9 8 7 6
0.5 V 2 3 4 5
1 5 10 15 20
100/T (K^-1)

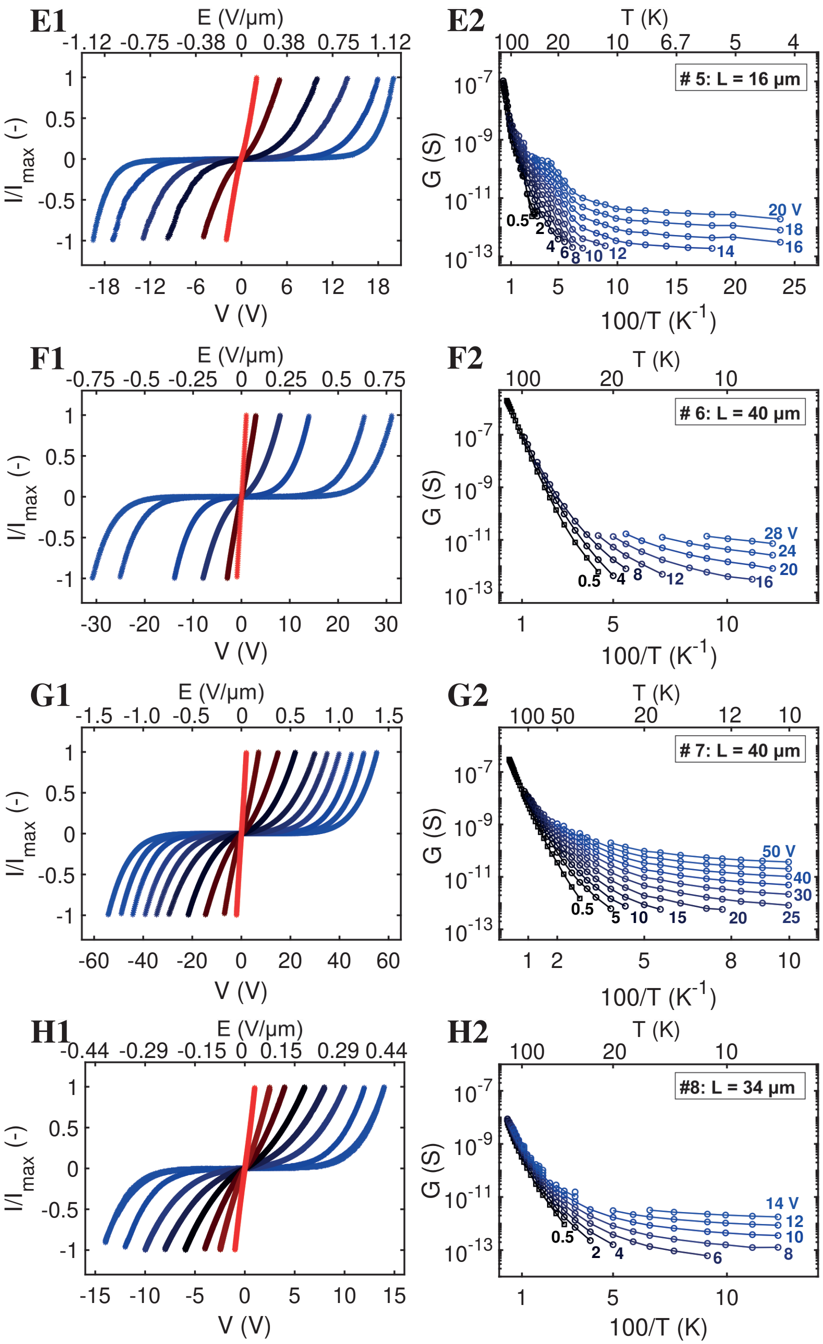
E1
E (V/μm)
-1.12 -0.75 -0.38 0 0.38 0.75 1.12
I/I_max (-)
1
0.5
0
-0.5
-1
-18 -12 -6 0 6 12 18
V (V)
E2
T (K)
100 20 10 6.7 5 4
5: L = 16 μm
G (S)
10^-7
10^-9
10^-11
10^-13
0.5
2
4
6
8
10
12
14
16
18
20 V
1 5 10 15 20 25
100/T (K^-1)
F1
E (V/μm)
-0.75 -0.5 -0.25 0 0.25 0.5 0.75
I/I_max (-)
-30 -20 -10 0 10 20 30
V (V)
F2
T (K)
100 20 10
6: L = 40 μm
G (S)
0.5
4
8
12
16
20
24
28 V
1 5 10
100/T (K^-1)
G1
E (V/μm)
-1.5 -1.0 -0.5 0 0.5 1.0 1.5
I/I_max (-)
-60 -40 -20 0 20 40 60
V (V)
G2
T (K)
100 50 20 12 10
7: L = 40 μm
G (S)
0.5
5
10
15
20
25
30
40
50 V
1 2 5 8 10
100/T (K^-1)
H1
E (V/μm)
-0.44 -0.29 -0.15 0 0.15 0.29 0.44
I/I_max (-)
-15 -10 -5 0 5 10 15
V (V)
H2
T (K)
100 20 10
#8: L = 34 μm
G (S)
0.5
2
4
6
8
10
12
14 V
1 5 10
100/T (K)

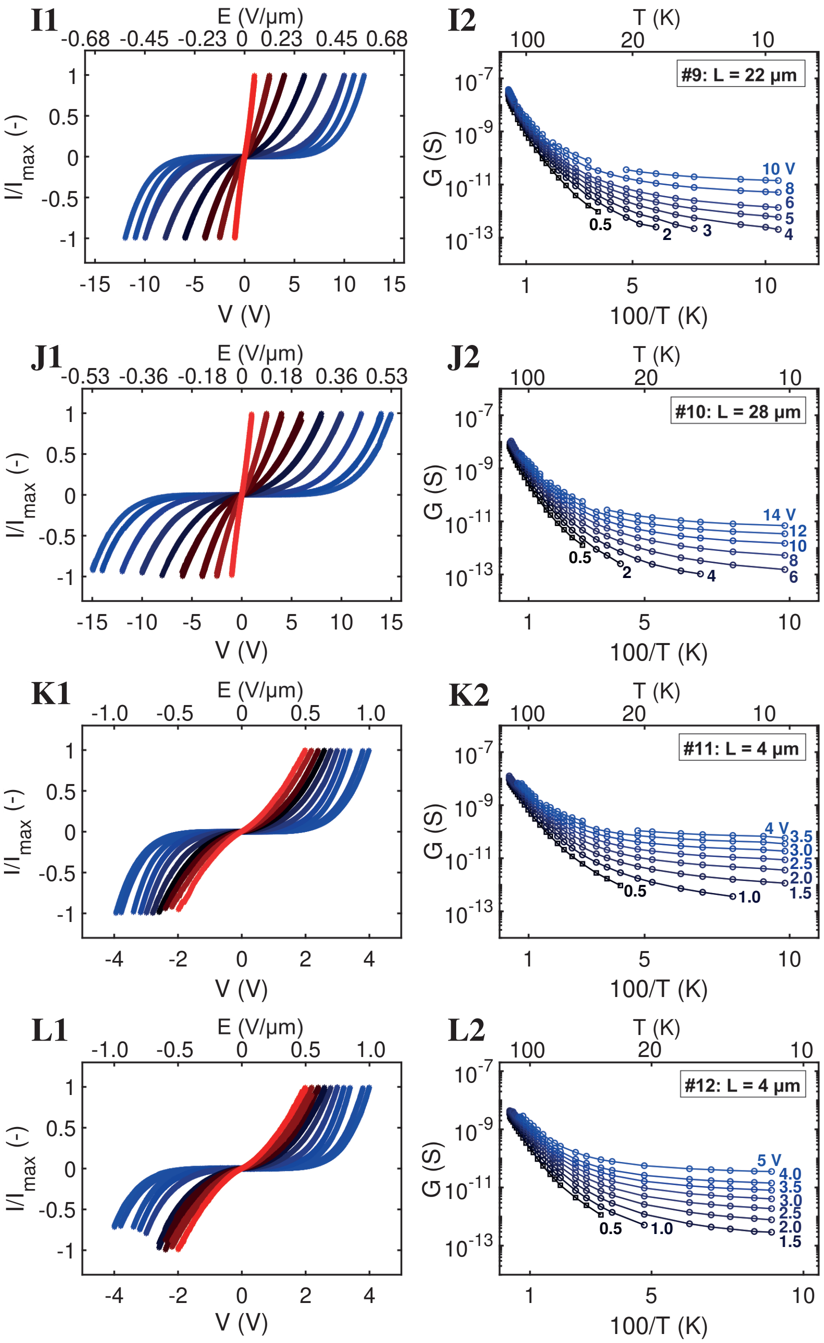
I1
E (V/µm)
-0.68 -0.45 -0.23 0 0.23 0.45 0.68
I/I$_{max}$ (-)
1 0.5 0 -0.5 -1
-15 -10 -5 0 5 10 15
V (V)
I2
T (K)
100 20 10
#9: L = 22 µm
G (S)
10^{-7} 10^{-9} 10^{-11} 10^{-13}
10 V
8
6
5
4
3
2
0.5
1 5 10
100/T (K)
J1
E (V/µm)
-0.53 -0.36 -0.18 0 0.18 0.36 0.53
I/I$_{max}$ (-)
1 0.5 0 -0.5 -1
-15 -10 -5 0 5 10 15
V (V)
J2
T (K)
100 20 10
#10: L = 28 µm
G (S)
10^{-7} 10^{-9} 10^{-11} 10^{-13}
14 V
12
10
8
6
4
2
0.5
1 5 10
100/T (K)
K1
E (V/µm)
-1.0 -0.5 0 0.5 1.0
I/I$_{max}$ (-)
1 0.5 0 -0.5 -1
-4 -2 0 2 4
V (V)
K2
T (K)
100 20 10
#11: L = 4 µm
G (S)
10^{-7} 10^{-9} 10^{-11} 10^{-13}
4 V
3.5
3.0
2.5
2.0
1.5
1.0
0.5
1 5 10
100/T (K)
L1
E (V/µm)
-1.0 -0.5 0 0.5 1.0
I/I$_{max}$ (-)
1 0.5 0 -0.5 -1
-4 -2 0 2 4
V (V)
L2
T (K)
100 20 10
#12: L = 4 µm
G (S)
10^{-7} 10^{-9} 10^{-11} 10^{-13}
5 V
4.0
3.5
3.0
2.5
2.0
1.5
1.0
0.5
1 5 10
100/T (K)

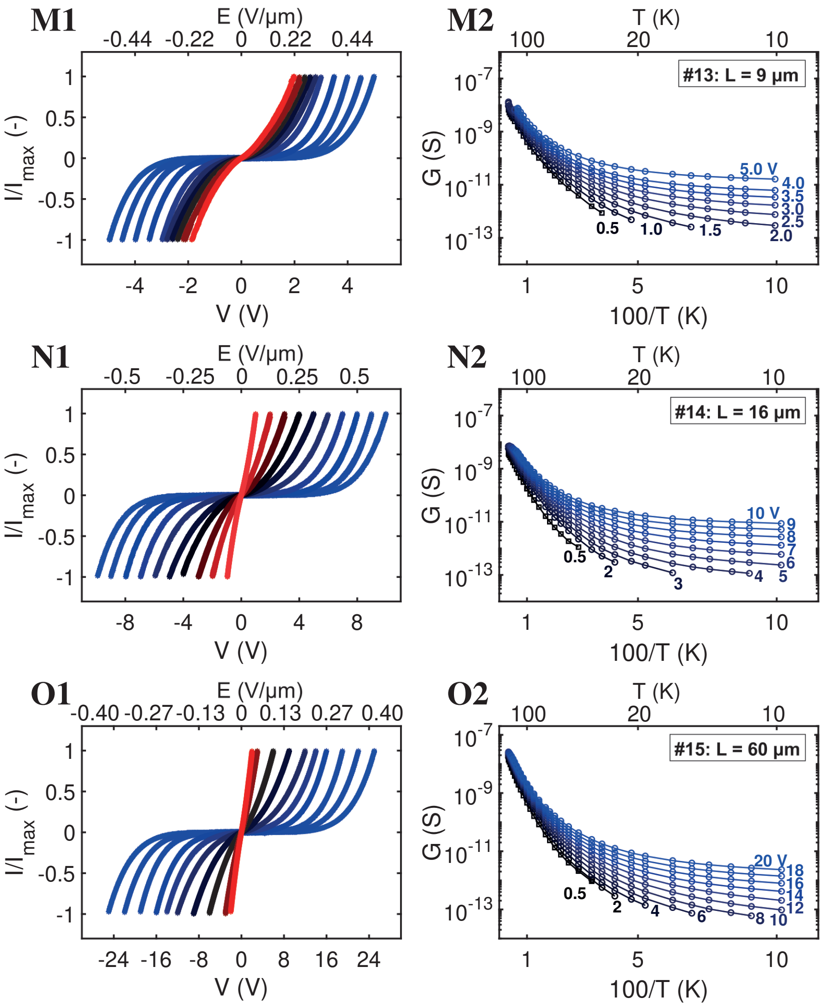
M1
E (V/μm)
-0.44 -0.22 0 0.22 0.44
I/I$_{max}$ (-)
1
0.5
0
-0.5
-1
-4 -2 0 2 4
V (V)
M2
T (K)
100 20 10
#13: L = 9 μm
G (S)
10^{-7}
10^{-9}
10^{-11}
10^{-13}
5.0 V
4.0
3.5
3.0
2.5
2.0
0.5
1.0
1.5
1 5 10
100/T (K)
N1
E (V/μm)
-0.5 -0.25 0 0.25 0.5
I/I$_{max}$ (-)
1
0.5
0
-0.5
-1
-8 -4 0 4 8
V (V)
N2
T (K)
100 20 10
#14: L = 16 μm
G (S)
10^{-7}
10^{-9}
10^{-11}
10^{-13}
10 V
9
8
7
6
5
4
3
2
0.5
1 5 10
100/T (K)
O1
E (V/μm)
-0.40 -0.27 -0.13 0 0.13 0.27 0.40
I/I$_{max}$ (-)
1
0.5
0
-0.5
-1
-24 -16 -8 0 8 16 24
V (V)
O2
T (K)
100 20 10
#15: L = 60 μm
G (S)
10^{-7}
10^{-9}
10^{-11}
10^{-13}
20 V
18
16
14
12
8 10
6
4
2
0.5
1 5 10
100/T (K)

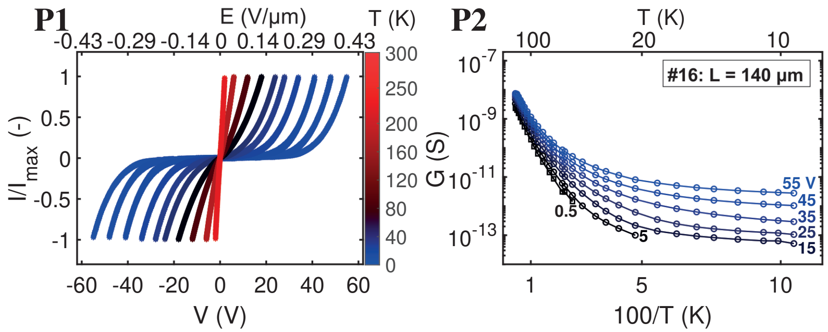

Figure S3: **Current/voltage measurements as a function of temperature.** The two panels in each row display data for a given fiber sheath segment of length L. Data are provided for 16 segments of different length. (**A1** to **P1**) Two-probe current-voltage ($I(V)$) characteristics recorded at different temperatures. To illustrate the change in shape of the $I(V)$ curve, the current is normalized to the maximum current obtained for the given trace. The top axis shows the applied electric field, $E = V/L$. The colour of the lines indicates the temperature (linearly changing from red to black in the range $300-80$ K and from black to blue in the range $80-4$ K). See colour bar next to panel (P1). (**A2** to **P2**) The same dataset is replotted in terms of the conductance, $G = I/V$, as a function the inverse temperature, $100/T$, for different bias voltages, V. The colour scale linearly ranges from black (zero-bias voltage) to blue (maximum bias voltage). Note that this voltage range differs per segment. The segment number and segment length are indicated in the right panels (see also table1).

Figure S4

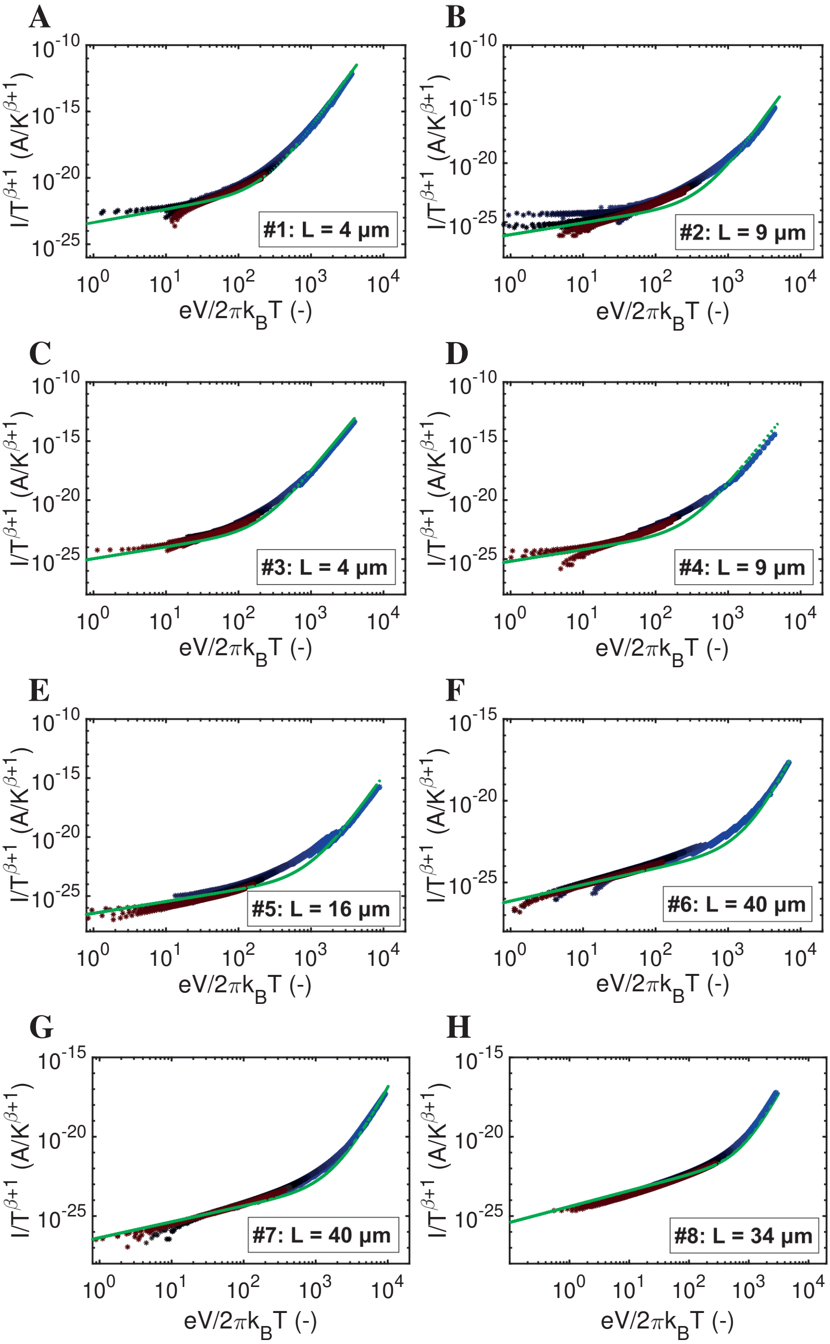
A
B
C
D
E
F
G
H
#1: L = 4 μm
#2: L = 9 μm
#3: L = 4 μm
#4: L = 9 μm
#5: L = 16 μm
#6: L = 40 μm
#7: L = 40 μm
#8: L = 34 μm
$I/T^{\beta+1}$ (A/K$^{\beta+1}$)
eV/2πk$_B$T (-)
10^{-10}
10^{-15}
10^{-20}
10^{-25}
10^0
10^1
10^2
10^3
10^4

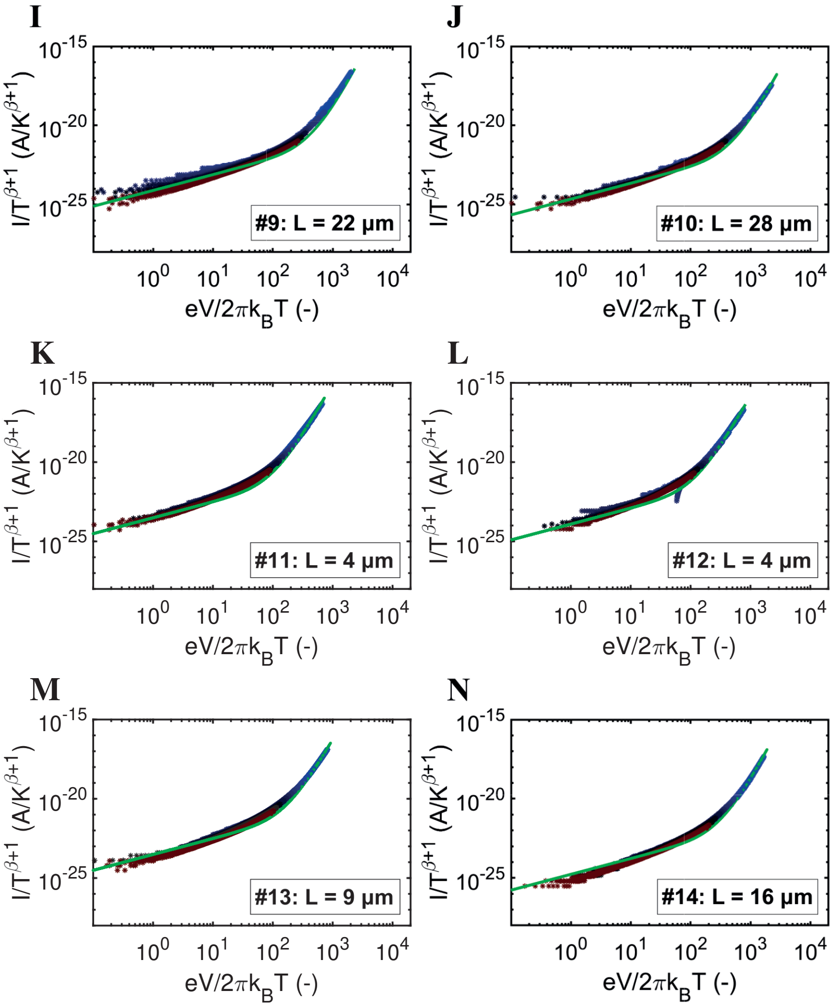
I
J
K
L
M
N
$I/T^{\beta+1}$ (A/K$^{\beta+1}$)
10^{-15}
10^{-20}
10^{-25}
10^{0}
10^{1}
10^{2}
10^{3}
10^{4}
$eV/2\pi k_B T$ (-)
#9: L = 22 μm
#10: L = 28 μm
#11: L = 4 μm
#12: L = 4 μm
#13: L = 9 μm
#14: L = 16 μm

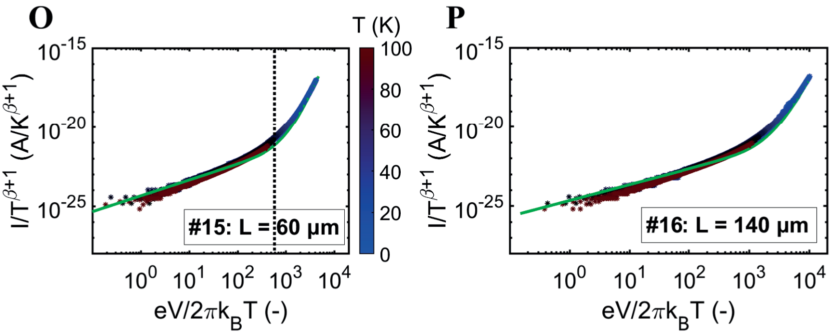

Figure S4: **Universal scaling behaviour of the conductance at low temperatures.** (**A** to **P**) Scaling curves are displayed for the 16 segments shown in Fig. S3. The plots display the scaled current $I/T^{\beta+1}$ on the y-axis versus the scaled bias $eV/2\pi k_B T$ on the x-axis. The $I(V)$ data in the temperature range below 100 K are used. The temperature at which individual data points were collected is indicated by the colour scale next to panel (**O**). The green solid line provides a fit of the universal scaling relation (Eq. S21) to the data. The power law exponent β is visually calibrated to obtain the best fit (precision ± 0.5). The transition from the low-bias, high-temperature regime to the high-bias, low-temperature regime occurs at a bias $eV \approx 2\pi N_S k_B T$. This transition point hence determines the parameter N_S, which signifies the apparent number of electron transfer steps in the hopping chain. In panel (**O**) this transition point is indicated by the dotted line. The resulting values for the power law exponent, β and the apparent number of hopping sites, N_S, are listed in tableS2. The parameter N_S scales with the segment length (see fig. S8).

Figure S5

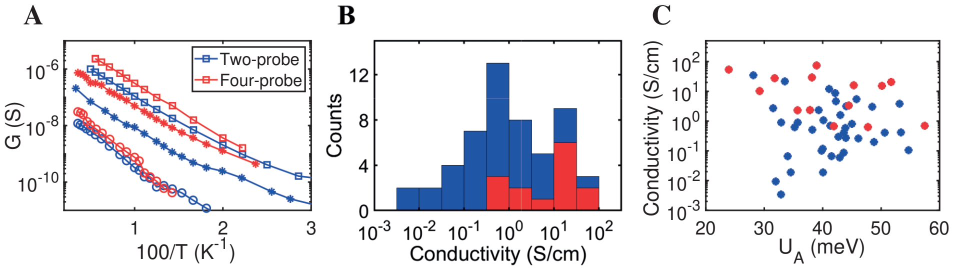

Figure S5: **High-temperature conductivity analysis.** (**A**) Temperature dependence of conductance, G, as measured by the two-probe and four-probe approach for three different segments. As expected, the four-probe conductance is systematically higher as it does not include the contact resistance. The two-probe and four-probe data show a very similar temperature dependence, demonstrating that both methods capture the same intrinsic temperature response of the conductance. The activation energy, U_A, is determined as the slope from an Arrhenius plot, i.e., a linear fit of $\ln(G)$ vs. $1/(k_\mathrm{B}T)$ for $T > 100$ K (see also fig. S6). We find similar activation energies for the two-probe and four-probe data: first segment (squares): 38.1 ± 0.2 meV vs. 38.2 ± 2 meV; second segment (stars): 41.2 ± 6.7 meV vs. 35.7 ± 2.3 meV; third segment (circles): 48.5 ± 2.3 meV vs. 50.6 ± 3.6 meV. (**B**) Histogram of the room-temperature conductivity for all fiber sheath segments investigated ($n = 53$). Conductivity was calculated via Eq. S1 as detailed in the Supplementary Text. Both four-probe (red bars) and two-probe (blue bars) estimates are shown. Note, that four-probe values are typically higher than two-probe values, due to the absence of the contact resistance. (**C**) Activation energy U_A of all segments investigated ($n = 53$) plotted against the room-temperature fiber conductivity, $\sigma_{0,\mathrm{F}}$. Two-probe data (blue markers) and four-probe data (red markers) are provided. The activation energy, U_A, and the room temperature conductivity, $\sigma_{0,F}$, are uncorrelated (Pearson correlation coefficient = 0.29). While the variance in $\sigma_{0,F}$ is rather large, the variation in U_A is small.

Figure S6

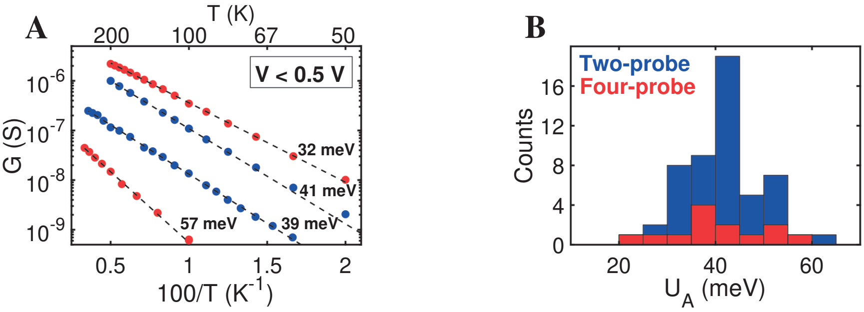

Figure S6: **Arrhenius temperature dependence of the conductance.** (**A**) Low-bias conductance as a function of temperature plotted above 50 K for two- and four-probe measurements, shown in blue and red respectively. Measurements taken on four different segments. Arrhenius fits (performed for data where $T > 100$ K) and corresponding activation energies are indicated. (**B**) Histogram with the activation energies measured in $n = 53$ segments (blue: two-probe measurements; red: four-probe measurements). The mean activation energy is 42 ± 8 meV ($n = 53$) and the mean goodness of fit across all samples as expressed by the coefficient of determination is $\langle R^2 \rangle \approx 0.982$.

FIGURE S7

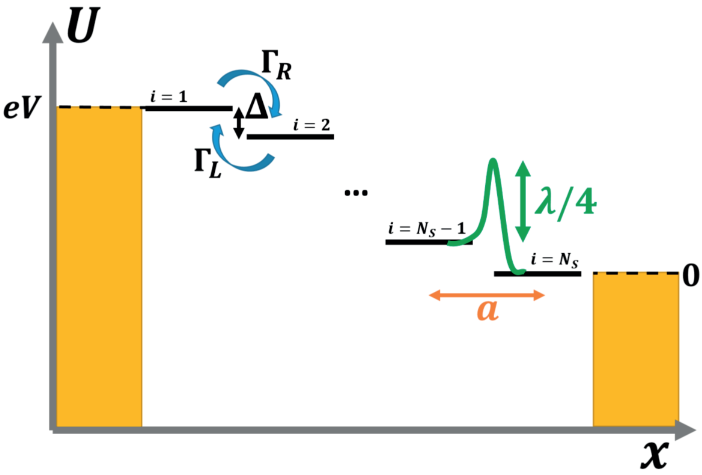

Figure S7: **Schematic of a one-dimensional hopping chain.** The vertical axis denotes the energy, U, and the horizontal axis the position, x, along the chain. The yellow rectangles represent the electrodes that have an applied voltage bias V ($U = 0$ at the right electrode and $U = eV$ at the left electrode). The horizontal black lines indicate the charge carrier sites, numbered from $i = 1$ to $i = N_S$, where N_S is the number of sites. The parameter a is the center-to-center distance between adjacent sites. There is an equal energy drop between neighboring sites, $\Delta = eV/N_S$. There are forward hopping rates, Γ_R, and backwards hopping rates, Γ_L, between any pairs of sites, but only hopping rates between nearest neighbour sites are taken into account. The reorganization energy, λ, determines the activation barrier for hopping (see Supplementary Text).

FIGURE S8

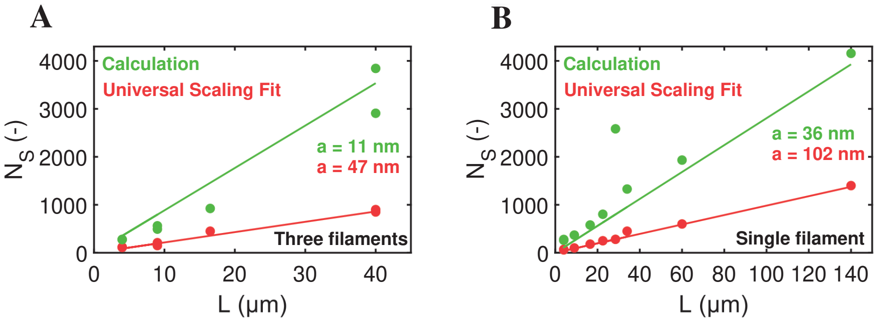

Figure S8: **Linear scaling of the number of hopping sites with the segment length.** The number of hopping steps, N_S, is determined in two ways. In a first approach (red markers), N_S is derived from the transition point in the universal scaling curves (see fig. S4). In a second approach (green markers), N_S is calculated via Eq. S26 in the Supplementary Text. In both cases, N_S linearly scales with the segment length L (solid lines provide linear fits, excluding offset). The center-to-center distance between hopping sites, a, is given by the slope $a = L/N_S$. Both methods imply a values that are in excess of 10 nm. (**A**) Data from three independent fiber sheaths. (**B**) Data obtained from different segments on a single fiber sheath.

FIGURE S9

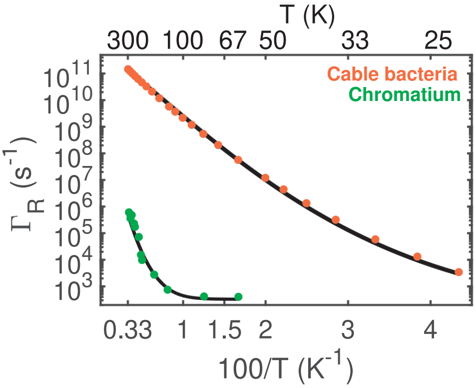

Figure S9: **Comparison of electron transfer rates in the purple bacterium *Allochromatium vinosum* versus the cable bacterium *Electrothrix gigas.*** Experimental data are respectively obtained from Ref. 18 for *A. vinosum* (green dots) and segment 6 (L = 40 μm) from the dataset provided here (green dots). The hopping model with a single effective vibronic mode (Jortner model; Suppl. Text) is fitted to both datasets (solid lines). Fitting parameters for *A. vinosum*: $\hbar\langle\omega\rangle = 60$ meV, $\lambda = 1.2$ eV and $V_{DA} = 1$ meV. For *E. gigas*, the measured current was first converted into an electron transfer rate via Eq. S7 with parameters: voltage bias $V = 0.5$ V, $N_S = 850$, $N_F = 60$ and $N_C = 125$. The parameters used for the Jortner model fit are: $\hbar\langle\omega\rangle = 9$ meV, $\lambda = 0.24$ eV and $V_{DA} = 6$ meV.

2.9. TABLES S1 AND S2

TABLE S1

Segment	L (µm)	G_0 (nS)	$\sigma_{0,\mathrm{F}}$ (S/cm)	U_A (meV)	T_C (K)
#1	4	850	1.1	40.1 ± 18	50
#2	9	285	0.81	45.2 ± 2.7	80
#3	4	69.3	0.087	43.1 ± 2.5	100
#4	9	23.3	0.066	31.9 ± 0.4	70
#5	16	80.4	0.42	53.4 ± 0.2	90
#6	40	957	12	41.6 ± 0.5	50
#7	40	305	3.8	53.4 ± 0.4	70
#8	34	6.20	0.066	41.8 ± 1.5	80
#9	22	16.6	0.12	40.3 ± 1.7	80
#10	28	6.67	0.060	43.3 ± 1.9	80
#11	4	7.45	0.0094	33.0 ± 0.6	60
#12	4	2.72	0.0034	33.1 ± 0.7	70
#13	9	6.70	0.019	35.1 ± 1.5	70
#14	16	3.64	0.019	40.1 ± 0.6	80
#15	60	13.9	0.26	46.1 ± 1.8	90
#16	140	2.30	0.10	39.8 ± 2.7	70

Table S1: **Parameters estimated from high-temperature conductance data**. The first column displays the sample identification number (16 segments have been analysed). L denotes the segment length probed between two gold electrode pads. G_0 is the conductance measured at room temperature, $T = 300$ K. $\sigma_{0,\mathrm{F}}$ is the fiber conductivity at $T = 300$ K calculated via Eq. S1. The activation energy, U_A, is determined by fitting the Arrhenius relation (Eq. S15) to the high-temperature conductance data ($T > 100$ K; see fig. S5). The cross-over temperature, T_C, is the first temperature where the conductance as predicted by the Arrhenius fit is 20% lower than the actually measured conductance.

TABLE S2

#	L (µm)	λ (eV)	V_{DA} (meV)	Γ_0 (ns^{-1})	α (−)	β (−)	β_{USC} (−)	$\hbar\omega_c$ (meV)	$N_{S,NUM}$ (−)	a_{NUM} (nm)	$N_{S,USC}$ (−)	a_{USC} (nm)
1	4	0.25 ± 0.02	2.0	11	5.15 ± 0.17	7.08 ± 0.04	6.5	28	275	15	120	33
2	9	0.27 ± 0.01	1.7	6.6	5.98 ± 0.46	8.19 ± 0.12	7.5	26	493	18	210	43
3	4	0.26 ± 0.11	0.42	0.49	3.78 ± 0.33	6.94 ± 0.02	6.5	29	279	14	110	36
4	9	0.22 ± 0.03	0.35	0.51	3.73 ± 0.53	6.17 ± 0.07	6.5	27	562	16	150	60
5	16	0.30 ± 0.01	1.4	3.6	4.93 ± 0.87	8.28 ± 0.14	7.5	29	924	18	450	37
6	40	0.24 ± 0.01	8.0	228	7.67 ± 0.58	6.68 ± 0.01	8.0	27	2910	14	850	47
7	40	0.30 ± 0.01	5.7	55	7.36 ± 0.24	5.23 ± 0.05	7.5	41	3840	10	900	44
8	34	0.25 ± 0.02	0.36	0.38	5.44 ± 0.32	4.76 ± 0.00	6.0	37	1330	26	250	90
9	22	0.25 ± 0.02	0.42	0.55	5.19 ± 0.25	4.64 ± 0.00	6.0	37	803	28	450	76
10	28	0.26 ± 0.02	0.51	0.69	5.07 ± 0.17	4.70 ± 0.01	6.0	39	2580	11	280	102
11	4	0.21 ± 0.01	0.14	0.089	4.60 ± 0.16	4.01 ± 0.00	5.5	36	278	14	60	67
12	4	0.21 ± 0.01	0.083	0.030	4.44 ± 0.13	4.39 ± 0.01	5.5	34	262	15	70	57
13	9	0.23 ± 0.01	0.16	0.10	4.68 ± 0.23	4.37 ± 0.00	5.5	36	368	24	100	90
14	16	0.25 ± 0.01	0.18	0.10	4.94 ± 0.12	4.95 ± 0.01	5.5	36	579	38	180	92
15	60	0.28 ± 0.02	0.73	1.16	5.22 ± 0.10	4.82 ± 0.01	5.5	41	1930	31	600	100
16	140	0.24 ± 0.01	0.45	0.68	5.36 ± 0.22	4.95 ± 0.01	6.0	35	4160	34	1400	100

Table S2: **Parameters estimated from fitting the proposed hopping model.** The first column displays the sample identification number (same 16 segments as in table1). L is the segment length between two electrode pads. The reorganization energy, λ, is obtained by fitting the Marcus expression (Eq. S12) to the high-temperature conductance data ($T > 100$ K; see Fig. 2.3A). The electronic coupling, V_{DA}, is obtained via Eq. S27. The transition rate, Γ_0, at 300 K is calculated from the Marcus rate expression (Eq. 12) using the values for λ and V_{DA} listed. The power law exponent, α, was obtained by fitting the temperature-based power law $G \propto T^{\alpha}$ to the conductance data in the region 20 - 100 K (Fig. 2.3C). The power law exponent, β, was obtained by fitting the electric field-based power law (Eq. S22 and Eq. S8) to the conductance data for $T < 10$ K (Fig. 2.3D). An alternative value for this exponent, β_{USC}, is obtained by fitting the universal scaling curve (fig. S4). The characteristic vibration energy, $\hbar\omega_c$, was determined via Eq. S19. The number of sites $N_{S,NUM}$ was obtained by Eq. S26 and the corresponding center-to-center distance is $a_{NUM} = L/N_{S,NUM}$. Alternatively, the number of sites $N_{S,USC}$ was also independently obtained from the universal scaling curves (fig. S4) and the corresponding center-to-center distance between sites, $a_{USC} = L/N_{S,USC}$ is also given.

2.10. SUPPLEMENTARY TEXT

2.10.1. CALCULATION OF THE FIBER CONDUCTIVITY

The fiber conductivity, $\sigma_{0,F}$, at room temperature (T = 300 K) was calculated from the experimental I/V data as:

$$\sigma_{0,\mathrm{F}} = G_0 \frac{L}{N_\mathrm{F} A_F} = G_0 \frac{4L}{N_\mathrm{F} \pi d_\mathrm{F}^2}. \tag{S1}$$

In this, G_0 represents the low-bias conductance of a single fiber sheath as determined at T = 300 K from the slope of the I/V curve, L is the length of the fiber sheath segment investigated as determined by microscopy, A_F is the cross-sectional area of one fiber, and N_F is the total number of fibers embedded in the fiber sheath. Experimentally determined values for G_0 and L are given for different segments in table 1. The number of parallel fibers N_F is determined by scanning electron microscopy or atomic force microscopy on individual filaments[41] and is here $N_\mathrm{F} = 60$ (see fig. S1). The cross-sectional area is taken the same value for all segments: d_F = 26 nm is the diameter of the conductive core of an individual fiber, which is invariant across different filaments[44].

2.10.2. HOPPING MODEL OF ELECTRON TRANSPORT IN CABLE BACTERIA

GEOMETRY OF THE CONDUCTIVE NETWORK

Cable bacteria possess a set of N_F fiber structures in their cell envelope, which are arranged in parallel and run continuously along the whole length of cm-long filaments [41] (N_F = 60; see above). The fibers themselves consist of a conductive core (diameter d_F = 26 nm), surrounded by an electrically insulating shell [44]. The large ratio of length (1 cm) to diameter (26 nm) suggests that the electron transport in the fibers is one-dimensional. Still, there could be multiple conduction channels acting in parallel in a single fiber, as d_F far exceeds the typical spacing between charge carrier sites in metalloproteins (1 – 2 nm).

At present, it is not known how many conduction channels are actually present. Here, we assume that a conductive fiber core consists of multiple parallel molecular conduction paths, each d_P = 2 nm in diameter. Assuming a hexagonal packing of cylinders, the number of parallel channels in one periplasmic fiber can then be estimated as $N_\mathrm{C} = 125$. The total number of parallel paths in a given cable bacterium filament thus amounts to $N_\mathrm{P} = N_\mathrm{F} \cdot N_\mathrm{C} = 7500$. This large number of conduction channels should be regarded as an upper limit of what's physically possible, thus providing a conservative estimate for the electron transfer rate. If less channels are present, then the conductivity of individual channels must be higher, and this in turn also necessitates higher electron transfer rates (see discussion in main text).

CURRENT THROUGH A SINGLE CONDUCTION CHANNEL

Each conduction channel is modelled as a one-dimensional chain of N_S equidistant hopping sites, which serve as temporary localization centers of an electron during the hopping process (fig. S7). The site at position, i, along the chain is characterised by the site energy, U_i. Transitions between sites represent the quantum-mechanical tunneling of electrons, and are characterised by a forward rate, $\Gamma_{\mathrm{i,j}}$, and a backward rate, $\Gamma_{\mathrm{j,i}}$. The ratio between forward and backward rates is governed by the detailed balance relation

[56, 78]:

$$\Gamma_{\mathrm{i,j}}/\Gamma_{\mathrm{j,i}} = \exp(\Delta/k_{\mathrm{B}}T). \tag{S2}$$

Here, k_{B} is the Boltzmann constant, T is temperature, and $\Delta = U_{\mathrm{i}} - U_{\mathrm{j}}$ is the driving force, i.e., the difference between the site energy of the initial position of the electron, U_{i}, and that of its final position, U_{j}. In our model, only nearest neighbour hopping is considered ($j = i \pm 1$). Moreover, the hopping sites are assumed to be identical and periodic in structure, with the same center-to-center distance a between them (fig. S7). As sites are identical, the transition rate is the same for every pair of sites ($\Gamma_{\mathrm{i,i+1}} = \Gamma_{\mathrm{R}}$; $\Gamma_{\mathrm{i+1,i}} = \Gamma_{\mathrm{L}}$). Moreover, if we connect the hopping chain to an electrode on either side, and impose a voltage bias V between the electrodes, the energy difference between two sites is constant and amounts to $\Delta = eV/N_{\mathrm{S}}$ (assuming there is no voltage drop over the electrode interface). The current between two consecutive hopping sites along a single conduction path is given by:

$$I_{\mathrm{P}} = e\left[\Gamma_{\mathrm{R}} p_{\mathrm{i}} \left(1 - p_{\mathrm{i+1}}\right) - \Gamma_{\mathrm{L}} p_{\mathrm{i+1}} \left(1 - p_{\mathrm{i}}\right)\right], \tag{S3}$$

where p_{i} and $p_{\mathrm{i+1}}$ are the occupation probabilities at the consecutive hopping sites, and e is the elementary charge (i.e., the magnitude of the charge carried by a single electron). This expression embeds the Pauli exclusion principle: an electron can only jump to a charge carrier site when this site is vacant.

Because the current is not dependent on the pair of sites where it is calculated, only certain combinations of p_i are possible. We make the simplification that our hopping chain is optimally filled for conductance ($p_{\mathrm{i}} = 1/2$), using the following justification. Because in the electrode many electron states can contribute to the effective hopping rates at the interface, these interfacial rates can be expected to be far greater than the internal hopping rates, $\Gamma_{\mathrm{R,L}}$. The occupation probability of the edge hopping sites, p_1 and p_{N}, are then expected to follow the Fermi-Dirac distribution in the metal electrodes:

$$p_{\mathrm{FD}} = \frac{1}{1 + \exp\left(\frac{\epsilon}{k_{\mathrm{B}}T}\right)}. \tag{S4}$$

Here, p_{FD} is the occupation probability of an electron state inside the electrode and ϵ is the energy difference of this electron state with respect to the energy of the electrode. If $\epsilon = 0$ for $i = 1, N$ (see fig. S7), then $p_1 = p_N = 1/2$ and no occupancy difference is expected to build up in the hopping chain, because all internal hopping rates $\Gamma_{\mathrm{R,L}}$ are the same. Therefore, all sites in the chain can be expected to have the occupancy $p_i = 1/2$.

Accounting for N_{P} parallel conduction channels, and implementing the detailed balance relation, the total current along a single filament, can be expressed as:

$$I = N_{\mathrm{P}} I_{\mathrm{P}} = e\frac{1}{4} N_{\mathrm{P}} (\Gamma_{\mathrm{R}} - \Gamma_{\mathrm{L}}). \tag{S5}$$

Implementing the detailed balance relation, we obtain:

$$I = e\frac{1}{4} N_{\mathrm{P}} \Gamma_{\mathrm{R}} \left(1 - \exp(-\Delta/k_{\mathrm{B}}T)\right). \tag{S6}$$

Two separate regimes can be discerned. In the low-bias, high-temperature regime ($k_{\mathrm{B}}T > eV/N_{\mathrm{S}}$), the current in Eq. S6 simplifies to:

$$I \approx \frac{e}{4} N_{\mathrm{P}} \Gamma_{\mathrm{R}} \frac{eV}{N_{\mathrm{S}} k_{\mathrm{B}} T}. \tag{S7}$$

Alternatively, in the low-temperature, high-bias regime ($eV/N_\mathrm{S} > k_\mathrm{B}T$), the exponential term in Eq. S6 vanishes, and the current reduces to:

$$I \approx e\frac{1}{4}N_\mathrm{P}\Gamma_\mathrm{R}. \tag{S8}$$

The objective is now to find a suitable expression for the transition rate, Γ_R.

TRANSITION RATE ESTIMATES

The fiber conductivity σ can be obtained from the current expression in the low-temperature, high-bias regime, Eq. S7, as:

$$\sigma = \frac{I}{V}\frac{L}{N_\mathrm{F}A_F} = \Gamma_\mathrm{R}\frac{e^2}{k_\mathrm{B}T}\frac{LN_\mathrm{C}}{N_\mathrm{S}\pi d_\mathrm{F}^2}, \tag{S9}$$

As described above, the fiber sheath has $N_\mathrm{F} = 60$ fibers with a diameter of $d_\mathrm{F} = 26$ nm, and a cross-sectional area $A_F = \pi d_\mathrm{F}^2/4$. Moreover, we estimate that a maximum of $N_\mathrm{C} = 125$ parallel conduction channels can be integrated in a single fiber (see 'Geometry of the conductive network'). The above expression can be rearranged to provide the transition rate Γ_R as a function of the measured conductivity

$$\Gamma_\mathrm{R} = \sigma\frac{k_\mathrm{B}T}{e^2}\frac{\pi d_\mathrm{F}^2}{aN_\mathrm{C}}, \tag{S10}$$

In this, $a = L/N_\mathrm{S}$ represents the mean center-to-center distance between two consecutive sites.

Conductivities on the order of $\sigma = 100$ S/cm have been estimated for the cable bacterium fibers (see also fig. S2). Moreover, typical center-to-center distances, a, between the cofactors in metalloproteins are in the range of $0.5 < a < 2$ nm. For a typical cable bacterium filament ($L = 1$ cm) this hence translates in between 5 and 20 million sites along the hopping chain. Using these numbers, Eq. 19 predicts that the transition rate must range between $\Gamma_R = 13 - 54 \text{ x } 10^{12}$ s^{-1}. This hopping rate exceeds the speed limit of 10^{13} s^{-1} for non-adiabatic electron transfer [71], thus illustrating the theoretical challenge of applying multistep hopping models in cable bacteria (see discussion in main text).

2.10.3. TRANSITION RATE MODELS

At low temperatures, the energy stored in vibrational modes can stimulate the hopping process. To account for this effect, several authors have formulated an extended, quantum version of the semi-classical Marcus electron transfer theory. These models explicitly account for vibrational modes that suitably couple to the electron transfer. Two prominent examples are the single effective mode formulation presented by Jortner [59] and the multiple mode formulation developed by Egger [56]. Below, we will integrate these two vibrational model formulations in the multistep hopping chain model introduced above. But first, we introduce the classical Marcus rate formalism as a reference for these more elaborate quantum-based models.

HIGH-TEMPERATURE REGIME: THE MARCUS MODEL FORMULATION

At a sufficiently high temperatures, the thermal energy, $k_B T$, sufficiently exceeds the quantum energy, $\hbar\omega$, of the intramolecular vibrations, and all vibrations are then thermally excited. Under these conditions, the transition rate between neighbouring sites is given by the classical Marcus rate expression [69],

$$\Gamma_R = \frac{2\pi}{\hbar}\frac{V_{DA}^2}{\sqrt{4\pi\lambda k_B T}}\exp\left[\frac{-(\lambda-\Delta)^2}{4\lambda k_B T}\right]. \tag{S11}$$

Here, λ is the reorganization energy, V_{DA} is the electronic coupling, and $\Delta = eV/N_S$ is the energy difference between adjacent sites introduced above. Upon substitution of this expression into the high-temperature regime current (Eq. S7), we obtain the conductance:

$$G = \frac{e^2 N_P}{4N_S k_B T}\frac{2\pi}{\hbar}\frac{V_{DA}^2}{\sqrt{4\pi\lambda k_B T}}\exp\left[\frac{-(\lambda-\frac{eV}{N_S})^2}{4\lambda k_B T}\right]. \tag{S12}$$

Because the bacterial filaments investigated are very long ($N_S > 10^2$), the driving force $\Delta = eV/N_S$ in the low-bias regime ($V < 0.5$ V) will be < 5 meV, which is substantially smaller than the reorganization energy, $\lambda \approx 270$ meV (Fig. 2.3). Consequently, the exponent in Eq. S12 reduces to $e^{-\lambda/4k_B T}$ and the conductance relation simplifies to:

$$G = g_0(k_B T)^{-3/2}\exp(-\frac{\lambda}{4k_B T}). \tag{S13}$$

The pre-factor g_0 is given by:

$$g_0 = \frac{e^2 N_P}{4N_S}\frac{2\pi}{\hbar}\frac{V_{DA}^2}{\sqrt{4\pi\lambda}}. \tag{S14}$$

Eq. S13 was fitted to the $G(T)$ data to provide values for λ and g_0 (non-linear least squares fit of G versus $1/T$ as displayed in Fig. 2.3A; values for λ and V_{DA} tabulated in table S2).

This fitting procedure assumes that g_0 itself is temperature independent. However, it is known that the electronic coupling V_{DA} is weakly temperature dependent [70]. Consequently, the exact temperature dependence of the pre-exponential factor in Eq. S13 is unknown. As a simplification, one can leave the $T^{-3/2}$ dependence out of the equation, to arrive at the classical Arrhenius relation:

$$G = g_1\exp\left(-\frac{U_A}{k_B T}\right). \tag{S15}$$

Here, the pre-factor $g_1 = g_0(k_B T)^{-3/2}$ is now considered to be a temperature-independent parameter. This basic Arrhenius relation was also fitted to the high temperature conductance data to arrive at values for the activation energy U_A (fig. S5; table 1).

LOW-TEMPERATURE REGIME, ONE EFFECTIVE VIBRATIONAL MODE: THE JORTNER MODEL FORMULATION

When the quantum energy of vibrations $\hbar\omega$ becomes smaller than the thermal energy, $k_B T$, the Marcus rate expression (Eq. 12) is no longer valid. In the Jortner model formulation, vibrational modes are characterised by a single effective mode $\langle\omega\rangle$, which provides a suitable average across all molecular vibrations. The corresponding transition rate becomes [59]:

$$\Gamma_{\mathrm{R}} = \Gamma_0 \cdot \exp(-S(2\overline{n}_{\mathrm{B}}+1)) \cdot I_{\mathrm{q}}(2S(\overline{n}_{\mathrm{B}}(\overline{n}_{\mathrm{B}}+1))^{1/2}) \cdot (\overline{n}_{\mathrm{B}}(\overline{n}_{\mathrm{B}}+1))^{q/2}. \tag{S16}$$

In this expression, Γ_0 is a temperature-independent pre-factor, $S = \lambda/\hbar\langle\omega\rangle$ is the electron-phonon coupling strength associated with $\langle\omega\rangle$, $\overline{n}_{\mathrm{B}} = 1/(\exp(\hbar\langle\omega\rangle/k_{\mathrm{B}}T) - 1)$ is the Bose-Einstein distribution for the single effective mode $\langle\omega\rangle$, the exponent $q = \frac{\Delta}{\hbar\langle\omega\rangle}$ is the ratio between the site energy drop between hopping sites and the mean quantum vibrational energy, and I_{q} is the modified Bessel function [59]. One can show that at high temperatures (when $\hbar\langle\omega\rangle \ll k_{\mathrm{B}}T$), the Marcus rate expression is recovered.

The Jortner expression for the transition rate, Eq. S16, can be combined with the expression for the current along a single filament, Eq. S6, in order to estimate the conductance G as a function of temperature and the electric field strength. The results are given in Fig. 2.2C and D. At high temperatures, the conductance follows an Arrhenius type dependence (Fig. 2.2C), while at low temperatures ($k_{\mathrm{B}}T \ll \hbar\langle\omega\rangle$), the conductance becomes temperature-independent (Fig. 2.2D). This calculated $G(T,E)$ response shows a good agreement with the data.

Low-temperature regime, multiple vibrational modes: the Egger model formulation

In the Egger model formulation[56], it is assumed that many vibrational modes are coupled to the electron hopping process. The phonon spectral density function $J(\omega)$ describes how much a certain vibrational mode contributes to the reorganization energy[79]:

$$\lambda = \hbar\int_0^\infty \omega J(\omega)\mathrm{d}\omega. \tag{S17}$$

The Egger model formulation assumes that the phonon spectral density function has an Ohmic form and can be expressed as:

$$J(\omega) = (\beta+2)\frac{e^{-\omega/\omega_{\mathrm{c}}}}{\omega}. \tag{S18}$$

Here, ω_{c} is the characteristic frequency of the spectrum. For the Ohmic spectral density, the reorganization energy is directly proportional to the characteristic frequency, ω_{c}, as stated in the original derivation of the Egger model [56]:

$$\lambda = (\beta+2)\hbar\omega_{\mathrm{c}}, \tag{S19}$$

Since the spectrum starts at zero frequency, some modes remain thermally activated at the lowest temperatures. This explains an important difference between the Jortner and Egger model formulations. Whereas in the Jortner model, the low-bias conductance remains constant at cryogenic temperatures, this is not the case in the Egger model: the low-bias conductance shows a power law behaviour, in which the conductance further decreases as the temperature decreases. Effectively, the modes that remain thermally activated at low temperatures force the low-bias conductance to die out.

When the temperature is much lower than the characteristic energy of vibration ($k_B T \ll \hbar\omega_c$), the Egger model provides following expression for the transition rate [56]:

$$\Gamma_R = \frac{1}{\gamma(\beta+2)\hbar}\frac{V_{DA}^2}{\hbar\omega_c}\left(\frac{2\pi k_B T}{\hbar\omega_c}\right)^{\beta+1}\left|\gamma\left(1+\beta/2+i\frac{eV}{2\pi N_S k_B T}\right)\right|^2 \exp\left(\frac{eV}{2N_S k_B T}\right). \tag{S20}$$

Here, γ is the complex gamma function and the exponent β provides a measure for the electron-phonon coupling strength. If we combine the expression for the current along a single filament, Eq. S6, with the above expression for the transition rate, Eq. S20, we obtain:

$$I = A_0 T^{\beta+1}\sinh\left(\frac{eV}{2N_S k_B T}\right)\left|\gamma\left(1+\beta/2+i\frac{eV}{2\pi N_S k_B T}\right)\right|^2. \tag{S21}$$

The pre-factor A_0 combines all temperature-independent parameters. Note, that the Egger model centrally depends on the assumption that the phonon spectral density function has an Ohmic form. However, at present, the details of electron-phonon coupling in the conductive fibers of cable bacteria are unknown, and so, alternative shapes phonon spectral density function could be relevant [79].

Universal scaling curve

Closer inspection of Eq. S21 reveals that the $I(V)$ data can be replotted as a single universal scaling curve, provided one normalizes the bias voltage as $eV/(2\pi k_B T)$ (the horizontal axis) and rescales the current as $I/T^{\beta+1}$ (vertical axis). If the Egger model applies, then the $I(V)$ data collected at different temperatures should fall onto a single curve, only depending on A_0, β, and the number of hopping sites N_S. These universal scaling plots are shown in fig. S4. In the low-bias, high-temperature regime ($eV/N_S < k_B T$), the approximation $\sinh(x) \approx x$ can be made and then $G = I/V \propto T^{\beta}$. Accordingly, one expects the conductance to follow a power law dependence on temperature, which is also seen in the data (Fig. 2.3C). Oppositely, in the high-voltage, low-temperature regime ($eV/N_S > k_B T$), the transition rate is given by [56]:

$$\Gamma_R = \frac{2\pi}{\hbar}\frac{V_{DA}^2}{\gamma(\beta+2)\hbar\omega_c}\left(\frac{eV}{N_S\hbar\omega_c}\right)^{\beta+1}\exp\left(-\frac{eV}{N_S\hbar\omega_c}\right). \tag{S22}$$

If we combine this expression with that for the current in the high-bias, low-temperature regime (Eq. S8), the conductance becomes:

$$G = \frac{e^2}{4}\frac{N_P}{N_S}\frac{2\pi}{\hbar}\frac{V_{DA}^2}{\gamma(\beta+2)(\hbar\omega_c)^2}\left(\frac{eV}{N_S\hbar\omega_c}\right)^{\beta}. \tag{S23}$$

In this equation, we have dropped the exponential decay factor in Eq. S22, as one can prove that for small $x = eV/(N_S\hbar\omega_c)$, this term is very close to one. The overall result is that the conductance depends on the bias voltage via a power law: $G \propto V^{\beta}$. This relation is indeed seen in the data (Fig. 2.3D).

The distance between hopping sites

Each conduction channel is modelled as a one-dimensional chain of N_S equidistant hopping sites with the same center-to-center distance $a = L/N_S$ between them (fig. S7).

We can estimate the number of hopping sites N_S from our data in two independent ways. In a first approach, we can extract N_S directly from the universal scaling curve (fig. S4). The scaling curves show a pronounced inflection point at the transition from the low-bias, high-temperature regime towards the high-bias, low-temperature regime. This transition occurs at a bias

$$eV \approx 2\pi N_S k_B T \tag{S24}$$

As a result, the value of $eV/2\pi k_B T$ at the inflection point of the scaling curve provides a direct estimate of the apparent number of hopping steps N_S. In fig. S4, panel (O), this transition point is indicated by the dotted line. In table S2, the resulting values of $N_{S,USC}$ are listed for each of the 16 segments investigated. The corresponding estimate for the center-to-center distance $a_{USC} = L/N_{S,USC}$ ranges between 33 and 102 nm.

In the second approach, a value for N_S is numerically calculated from other parameters available. To this end, we first note that for low temperatures and high voltages ($eV/N_S \gg k_B T$), the conductance scales as $G = B_0 V^\beta$, where B_0 is the pre-factor in the power law fit. Using Eq. S23, this pre-factor can be explicitly written as:

$$B_0 = \frac{e^2}{4}\frac{N_P}{N_S}\frac{2\pi}{\hbar}\frac{V_{DA}^2}{\gamma(\beta+2)(\hbar\omega_c)^2}\left(\frac{e}{N_S\hbar\omega_c}\right)^{\beta}. \tag{S25}$$

Rearrangement provides an expression for the number of hopping sites:

$$N_S = \frac{e}{\hbar\omega_c}\left[\frac{eN_P}{4}\frac{2\pi}{\hbar}\frac{V_{DA}^2}{\hbar\omega_c\gamma(\beta+2)}\frac{1}{B_0}\right]^{1/(\beta+1)}. \tag{S26}$$

This expression requires an estimate for the electronic coupling V_{DA}. To arrive at this, we note that the pre-factor g_0 (as derived from the fitting of the Marcus rate expression, Eq. S14) can be transformed into an expression for the electronic coupling:

$$V_{DA}^2 = \left[g_0\frac{\hbar}{2\pi}\frac{4N_S}{e^2N_P}\sqrt{4\pi\lambda}\right]. \tag{S27}$$

Substitution of Eq. S27 into Eq. S26 finally gives:

$$N_S = \frac{e}{\hbar\omega_c}\left[\frac{\sqrt{4\pi\lambda}}{\gamma(\beta+2)(\hbar\omega_c)^2}\frac{g_0}{B_0}\right]^{1/\beta}. \tag{S28}$$

From this, N_S can be calculated provided that we supply parameters that are fitted in the low-temperature regime (the pre-factor B_0, the coupling exponent β, the characteristic frequency $\hbar\omega_c$) as well as parameters that are determined in the high-temperature regime (pre-factor g_0, reorganization energy λ).

The above derivation essentially assumes that the electronic coupling is independent of temperature (the high-temperature value is substituted into the low-temperature expression). It is, however, known that V_{DA} is enhanced by thermal fluctuations. So in reality, the value of V_{DA} could be smaller at lower temperatures, and as a consequence, the value of N_S will be overestimated by Eq. S28. This could explain the differences obtained for N_S by the two separate estimation procedures (see fig. S8). However, in high-mobility organic semiconductors, this temperature effect changes the V_{DA} value by less than one order of magnitude [70]. Because of the power law dependence $1/\beta$ in Eq. S28, such a tenfold difference in electronic coupling only causes a two-fold difference in the N_S estimate.

The resulting values of $N_\mathrm{S,NUM}$ are listed in table S2 for all 16 segments investigated. The associated center-to-center distance $a_\mathrm{NUM} = L/N_\mathrm{S,NUM}$ ranges between 10 and 36 nm, which is a factor of 3 lower than the corresponding estimate based on the universal scaling curve. fig. S8 shows that the number of hopping sites linearly scales with the segment length. This trend is seen for both approaches.

3

A MODEL ANALYSIS OF LONG-DISTANCE ELECTRON TRANSPORT IN CABLE BACTERIA

**Jasper VAN DER VEEN, Stephanie Valianti,
Herre S.J. van der Zant, Yaroslav M. Blanter and Filip J.R. Meysman**

ABSTRACT

The recent discovery of cable bacteria has greatly expanded the known length scale of biological electron transport, as these multi-cellular bacteria are capable of mediating electrical currents across centimeter-scale distances. To enable such long-range conduction, cable bacteria embed a network of regularly spaced, parallel protein fibers in their cell envelope. These fibers exhibit extraordinary electrical properties for a biological material, including an electrical conductivity that can exceed 100 S/cm. Traditionally, long-range electron transport through proteins is described as a multi-step hopping process, in which the individual hopping steps are described by Marcus electron transport theory. Here, we investigate to what extent such a classical hopping model can explain the conductance data recorded for individual cable bacterium filaments. To this end, the conductive fiber network in cable bacteria is modelled as a set of parallel one-dimensional hopping chains. Comparison of model simulated and experimental current(I)/voltage(V) curves, reveals that the charge transport is field-driven rather than

---

This chapter is a version of the article 'A model analysis of long-distance electron transport in cable bacteria', published in the journal PCCP.

concentration-driven, and there is no significant injection barrier between electrodes and filaments. However, the observed high conductivity levels (>100 S/cm) can only be reproduced, if we include much longer hopping distances ($a > 10$ nm) and lower reorganisation energies ($\lambda < 0.2$ eV) than conventionally used in electron relay models of protein structures. Overall, our model analysis suggests that the conduction mechanism in cable bacteria is markedly distinct from other known forms of long-range biological electron transport, such as in multi-heme cytochromes.

3.1. INTRODUCTION

Electron flow through proteins is central to the functioning of living organisms, as it connects the sites where oxidation and reduction half-reactions occur that support vital biochemical processes [80]. The best studied systems in terms of biological electron transport are the membrane complexes that enable photosynthesis in chloroplasts or respiration in mitochondria [47, 55]. These protein structures incorporate a series of non-protein cofactors (e.g., hemes, FeS clusters) that act as relay centres for electron transport. Electrons migrate through the electrically insulating protein medium by quantum-mechanical tunneling from one center to the next. As the tunneling rate exponentially decreases with distance, cofactors must be closely spaced (< 1.4 nm apart) to allow for sufficiently fast rates (> 10^3 s^{-1} time scale) that can sustain metabolism [55]. Typically, electron transport chains incorporate up to 10-20 cofactors, and so the overall length scale of conduction is limited to < 20 nm. This has fueled the idea that biological electron transport takes place at the nanometer scale, and so, any electron current exceeding 3 nm in biology is generally referred to as “long-range electron transport” [47].

The recent discovery that cable bacteria can channel electrical currents across centimeter distances [1], i.e. 10^6 times further, thus gives a radically new meaning to the concept of “long-range electron transport” [49]. Cable bacteria are long, motile, filamentous bacteria that thrive in the surface sediments of rivers, lakes, and oceans [81–84]. Their respiratory metabolism couples the oxidation of free sulfide (H_2S) to the reduction of oxygen (O_2), which is an energetically favorable reaction [85, 86]. The remarkable feature is that these two half-reactions are carried out by different parts of the long filaments, and so the sites of oxidation and reduction can be millimetres to centimetres apart [1]. To ensure that the redox half-reactions remain electrically coupled, electrons are internally conveyed through the cable bacterium filaments [2, 3, 43].

To mediate this centimeter-scale electron transport, cable bacteria harbor an electrical grid consisting of thin protein fibers embedded in the cell envelope [2] (Fig. 1a). Recent studies have resolved the intricate architecture of this highly organized fiber network [41, 44, 50] (see Fig.1b and discussion below). Additionally, it has been shown that these protein fibers display extraordinary electrical properties for a biological material. Electrical measurements demonstrate that the fiber conductivity can reach up to 100 S/cm, which is comparable to that of highly doped conductive polymers [2, 45]. Because of this, the protein fibers are regarded as a promising new material for bio-based electronics [2]. Such technological application however necessitates the resolution of some fundamental questions. What mechanism allows for such highly efficient centimeter-scale conduction in proteins? Does the electron transport in cable bacteria bear any similarity to the mechanisms seen in the well-studied protein systems of photosynthesis and respiration?

At present, the molecular structure of the fiber network remains unresolved, and as a result, the conduction mechanism remains elusive. Model analysis, however, allows us to explore potential mechanisms. Nanoscale electron transport across proteins, as seen in multi-heme cytochromes, is conventionally described by the multistep hopping formalism [48]. Here, we investigate whether this same model formalism can describe the highly efficient, centimeter-scale electron transport in cable bacteria. In the multi-hopping picture, it is assumed that charges are temporarily localized at particular sites, and that electron transport occurs by incoherent "hopping" between consecutive sites along a chain. The electron transfer during a single hop is described by Marcus theory, which requires that the reorganization energy, λ, is significantly larger than electronic coupling, H, so that localized charge carriers form in the initial and final states [15]. These Marcus-type hopping models comprise the default modelling approach for biological conduction, and have been used previously to describe nanometer scale electron transport in multi-heme cytochromes [23] and protein-based molecular junctions [87–89], as well as micrometer scale electron transport in the nanowires of metal-reducing bacteria [24, 71, 90].

The distance over which electron transport occurs in cable bacteria is however very different from the length scale for which the Marcus multi-stepping model has been originally developed. To test the validity of the Marcus formalism, we describe the conductive fiber network in cable bacteria as a set of parallel one-dimensional hopping chains. This is the most parsimonious model description, given that the molecular structure of the fibers still remains unresolved. The model describes the electron transport through the hopping chains when a voltage bias is imposed by connecting electrodes (Fig.1). In our analysis, we simulate the site occupancy along the chain as well as the resulting current/voltage response, and investigate the relationship between the hopping rate and the electrical conductivity. The model output is compared to an experimental dataset that was recently obtained by detailed electrical characterization of individual fiber networks of cable bacteria [91].

3.2. MODEL FRAMEWORK

3.2.1. THE CONDUCTIVE STRUCTURE IN CABLE BACTERIA

Cable bacteria possess a set of N_F fibre structures in their cell envelope, which are arranged in parallel and run continuously along the whole length of the centimeter-long cable bacterium filaments (Fig. 1a, b). These fibres consist of a conductive core (diameter $d_\mathrm{F} = 26$ nm), surrounded by an electrically insulating shell[44], and always appear to have a similar geometry[41]. Thicker cable bacteria simply embed more parallel fibers in the cell envelope (N_F ranges from 15 to 75[41]). Here, we adopt $N_F = 60$ as a reference value, which is a characteristic value for *Electrothrix gigas*, the larger strain of cable bacteria [42] that was used in our electrical characterization experiments.

The large ratio of the fiber length (10^7 nm) to the fiber diameter (26 nm) suggests that charge transport in the fibers is largely one-dimensional. Still, the fiber core diameter is considerably larger than the typical spacing between charge carrier sites in metalloproteins [55] (≈ 1 nm). Hence, there could be multiple conduction channels acting in

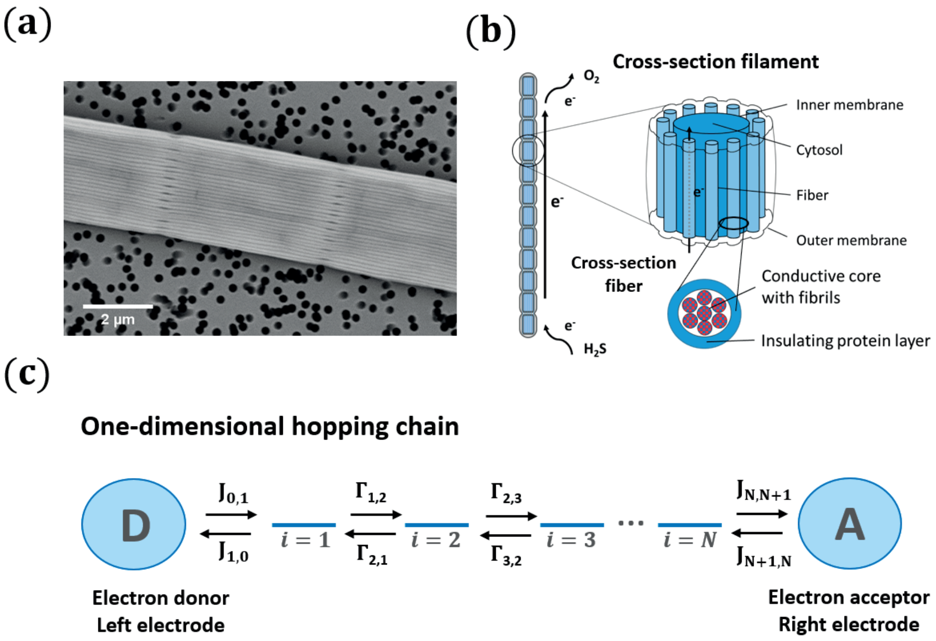

Figure 1: **Conduction in cable bacteria is modelled as a set of parallel one-dimensional hopping chains** (a) Scanning electron microscope image of a cable bacteria filament. The outer surface shows a set of parallel ridges, each embedding a conductive fibre. (b) Schematic of the conductive structure of cable bacteria based on recent investigations. A filament consists of a long chain of cells. Electrons are uploaded through H_2S oxidation, transported along the filament, and downloaded via O_2 reduction. The cell envelope incorporates a set of conductive fibres, with diameter d_F, that consist of thinner fibrils, with diameter d_C, which each act as a single independent conduction path. (c) A single conduction path is schematically represented as a linear chain of hopping sites (blue stripes). Between two adjacent sites $(i, i+1)$, there is a forward transition rate, $\Gamma_{i,i+1}$, and a backward transition rate, $\Gamma_{i+1,i}$. At the terminal ends, electron exchange occurs with electrodes or donor/acceptor molecules, formally represented by the sites $i = 0$ and $i = N+1$.

parallel in a single fiber. Here, we assume that each conductive fiber core consists of N_C parallel conduction paths, each $d_C = 2$ nm in diameter (Fig. 1b). Assuming a hexagonal packing of cylinders, this implies that each fiber embeds $N_C = 125$ parallel conduction channels. This large number of conduction channels can be regarded as an upper limit, thus providing a conservative estimate for the conductivity estimated by the model. If less channels are present, then the conductivity of individual channels must be higher. We disregard electron transport between channels, and so the total electrical current through a single bacterial filament is due to electron transport in $N_P = N_F \cdot N_C = 7500$ parallel one-dimensional conduction channels.

3.2.2. ELECTRON FLOW IN A ONE-DIMENSIONAL HOPPING CHAIN

Each conduction channel is described as a one-dimensional chain of charge carrier sites that spans a length L. From a biological perspective, a charge carrier site can be interpreted as a electron-carrying cofactor embedded in a non-conductive protein matrix.

Parameter	Symbol	Units	Value
Fibre diameter	d_F	nm	26
Number of fibres	N_F	-	60
Conduction channel diameter	d_C	nm	2
Number of conduction channels per fibre	N_C	-	125
Total number of parallel conduction channels	N_P	-	7500

Table 1: Parameterization of the conductive network in cable bacteria.

Electrons are assumed to be solely transported by hopping, i.e., sequential tunneling through the protein matrix from one cofactor to the next. A site can be in two states: uncharged (carrying no electron; X_i) or charged (carrying an electron; X_i^-). The resulting electron transfer can be represented by a biomolecular self-exchange reaction between electron carriers

$$X_i^- + X_j \longrightarrow X_i + X_j^- . \tag{1}$$

Between any pair of charge carrier sites i, j, the forward transition rate is denoted by $\Gamma_{i,j}$ and the reverse rate is given by $\Gamma_{j,i}$ (Fig. 1c). To keep the analysis tractable, we assume that these transfer rates are only dependent on the present state of the protein complex, and not on past states (Markov assumption). The hopping transitions at different locations are also assumed to be uncorrelated [92].

When the energies of the departure and destination sites differ ($U_i \neq U_j$), energy must be exchanged with the environment during the electron transfer from i to j to ensure energy conservation. If this energy is dissipated to an environment at constant temperature T (heat bath), the ratio of the transition rates must follow the detailed balance relation [56, 78]:

$$\frac{\Gamma_{i,j}}{\Gamma_{j,i}} = \exp\left(-\frac{U_j - U_i}{k_\mathrm{B} T}\right), \tag{2}$$

where k_B is Boltzmann's constant. The electron flow (i.e., number of electrons transported per unit time) between two sites is given by:

$$J_{i,j} = \Gamma_{i,j} p_i (1 - p_j). \tag{3}$$

Here, p_i is the site occupancy. An electron can only jump to a site when it is vacant (Pauli exclusion principle without electron spin). The transition rate is hence weighted by the probability that the starting site is occupied, p_i, and that the destination site is empty, $(1 - p_j)$. The dynamics of the site occupancy is governed by the combined effect of all electron currents that arrive at or leave a given site:

$$\frac{dp_i}{dt} = \sum_j \left(J_{j,i} - J_{i,j}\right). \tag{4}$$

The net electrical current that passes through the chain segment between sites i and $i+1$ becomes:

$$I_{i,i+1} = e \sum_{m=1,..,i} p_m \sum_{n=i+1,..,N} \Gamma_{m,n}(1-p_n) - e \sum_{m=i+1,..,i} p_m \sum_{n=1,..,i} \Gamma_{m,n}(1-p_n). \tag{5}$$

The quantity $e = 1.6 \cdot 10^{-19}$ C is the elementary charge. The first term represents the electrons travelling to the right (i.e. the forward currents passing site i), while the second term represents the electrons travelling to the left (i.e. the backward currents passing site $i+1$). Our interest is in the steady state situation, where no charge builds up in the hopping chain, and so the net electron flow from/to a particular hopping site must be zero ($dp_i/dt = 0$). In the steady state, the current must be the same across all segments the chain ($I_{i,i+1} = I$).

3.2.3. NEAREST NEIGHBOUR HOPPING

Electron tunneling in protein structures is known to have a strong exponential dependence on distance [11, 93–95]. Therefore, the chance that an electron hops to a remote site in the chain is improbable. We can implement this by only allowing transitions between adjacent sites, i.e., nearest neighbour hopping. Moreover, when the protein structure that forms the conduction channel is highly regular, all charge carriers will be identical, and the interdistance and site energy (without an imposed electrical field) will show little variation. As a result, the transition rates between neighbouring sites will be identical throughout the whole chain ($\Gamma_{i,i+1} = \Gamma_\mathrm{R}$ and $\Gamma_{i+1,i} = \Gamma_\mathrm{L}$). Assuming nearest neighbour hopping in a regular chain with identical sites, the net current (Eq. 5) simplifies to:

$$I = e\Gamma_\mathrm{R} p_i(1-p_{i+1}) - e\Gamma_L p_{i+1}(1-p_i). \tag{6}$$

Similarly, the site occupancy balance reduces to

$$\frac{dp_i}{dt} = \Gamma_\mathrm{R} p_{i-1}(1-p_i) - \Gamma_L p_i(1-p_{i-1}) + \Gamma_\mathrm{R} p_i(1-p_{i+1}) - \Gamma_L p_{i+1}(1-p_i). \tag{7}$$

When the hopping chain is very long, as is the case for cable bacteria, we can describe the occupancy profile as a continuous function of the position along the chain, $p_{i\pm1} = p(x_i + a)$, where x_i is the center position of site i, and a is the center-to-center distance between sites. The total number of sites in the chain hence amounts to $N = L/a$. Expansion to second order,

$$p(x_i \pm a) = p(x_i) \pm a \left[\frac{dp}{dx}\right]_{x_i} + \frac{a^2}{2}\left[\frac{d^2p}{dx^2}\right]_{x_i}, \tag{8}$$

and substitution into the site occupancy balance (Eq. 7), leads to the differential equation:

$$\frac{d^2p}{dx^2} + \frac{2}{a}\tanh\left(\frac{\Delta}{2k_\mathrm{B}T}\right)(2p-1)\frac{dp}{dx} = 0. \tag{9}$$

Here, $\Delta = U_i - U_{i+1} = eV(1-\alpha)/N$ represents the difference in site energy between two sites ($\alpha = \alpha_L + \alpha_R$ specifies the total voltage drop at the electrodes; see Fig. 2 and below). In a similar fashion, the normalized current can be written as (see S.I.):

$$\frac{I}{e\Gamma_\mathrm{R}} = \left(1 - \exp\left(\frac{-\Delta}{k_\mathrm{B}T}\right)\right) p(x)(1-p(x)) \; - a\frac{dp}{dx}\left(p(x) + \exp\left(\frac{-\Delta}{k_\mathrm{B}T}\right)(1-p(x))\right). \tag{10}$$

For a given temperature T, site spacing a and site energy difference Δ, the site occupancy profile $p(x)$ along the chain can be calculated from Eq. 9, and then implemented into Eq. 10 to provide the current.

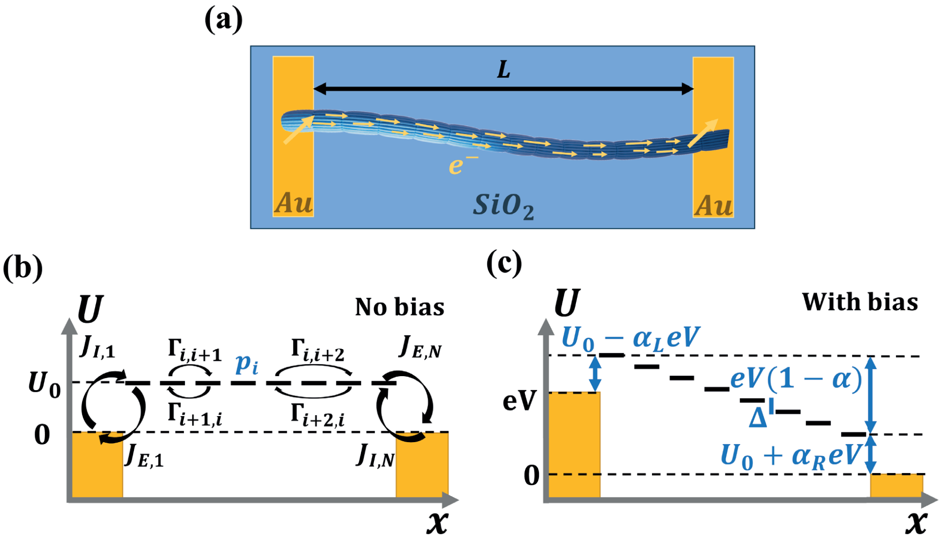

Figure 2: **Electrical investigation of cable bacteria filaments between electrodes.** (a) Schematic of the electrical characterization approach. A filament is deposited onto insulating silicon dioxide (SiO_2) substrate and connected to two gold (Au) electrodes with a gap length L. Electrons flow from one side to the other, through the conductive fiber network of the filament. (b) Site energy vs. position along the hopping chain for the case without any voltage bias. Transfer rates between hopping sites are denoted Γ, and injection/ejection rates from electrodes J. Electron states in the metal electrode (dark yellow) are filled up until the chemical potential, chosen as $\mu = 0$. Site energies are equal to the injection barrier ($U_\mathrm{i} = U_0$). (c) Site energy vs. position for an electrode bias V. The left electrode is at chemical potential $\mu_\mathrm{L} = eV$, and the right electrode at $\mu_\mathrm{R} = 0$. An electron looses an energy $\alpha_\mathrm{L} eV$ at the biased electrode and $\alpha_\mathrm{R} eV$ at the grounded electrode, while the rest of the energy is lost in the hopping chain ($eV(1-\alpha)$ with $\alpha = \alpha_\mathrm{L} + \alpha_\mathrm{R}$). As long as the voltage drops linearly inside the hopping chain, there is an constant voltage drop between adjacent hopping sites, $\Delta = eV(1-\alpha)/N$. The injection barrier at the left electrode is $U_0 - \alpha_\mathrm{L} eV$, and the other side, it is $U_0 + \alpha_\mathrm{R} eV$.

3.2.4. CHARGE TRANSFER TO AND FROM THE CHAIN

The site occupancy equation (Eq. 9), which governs the electron transport within the hopping chain, requires suitable boundary conditions. For this, we need to consider how electrons are either injected or ejected from the chain at the left and right boundaries. Two different situations can be considered: the metabolic operation of cable bacteria under in vivo conditions (in which electrons are supplied and removed through redox half-reactions; Fig. S2 in the S.I.), and the situation under which cable bacteria are electrically investigated in the laboratory (in which electrons are exchanged with electrodes; Fig. 2). The latter will be the focus of our analysis here, as it represents the situation under which the conductance data are collected.

In the laboratory, the conductance of cable bacteria is studied by connecting individual filaments to metal electrodes [2, 45, 91]. A bias voltage, V, is applied to the two terminal electrode contacts, and the electrical current, I, that flows through the cable bacterium segment is recorded (operation of the electrode set-up is illustrated in Fig. 2a). If charge injection from the electrode is non-limiting ($J \gg \Gamma_{\mathrm{R,L}}$; see Fig. S3 and additional derivations in S.I.), the occupation probability at the edges reads:

$$p_{L,R} = \frac{1}{\exp\left(\frac{U_{L,R}-\mu_{L,R}}{k_{\mathrm{B}}T}\right)+1} = \frac{1}{\exp\left(\frac{U_0 \pm \alpha_{L,R} eV}{k_{\mathrm{B}}T}\right)+1}. \tag{11}$$

In this expression, $U_{L,R}$ is the site energy of the start $x=0$ and end $x=L$ of the hopping chain and $\mu_{\mathrm{L,R}}$ is the chemical potential of the left/right electrode (Fig. 2b). The site energy at the terminal ends is given by $U_{L,R} = \mu_{L,R} + U_0 \pm \alpha_{L,R} eV$. In this approximation, the edge occupancies, $p_{L,R}$, follow the Fermi-Dirac distribution of the corresponding electrodes. In the general case, an injection barrier, U_0, is present (difference between Fermi level of the electrodes and the site energy in the hopping chain), and voltage drops (α_{L}, α_{R}) may occur at the interface between filaments and electrodes (see details in Fig. 2).

3.2.5. MARCUS HOPPING RATE

Semi-classical Marcus theory provides the following expression for the electron transfer rate between two sites in the hopping chain[15]:

$$\Gamma_{\mathrm{R}} = \frac{2\pi}{\hbar} \frac{H^2}{\sqrt{4\pi\lambda k_{\mathrm{B}}T}} \exp\left(-\frac{(\lambda-\Delta)^2}{4\lambda k_{\mathrm{B}}T}\right). \tag{12}$$

Here, H represents the electronic coupling between the initial and final states, and λ is the reorganisation energy. The Marcus expression only holds for the case of weak electronic coupling, i.e., when $H \ll \lambda$ [15, 70, 96]. When the driving force is small compared to the reorganization energy ($\Delta \ll \lambda$), the approximation $(\lambda-\Delta)^2 \sim \lambda(\lambda - 2\Delta)$ holds, and the Marcus rate can be written as:

$$\Gamma_{\mathrm{R}} = \Gamma_{\mathrm{R}}^{0} \exp\left(\frac{\Delta}{2k_{\mathrm{B}}T}\right). \tag{13}$$

The prefactor Γ_{R}^{0} represents the unbiased Marcus rate at a given temperature (Eq. 12 with $\Delta = 0$). If the electronic coupling H is only weakly dependent on the driving force, this prefactor can be considered to be independent of the applied voltage bias.

3.2.6. NUMERICAL APPROACH

The solution of the occupancy balance equation (Eq. 4) with suitable boundary conditions (Eq. 11) fully describes the electron transport through the hopping chain. To solve this differential equation, we implemented a numerical solution procedure (see S.I.) that calculates the site occupancy profile, $p(x)$, as a function of the position along the chain x and the applied bias voltage V. Subsequently the normalized current $I/(e\Gamma_{\mathrm{R}})$ is calculated, and this is then combined with the Marcus expression (Eq.12) to simulate the full $I(V)$ curve (see Fig. S1). We also derived a set of analytical expressions for the occupancy profile and normalized current for the case when there's a symmetric voltage drop at the electrodes ($\alpha_L = \alpha_R$). Expressions are derived for the absence ($U_0 = 0$) or presence ($U_0 > 0$) of an injection barrier. These analytical expressions allow to identify how different end-member transport regimes influence the shape of the I/V curve. The details of the derivations are given in the S.I. and the resulting expressions are summarized in Tables S1 and S2.

3.3. RESULTS

The mapping of the electrical current, I, as a function of the applied bias voltage, V, forms a key analysis in the electrical characterisation of materials. As a baseline and reference situation, we simulated a hopping chain with following parameters: $N = 200$, transport is predominantly field-driven ($\alpha = 0.2$), resides in the resonant regime ($U_0 = 0$), and has a reorganisation energy, $\lambda = 200$ meV, and electronic coupling, $H = 16$ meV. Subsequently, we systematically varied each parameter individually to verify its impact on the $I(V)$ curve. We also compared the output of the model simulations to an extensive experimental dataset, consisting of $I(V)$ curves collected at different temperatures ($T = 80 - 300$ K) for cable bacterium filaments of different length. The data collection procedure is presented in detail elsewhere [91]. Fig. 5 displays relevant $I(V)$ curves for three segments of different length (L = 4, 40, 300 μm).

3.3.1. CONCENTRATION-DRIVEN VERSUS FIELD-DRIVEN REGIME

A first question is whether the electron transport in cable bacteria is concentration-driven or field-driven. These regimes correspond to two limiting cases for the behaviour of the electrical field at the electrode interfaces (see Fig. 3): either the applied voltage completely drops over the electrode interfaces ($\alpha = 1$), or there is no voltage drop at the electrodes ($\alpha = 0$). In our simulations, we assume that the voltage drop is similar at both electrodes ($\alpha_L = \alpha_R = \alpha/2$).

When the current is exclusively concentration-driven, the entire voltage drop occurs at the interface of the electrodes ($\alpha = 1$, Fig. 3a), and there is no electric field or electric potential gradient present in the hopping chain ($\Delta = 0$). As a result, all sites reside at the same site energy, and the detailed balance relation (Eq. 2) implies that the forward and backward transition rates must be equal. In this regime, the electron transport is purely "diffusive", i.e., driven by the difference in site occupation probability along the chain. The differential equation describing the occupancy profile (Eq. 9), becomes the stationary diffusion equation and has a linear solution (Fig. 3c):

$$p(x) = p_L - (p_L - p_R)\frac{x}{L}, \tag{14}$$

with $p_L = p(x = 0)$ and $p_R = p(x = L)$.

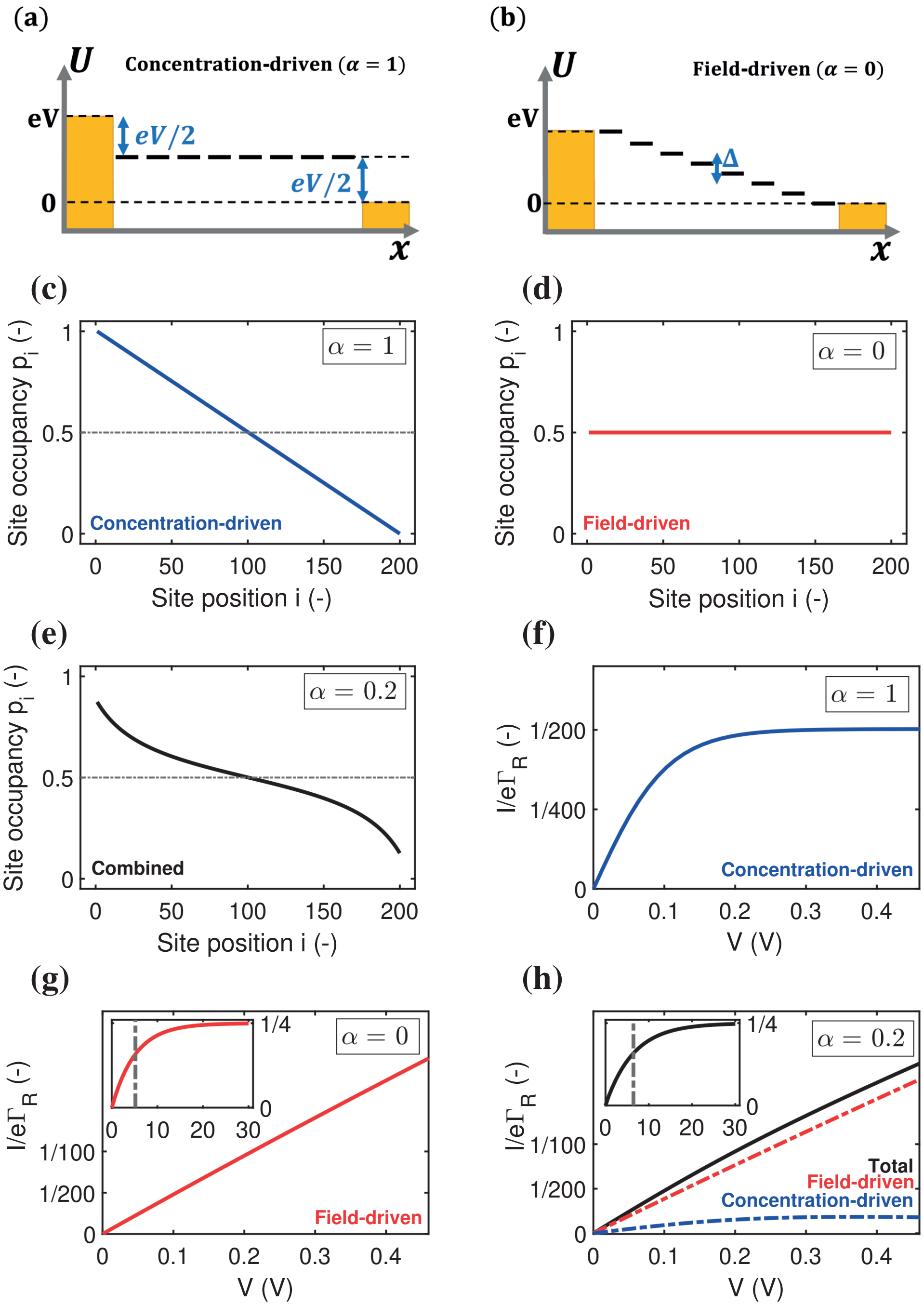

Figure 3: **Concentration-driven versus field-driven electron transport.** **(a) and (b)** Energy vs. position diagram in the concentration-driven end-member ($\alpha = 1$) and field-driven end-member ($\alpha = 0$). **(c)** Site occupancy, p_i vs. site position, i, in the concentration-driven limit ($\alpha = 1$). **(d)** Site occupancy, p_i vs. site position, i, in the field-driven limit ($\alpha = 0$). **(e)** Site occupancy, p_i vs. site position, i, in the combined scenario ($\alpha = 0.2$). **(f)** Normalized electron current, $I/(e\Gamma_R)$ as a function of the applied voltage, V, in the concentration-driven limit ($\alpha = 1$). **(e)**, Same graph in the field-driven limit ($\alpha = 0$). The inset shows higher-voltage regime, with a vertical line plotted at $eV = Nk_BT$. **(f)**, Same in the combined scenario ($\alpha = 0.2$), with the field- and concentration-driven terms (red and blue respectively). The inset shows higher-voltage regime, with a vertical line plotted at $eV(1-\alpha) = Nk_BT$.

he normalized current shows an hyperbolic tangent dependence on the applied voltage (Fig. 3f, derivation in S.I.):

$$\frac{I}{e\Gamma_{\mathrm{R}}} = \frac{1}{N}\tanh\left(\frac{eV}{4k_{\mathrm{B}}T}\right). \tag{15}$$

Because there is no electric field within the hopping chain ($\Delta = 0$), the transition rate matches the unbiased Marcus rate ($\Gamma_{\mathrm{R}} = \Gamma_{\mathrm{R}}^{0}$), and so the I/V curve attains the form:

$$I = \frac{e\Gamma_{\mathrm{R}}^{0}}{N}\tanh\left(\frac{eV}{4k_{\mathrm{B}}T}\right). \tag{16}$$

The current starts out linearly ($I \propto V$), and saturates around $eV \approx 4k_{\mathrm{B}}T$, as the occupancy gradient approaches its maximum ($p_{\mathrm{L}} = 1$; $p_{\mathrm{R}} = 0$). At room temperature, this saturation should occur around $V = 0.1$ V. The experimental $I(V)$ curves (Fig. 5a,b,c), however, do not show this saturation effect. When the bias voltage is increased beyond 0.1, the I(V) curve still remains linear. Therefore, the electron transport in fiber network of cable bacteria does not appear to be concentration-driven.

Oppositely, when the current is exclusively field-driven ($\alpha = 0$, Fig. 3b), the site occupancy does not show a gradient ($p_i = 1/2$, Fig. 3d). In this field-driven scenario, electron transport is solely "drift" based, i.e., it is driven by the difference in the forward and backward transition rates. The normalized $I(V)$ curve becomes (Fig. 3g, derivation in S.I.):

$$\frac{I}{e\Gamma_{\mathrm{R}}} = \frac{1}{4}\left[1 - \exp\left(\frac{-eV}{Nk_{\mathrm{B}}T}\right)\right]. \tag{17}$$

This relation predicts that the normalized current becomes constant ($I/(e\Gamma_{\mathrm{R}}) = 1/4$), when the applied voltage becomes sufficiently high, i..e, when $eV/N > k_{\mathrm{B}}T$ (inset in Fig. 3g). Yet, when the chain includes many hopping sites, this transition voltage $V = Nk_{\mathrm{B}}T/e$ is very large. For example, for a long cable bacterium segment (~ 2 mm) and a short hopping distance (~ 1 nm), the number of hopping sites becomes $N = 2 \cdot 10^{6}$, and so the corresponding transition voltage at room temperature ($k_B T \approx 25$ meV) equals $V = 50 \times 10^{3}$ V. This explains why the transition is not seen in the experimental I/V data.

When the voltage bias is sufficiently small compared to the reorganization energy ($eV/N < \lambda$), we can use the Marcus rate expression, Eq. 13, and so the I/V curve attains the form:

$$I = \frac{e\Gamma_{\mathrm{R}}^{0}}{2}\sinh\left(\frac{-eV}{2Nk_{\mathrm{B}}T}\right) \approx \frac{e\Gamma_{\mathrm{R}}^{0}}{4}\frac{eV}{Nk_{\mathrm{B}}T}. \tag{18}$$

The experimentally recorded $I(V)$ curves closely fit the temperature-dependent response that is predicted by the above relation (Fig. 5d-f). When the temperature is high and the bias is sufficiently small, i.e., when $eV/N < k_{\mathrm{B}}T$, the approximation in Eq. 18 is valid and the I/V becomes linear. Such linear I/V curves are indeed observed near room temperature. Moreover, when the temperature is lowered, the experimental I/V curves become more non-linear and adopt a hyperbolic sinus shape, as predicted by Eq. 18. This hence suggests that conduction in cable bacteria is field-driven.

When $\alpha = 0.2$, the site occupancy profile adopts a non-linear shape, which lies in between the linear concentration-driven and flat field-driven profile (Fig. 3e). Likewise, it can be shown that the resulting $I(V)$ curve can be decomposed into the sum of a field-driven and a concentration-driven contribution (Fig. 3h; see derivation in S.I.). At higher voltages, the field-driven current becomes dominant (Fig. S5).

When $\alpha = 0.2$, the occupancy profile adopts a non-linear curve, which lies in between the linear concentration-driven and flat field-driven profile (Fig. 3e). Likewise, it can be shown that the resulting $I(V)$ curve can be decomposed into the sum of field-driven contribution and a concentration-driven contribution (Fig. 3h; see Appendix: 'Combination field- and concentration-driven current' for additional derivation and discussion).

3.3.2. RESONANT VERSUS OFF-RESONANT TRANSPORT

A second question is whether the electron transport in the conductive fibers of cable bacteria is affected by an injection barrier, U_0, or not. When the charge transport is not hampered by the barrier, it resides in the resonant regime. Oppositely, when the injection barrier is slowing down the transport, it is off-resonant. Figure 4 shows the transition from the off-resonant to resonant transport regime for the reference parameters, but with $U_0 = 0.1$ eV instead of zero. Analytical expressions can be derived for the occupancy profile and the normalized $I(V)$ curve (see S.I.). For low bias voltages, transport is off-resonant ($\alpha_L eV < U_0$), and the site occupancy stays low throughout the chain (Fig. 4a). As the bias voltage increases, the conduction enters the resonant regime when $\alpha_L eV = U_0$ and the occupancy profile evolves towards a static tangent-shaped profile (Fig. 4a, similar to that displayed in Fig. 3e). The normalized $I(V)$ curve shows the transition from off-resonant to resonant transport, which occurs at $V = U_0/(e\alpha_L)$ (Fig. 4b). At low bias, in the off-resonant regime, the normalized current is non-linear, while in the resonant regime, the normalized current increases linearly with the applied voltage bias.

In the off-resonant regime, the temperature has a large effect on the site occupancy profile, and induces an overall decrease of the site occupancy upon cooling. In contrast, in the resonant regime, the occupancy profile is only marginally influenced by the temperature (Fig. 4c). Overall, the full $I(V)$ curves show the same strong non-linear shape as the normalized $I(V)$ (Fig. 4d). The experimental $I(V)$ curves do not display this strong non-linearity (Fig. 5). This indicates that there is no significant injection barrier present, when the cable bacterium filaments are interfaced to gold electrodes.

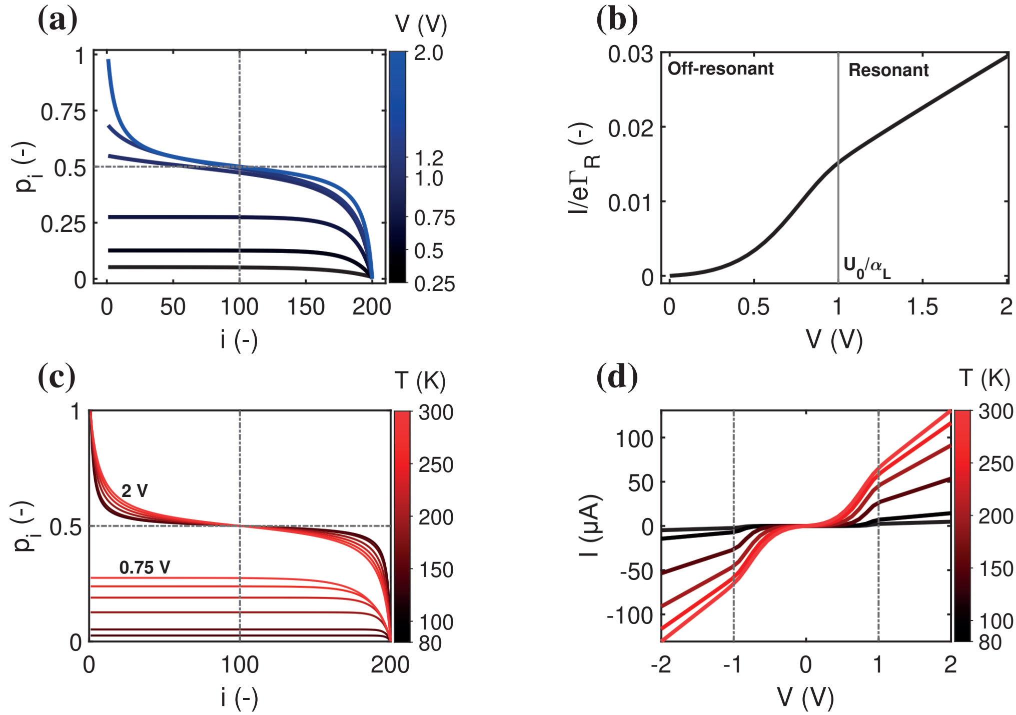

Figure 4: **Resonant and off-resonant electron transport in a hopping with an injection barrier.** Model parameters are: $N = 200$, $U_0 = 0.1$ eV, $\alpha = 0.2$, $T = 300$ K. (a) Simulated occupancy profile for six different voltages (as indicated by numbers next to the colour bar). The dashed lines indicate the crossing at $p_{N/2} = 1/2$. (b) Normalized current, $I/e\Gamma_R$, plotted as a function voltage bias, V. The transition from off-resonant to resonant occurs at $eV = U_0/\alpha_L = 1$ V. (c) Occupancy profile at two fixed voltages (off-resonant $V = 0.75$ V and resonant $V = 2$ V) for six different temperatures (indicated by numbers next to the colour scale). (d) Simulated current-voltage response for six different temperatures, using the Marcus rate (Eq. 12) with parameters $H = 16$ meV and $\lambda = 0.2$ eV.

3.3.3. LENGTH DEPENDENCE OF THE $I(V)$ CURVE

A third aspect relates to the impact of the hopping chain length on the $I(V)$ curve. As clearly seen in the experimental data (Fig. 5a-c), the shape of the $I(V)$ curve becomes more linear as the length of the investigated segment increases. This phenomenon is well represented by Eq. 18, which predicts that the $I(V)$ curve becomes more linear as the number of sites N increases (simulated I/V curves are displayed in Fig. 5d-f). The explanation is rather straight forward: as the number of sites N decreases, the site energy difference $\Delta = eV/N$ increases at a given fixed voltage. When Δ increases, the expression for the normalized current (Eq. 17) becomes non-linear, while also the Marcus rate (Eq. 13) adds to the non-linearity. As a result, the full $I(V)$ curve becomes increasingly hyperbolic, when the temperature decreases and/or the segment length decreases (Fig. 5).

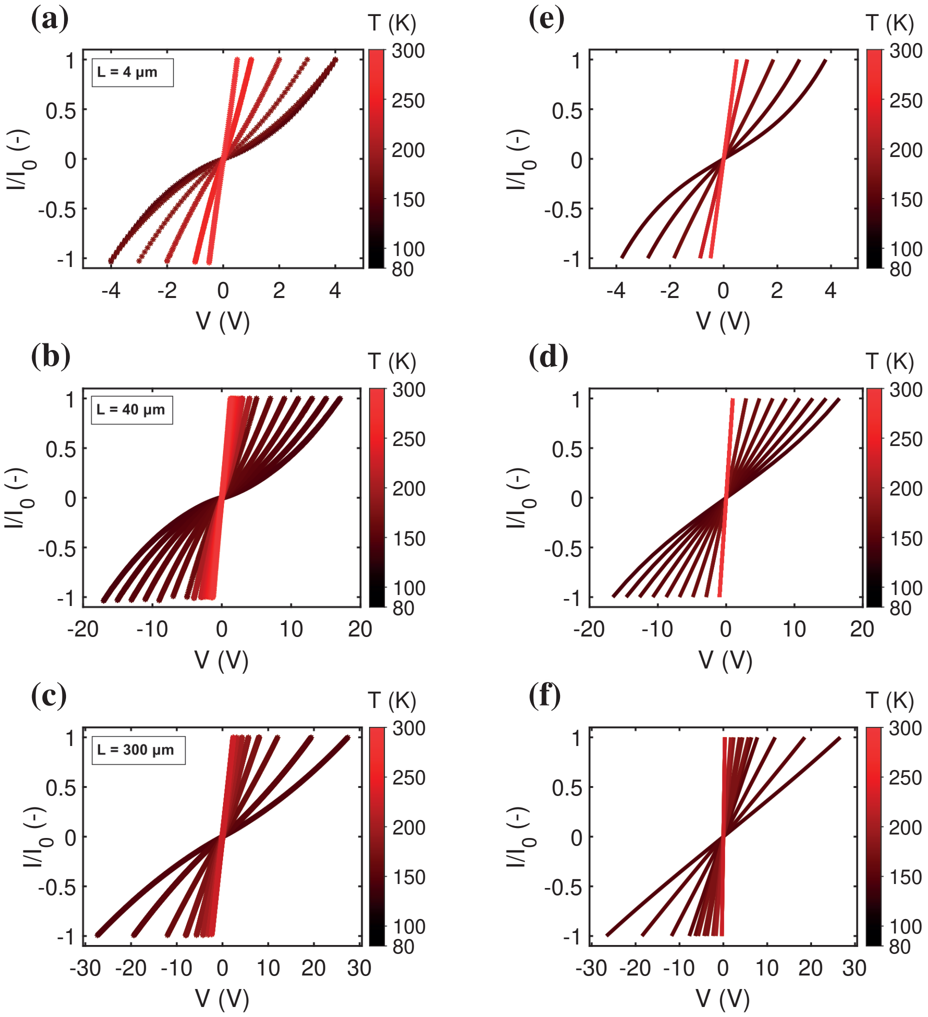

Figure 5: **Dependence of $I(V)$ curves on temperature in the range 80-300 K. (a-c)** Experimental data showing the rescaled current, I/I_0, as a function of voltage, V. The current, I, is rescaled to its maximum value, I_0, per $I(V)$-trace, to illustrate the shape of the curve. The three panels (a),(b) and (c) correspond to three different segment lengths ($L = 4$ μm, $L = 40$ μm, and $L = 300$ μm). **(d-f)** Simulated $I(V)$'s with $N = 70$ (d), $N = 450$ (e) and $N = 3000$ (f). The other parameters are: $U_0 = 0, \alpha = 0, H = 16$ meV and $\lambda = 0.2$ eV.

3.3.4. CONDUCTIVITY

Overall, the multistep hopping model appears to adequately simulate the experimental $I(V)$ curves, in the field-driven regime with no significant injection barrier. Therefore, a prominent question is whether the model can also reproduce the conductivity of the cable bacteria fibers, which is extremely high for a biological system (reaching up to > 100 S/cm at room temperature). To this end, we now investigate the relationship between the hopping rate and the electrical conductivity.

Assuming a suitably long chain (such that the low-bias limit $eV/N \ll k_B T$ holds), and adopting field-driven transport ($\alpha = 0$) and no injection barrier ($U_0 = 0$), we can use Eq. 18 to express the conductivity of a fiber of length L and cross-section A:

$$\sigma = \frac{I}{V}\frac{L}{A} = \frac{e^2\Gamma_R^0}{4k_B T}\frac{a}{\pi(d_C/2)^2}. \tag{19}$$

This expression is insightful, because it has the familiar form, $\sigma = ne\mu$, with the charge carrier density $n = 1/(4a\pi(d_C/2)^2)$ and mobility, $\mu = e\Gamma_R^0 a^2/(k_B T)$. The factor 1/4 in the charge carrier density n arises from the occupation factor $p(1-p)$ with $p = 1/2$ the site occupancy in the resonant, field-driven regime (Fig. 4).

Equation 19 provides a direct relation between the hopping rate and the conductivity, and readily illustrates the problem of explaining the high conductance in cable bacteria. If we assume that multistep hopping in cable bacteria occurs over a similar length scale as in multi-heme cytochromes [23], the center-to-center distance between sites would be $a \sim 1$ nm. Using this value in Eq. 19, the required hopping rate for a conductivity of 100 S/cm becomes $\Gamma_R \approx 2\cdot 10^{13}$ s^{-1}. This value exceeds by far the fastest hopping rate reported in literature for a biological protein structure (10^9 s^{-1}) [97, 98]. More problematically, it also exceeds the typical relaxation rate of vibrational modes in cofactors, $\sim 10^{13}$ s^{-1}, which is considered as a "speed limit" for hopping conduction [99]. The relaxation rate of vibrational modes must be higher than the hopping rate itself, so that the electron has time to dissipate energy before hopping onwards (see S.I.: 'Non-adiabatic constraint' for further detail).

To examine the maximum conductivity that a hopping model for cable bacteria can support, we can evaluate the theoretical limits of the Marcus rate expression Eq. 12. Marcus theory requires that the inter-site electronic coupling H is weak [15], so that it remains small with respect to the reorganisation energy ($H \ll \lambda$). When $H \approx \lambda$ or beyond, the electron will no longer be localised on the hopping site [70, 96, 100]. To quantitatively evaluate the maximum conductivity allowed by the Marcus formalism, we adopt the working assumption that the maximum electronic coupling is $H_{\max} = 0.1\lambda$ (see S.I. for additional discussion of this 'weak coupling' constraint).

As a result, the conductivity in Eq. 19 only varies with the reorganisation energy λ and the center-to-center distance a. The resulting model simulations are shown in Fig. 6a. For parameters representing electron transport through multi-heme cytochromes [23] ($\lambda = 0.8$ eV, $a = 1$ nm), a hopping rate of $5\cdot 10^{10}$ s^{-1} and a conductivity level of 0.2 S/cm form the theoretical maximum within the Marcus framework. Note however that this conductivity limit is based upon an unrealistically high electronic coupling, $H \approx \lambda/10 =$ 80 meV. As known from experimental and theoretical assessments, $H = 10$ meV is already on the high side for multi-heme cytochromes [23]. Adopting the latter value lowers the

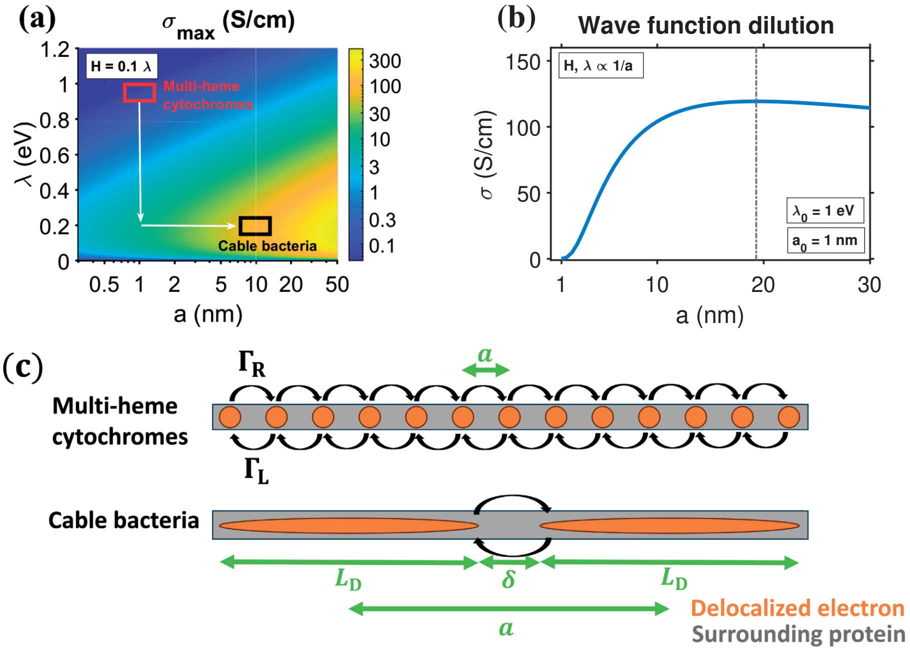

Figure 6: **Idealized hopping conductivity and mobility within the one-dimensional hopping chain**, using Marcus rates (Eq. 12). (a) Conductivity colour map, under the constraint $H = 0.1\lambda$, as a function of reorganisation energy λ and center-to-center distance between hopping sites a. The red and black square are indicators for the typical reorganisation energy and center-to-center distance in hemes and cable bacteria, respectively (see panel (c)). Directions for increased conductivity compared to cytochromes are drawn in white. (b) Conductivity, σ, as a function of center-to-center hopping distance, a, for a biological system that improves on heme-to-heme hopping with distance $a_0 = 1$ nm, reorganisation $\lambda_0 = 1$ eV and electronic coupling $H_0 = 0.1\lambda_0 = 100$ meV, by wave function dilution ($H, \lambda \propto 1/a$). (c) Scheme of heme-to-heme transport and the proposed hopping mechanism in cable bacteria, with center-to-center distance, a, between regions in which is the electron is unobstructed (orange, zero resistance) with repetitive surrounding protein structure (grey). Electrons hop between repeated structures with hopping rates $\Gamma_{R,L}$.

maximum allowed conductivity to 4 mS/cm (hopping rate: $8 \cdot 10^8$ s^{-1}).

We conclude that a multi-step hopping model with cytochrome-like parameters cannot explain the conductivities measured in cable bacteria. As illustrated in Fig. 6a, there are two ways to achieve a higher conductivity. A first way is to reduce the reorganisation energy, and effectively, cable bacteria appear to do this. Recent studies [45, 91] indicate that the reorganisation energy of conductance in cable bacteria is remarkably low ($\lambda = 0.2$ eV), i.e., a factor 4 lower compared to heme-to-heme transport in multi-heme cytochromes.

Still, a reduction of the reorganization energy alone is not enough to explain the high conductivity in cable bacteria. With $\lambda = 0.2$ eV and $a = 1$ nm, we can only reach a hopping rate of $2 \cdot 10^{12}$ s^{-1} and a conductivity level of 10 S/cm (vertical arrow in Fig. 6a). Therefore, a second way is to increase increase conductivity is to increase the center-to-center distance a, thus lowering the number of hopping steps. To attain a conductivity of $\sigma = 100$ S/cm as reported for cable bacterium fibers, we need to increase the hopping distance to $a \approx 10$ nm, under the constraint $H_{max} = 0.1\lambda$ with $\lambda = 0.2$ eV (horizontal arrow in Fig. 6a). This provides a hopping rate $2.2 \cdot 10^{12}$ s^{-1}, which is still high, but below the "speed limit" for hopping conduction [99]. For more stringent constraints with lower H/λ ratios, higher a values are required (see Fig. S10 and additional results in SI).

The predicted electron mobility accompanying $\lambda = 0.2$ eV and $a = 10$ nm is $\mu =$ 80 cm^2/Vs (Fig. S10). This mobility value is high and similar to that of metals (∼ 50 cm^2/Vs). Metals are highly conductive because many electrons contribute to transport ($n \approx 10^{22} cm^{-3}$), but their charge carrier mobilities are not exceptionally high, since electrons frequently collide with the crystal lattice. The predicted charge carrier density in the one-dimensional hopping chain model with $a = 10$ nm, is $n = 1/(4a\pi(d_C/2)^2) \approx 8 \cdot 10^{18}$ cm^{-3}, which is much lower than for metals, thus explaining why the conductivity in cable bacteria is 4 orders of lower than in metals.

3.4. DISCUSSION AND CONCLUSIONS

We have developed a one-dimensional hopping model to describe the extremely long-range electron transport in the periplasmic fiber network of cable bacteria. When filaments are connected to metal electrodes, we propose that the edge occupation probabilities in the hopping chain can be treated as if they were part of the electrode (see Eq. 11). This allows simplified analytical expressions to be derived for the current-voltage characteristics in the field- and concentration-driven regimes (Tables S1 and S2). For more general cases, I/V curves can be numerically simulated.

The conductive fiber network in cable bacteria has been shown to consist of a metalloprotein that incorporates a nickel cofactor [44]. Yet, the detailed molecular structure of this cofactor remains unresolved, and consequently, any model of charge transport in cable bacteria remains somehow speculative. Still, the model analysis here allows to exclude certain transport models, while at the same time, it provides guidance for further experimental investigations and theoretical developments.

3.4.1. THE SHAPE OF THE I/V CURVE

When cable bacterium filaments are connected to electrodes and electrically investigated at room temperature, the resulting I/V curves are conspicuously linear [2, 45, 91]. Comparison of our model results to these experimentally recorded I/V curves, shows that the model adequately reproduces the impact of segment length and temperature on the shape of the I/V curve, provided that we adopt a field-driven regime with no significant injection barrier (Fig. 5).

The linearity is explained by the fact that the filaments investigated are long, and so the charge transfer involves a large number of charge transfer steps N. As a result, the driving force $\Delta = eV/N$ remains small compared to the thermal energy scale ($\Delta \ll k_B T$ and so Eq. 17 becomes valid). Moreover, the driving force also stays well below the reorganization energy ($\Delta \ll \lambda$), implying that the electron transfer rate Γ_R remains largely independent of the applied voltage bias (see Eq. 12). These conditions generate linear I/V curves near room temperature, which become increasingly non-linear (sinus hyperbolic) for lower temperatures and shorter segments, as seen in the experimental data (Fig. 5). Note that the condition ($\Delta \ll \lambda$) also implies that the charge transport well remains within the normal Marcus regime (and hence does not enter into the inverted regime).

When using gold electrodes, there appears to be no injection barrier involved in the charge transport. This absence of an injection barrier is intriguing, and requires further experimental examination. The work function, which directly influences the barrier, varies among metals (the energy to bring an electron from the electrode to vacuum of the electrode) [101, 102]. Therefore, it could be that for electrode materials other than gold, there is a sizable injection barrier.

3.4.2. IMPACT OF REORGANIZATION ON CONDUCTIVITY

Our model analysis demonstrates that a low reorganization energy is key to achieving a high conductivity in cable bacteria (Fig. 6a). Recent studies have shown that the reorganisation energy in cable bacteria is indeed considerably lower than in other conductive protein systems [45, 91]. Yet at present, the molecular structure of the conductive fibers in cable bacteria remains largely unresolved, and therefore, it is not understood why the reorganisation energy of cable bacteria is so small. One potential explanation could be delocalization along the electron transport path, as would result from an ordered aggregation or tight stacking of cofactors. Recently, an extension of Marcus theory has been developed that accounts for charge transfer between so-called donor and acceptor “aggregates”, in which the charge is no longer localized on a single cofactor, but delocalized across a cluster of multiple cofactor molecules [69]. It was shown that such delocalization can substantially reduce the reorganization energy below what is possible with a single donor and a single acceptor. For example, for a donor aggregate with a fully delocalized state of N identical donors, the reorganisation energy is decreased N-fold [69]. For example, if we assume that the reorganization energy λ between a single donor and a single acceptor would be similar to that between consecutive hemes in multi-heme cytochromes, the observed 4 times reduction in λ for cable bacteria as compared to multi-heme cytochromes [45, 91] then would imply a delocalization of the charge across ~ 4 cofactor molecules. Yet, to verify whether such a delocalization mechanism is truly at play, we need a better insight into the actual identity and structure of the cofactor molecules in cable bacteria.

3.4.3. A TENTATIVE MODEL OF CHARGE TRANSPORT IN CABLE BACTERIA

Our model analysis reveals that the high conductivity recorded in the conductive fibers of cable bacteria (> 100 S/cm) can only be explained by a Marcus-type hopping model, unless the number of hopping steps is substantially reduced and the center-to-center distance a becomes very large (Fig. 6a). Clearly, a hopping distance of $a \approx 10$ nm exceeds by far the known hopping distances in metalloproteins such as multi-heme cytochromes. If electrons are transported by quantum mechanical tunneling, the center-to-center distance a must be lower than 1.4 nm to attain metabolically relevant electron transport rates (see Moser et al. [55]). How can such a large value for a be reached?

A tentative model is depicted in Fig. 6c. The key difference with classical hopping models of biological transport (e.g. heme-based electron transport) is the amount of delocalization, as reflected by the size of the charge carrier sites. Instead of being localized on a small cofactor molecule, electrons are delocalized across wide "relay segments" (distance $L_D \sim 10$ nm) that are connected through small non-conductive bridges (distance δ). The electron transport through this protein connection is the rate limiting process, and follows a Marcus-type hopping mechanism. In contrast, the electron transport in the delocalized segments is very fast, and needs to have a far higher mobility than the hopping transport. These relay segments could either be large conjugated molecules, as seen in pi-conjugated polymers and graphene nanoribbons [103], or alternatively, they could involve sets of tightly stacked cofactor molecules that induce electron delozalization (the donor and acceptor “aggregates” discussed above).

This model immediately provokes the question of how biology can synthesize such a structure. Clearly, to ensure high charge transport rates, the "relay segments" should be carefully positioned and oriented, which hence requires a precise coordination by ligating proteins. Furthermore, it is known that delocalized regions are particularly sensitive to disorder effects, as impurities and defects will induce Anderson localisation of electrons [104], and hence reduce the conductivity. Effectively, the latter phenomenon may help explaining the observation that the conductivity in cable bacteria fibers is variable (ranging from 0.1 to >100 S cm-1; see [2]). Differences in levels of defects/impurities may induce variability in conductance between filaments.

3.4.4. IMPACT OF DELOCALIZATION ON CONDUCTIVITY

As detailed above, the conductivity can be increased by lowering the reorganization energy and increasing the the center-to-center distance (Fig. 6a). To quantitatively assess the conjoint impact of both factors, we can introduce reference values for the hopping distance ($a_0 \sim 1$ nm) and reorganization energy ($\lambda_0 \sim 1$ eV) for conventional biological electron transport. We can now increase a while keeping δ constant, thus simulating the process of wave function dilution (Fig. 6c). When a becomes much larger than a_0, we can approximate the delocalization length $L_D \approx a$ and write the reorganisation energy as $\lambda = \lambda_0(a_0/a)$ and the electronic coupling as $H = H_0(a_0/a)$, where λ_0 is the original reorganisation energy and H_0 the original electronic coupling. With these constraints, the ratio between H and λ stays constant, and so the transport remains within the Marcus regime. Moreover, the conductivity can be calculated as a sole function of the center-to-center distance:

$$\sigma(a) \propto a^{-1/2} \exp\left(-\frac{a_0}{a}\frac{\lambda_0}{4k_B T}\right). \tag{20}$$

The impact of wave function dilution on conductivity is shown in Fig. 6b. With increasing a, the conductivity first increases, after which it reaches a maximum at $a = a_0\,\lambda_0/(2k_B T) = 19$ nm, which is equivalent to $\lambda = 2k_B T$. At higher values of a, the impact of λ fades and the influence of H becomes dominant, and as a result, the conductivity decreases again. This analysis demonstrates that delocalization may indeed form a mechanism that can substantially increase the conductivity in cable bacteria.

3.4.5. HOPPING VERSUS BAND TRANSPORT?

In our model analysis, we described the electron transport in cable bacteria as thermally assisted hopping, as this is the default modelling approach employed to describe long-range biological conduction. Is there a possibility that the charge transport is not due to hopping, but rather acts as a form of band transport? In a hopping regime, the charge carrier is localized on a single molecule whereas in the band regime, the charge carrier (wave function) is delocalized over the entire system. In order to achieve a band regime, one must have a highly ordered structure with only a few defects or impurities, and a large electronic coupling between adjacent sites. In highly purified molecular single crystals such as pentacene, transport at low temperature can be described within a band picture [105]. However, at higher temperatures, the charge carriers get localized over single polymer strands and transport operates by a thermally activated hopping mechanism between adjacent polymer chains [106].

As impurities, disorder and structural defects seem hard to avoid in the cm-long fiber structures in cable bacteria, a hopping regime is expected to operate at room temperature, as in organic crystals. Nevertheless, the models investigated here consider only one electronic state in a given "relay segment". This leaves the possibility that there is more than one electronic state in a given "relay segment". Recall that the driving force behind localisation in our model is a weak electronic coupling at the edge of the hopping site ($H < \lambda$). If a relay segment would be composed of N tightly stacked molecules, these must all be strongly coupled with an interaction energy, $t > \lambda$, if not, the electron would localise in a smaller region [96]. According to the tight binding model, this results in multiple electronic states lying in an energy band of width $4t$ [71, 107]. Within a 10 nm wide "relay segment", and assuming a stacking distance of 0.35 nm (a typical intermolecular distances in organic conjugated crystals and films), each molecule ($N = 30$) would add a single state to an energy band with an expected level spacing $4t/N \sim 4\lambda/N \approx 27$ meV. At room temperature, the majority of states would contribute to the conductance (thermal window $k_B T \approx 25$ meV). Therefore, while pure band transport is not expected in the conductive fiber network of cable bacteria, future studies should consider more elaborate model approaches that allow the existence of multiple electronic states within "relay segments".

3.5. SUPPLEMENTARY INFORMATION

3.5.1. NUMERICAL SIMULATION OF OCCUPANCY PROFILES

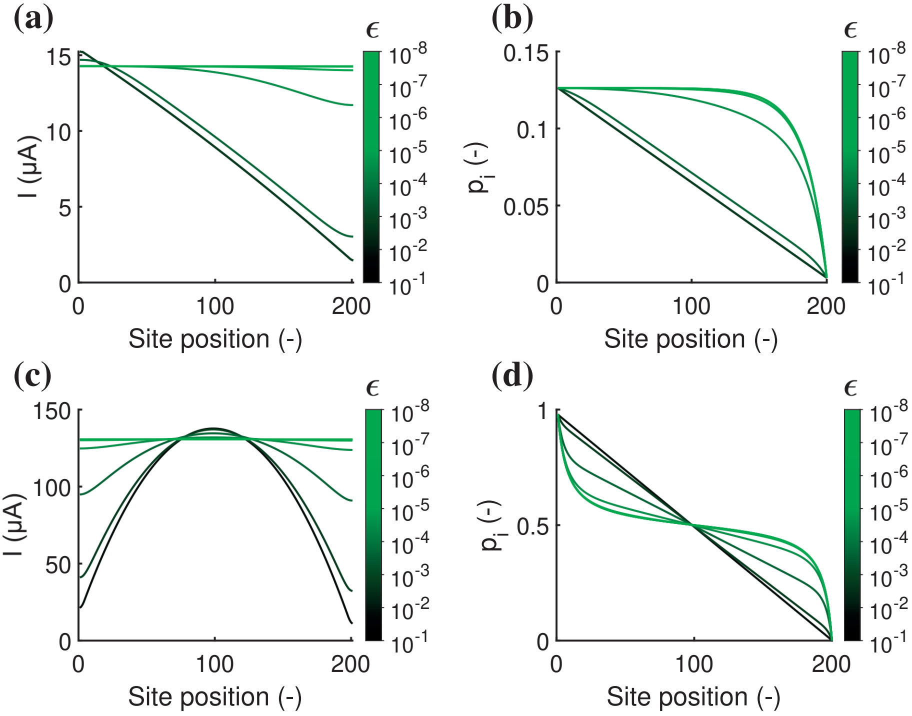

Figure S1: **a-d** Iterative simulation of occupancy profiles. The simulated electrical current (a,c) and the occupation profile (b,d) are shown at different stages on the path towards convergence (indicated by different values of the convergence parameter ϵ). The model parameters used are: $N = 200$, $\alpha_{L,R} = 0.1$, $U_0 = 0.1$ eV, $T = 300$ K, $H = 16$ meV and $\lambda = 0.2$ eV. In the first case (panels (a) and (b)), the voltage bias is $V = 0.5$ V and the current resides in the off-resonant regime. In the second case (panels (c) and (d)), the voltage is $V = 2$ V and the current is in the resonant regime.

Combining the equations for the occupancy balance (Eq. 3 and Eq. 4), and adopting steady state, gives:

$$e\frac{dp_i}{dt} = 0 = (1-p_i)\sum_j e\Gamma_{j,i}p_j - p_i\sum_j e\Gamma_{i,j}(1-p_j). \tag{S1}$$

By rearranging this expression so that p_i becomes isolated, we find:

$$p_i = \frac{\sum_j e\Gamma_{j,i}p_j}{\sum_j e\Gamma_{j,i}p_j + \sum_j e\Gamma_{i,j}(1-p_j)}, \tag{S2}$$

Note that p_i features both on the left and right hand side. This non-linear equation can be iteratively solved given an initial set of occupation probabilities, p_i. The initial condition chosen is:

$$p(x) = p_{\mathrm{L}} - (p_{\mathrm{R}} - p_{\mathrm{L}})\frac{x}{L}, \tag{S3}$$

where p_L and p_R are determined by the edge occupancy relation (Eq. 11). After a suitable number of iterations, the electrical current and the occupancy will converge (Fig. S1). The criterion when to stop the iterative calculations is based on the difference between the newly calculated site occupancies, $\{p_{i,new}\}$, and those from the previous iteration, $\{p_{i,old}\}$:

$$\epsilon = \max\left(\frac{\{p_{i,new}\} - \{p_{i,old}\}}{\{p_{i,old}\}}\right). \tag{S4}$$

As long as the convergence indicator ϵ exceeds a predefined error value, the iterative calculation continues. After convergence of the occupancy profile, the net electrical current to all sites beyond hopping site i, is evaluated via Eq. 5. As a quality check, we verified whether the current is constant throughout the hopping chain: the net electrical current calculated at each site must not vary more than 1% (otherwise the calculation has not properly converged). In Fig. S1, we illustrate the iterative calculation of the occupancy profile for two separate values of the voltage bias (leading to resonant and off-resonant regimes).

3.5.2. ELECTRON TRANSFER AT THE BOUNDARIES

In vivo SITUATION

Under *in vivo* conditions, cable bacteria interact with mobile redox species in an aqueous solution. Electrons are injected onto, or withdrawn from, the internal conductive fiber network through metabolic redox reactions. Free sulfide (H_2S) acts as the electron donor within the sulfidic zone of the sediment, while oxygen (O_2) acts as the electron acceptor near the sediment surface. We can describe this process of electron exchange by incorporating two additional sites at the terminal ends of the hopping chain, which represent the electron donor and electron acceptor respectively ($i = 0, N+1$). These two sites show a difference in site energy that matches the difference in reduction oxidation potential ($U_0 - U_{N+1} = E_{\text{redox}}$). In reality, this difference in redox potential will be very large, and hence, this will provide a non rate limiting concentration of donor and acceptor molecules (electron donor site fully reduced, $p_0 = 1$; electron acceptor site fully oxidized, $p_{N+1} = 0$).

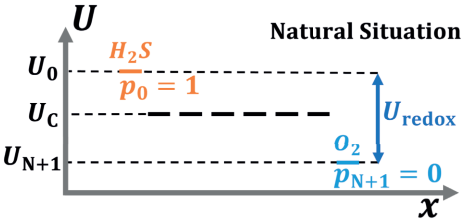

Figure S2: **Boundary conditions in the natural situation.** Under in vivo conditions, the electron transport in cable bacteria is driven by redox reactions at the terminal ends. On one end, an electron is produced by the oxidation of hydrogen sulphide (H_2S) at energy U_0, and introduced into the hopping chain. At the other end, the electron participates in the reduction of oxygen (O_2) at energy U_{N+1}, and is removed from the hopping chain. It is assumed that the electron donor (H_2S) and the electron acceptor (O_2) can be modelled as edge hopping sites with a fixed occupancy. Furthermore, it is assumed there is no voltage build-up in the hopping chain due to ionic screening as suggested by Strycharz-Glaven *et al.* [90] ($\alpha = 1$).

Electrode contact and edge occupancy

When using metal electrodes to inject/eject charges, there is not a single donor/acceptor state at the ends of the hopping chain. Instead, many possible electronic states are involved, so that the transition rates are determined by charge transfer integrals (Fig. 1c):

$$J_{0,1} \text{ or } J_{N+1,N} = \int_{-\infty}^{\infty} f(\epsilon) g(\epsilon) K(\epsilon - U_{1,N}) d\epsilon, \tag{S5}$$

$$J_{1,0} \text{ or } J_{N,N+1} = \int_{-\infty}^{\infty} (1 - f(\epsilon)) g(\epsilon) K(U_{1,N} - \epsilon) d\epsilon. \tag{S6}$$

The quantity $g(\epsilon)$ is the density of electronic states in the electrode, while $K(\epsilon - U_{1,N})$ represents the transfer rate between a single electron state in the electrode and the injection/ejection site in the hopping chain (Fig. 2b). For an electrode in thermal equilibrium, the occupancy follows the Fermi Dirac distribution:

$$f(\epsilon) = \frac{1}{\exp\left(\frac{\epsilon-\mu}{k_B T}\right) + 1}, \tag{S7}$$

where μ is the chemical potential of the electrode. For the boundary at the left electrode, the occupancy balance is:

$$\frac{dp_1}{dt} = 0 = \Gamma_{2,1} p_2 (1 - p_1) - \Gamma_{1,2} p_1 (1 - p_2) + (1 - p_1) J_{0,1} - p_1 J_{1,0}. \tag{S8}$$

The first two terms represent contributions from neighbouring hopping sites, while the last two terms include contributions from the electrodes. An analogous equation can be derived for the electrode at the right boundary.

In general, the metal-chain transfer integrals must be calculated numerically. However, the analysis becomes simpler when the metal-chain transfer rates are much larger than the internal hopping rate ($J \gg \Gamma$). We can evaluate this by assuming that the metal-chain hopping rate, K, is of the same form as the internal hopping rate, Γ (the Marcus rate, Eq. 12). Then J is likely to be relatively high, because in the electrode, the density of states is very high. If the metal electrode acts like a 3D free electron gas, the density of states becomes:

$$g(\epsilon) = \frac{V}{2\pi^2} \frac{2m}{\hbar^2}^{3/2} \sqrt{U_F}. \tag{S9}$$

Here, V is the volume of the free electron gas, m is the mass of an electron, $\hbar$ is the reduced Planck's constant and U_F is the Fermi energy. Taking a gold electrode as an example with a Fermi energy, $U_F = 5.5$ eV [108], and assuming that the electrode has a volume of $V = 0.1\ \mu\mathrm{m}^3$, the density of states near the Fermi Energy can be estimated as $g(U_F) \approx 10^7\ \mathrm{meV}^{-1}$. This gives a large number of contributing states to the effective transfer rate from metal to hopping chain, ensuring that $J \gg \Gamma_{\mathrm{R,L}}$ (Fig. S3). When the metal-chain transfer integrals dominate the edge occupancy balance (Eq. S8), the occupancy of the first site can be written as:

$$p_1 = \frac{J_{0,1}}{J_{1,0} + J_{0,1}}. \tag{S10}$$

The injection rate, for $i = 1$, becomes:

$$J_{0,1} = \int_{-\infty}^{\infty} f(\epsilon)g(\epsilon)K(\epsilon - U_1)d\epsilon, \tag{S11}$$

whereas the ejection rate, for $i = 1$, is:

$$J_{1,0} = \int_{-\infty}^{\infty} (1 - f(\epsilon))g(\epsilon)K(U_1 - \epsilon)d\epsilon. \tag{S12}$$

Using the detailed balance relation (Eq. 2), this ejection integral can be written in terms of the injection rate:

$$J_{1,0} = \int_{-\infty}^{\infty} (1 - f(\epsilon))g(\epsilon)K(\epsilon - U_1)\exp\left(\frac{U_1 - \epsilon}{k_{\mathrm{B}}T}\right)d\epsilon. \tag{S13}$$

Recall that the Fermi-Dirac distribution for the left electrode is:

$$f(\epsilon) = \frac{1}{\exp\left(\frac{\epsilon - \mu_L}{k_{\mathrm{B}}T}\right) + 1}, \tag{S14}$$

where $\mu_{\mathrm{L}} = eV$ is the chemical potential of the left electrode. A useful property of the Fermi-Dirac distribution is:

$$1 - f(\epsilon) = \frac{\exp\left(\frac{\epsilon - \mu_L}{k_{\mathrm{B}}T}\right)}{\exp\left(\frac{\epsilon - \mu_L}{k_{\mathrm{B}}T}\right) + 1} = \exp\left(\frac{\epsilon - \mu_L}{k_{\mathrm{B}}T}\right)f(\epsilon), \tag{S15}$$

As a result, the ejection rate can be reformulated as:

$$J_{1,0} = \int_{-\infty}^{\infty} f(\epsilon)g(\epsilon)K(\epsilon - U_1)\exp\left(\frac{U_1 - \mu_{\mathrm{L}}}{k_{\mathrm{B}}T}\right)d\epsilon. \tag{S16}$$

The energy of the first site, U_1, can be written as $U_1 = \mu_{\mathrm{L}} + U_0 - \alpha_{\mathrm{L}}eV$ and the exponential factor can be taken out of the integral. This provides following relation between the injection and ejection rates:

$$J_{1,0} = \exp\left(\frac{U_0 - \alpha_{\mathrm{L}}eV}{k_{\mathrm{B}}T}\right)J_{0,1} \tag{S17}$$

If we substitute this relation into Eq. S10, we obtain:

$$p_1 = \frac{1}{1 + \exp\left(\frac{U_0 - \alpha_{\mathrm{L}}eV}{k_{\mathrm{B}}T}\right)}. \tag{S18}$$

With the same considerations, it can be shown that:

$$p_N = \frac{1}{1 + \exp\left(\frac{U_0 + \alpha_{\mathrm{R}}eV}{k_{\mathrm{B}}T}\right)}. \tag{S19}$$

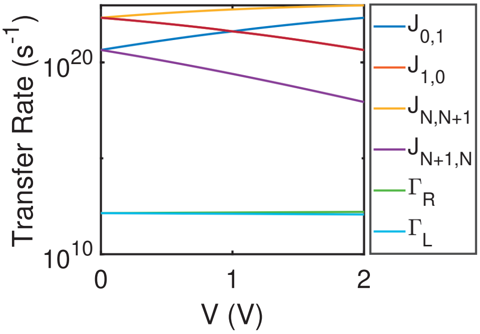

Figure S3: **Estimation of metal-chain hopping integrals.** In the figure are indicated: the injection metal-chain hopping integral at the first last, $J_{0,1}$, the ejection integral at the same site, $J_{1,0}$, both integrals at the last site ($J_{N+1,N}$, $J_{N,N+1}$), and the right-moving and left-moving hopping rates ($\Gamma_\mathrm{R}, \Gamma_\mathrm{L}$). Parameters in the hopping chain, are chosen in accordance with the off-resonant case in the main text: $N = 200$, $U_0 = 0.1$ eV, $\alpha_{L,R} = 0.1$, $T = 300$ K. It was assumed that the internal hopping rates and the same as the metal-chain hopping rates, K (Eq. S17). The Marcus hopping rate (Eq. 12) with $\lambda = 0.2$ eV and $H = 16$ meV was used, both for calculating J and Γ. For the electrode, the density of states was estimated from the 3D Electron Gas model (Eq. S9), with $E_F = 5.5$ eV. At $V = U_0/\alpha_\mathrm{L}$ there is a transition between off-resonant and resonant transport, which can be seen as the crossing of $J_{0,1}$ and $J_{1,0}$ at $V = 1$ V.

3.5.3. ELECTRICAL CURRENT

The net electrical current between the consecutive sites i and $i+1$ is given by the difference between the forward and backward electron flows between these sites:

$$I = e\Gamma_\mathrm{R} p_i (1 - p_{i+1}) - e\Gamma_\mathrm{L} p_{i+1}(1 - p_i). \tag{S20}$$

If we use the Taylor approximation

$$p_{i+1} = p(x_i + a) = p(x_i) + a\left[\frac{dp}{dx}\right]_{x_i}, \tag{S21}$$

and we substitute this in the net current expression, Eq. S20, we obtain:

$$I = e(\Gamma_\mathrm{R} - \Gamma_\mathrm{L}) p(x)\left(1 - p(x)\right) - e\left(\Gamma_\mathrm{R} p(x) + \Gamma_\mathrm{L}\left(1 - p(x)\right)\right) a \left[\frac{dp}{dx}\right] \tag{S22}$$

The detailed balance relation for a regular 1D hopping chain with N equidistant sites becomes

$$\frac{\Gamma_R}{\Gamma_L} = \exp\left(\frac{\Delta}{k_\mathrm{B} T}\right), \tag{S23}$$

In this, $\Delta = eV(1-\alpha)/N$ is the energy difference between two adjacent sites. The two terms in Eq. S22 can be identified as the field-driven current (drift current) I_{FD} and the concentration-driven current (diffusion current) I_{CD}. The normalized versions of these currents hence become:

$$\frac{I_{FD}}{e\Gamma_\mathrm{R}} = \left(1 - \exp\left(\frac{-\Delta}{k_\mathrm{B} T}\right)\right) p(x)\left(1 - p(x)\right) \tag{S24}$$

$$\frac{I_{CD}}{e\Gamma_{\mathrm{R}}} = -a\left(p(x) + \exp\left(\frac{-\Delta}{k_{\mathrm{B}}T}\right)(1-p(x))\right)\left[\frac{dp}{dx}\right] \tag{S25}$$

The total current is given by the sum of the field-driven and concentration-driven currents, $I = I_{FD} + I_{CD}$, thus providing:

$$\begin{aligned}\frac{I}{e\Gamma_{\mathrm{R}}} = \left(1-\exp\left(\frac{-\Delta}{k_{\mathrm{B}}T}\right)\right)p(x)\,(1-p(x)) - \\ a\left(p(x) + \exp\left(\frac{-\Delta}{k_{\mathrm{B}}T}\right)(1-p(x))\right)\left[\frac{dp}{dx}\right]\end{aligned} \tag{S26}$$

This provides Eq. 10 in the main text. In the next sections, we derive a set of analytical expressions for the occupancy profile and normalized current under various conditions.

3.5.4. HOPPING CHAIN WITHOUT INJECTION BARRIER ($U_0 = 0$)

In this section, we restrict ourselves here to the situation without an injection barrier ($U_0 = 0$) and a similar voltage drop at the terminal ends ($\alpha_{\mathrm{L}} = \alpha_{\mathrm{R}} = \alpha/2$). The resulting expressions are summarized in table S1.

GENERAL TREATMENT ($0 \leq \alpha \leq 1$)

For general α, and using the edge occupancy relation (Eq. 11), the occupancy at the terminal ends can be written as:

$$p_{\mathrm{L}} = p(x=0) = \frac{1}{2} + \frac{1}{2}\tanh\left(\frac{\alpha eV}{4k_{\mathrm{B}}T}\right), \tag{S27}$$

$$p_{\mathrm{R}} = p(x=L) = \frac{1}{2} - \frac{1}{2}\tanh\left(\frac{\alpha eV}{4k_{\mathrm{B}}T}\right) \tag{S28}$$

Consequently, we find that the relation $p_{\mathrm{L}} + p_{\mathrm{R}} = 1$ always holds [11]. In addition, the occupancy profile will show symmetry, and it always adopts the value $p(x = L/2) = 1/2$ in the middle of the hopping chain. Under these conditions, the differential equation for the occupancy profile (Eq. 9) has a solution of the form:

$$p(x) = \frac{1}{2} - A\tan(\kappa A(x - L/2)). \tag{S29}$$

The parameter κ is defined as:

$$\kappa = \frac{2}{a}\tanh\left(\frac{\Delta}{2k_{\mathrm{B}}T}\right) = \frac{2}{a}\tanh\left(\frac{eV(1-\alpha)}{2Nk_{\mathrm{B}}T}\right). \tag{S30}$$

Application of the occupancy profile Eq. S29 to the left boundary, gives the self-consistency relation that determines the parameter A:

$$\arctan\left(\frac{p_{\mathrm{L}} - 1/2}{A}\right) = \frac{\kappa AL}{2}. \tag{S31}$$

By numerically solving this non-linear equation, the parameter A can be determined for each κ value (i.e, for different values of the voltage bias V). The occupancy profile provided by Eqs. S29-S31 is in excellent agreement with that obtained by direct numerical simulation (Fig. S4).

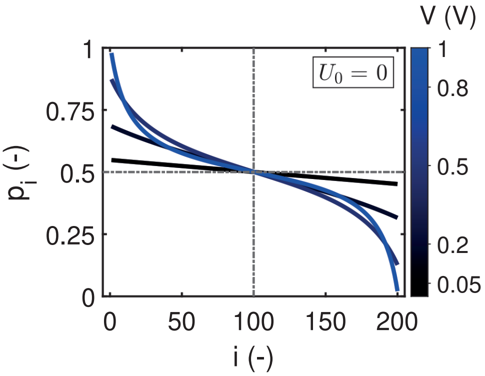

Figure S4: **Simulated occupancy profiles for a hopping chain without injection barrier.** Occupation probability p_i vs. site position i as a function of the bias voltage, V. The plotted voltages are indicated next to the colour bar. The fixed model parameters are: $N = 200$, $\alpha = 0.2$ and $T = 300$ K.

The derivative of the occupancy profile is given by:

$$\frac{dp}{dx} = -\kappa A^2 \frac{1}{\cos^2(\kappa A(x - L/2))}. \tag{S32}$$

If we implement this in Eq. S26, and evaluate this at the mid-site, we obtain:

$$\frac{I}{e\Gamma_\mathrm{R}} = \frac{1}{4}\left(1 - \exp\left(\frac{-\Delta}{k_\mathrm{B}T}\right)\right) + \frac{\alpha\kappa A^2}{2}\left(1 + \exp\left(\frac{-\Delta}{k_\mathrm{B}T}\right)\right) \tag{S33}$$

This provides the general expression for the normalized current when there is no injection barrier. The first term is the field-driven part of the current, and the second term is the concentration-driven part, which eventually goes to zero (see Fig. S5).

When the voltage bias on the electrodes is small, so that the voltage drop inside the hopping chain is small compared to the thermal energy ($eV(1-\alpha) \ll 4k_\mathrm{B}T$), the arctangent function in the self-consistency relation can be linearized and the parameter A can be solved for analytically:

$$A^2 = \frac{2(p_\mathrm{L} - 1/2)}{\kappa L}. \tag{S34}$$

As as result, the normalized current in Eq. S33 simplifies to:

$$\frac{I}{e\Gamma_\mathrm{R}} = \frac{1}{4}\left(1 - \exp\left(\frac{-\Delta}{k_\mathrm{B}T}\right)\right) + \frac{1}{2N}\tanh\left(\frac{\alpha eV}{4k_\mathrm{B}T}\right)\left(1 + \exp\left(\frac{-\Delta}{k_\mathrm{B}T}\right)\right) \tag{S35}$$

CONCENTRATION-DRIVEN LIMIT ($\alpha = 1$)

When the current is exclusively concentration-driven, the entire voltage drop occurs at the interface of the electrodes ($\alpha = 1$), and there is no electrical field present in the hopping chain ($\Delta = 0$). The occupancies at the terminal ends are given by:

$$p_\mathrm{L} = p(x = 0) = \frac{1}{2} + \frac{1}{2}\tanh\left(\frac{eV}{4k_\mathrm{B}T}\right), \tag{S36}$$

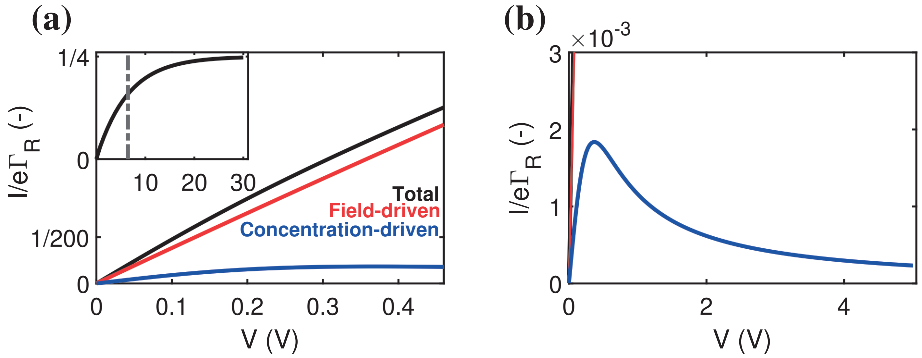

Figure S5: **Field-driven and concentration-driven currents in a hopping chain without barrier** (a) The normalized current $I/e\Gamma_{\mathrm{R}}$ is plotted against bias voltage V, showing the total current (black) as well as the field-driven (red) and concentration-driven (blue) components. The inset shows the higher-voltage regime, with a vertical line plotted at $eV(1-\alpha) = Nk_{\mathrm{B}}T$.(b) Normalized current against bias voltage V, zooming in on the concentration-driven current, which is suppressed at higher voltages. This figure is an extension of panel (a) to a larger voltage range $(0-5\ \mathrm{V})$. The model parameters used are: $\alpha_{L,R} = 0.1$, $U_0 = 0$, $N = 200$, $T = 300$ K.

$$p_{\mathrm{R}} = p(x=L) = \frac{1}{2} - \frac{1}{2}\tanh\left(\frac{eV}{4k_{\mathrm{B}}T}\right) \tag{S37}$$

The differential equation for the site occupancy, Eq. 9 from the main text, simplifies to:

$$\frac{d^2p}{dx^2} = 0. \tag{S38}$$

Accounting for the boundary conditions at the terminal ends, this linear differential equation has the solution:

$$p(x) = p_{\mathrm{L}} - (p_{\mathrm{L}} - p_{\mathrm{R}})\frac{x}{L}, \tag{S39}$$

The expression for the normalized current, Eq. S26, now becomes:

$$\frac{I}{e\Gamma_{\mathrm{R}}} = -a\left[\frac{dp}{dx}\right] = \frac{a}{L}(p_{\mathrm{L}} - p_{\mathrm{R}}) = \frac{1}{N}\tanh\left(\frac{eV}{4k_{\mathrm{B}}T}\right) \tag{S40}$$

This expression matches Eq. S52 when $\Delta = 0$ and $\alpha = 1$.

FIELD-DRIVEN LIMIT ($\alpha = 0$)

When the current is exclusively field-driven, there is no voltage drop occurs at the interface of the electrodes ($\alpha = 0$), and there is a constant electrical potential gradient within in the hopping chain ($\Delta = eV/N$).The occupancies at the terminal ends are given by:

$$p_{\mathrm{L}} = p(x=0) = \frac{1}{2} \tag{S41}$$

$$p_{\mathrm{R}} = p(x=L) = \frac{1}{2} \tag{S42}$$

The differential equation for the site occupancy, Eq. 9 from the main text, simplifies to:

$$\frac{dp}{dx} = 0. \tag{S43}$$

The site occupancy therefore has be the same throughout the hopping chain:

$$p(x) = \frac{1}{2} \tag{S44}$$

The expression for the normalized current, Eq. 10 from the main text, now becomes:

$$\frac{I}{e\Gamma_\mathrm{R}} = \frac{1}{4}\left(1 - \exp\left(\frac{-eV}{Nk_\mathrm{B}T}\right)\right) \approx \frac{1}{4}\frac{eV}{Nk_\mathrm{B}T} \tag{S45}$$

This expression matches Eq. S61 when $\alpha = 0$. The linear approximation holds for sufficiently small bias voltages $V < Nk_\mathrm{B}T/e$. Under these conditions, the resulting I/V curve tends to be linear.

Case	**Site Occupancy, $p(x)$**	**Electrical Current, I**
Concentration – driven $\alpha = 1$	$p_L - (p_L - p_R)\frac{x}{L}$	$\frac{e\Gamma_\mathrm{R}}{N}\tanh\left(\frac{eV}{4k_\mathrm{B}T}\right)$
Field –driven $\alpha = 0$	$\frac{1}{2}$	$\frac{e\Gamma_\mathrm{R}}{4}\left[1 - \exp\left(\frac{-eV}{Nk_\mathrm{B}T}\right)\right]$
General $0 < \alpha < 1$	$-A\tan\left(\kappa A\left(x - \frac{L}{2}\right)\right) + \frac{1}{2}$	$\frac{e\Gamma_\mathrm{R}}{4}\left[1 - \exp\left(\frac{-\Delta}{k_\mathrm{B}T}\right)\right]$ $+e\Gamma_\mathrm{R}\frac{\kappa a A^2}{2}\left[1 + \exp\left(-\frac{\Delta}{k_\mathrm{B}T}\right)\right]$

Table S1: **Summary of relevant expressions for the site occupancy profile,** $p(x)$ **and the electrical current,** I**, without injection barrier.** $P_{L,R}$ denotes the site occupancy at the terminal ends (Left, Right) . The position variable, x, runs from $x = 0$ to $x = L$. e is the electron charge, N is the number of hopping sites, Γ_R is the forward hopping rate, V is the applied bias voltage. x_0 is the solution of Eq. S50 and A is the solution of Eq. S49. $\kappa = \frac{2}{a}\tanh(\frac{eV(1-\alpha)}{2Nk_\mathrm{B}T})$, where a is the center-to-center distance between hopping sites.

3.5.5. HOPPING CHAIN WITH INJECTION BARRIER ($U_0 > 0$)

In this section, we account for the situation with an injection barrier ($U_0 > 0$). The voltage drop at the terminal ends is again considered to be the same ($\alpha_\mathrm{L} = \alpha_\mathrm{R} = \alpha/2$). The resulting expressions are summarized in table S2.

In the case with an injection barrier, U_0, the site occupancies at the terminal ends are given by:

$$p_\mathrm{L} = \frac{1}{1 + \exp\left(\frac{U_0 - \alpha_\mathrm{L} eV}{k_\mathrm{B}T}\right)}. \tag{S46}$$

$$p_\mathrm{R} = \frac{1}{1 + \exp\left(\frac{U_0 + \alpha_\mathrm{R} eV}{k_\mathrm{B}T}\right)}. \tag{S47}$$

As a results, the constraints $p_\mathrm{L} + p_\mathrm{R} = 1$ and $p(x = l/2) = 1/2$ are no longer applicable. There is no general analytical solution to the differential equation (Eq. 9), but we can still derive approximate solutions for two separate regimes.

CURRENT IN THE RESONANT REGIME ($\alpha_L eV > U_0$)

When the bias voltage is sufficiently raised above the energy barrier $V > 2U_0/(\alpha e)$, the system will no longer be influenced by the barrier. As a result, the occupancy profile and normalized current should tend towards those from the no-barrier regime. This regime is called the "resonant regime".

When the condition $V > U_0/(\alpha_L e)$ is satisfied, we know that $p_L > 1/2$ and $p_R < 1/2$ for $U_0 > 0$. Therefore, we know that the occupancy profile must cross the 1/2 line, and so we can evaluate the following solution to the differential equation (Eq. 9):

$$p(x) = 1/2 - A\tan(\kappa A(x - x_0)). \tag{S48}$$

This expression forms a generalisation of Eq. S29. Here, x_0 is the location of the hopping site where the occupancy attains the value $p = 1/2$. Substituting this solution back into the differential equation Eq. 9, provides the self-consistency relations:

$$\kappa AL = \arctan\left(\frac{p_L - 1/2}{A}\right) - \arctan\left(\frac{p_R - 1/2}{A}\right), \tag{S49}$$

$$\kappa A x_0 = \arctan\left(\frac{p_L - 1/2}{A}\right). \tag{S50}$$

From these expressions, the quantities A and x_0 can be calculated. Equations S48, S49 and S50 describe the shape of the occupancy profile well (Fig. S6). For large enough V, we attain $x_0 \sim L/2$, and as a result, the expressions from the previous section are recovered.

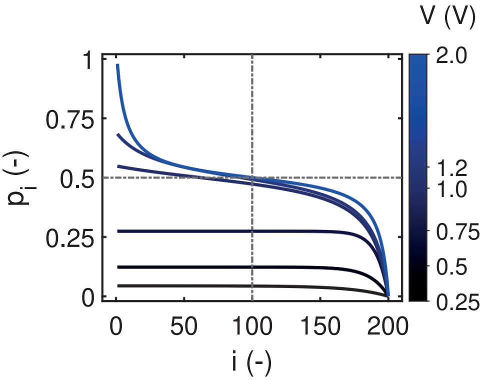

Figure S6: **Simulated occupancy profiles in a hopping chain with an injection barrier.** Occupation probability p_i vs. site position i. The dots represent direct numerical simulation results and the lines analytical expressions. Model parameters: $N = 200$, $\alpha_L = \alpha_R = 0.1$, $U_0 = 0.1$ eV, $T = 300$ K. The dashed lines indicate the crossing at $p_{N/2} = 1/2$. The six voltages next to the colour bar correspond to the six lines drawn. They show the transition from the off-resonant ($V < 1$ V) to the resonant regime ($V > 1$ V). The lines represent predictions from Eq. S54 for $V < 1$ V, Eq. S48 for $1\text{ V} < V < 2\text{V}$, Eq. S29 for $V = 2$ V.

The derivative of the occupancy profile is given by:

$$\frac{dp}{dx} = -\kappa A^2 \frac{1}{\cos^2(\kappa A(x - x_0))}. \tag{S51}$$

If we implement this in Eq. S26, and evaluate this at $x = x_0$, we obtain:

$$\frac{I}{e\Gamma_R} = \frac{1}{4}\left(1-\exp\left(\frac{-\Delta}{k_B T}\right)\right) + \frac{\alpha\kappa A^2}{2}\left(1+\exp\left(\frac{-\Delta}{k_B T}\right)\right) \tag{S52}$$

This expression for the normalized current is identical to that when there is no injection barrier, Eq. S33. Note however that the value of A will differ between the two cases.

CURRENT IN THE OFF-RESONANT REGIME ($\alpha_L eV < U_0$)

When the bias voltage remains sufficiently low $V < U_0/(\alpha_L e)$, the energy barrier will have an influence on the occupancy profile and the I/V curve. In this so-called off-resonant regime, the site occupancies are low and the approximation $1 - p \approx 1$ can be made. As a result, the differential equation for the occupancy profile, Eq. 9, becomes:

$$\frac{d^2 p}{dx^2} - \frac{2}{a}\tanh\left(\frac{\Delta}{2k_B T}\right)\frac{dp}{dx} = 0. \tag{S53}$$

This gives an exponential occupancy profile (Fig. S6; $V < 1$ V):

$$p(x) = p_L \frac{e^{\kappa L} - e^{\kappa x}}{e^{\kappa L} - 1} + p_R \frac{e^{\kappa x} - 1}{e^{\kappa L} - 1}, \tag{S54}$$

The derivative of occupancy profile is:

$$\frac{dp}{dx} = -\kappa(p_L - p_R)\frac{e^{\kappa x}}{e^{\kappa L} - 1} \tag{S55}$$

Upon substitution into Eq. S26, and evaluation at $x = 0$, we arrive at the field-driven current,

$$\frac{I_{FD}}{e\Gamma_R} = \left(1-\exp\left(\frac{-\Delta}{k_B T}\right)\right) p_L (1 - p_L) \tag{S56}$$

and the concentration-driven current current,

$$\frac{I_{CD}}{e\Gamma_R} = 2\tanh\left(\frac{\Delta}{2k_B T}\right)\frac{p_L - p_R}{e^{\kappa L} - 1}\left(p_L + \exp\left(\frac{-\Delta}{k_B T}\right)(1 - p_L)\right) \tag{S57}$$

The total current becomes:

$$\frac{I}{e\Gamma_R} = \left(1-\exp\left(\frac{-\Delta}{k_B T}\right)\right) p_L (1 - p_L) + 2\tanh\left(\frac{\Delta}{2k_B T}\right)\frac{p_L - p_R}{e^{\kappa L} - 1}\left(p_L + \exp\left(\frac{-\Delta}{k_B T}\right)(1 - p_L)\right) \tag{S58}$$

The concentration-driven term, I_{CD}, vanishes when the voltage drop inside the hopping chain becomes higher than the thermal energy ($eV(1-\alpha) > k_B T$; see Fig. S7). When plotting the current, the transition between off-resonant and the resonant regime can be clearly seen (Fig. 4b).

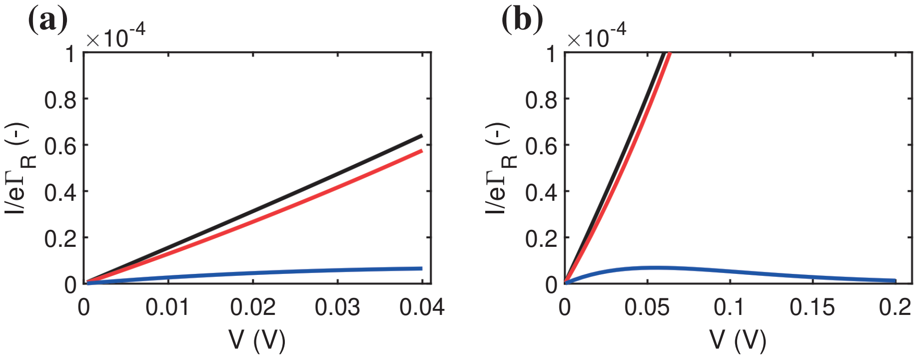

Figure S7: **Field-driven and concentration-driven currents in a hopping chain with an injection barrier.** (a) Normalized current, $I/e\Gamma_{\mathrm{R}}$, is plotted against the bias voltage V. The total current (black) is decomposed into the field-driven current (red) and the concentration-driven current (blue). The model parameters are: $N = 500$, $\alpha_{L,R} = 0.1$, $U_0 = 0.1$ eV, $T = 300$ K. In panel (a), the bias voltage range is $0-0.04$ V, while in panel (b), the bias voltage range is $0-0.2$ V.

OFF-RESONANT REGIME: CONCENTRATION-DRIVEN LIMIT

In the concentration-driven limit, $\alpha_L = \alpha_R = 0.5$ and $\alpha = 1$, and so the edge occupancies become

$$p_{\mathrm{L}} = \frac{1}{1+\exp\left(\frac{U_0 - eV/2}{k_{\mathrm{B}}T}\right)} \qquad p_{\mathrm{R}} = \frac{1}{1+\exp\left(\frac{U_0 + eV/2}{k_{\mathrm{B}}T}\right)} \tag{S59}$$

The occupancy profile is linear:

$$p(x) = p_{\mathrm{L}} - (p_{\mathrm{L}} - p_{\mathrm{R}})\frac{x}{L}, \tag{S60}$$

and the associated current becomes:

$$\frac{I}{e\Gamma_{\mathrm{R}}} = \frac{1}{N}(p_{\mathrm{L}} - p_{\mathrm{R}}) = \frac{1}{N}\left(\frac{1}{1+\exp\left(\frac{U_0 - eV/2}{k_{\mathrm{B}}T}\right)} - \frac{1}{1+\exp\left(\frac{U_0 + eV/2}{k_{\mathrm{B}}T}\right)}\right). \tag{S61}$$

As required, this equation reduces to Eq. S40 for $U_0 \to 0$. The simulation results are shown in Fig. S8c. The $I(V)$ starts out non-linear due to the injection barrier, U_0, but quickly saturates upon increasing the bias voltage, which compensates the injection barrier.

OFF-RESONANT REGIME: FIELD-DRIVEN LIMIT

In the field-driven limit, $\alpha = 0$, and the edge occupancies become

$$p_{\mathrm{R}} = p_{\mathrm{L}} = \frac{1}{1+\exp\left(\frac{U_0}{k_{\mathrm{B}}T}\right)} \tag{S62}$$

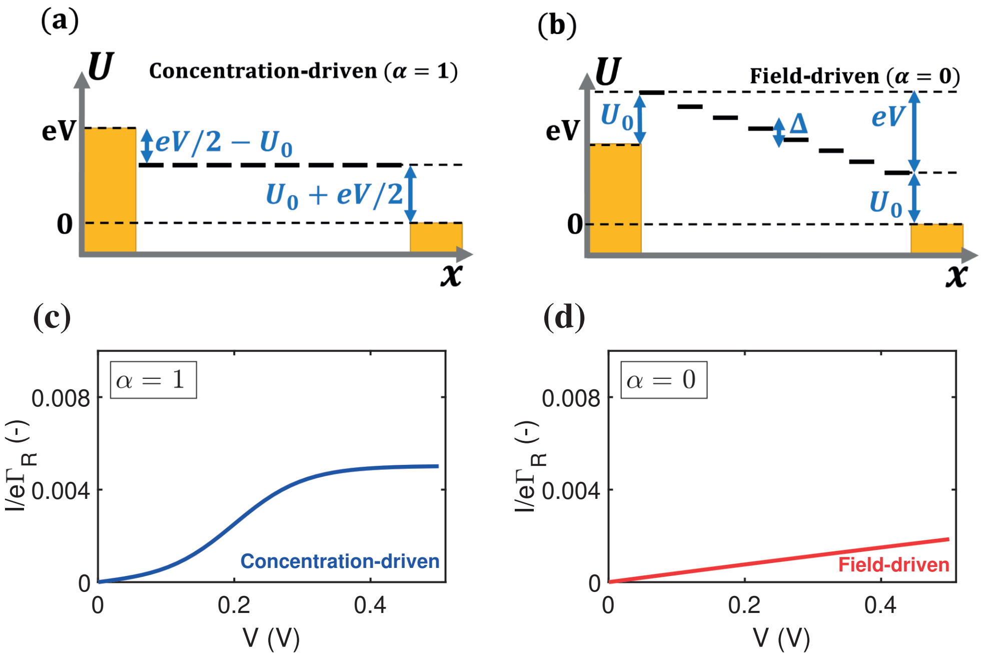

Figure S8: **Field-driven and concentration-driven currents in a hopping chain with an injection barrier.** (a) Energy vs. position diagram of the field-driven limit ($\alpha = 0$). (b) Energy vs. position diagram of the concentration-driven limit ($\alpha = 1$) with a symmetric barrier ($\alpha_L = \alpha_R = 1/2$). (c) Normalized current, $I/e\Gamma_R$ as a function of the applied voltage bias V in the concentration-driven limit ($\alpha = 1$). The model parameters are: $N = 200$, $U_0 = 0.1$ eV, $T = 300$ K.

The occupancy profile is hence constant:

$$p(x) = p_R = p_L, \tag{S63}$$

and the associated current becomes:

$$\frac{I}{e\Gamma_R} = \left(1 - \exp\left(\frac{-\Delta}{k_B T}\right)\right) p_L (1 - p_L) = \frac{1}{2}\left[1 - \exp\left(\frac{-eV}{N k_B T}\right)\right]\left[\frac{1}{1 + \cosh(U_0/k_B T)}\right]. \tag{S64}$$

As required, this equation reduces to Eq. S45 for $U_0 \to 0$. The simulation results are shown in Fig. S8d.

Case	**Site Occupancy, $p(x)$**	**Electrical Current, I**
Concentration – driven $\alpha = 1$	$p_L - (p_L - p_R)\frac{x}{L}$	$\frac{e\Gamma_R}{N}\left[\frac{1}{1+\exp\left(U_0-\frac{eV}{2}\right)} - \frac{1}{1+\exp\left(U_0+\frac{eV}{2}\right)}\right]$
Field –driven $\alpha = 0$	$\frac{1}{1+\exp\left(\frac{U_0}{k_BT}\right)}$	$\frac{e\Gamma_R}{2}\left[1-\exp\left(\frac{-\Delta}{k_BT}\right)\right]\left[\frac{1}{1+\cosh\left(\frac{U_0}{k_BT}\right)}\right]$
Resonant $\mathbf{U_0 - \alpha_L eV < 0}$	$-A\tan(\kappa A(x-x_0))+\frac{1}{2}$	$e\Gamma_R\left[1-\exp\left(\frac{-\Delta}{k_BT}\right)\right]p_{x_0}(1-p_{x_0})$ $+\kappa a A^2 e\Gamma_R\left[\exp\left(\frac{-\Delta}{k_BT}\right)(1-p_{x_0})+p_{x_0}\right]$
Off – Resonant $1-p \approx 1$ $\mathbf{U_0 - \alpha_L eV > 0}$	$p_L\frac{e^{\kappa L}-e^{\kappa x}}{e^{\kappa L}-1}+p_R\frac{e^{\kappa x}-1}{e^{\kappa L}-1}$	$e(\Gamma_R-\Gamma_L)p_1(1-p_1)$ $+\frac{(p_1-p_N)\kappa a}{e^{\kappa L}-1}[\Gamma_L(1-p_1)+\Gamma_R p_1]$

Table S2: **Summary of relevant expressions for the site occupancy profile,** $p(x)$ **and the electrical current,** I**, with injection barrier.** $P_{L,R}$ denotes the site occupancy at the terminal ends (Left, Right) . The position variable, x, runs from $x = 0$ to $x = L$. e is the electron charge, N is the number of hopping sites, Γ_R is the forward hopping rate, V is the applied bias voltage. x_0 is the solution of Eq. S50 and A is the solution of Eq. S49. $\kappa = \frac{2}{a}\tanh(\frac{eV(1-\alpha)}{2Nk_\mathrm{B}T})$, where a is the center-to-center distance between hopping sites

3.5.6. NON-ADIABATIC CONSTRAINT

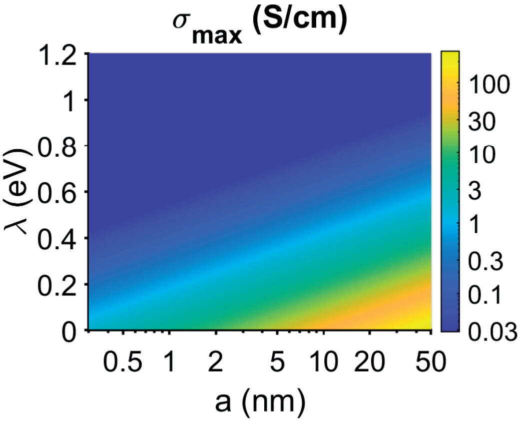

Figure S9: Maximum possible conductivity based on the non-adiabatic constraint (calculated for $k = 0.5$), as a function of the reorganisation energy, λ, and the center-to-center hopping distance, a, at $T = 300$ K

In the main text, the "weak coupling condition" $H/\lambda < 0.1$ is used to calculate the allowed maximum conductivity. A small value for the H/λ ratio ensures that no delocalization occurs between nearest neighbour sites, and so the Marcus hopping theory can be utilized [70]. Here we examine the same problem (What conductivity is allowed by Marcus theory?) with an alternative approach.

Our starting point is that the Marcus rate is a non-adiabatic rate. Whether a rate is non-adiabatic or not depends on the magnitude of the electron transition rate as compared to the frequency of molecular vibrational modes that facilitate the hopping. When the (average) frequency of vibrational modes, $\langle\hbar\omega\rangle$, is much higher than the hopping rate, Γ, Marcus theory is valid. When this condition no longer holds, the electron transfer process turns adiabatic and the Marcus expression for the transition rate can no longer be used. More specifically, the transition process is non-adiabatic when the transition probability is low [109]:

$$P_0 = 1 - \exp(2\pi\gamma) \ll 1, \tag{S65}$$

In this, the adiabatic parameter, γ, depends on the electronic coupling, H, the (average) frequency of vibrations, $\hbar\langle\omega\rangle$, the reorganisation energy, λ, and the temperature, T:

$$\gamma = \frac{H^2}{2\hbar\langle\omega\rangle}\sqrt{\frac{\pi}{\lambda k_B T}}. \tag{S66}$$

The calculations are made for room temperature ($T = 300$ K) and a typical frequency of vibrations [91] $\hbar\langle\omega\rangle = 7$ meV . Following Zhu *et al.* [109], for the electron transfer to be adiabatic, the adiabatic parameter γ must be chosen in such a way, that the electronic transmission coefficient, κ, stays below one-half [109]:

$$\kappa = \frac{2P_0}{1+P_0} \leq 0.5. \tag{S67}$$

For this regime, it has been shown that the hopping behaviour is nearly identical to that predicted by Marcus theory. The maximum possible γ that satisfies Eq.S67 gives the maximum possible electronic coupling H^2. From this, we can then calculate the maximum allowed conductivity, σ, that satisfies the "non-adiabatic condition"

$$\sigma = \frac{e^2\Gamma_R^0}{4k_B T}\frac{a}{\pi(d_C/2)^2}. \tag{S68}$$

A map of this maximal non-adiabatic conductivity as a function of the reorganisation energy, λ, and the center-to-center distance, a, is given in Fig. S9. For the parameters implemented ($\hbar\langle\omega\rangle = 7$ meV; $T = 300$ K), the plot shows that the ~ 100 S/cm conductivity level is only compatible with non-adiabatic hopping for very low reorganisation energy ($\lambda < 0.1$ eV) and high center-to-center hopping distance ($a > 20$ nm). Compared to the "weak coupling condition", the "non-adiabatic" constraint requires a lower reorganisation energy, λ, and higher center-to-center hopping distance, a, to reach the 100 S/cm conductivity level.

3.5.7. EFFECT OF COUPLING CONSTRAINTS ON THE MAXIMUM CONDUCTIVITY

In the main text, the "weak coupling" condition was implemented by using a ratio " $H/\lambda = 0.1$. This cut-off value for the H/λ ratio is to some extent arbitrary. In Fig. S10, lower (and hence more conservative) ratios for H/λ are explored (varying from 0.1 to 0.01). Separate plots are made the maximum conductivity and the maximum mobility. The conductivity is calculated from Eq. 19. The mobility is given by $\mu = e\Gamma_{\mathrm{R}}^{0} a^{2}/(k_{\mathrm{B}}T)$. In these, the hopping rate, Γ_{R}^{0}, is determined from the Marcus expression (Eq. 13), which only depends on H, λ and physical parameters (T = 300 K). For H/λ ratios under 0.1, lower reorganization energies λ and higher center-to-center distances a are required to reach the 100 S/cm conductivity level as observed for the fibers in cable bacteria . For H/λ ratios below 0.05, this conductivity level even seems unreachable for $a < 50$ nm.

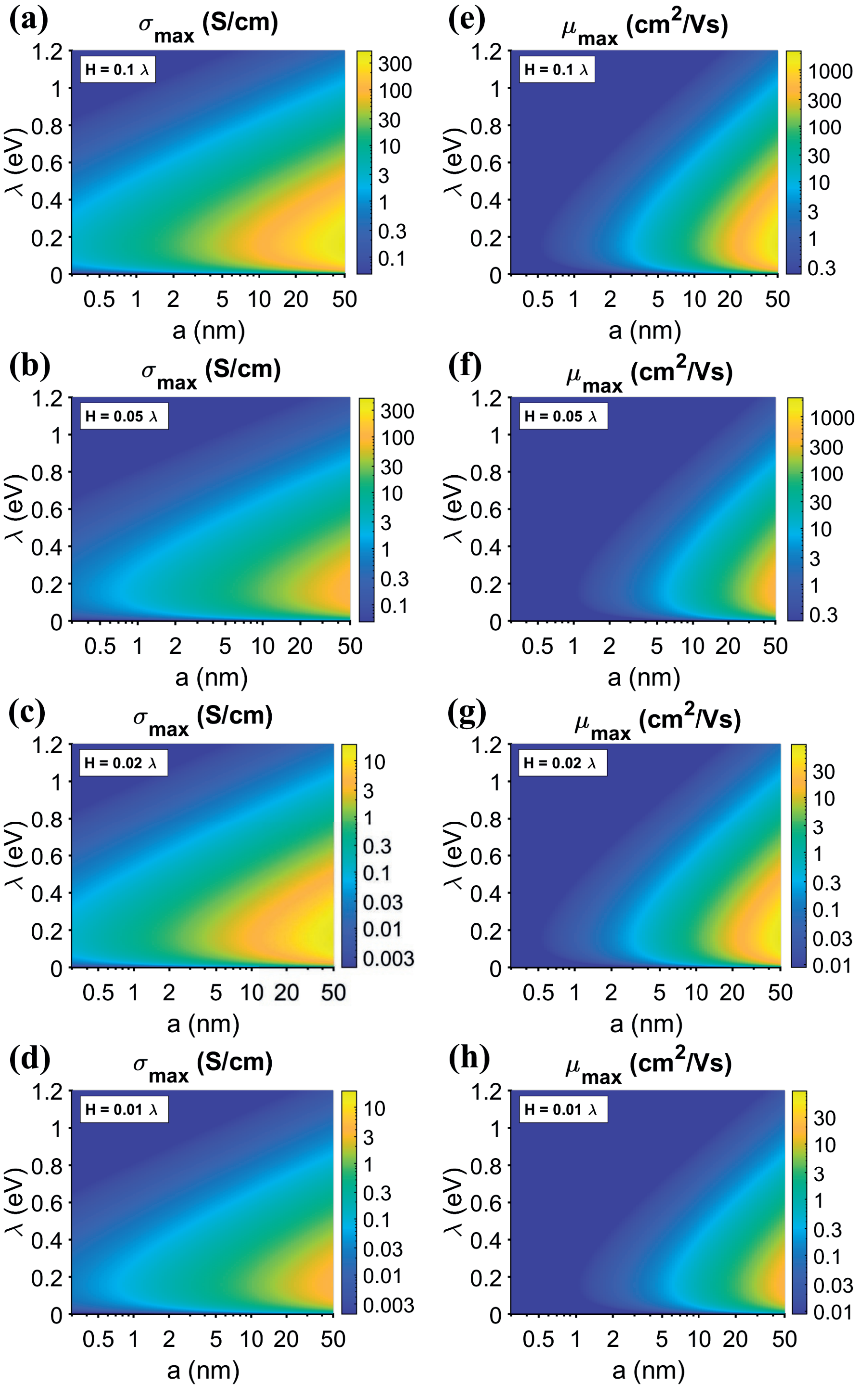

Figure S10: **a-d** Maximum attainable conductivity with the "weak coupling" condition. Conductivity and mobility are plotted as a function of the reorganisation energy, λ, and the center-to-center hopping distance, a, for different values of the ratio between electronic coupling and reorganisation energy, H/λ, as indicated in the top left corner of each color map.

4

CONDUCTION IN CABLE BACTERIA FIBERS DISPLAYS A WEAK ELECTRICAL GATE EFFECT

**Jasper VAN DER VEEN, Matteo De Pellegrin, Albert Wieland,
Filip J.R. Meysman and Herre S.J. van der Zant**

ABSTRACT

Cable bacteria display an exceptional type of biological conduction, as electrical currents are channeled over centimeter distances through a network of protein fibers embedded in the cell envelope. These fibers display a high conductivity, and their electronic properties bear some resemblance to doped organic semiconductors, such as polyaniline and polyacetylene. In semiconducting nanowires, the conductivity can be tuned over several orders of magnitude by applying an external electric field through a global back gate. Here, we demonstrate that such a strong gating effect is not present in cable bacteria. At room temperature, the conductance can only be marginally tuned by electrical gating (< 2 %). At cryogenic temperatures, the gating effect is slightly stronger (< 65 % modulation of the conductance at $T = 30$ K). The gating effect attains a minimum near the zero gate voltage, and displays saturation for both positive and negative gate voltages. An electron transport model with a small energy gap (~ 1 meV) and a constant density of states adequately reproduces the observed gating response at low temperatures. These findings challenge the conventional model of biology electron transport, in which electrons move through hopping and only a single electronic state per charge carrier site contributes to the conduction.

4.1. INTRODUCTION

Bio-based conductive materials are increasingly receiving interest, as they potentially provide an alternative to conventional electronic materials, like silicon and metals, that have a large environmental footprint. The prospect of a biodegradable electronic material could also form a solution to the problem of electronic waste [110]. However, to ensure functionality, biomaterials must have electrical properties that are sufficiently competitive to standard electronic materials. A natural system that has recently attracted considerable attention in this regard is the highly conductive fiber network inside cable bacteria. Cable bacteria are multicellular microorganisms that live in aquatic sediments and grow to form centimeter-long filaments [1]. Electrical currents are guided along these filaments through a regular network of protein fibers that are embedded in parallel within the cell envelope [2]. These protein fibers display an extraordinarily high conductivity (up to ~100 S/cm), and as such, they emerge as a promising new bio-electronic material [2].

Detailed electrical investigation has recently shown that the conduction in cable bacteria shares features with some organic semiconductors, such as polyaniline and polyacetylene [111–114]. As such, conduction in cable bacteria somehow resembles that of an organic conductor with a high charge carrier density and polaron delocalization across multiple sites. The conductivity levels in the periplasmic fibers of cable bacteria are very high, and the conductance does not show any redox signature and has a low thermal activation energy (~40 meV). Electronic transport in other natural protein systems (e.g., electron transport through multi-heme cytochromes in the metal-reducing bacteria Shewanella and Geobacter [115, 116]) usually has a much lower conductivity, a much higher activation energy (> 0.3 eV) [23], and often shows the signature of a redox process.

Here, our objective is to examine to what extent the conductance in cable bacteria is similar to that in organic semiconductors, such as polyaniline and polyacetylene. These organic semiconductors have the critical property of being amenable to gating: in a classical Schottky transistor configuration, the conductivity can be modulated over several orders of magnitude [117–119]. To examine whether the conductance in cable bacteria also shows this field effect, we investigated single filaments of cable bacteria in a global back gate set-up. The resulting data provide insight into the underlying charge transport mechanism.

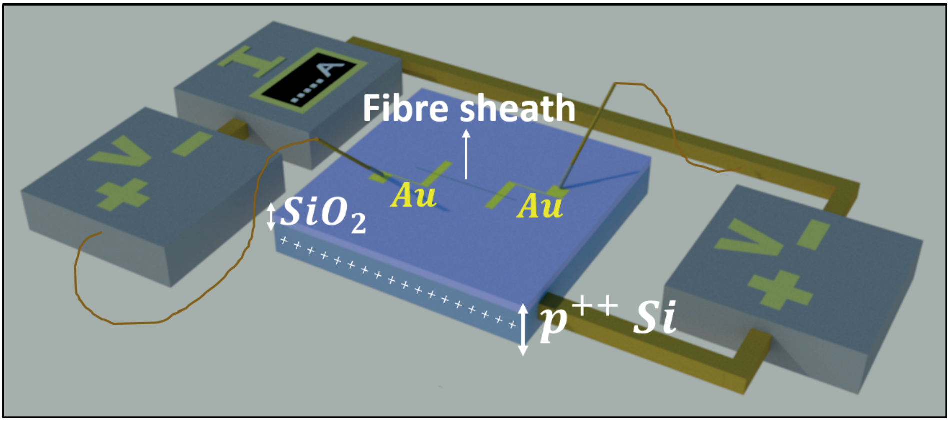

Figure 1: **Gating setup used to examine the field effect in cable bacteria.** Gold patterned electrodes (Au) are deposited on a 285 nm thick non-conductive SiO_2 layer that overlays a conductive silicon substrate (p^{++} doped). A fiber skeleton of cable bacteria is aligned across two electrode contacts. A bias voltage, V, is applied across the electrodes using probe tips, and the current, I, through the fiber skeleton is measured. A gate voltage, V_G, is applied to the underlying silicon substrate to modulate the current.

4.2. RESULTS

4.2.1. DATA COLLECTION

To study the field effect on the conductance of cable bacteria, native cable bacterium filaments were individually isolated from enrichment cultures. A sequential extraction procedure allows to remove the lipid membranes and cytoplasm, thus retaining a “fiber skeleton” that comprises the conductive fiber network connected by a polysaccharide sheath [2]. These fiber skeletons display a similar conductivity as native filaments, thus demonstrating that the electron transport remains fully functional after extraction.

To study the field effect on the conductance of cable bacteria, we deposited fiber sheaths onto a transistor set-up consisting of a silicon substrate (a 0.5 mm p^{++}-doped silicon layer covered by a 285 nm silicon dioxide layer) with gold-patterned electrodes (Fig. 1). The current-voltage characteristic, $I(V)$, was recorded as a function of the gate voltage, V_G. The conductance, $G = I/V$, then can be calculated from the $I(V)$ curve at a certain bias voltage, V. This G value can be compared to the minimum conductance obtained over the gate voltage range measured ($G_0 = \min(G(V_G))$). The ratio of the two, G/G_0, is referred to as ’the gate effect’.

We measured the gate dependence on 8 separate segments from three individual fiber skeleton filaments. These segments had different non-conductive interspacings between the electrodes, ranging from 4 to 600 μm (the positioning of the filaments on the electrodes is displayed in Fig. S1). For each segment, we first determined how the conductance G varied as a function of the bias voltage V and temperature T, without any gate voltage imposed. This non-gated conductance showed a similar temperature dependence for all the segments investigated (Fig. S2).

The gate effect was determined for all segments at different temperatures, T. For all segments, gate-dependent measurements were performed at low temperatures (11 K to 50 K). Segment 1 was a well conducting sample (room temperature conductivity of 14 S/cm, Table S1) and was measured in more detail: gate-dependent measurements were performed over a wider range of temperatures (21 K to 200 K). For this segment, the electrode spacing was 300 µm and the electrode width was 100 µm with no electrode material in between (Fig. S1).

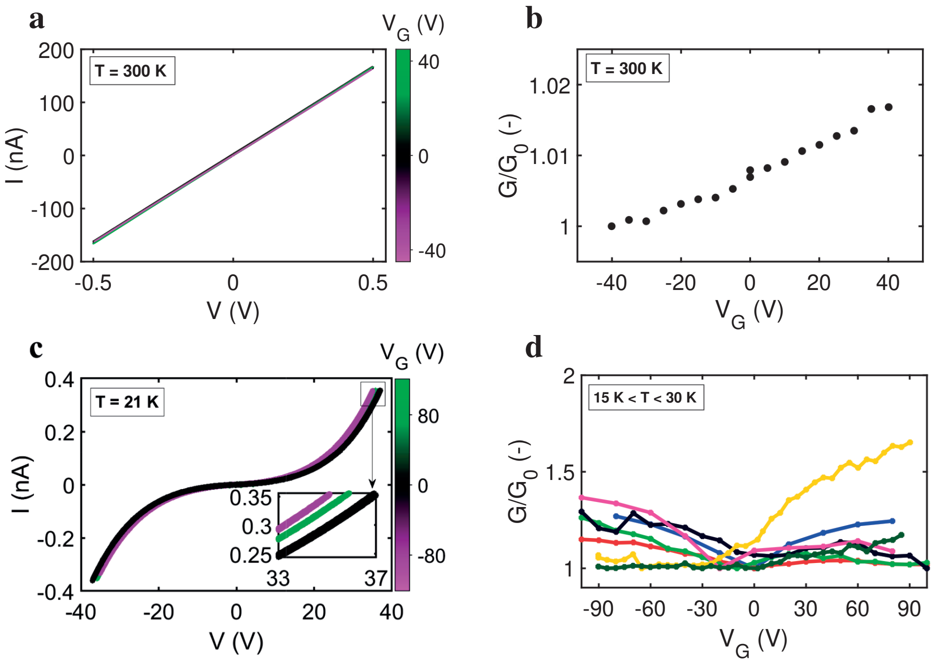

Figure 2: **Current-voltage characteristics and conductance as a function of gate voltage. a** Current, I, versus bias voltage, V, for zero gate voltage (black), for maximum positive gate voltage (green) and for maximum negative gate voltage (magenta). The temperature, T, is indicated in the upper left corner. The spacing between electrodes is 600 µm (Segment 8 in Fig. S1). **b**, Same segment as in panel (a). The conductance, G, versus gate voltage, V_G. the conductance is determined from a linear fit in the $I(V)$. **c**, Current, I, versus bias voltage, V_B, for zero gate voltage ($V_G = 0$, black), for maximum positive gate voltage ($V_G = 80$ V, green) and for maximum negative gate voltage ($V_G = -80$ V, magenta). These $I(V)$ curves were taken at a temperature of $T = 21$ K. The inset shows the $I(V)$ curves in the region $V = [33, 37]$ V. **d**, Gate effect versus gate voltage, V_G, where each colour is a different segment. Measurements taken in temperature range $T = [15, 30]$ K, plotted at the lowest analysed bias voltage ($V < 14$ V).

4.2.2. GATING EFFECT

Our results show that the conductance in cable bacteria shows a limited gate effect. At room temperature ($T \approx 300$ K), the gate effect is hardly noticeable. The I(V) curves are linear and only marginally dependent on the gate voltage V_G (Fig. 2a). The gate effect is smaller than 2% over the gate voltage range examined [-40 V,+40 V] (Fig. 2b). The gate effect also changes linearly over the investigated gate voltage range (Fig. 2b). At a temperature of 200 K and over the extended gate voltage range [-80,+80] V, the effect was at most 3 % (Fig. S3h). In this case, the conductance was higher for negative gate voltage instead of positive. Both for the low and high temperature data, it is not predictable for which sign of the gate voltage the conductance is highest.

When the temperature was lowered further, the gate effect changes from linear to bipolar, reaching a minimum near the zero gate voltage. The gate effect also increases in magnitude. For 'Segment 1' at $T = 20$ K, there was a 28% increase in conductance at $V_G = -80$ V and 26% increase at $V_G = +80$ V (Fig. 2c,d). This positive increase in the conductance on both sides of the gate voltage polarity was observed for most other segments (6 out of 7) within the low temperature range (< 150 K). Such behaviour was already previously observed down to a temperature of 77 K [45]. For some segments, the bipolarity effect was not symmetric, showing a higher increase for one of the gate polarities (Fig. 2d, Fig. S3).

For segment 1, we monitored the gate effect in detail for increasing temperatures in the range between 20 K and 160 K. We observed that the gate response changes from bipolar to linear, and that the gate effect gradually diminishes (Fig. 3a).

When the I(V) curve does not display a linear Ohmic response, the conductance $G = I/V$ becomes dependent on the voltage bias V. At a fixed temperature, the gate effect hence tends to be reduced with increasing bias voltage (Fig. 2b). However, this dependence on voltage bias is weak compared to the temperature dependence of the gate effect. When the temperature is increased by a factor 5 (from $T \approx 20$ K to $T \approx 100$ K) the gate effect decreases from 27 % to 3 %. Oppositely, when the voltage bias is increased by a factor 5 (from 5 V to 25 V), the gate effect only drops from 28 % to 18 %.

Fig. 3c and d show these effects in more detail. At a high gate voltage ($V_G = -80$ V), we see that the gate effect, G/G_0, linearly decreases as a function of V (Fig. 3d). This effect is more pronounced at lower temperatures. At $T = 21$ K, the slope of the linear fit provides a decrease rate of 0.43%/V, while at 50 K it only decreases at a pace of 0.15%/V.

Consequently, if the blue data points in Fig. 3d were to be linearly extrapolated to the vertical axis (see dashed line), the zero-bias gate effect at low temperature ($T = 21$ K), is expected to be only slightly greater than the high-bias gate effect. It is therefore not expected that the gate effect is much larger for low bias voltage.

4.3. DISCUSSION

4.3.1. CONDUCTION IN CABLE BACTERIA DISPLAYS A WEAK GATING EFFECT

Organic semiconductors such as polyaniline and polyacetylene display a temperature dependence of conductivity similar that is similar to that of the protein fibers in cable bacteria (Chapter 2). These organic semiconductors typically also show a strong gate effect [117, 120–122]. For example, when HCl doped polyacetylene was investigated in a comparable transistor set-up as done here (channel length: 100 µm, gate oxide thickness: 200 nm), the gating effect at room temperature amounted to a factor 10^3 for a gate voltage of $V_G = -30$ V [117]. The fact that we only observe a very weak gate effect at room temperature (factor <0.02; 5 orders of magnitude lower) is hence a key difference between cable bacteria and these organic semiconductor systems.

This near absence of a gate response is surprising. In semiconducting materials, the gate effect arises from the presence of a band gap energy. The gap energy, U_g, thermally suppresses the charge carrier density in the conduction band under normal, zero-gate

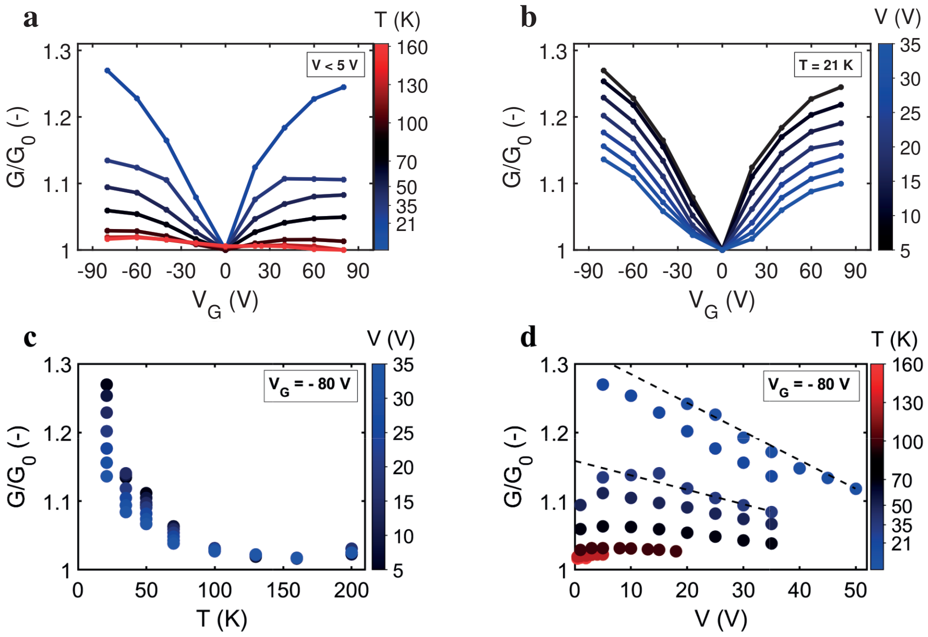

Figure 3: **Temperature and bias voltage dependence of the gate effect**, for segment 1. **a**, On the vertical axis the normalized conductance, G/G_0, and on the horizontal axis the gate voltage, V_G. The gate response is plotted for temperatures indicated next to the colour bar. All conductance values are determined at the lowest bias voltage ($V < 5$ V). **b**, The normalized conductance, G/G_0, versus gate voltage, V_G. The gate response is plotted for multiple bias voltages, V, indicated next to the colour bar. **c**, The magnitude of the gate effect, G/G_0, is shown as a function of temperature, T, for the maximum negative gate voltage ($V_G = -80$ V). The data is plotted at different bias voltage, V, indicated by the colour scale to the right. **d**, The magnitude of the gate effect, G/G_0, is shown as a function of bias voltage, V, for the maximum negative gate voltage ($V_G = -80$ V). The data is plotted at different temperatures, T, indicated by the colour scale to the right. The dashed line is a guide for the eye for linear extrapolation.

conditions ($n \propto \exp[-U_g/(2k_B T)]$). By applying a gate voltage, the charge carrier density can be substantially increased. When a positive gate voltage is applied, the conduction band is moved closer to the Fermi energy level, thus increasing the charge carrier density. For the opposite polarity, the number of holes in the valence band is increased. The fact that there is only a weak gate response at room temperature in cable bacteria fibers, thus could indicate the absence of a band gap. When there is a non-zero density of states at or near the Fermi energy, the charge carrier density cannot by changed much through the application of an electrical field as imposed by the gate voltage. The latter is an important feature of a (semi)metallic system.

Furthermore, at the interface between electrode and semiconductor, one would also expect Schottky diode behaviour, which implies that one would observe a strongly asymmetric I(V) response. Instead, we see a linear current-voltage ($I(V)$) curve, which is also characteristic for systems that display a metallic type of conduction. Still, the temperature dependence of the conductance in cable bacteria does not show any true metallic behaviour. Rather than decreasing, the conductance increases with temperature, albeit with a low activation energy of 40 meV (Chapter 2) [91].

4.3.2. TEMPERATURE DEPENDENCE OF THE GATING EFFECT

When moving to lower temperatures, we observed that the gate effect gradually increases, which hence could result from the limited size of the energy gap. This small energy gap must be on the order of 1 - 10 meV, given that is it only visible at low temperatures (< 150 K, $k_B T_g \approx 13$ meV). The band gap could originate from the charging energy of the electron on the charge carrier site. The charge of the electron, e, leads to a voltage with respect to the matter around the hopping site, $V = e/C$, where C is the capacitance between the hopping site and its material surroundings. For a sufficiently small capacitance C, this voltage is significant. For example, for a single fullerene (C-60) particle connected between electrodes, the charging energy amounts to ~ 0.5 eV [123–125]. This fullerene particle has a diameter of approximately 1 nm. Our inferred energy gap is two to three orders of magnitude lower. If the observed energy gap in cable bacteria is due to a charging effect, than the electronic states is possibly more extended than in such a particle, since the capacitance scales directly with size.

The gate effect rapidly decreases in a non-linear fashion when the temperature increases (Fig. 3d). In semiconductors this effect is explained as follows. The conductivity, $\sigma = ne\mu$, is essentially the product of carrier mobility, μ, and the charge carrier density, n. The charge carrier concentration, n, is thermally influenced and is dependent on the magnitude of the band gap ($n \propto \exp\left(\frac{U_g}{2k_B T}\right)$ [5]). When the energy gap is small with respect to the thermal energy, the gate effect will be negligible.

The gate voltage can move the electronic states closer to the Fermi level and thereby reduce the effective band gap [5], such that the activation energy of transport is $U_A = U_g/2 - \gamma V_G$. Assuming the gate has reduced the activation energy of transport, the conductance can be written as:

$$G \propto \exp\left(\frac{U_A}{k_B T}\right)\exp\left(\frac{-\gamma V_G}{k_B T}\right). \tag{1}$$

The gate effect closely follows this Arrhenius relation (Fig. 4). From this, we can estimate that the gate effect at V_G = - 80 V induces a shift in the activation energy caused of 0.43 meV. From this, the coupling parameter γ, which determines how much the gate voltage is able to shift the activation energy, can be estimated as $\gamma = 6\,\mu\text{eV/V}$. This limited change is another way to express that the gate effect is small.

4.3.3. A THEORETICAL MODEL

To provide theoretical model support to the observed gate effect, we expanded the hopping model presented in Chapter 3. To this end, we introduced a small energy gap, with one chain of hopping states slightly above and below the Fermi energy ($\pm t$, one hopping site/location now has two states/orbitals). This coincides with the situation in Chapter 3 with an injection barrier, but now with two states instead of one. We assume that these states independently contribute to the current, I (other assumptions in the Appendix). The current per hopping chain is (see Chapter 3):

$$I = e\Gamma_R p_{j,i}(1 - p_{j,i+1}) - e\Gamma_L p_{j,i+1}(1 - p_{j,i}), \tag{2}$$

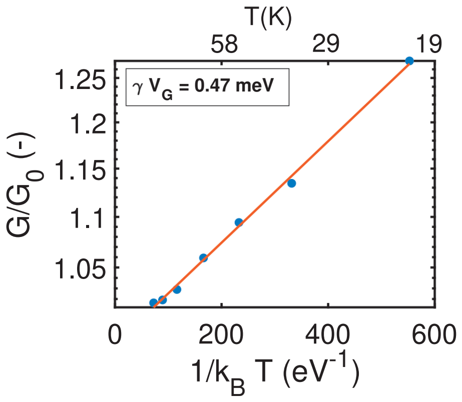

Figure 4: **Gate effect as a function of temperature on an Arrhenius plot**, at maximum negative gate voltage ($V_\mathrm{G} = -80$ V). Using the Arrhenius relationship, $G \propto \exp\left(\frac{-\gamma V_\mathrm{G}}{k_\mathrm{B}T}\right)$ (Eq.), an estimate of the energy shift applied by the gate voltage at $V_\mathrm{G} = -80$ V can be translated to a gate coupling $\gamma = 6$ µeV/V.

where $j = 1,2$ refers to the two states slightly above and below the Fermi energy (Fig. 5a). The model does not allow the conductance at one side of the gate voltage polarity to be higher. To describe such a difference, the hopping rate for $j = 1$ would need to be chosen different from the one for $j = 2$. For low voltage ($\Delta \ll k_\mathrm{B}T$) and field-driven transport ($p_{j,i} \approx p_{j+1,i}$, Chapter 3), the current is:

$$I = e\Gamma_\mathrm{R}\frac{eV}{2N_S k_\mathrm{B}T}\left[\frac{1}{1+\cosh(\frac{t-\gamma V_\mathrm{G}}{k_\mathrm{B}T})}+\frac{1}{1+\cosh(\frac{-t-\gamma V_\mathrm{G}}{k_\mathrm{B}T})}\right]. \tag{3}$$

This model roughly reproduces the observed effect (Fig. 5c). However, the shape of gate effect curve and the size of the gate effect is relatively insensitive to the choice of the gap size. For a large range of gap sizes ($t = 5-100$ meV), the same gate response is simulated (Fig. S5). This is because the gate effect is determined by the energy shift that the gate causes, γV_G, and not by the gap size. Therefore, nothing can be said about the gap size, t.

Nevertheless, we know that the sum of the activation energy from the hopping rate, Γ_R, and gap energy, t, cannot be greater than the total activation energy (~ 40 meV), so from the activation energy itself it can already be concluded that can be no large energy gap in cable bacteria. However, in this model, the conductance is at a maximum for zero gate voltage at high temperatures (Fig. 5c), which is not consistent with the observations. So, an alternative model is needed.

An important observation in the data is that there is a saturation effect apparent in the gate response at high voltages (Fig. 3a,b). Such a saturated response can be explained by a model that expands upon the model introduced above. This expansion introduces many more electronic states, but keeps a small gap energy window, in which no states are allowed U_g (Fig. 5b). In the model simulations, the conductance is saturated when the shift in gate energy, γV_G, is much greater than the energy gap U_g. The thermal energy, $k_\mathrm{B}T$, smoothens the response (at zero T, it would be a step function).

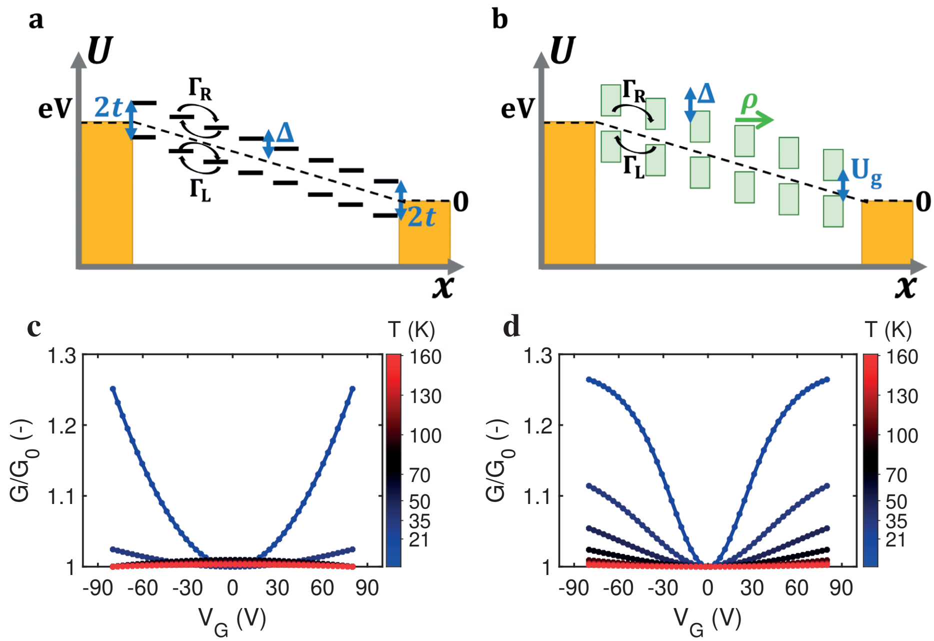

Figure 5: **Scenarios to explain the gate effect.** **a**, Energy vs. position diagram, where one hopping chain of electron states lies at energy $+t$ above the Fermi energy of the conductive protein (indicated by the dashed line), and another at energy $-t$. Between every hopping site, there is an energy dissipation, $\Delta = eV/N_S$, where N_S is the number of hopping sites. **b**, An expanded version of the scenario in **(a)**, but now with many electronic states per site. In green, the density of states, ρ. There is an energy gap, U_g. The energy dissipation per hopping site, Δ, is the same as in panel (a). **c**, Theoretical gate effect in system **(a)**. Normalized conductance, G/G_0, versus the gate voltage, V_G. The gate effect is plotted for the temperatures indicated in the colour scale to the right. Parameters: gap, $t = 5$ meV and gate coupling, $\gamma = 20$ µeV/V. **d**, Theoretical gate effect in system **(b)**. Parameters: gap, $U_g = 1$ meV and gate coupling, $\gamma = 20$ µeV/V.

This model, which has a constant density of states, ρ, outside the gap, qualitatively provides the best agreement with the experimental data (Fig. 5d, Fig. S6). It captures both the tendency towards gradual saturation in the data, as well as the enhancement of the effect for lower temperatures. Fig. 5d was constructed with $U_g = 1$ meV and $\gamma = 0.1$ meV/V, which is close to optimal for the two fitting parameters. The parameters can be systematically varied to arrive at this conclusion. From the parameters of Fig. 5d, if the coupling, γ, is significantly decreased, the saturation will not be visible anymore. If γ is increased, most of the gate response will be characterised by a saturated response (a flat line at $G/G_0 > 1$ for higher gate voltages, see Fig. S6). From the base situation, if the energy gap is decreased below 0.5 meV, there will be no gate effect, because the thermal energy $k_B T$ is always larger than the gap in the experimental temperature range ($T > 4$ K, $k_B T \approx 0.4$ meV). If the energy gap is increased above 2 meV, a stronger maximum gate effect is predicted ($G/G_0 > 2$). If the coupling is reduced to weaken the effect back to the experimental levels, the saturation disappears, so a combination of weaker coupling and a larger gap is not an option. As already mentioned, in the opposite case, i.e. a combination of stronger coupling and a small gap, gives a response mostly dominated by saturation (Fig. S6). We conclude that the size and temperature dependence of the effect are consistent with an energy gap $U_g \approx 0.5 - 2$ meV (Fig. S6a,b,c) with $\gamma \approx 0.1$ meV/V. This model only is sensible if the energy spacing between electronic levels is equal or smaller than the gap size ($\sim$ 1 meV), so at least tens of states could be contributing to conductivity at room temperature (1 meV fits 25 times in $k_B T$). We conclude, based on the gate dependent measurements, that cable bacteria conductivity is effectively gapless at room temperature. Based on the model presented here, there could be many states contributing to conductivity, just like in metallic transport.

4.4. SUMMARY AND CONCLUSION

The observation of virtually no gate effect at room temperature, combined with the low-temperature measurements, that show a positive gate effect for both polarities and saturation for high gate voltages, lead us to conclude that cable bacteria are not semiconducting. At room temperature, there is no significant energy gap at the Fermi energy. This means that the charge carrier density, n, cannot be improved by gating. This conclusion supports the notions in Chapter 2, in which the temperature dependence of conductivity was proposed to come from the charge carrier mobility, determined by a hopping process. A model in which there is a small energy gap of the order of $\sim$ 1 meV, but otherwise a constant density of states, qualitatively fits the experimental data at low temperature.

4.5. METHODS

FABRICATION

A p^{++}-doped silicon four inch wafer with a 285 nm silicon dioxide layer is diced into 19 mm^2 pieces, after which a single piece is cleaned for 5 minutes in nitric acid (HNO$_3$ and demineralized water, inside the Kavli Cleanroom at Delft University of Technology. In a next step, a photoresist is spin coated onto it (AZ ECI 3007 or 3012). Using the Heidelberg uMLA Laserwriter, with optical wave length 365 nm, the electrode pattern is exposed in the photoresist layer (Dose ~ 250 mJ/cm^2). The exposed photoresist layer is stripped with developer MF321, by submerging the silicon piece for 1 minute in it, after which for 30 seconds the piece is submerged in water, to stop the development. With a diamond pen, at 0.5 mm^2 squares stripped from photoresist, the silicon dioxide layer is locally pierced through. This forms a reliable gate connection. Within one hour, 5 nm of titanium is evaporated onto the sample, and 60 - 100 nm of gold, which also overlays the air-exposed silicon gate connections. N-Methyl-2-pyrrolidone at 70 degrees Celsius lifts off the remaining resist and unwanted gold.

GATE MEASUREMENTS

Measurements of the gate effect were performed in a LakeShore Cryogenic Probe Station (Type CRX 6.5 K). A bias voltage, V, is fed to one of the probes, which is landed on one of the electrodes. The other probe, is connected to another electrode and kept at zero voltage. Due to this, a current, I, will flow from one to the other probe, via the fibre sheath that is lying across the two electrodes. A third probe is connected to one of the pierced through gate contacts (0.5 mm^2 size) and a fourth probe is connected to another gate contact. With an electronic device that applies 10 mV and estimates the resistance at that voltage ("beeper box"), it is checked whether a good connection through the gate contacts via the doped silicon layer is achieved ($< 100\ \Omega$). With the same electronic device, it is checked whether a very high resistance between the gate contact and the biased electrodes is achieved ('open'). When the actual gate measurement is performed, the gate voltage, V_G, is slowly ramped up (~ 1 V/s). During the ramping, the current between the two biased electrodes is measured. During the ramping, this current is typically not zero, even though the bias voltage is zero, because of capacitive charging of the gold electrodes or elsewhere in the system. After the ramping, the current reverts back to zero. When the capacitive current is back at zero, the bias voltage, V, is swept from zero, to a maximum positive value, to the same but negative value, and back to zero. During this time, the current, I, and the temperature, T, are recorded.

4.6. APPENDIX

4.6.1. SAMPLE-LAYOUT FOR MEASURED SEGMENTS

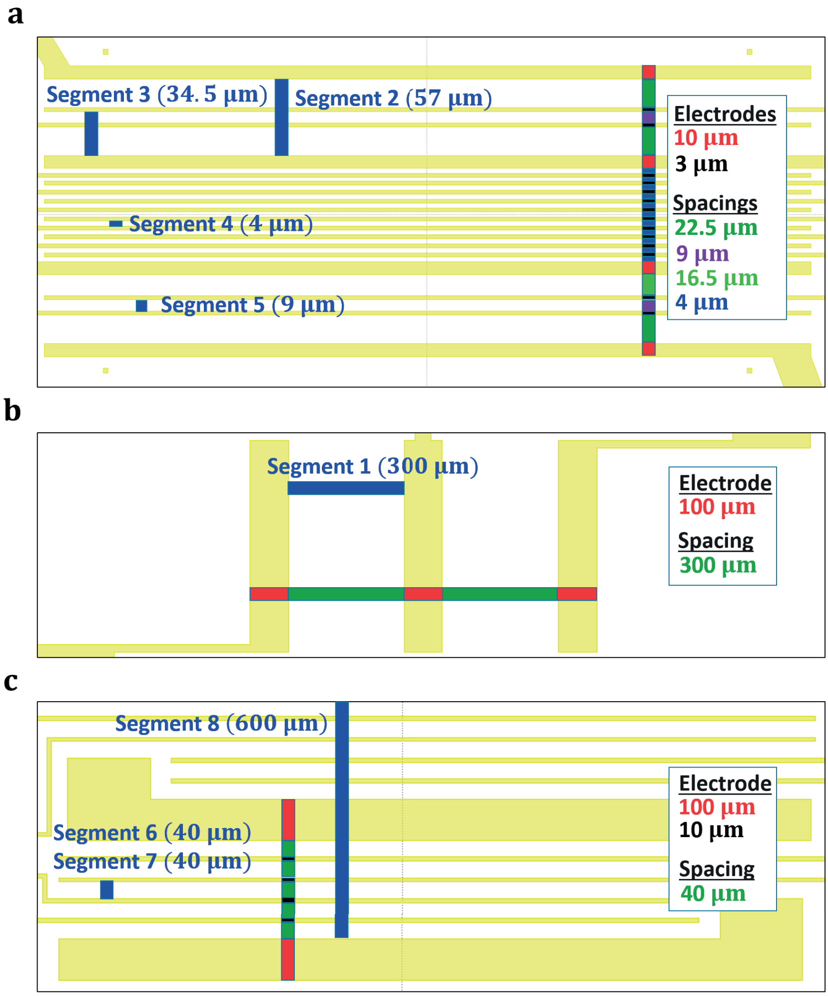

Figure S1: **Sample-layout for all segments.** Each subfigure is one of the used electrode pattern lay-outs. For each design, electrode width and electrode spacing is given in the graph, using colour coding to indicate the relevant length. For each segment, the electrode configuration is given (the segment was not necessarily at the exact given location).

4.6.2. TEMPERATURE DEPENDENCE OF MEASURED SEGMENTS

Segment 1

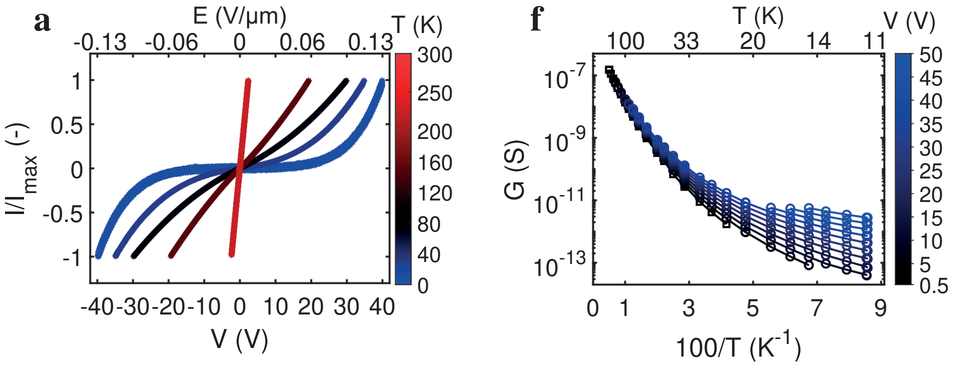

Segment 2

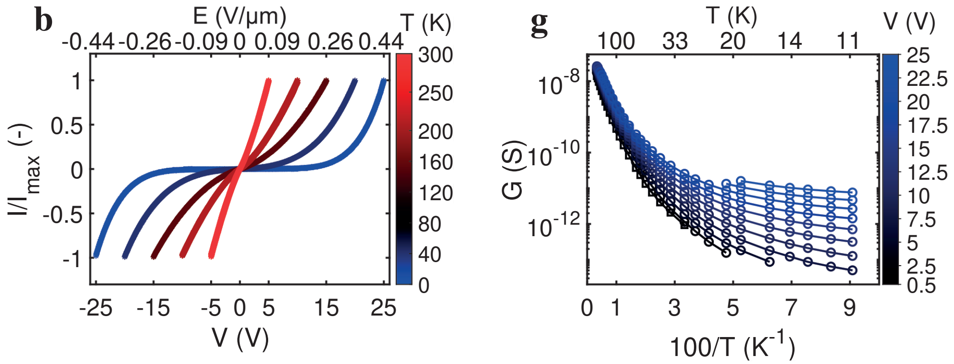

Segment 3

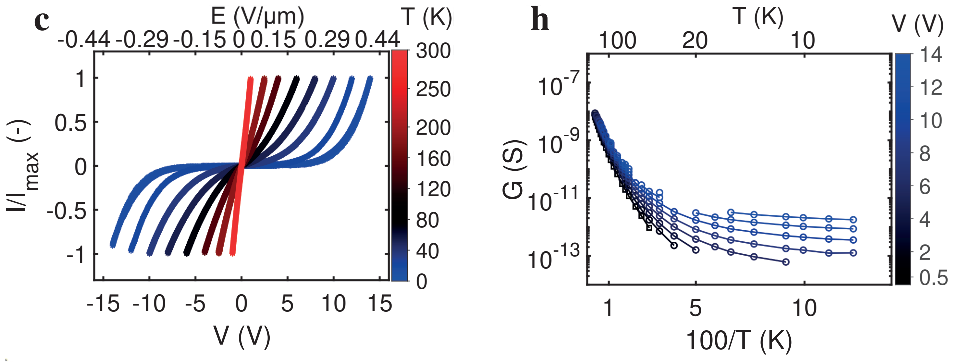

Segment 4

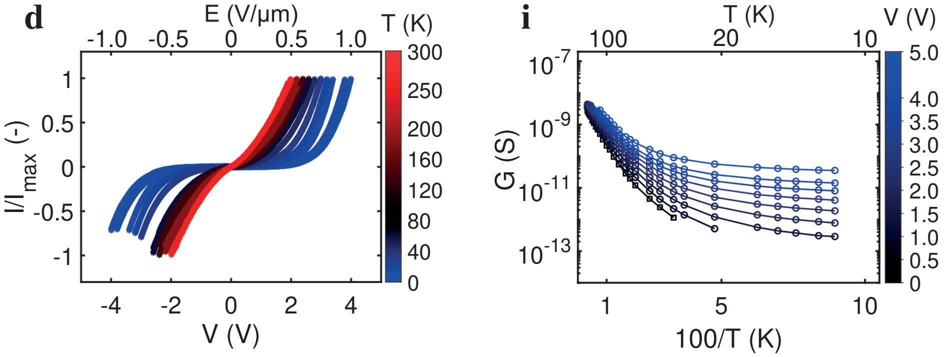

Segment 5

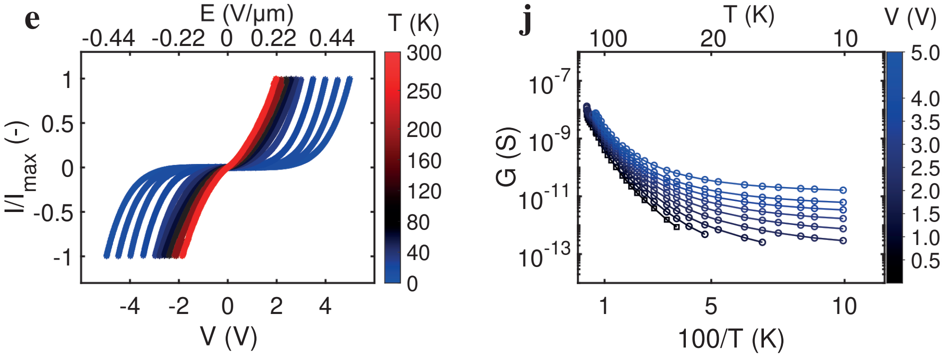

Figure S2: **Temperature dependence of segments for which the gate effect was characterized.** Segments 3, 4, 5 are 8, 12, 13 in Chapter 2. **a-e** Current-voltage ($I(V)$) characteristics recorded at different temperatures and zero gate voltage ($V_G = 0$). To illustrate the change in shape of the $I(V)$ curve, the current is normalized to the maximum current, I_{max}, obtained per $I(V)$ trace. The line color indicates temperature, linearly changing from red to black in the range 300 – 80 K and from black to blue in the range 80 – 0 K (see color bar). On the top axis, the electric bias field is shown ($E = V/L$), see Table 1 for segment lengths, L). **f-j** The data is plotted as $G = I/V$, as a function the inverse temperature, $100/T$, for different bias voltages, V. The colour scale linearly ranges from black (zero bias voltage) to blue (maximum bias voltage). The values in the colour bars next to the plot correspond to the lines plotted in the graph.

4.6.3. CURRENT-VOLTAGE CHARACTERISTICS AND GATE EFFECT

Segment 1

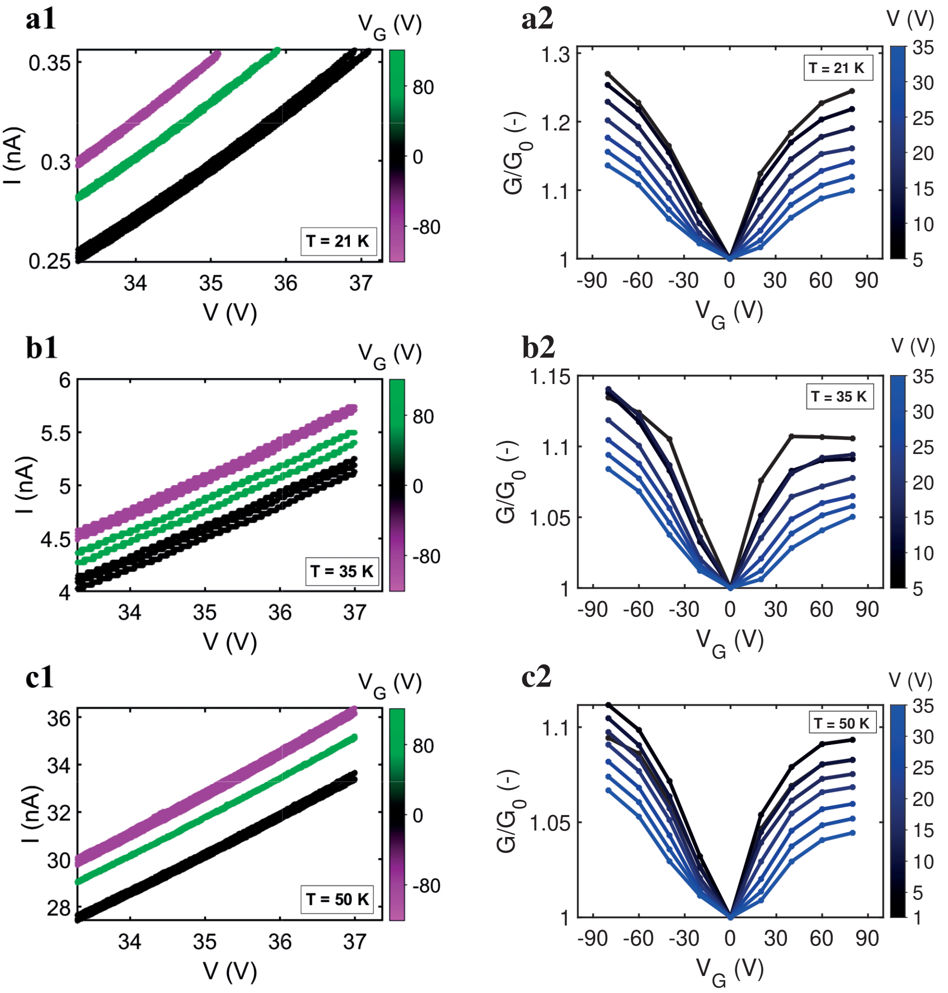

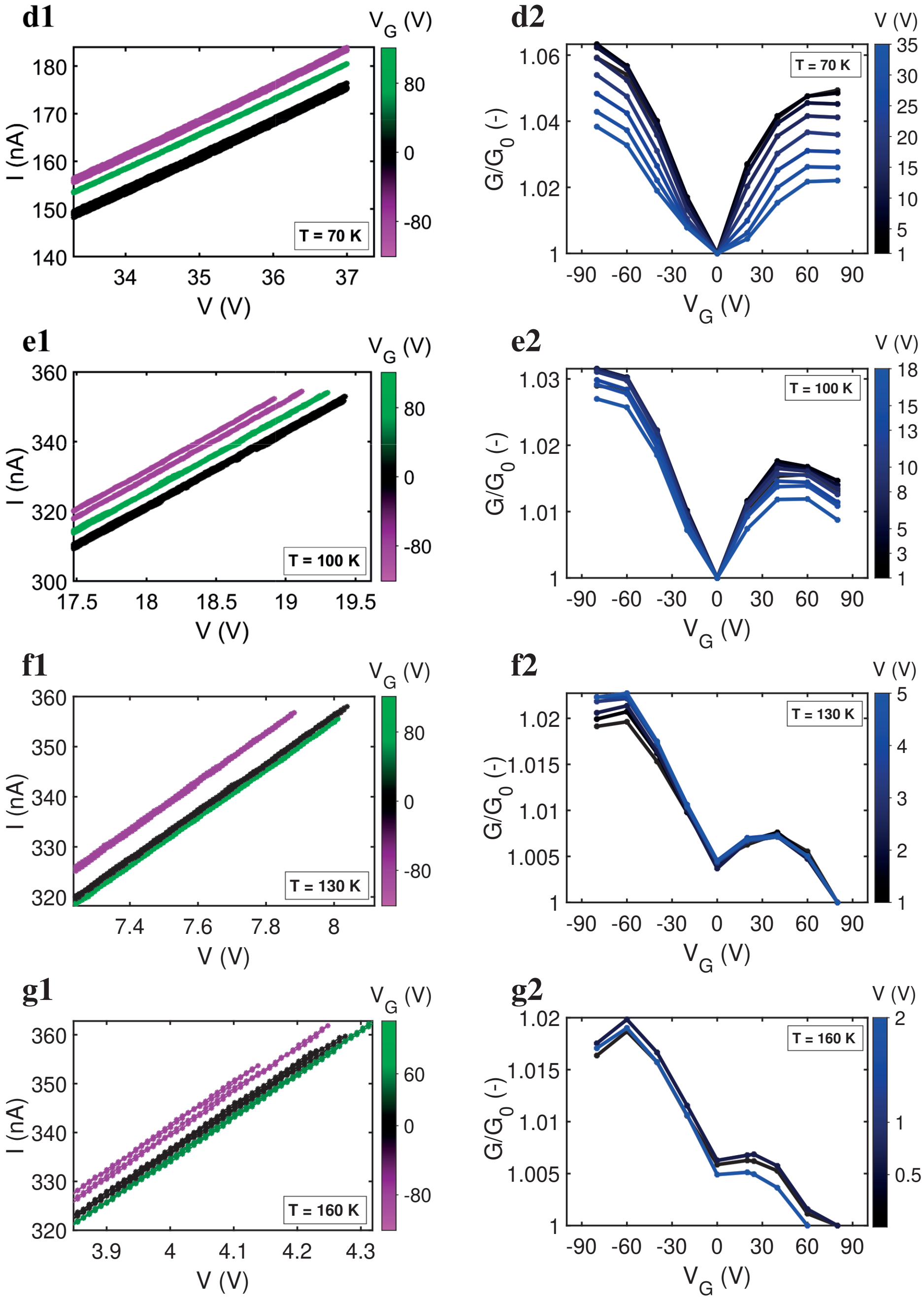
d1
I (nA)
140
150
160
170
180
34
35
36
37
V (V)
T = 70 K
V_G (V)
80
0
-80
d2
G/G_0 (-)
1
1.02
1.04
1.06
-90
-60
-30
0
30
60
90
V_G (V)
T = 70 K
V (V)
35
30
25
20
15
10
5
1
e1
I (nA)
300
320
340
360
17.5
18
18.5
19
19.5
V (V)
T = 100 K
V_G (V)
80
0
-80
e2
G/G_0 (-)
1
1.01
1.02
1.03
-90
-60
-30
0
30
60
90
V_G (V)
T = 100 K
V (V)
18
15
13
10
8
5
3
1
f1
I (nA)
320
330
340
350
360
7.4
7.6
7.8
8
V (V)
T = 130 K
V_G (V)
80
0
-80
f2
G/G_0 (-)
1
1.005
1.01
1.015
1.02
-90
-60
-30
0
30
60
90
V_G (V)
T = 130 K
V (V)
5
4
3
2
1
g1
I (nA)
320
330
340
350
360
3.9
4
4.1
4.2
4.3
V (V)
T = 160 K
V_G (V)
60
0
-80
g2
G/G_0 (-)
1
1.005
1.01
1.015
1.02
-90
-60
-30
0
30
60
90
V_G (V)
T = 160 K
V (V)
2
1
0.5

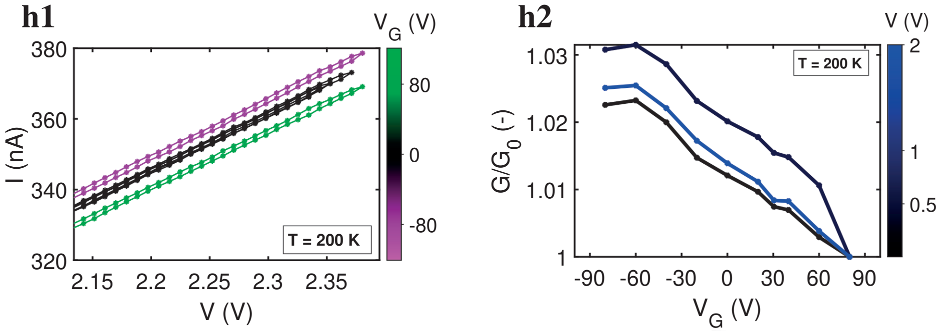
h1
V_G (V)
380
360
340
320
I (nA)
2.15
2.2
2.25
2.3
2.35
V (V)
80
0
-80
T = 200 K
h2
V (V)
1.03
1.02
1.01
1
G/G_0 (-)
-90
-60
-30
0
30
60
90
V_G (V)
2
1
0.5
T = 200 K

Segment 2

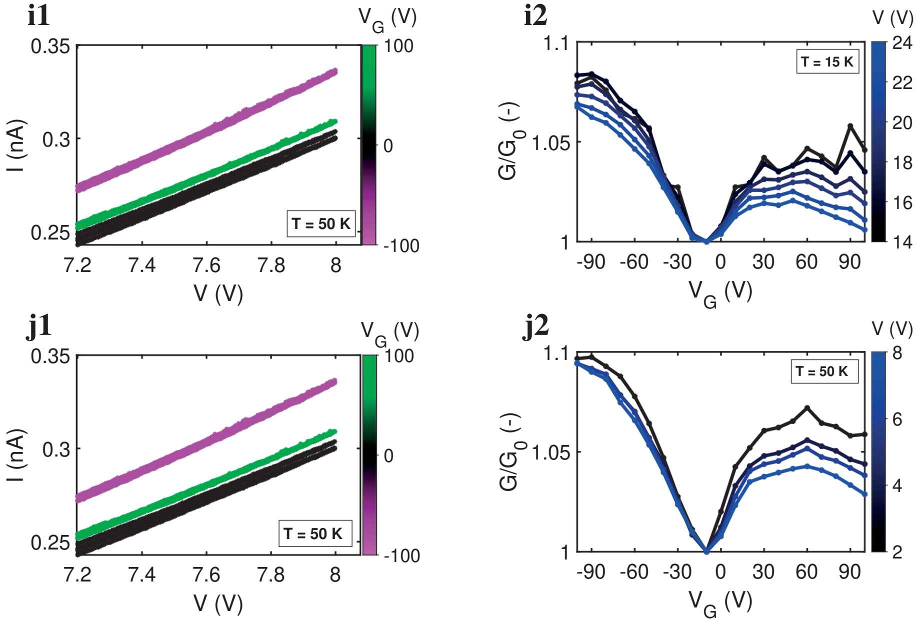
i1
V_G (V)
0.35
0.3
0.25
I (nA)
7.2
7.4
7.6
7.8
8
V (V)
100
0
-100
T = 50 K
i2
V (V)
1.1
1.05
1
G/G_0 (-)
-90
-60
-30
0
30
60
90
V_G (V)
24
22
20
18
16
14
T = 15 K
j1
V_G (V)
0.35
0.3
0.25
I (nA)
7.2
7.4
7.6
7.8
8
V (V)
100
0
-100
T = 50 K
j2
V (V)
1.1
1.05
1
G/G_0 (-)
-90
-60
-30
0
30
60
90
V_G (V)
8
6
4
2
T = 50 K

Segment 3

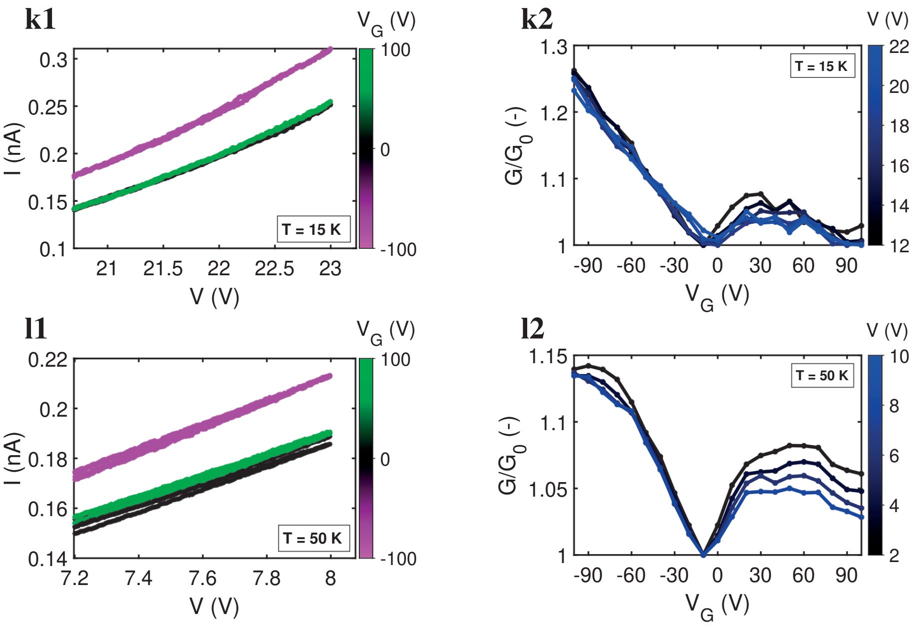

Segment 4

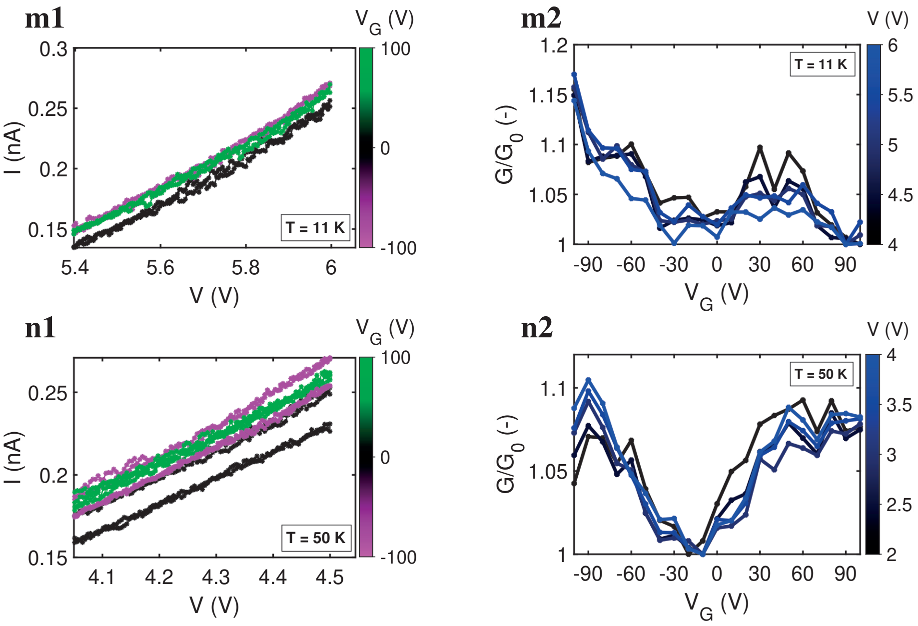

Segment 5

o1

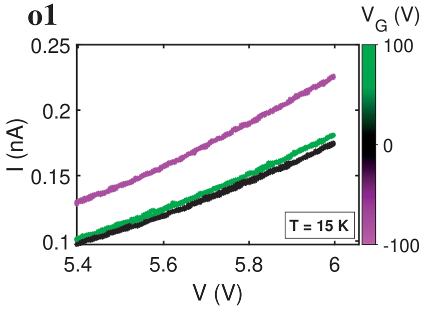

o2

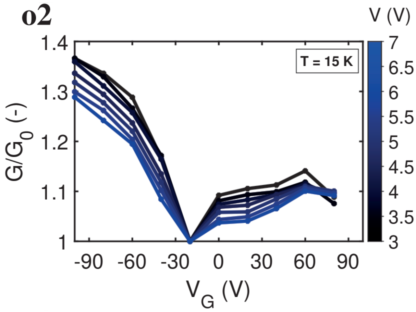

p1

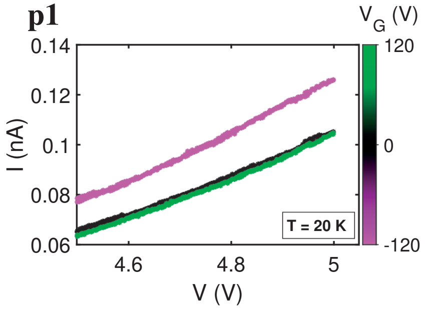

p2

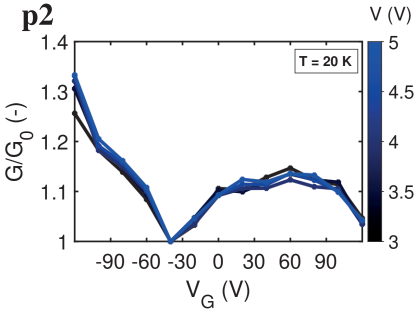

q1

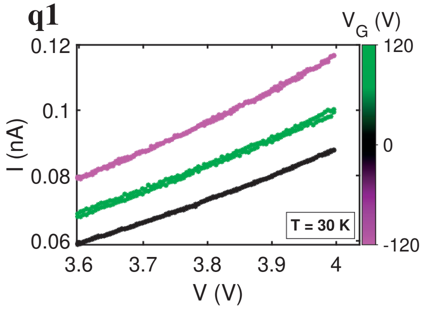

q2

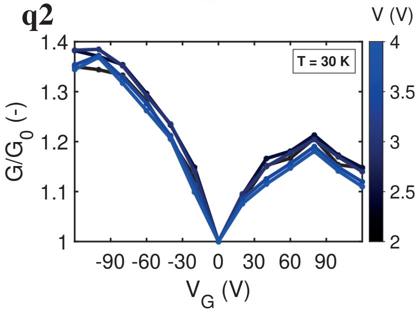

Segment 6

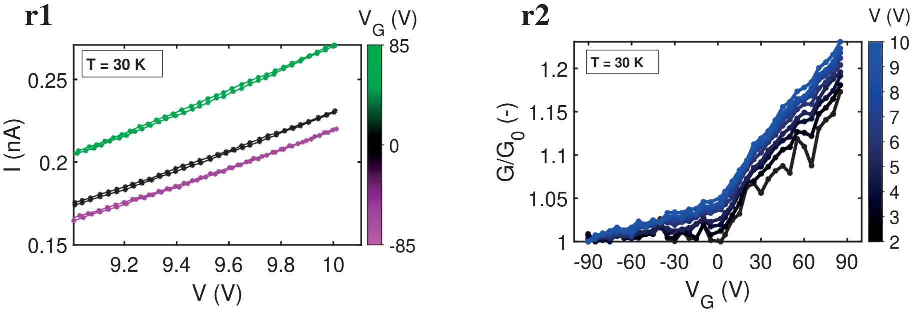

Segment 7

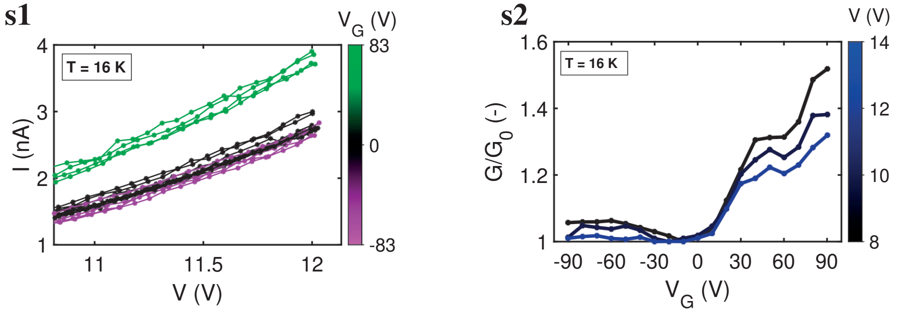

Figure S3: **Current-voltage characteristics and relative gate effect**, for the entire dataset, encompassing multiple temperatures and segments of cable bacteria. **a1-s1** Current, I, versus bias voltage, V, for zero gate voltage (black), for maximum positive gate voltage (green) and for maximum negative gate voltage (magenta). The temperature, T, is indicated in the inset. **a2-s2**, The normalized gate effect, G/G_0, versus gate voltage, V_G. the gate effect is shown at multiple applied bias voltages, indicated at the colour bar next to the figure. The temperature, T, is indicated in one of the corners.

4.6.4. UNIVERSAL SCALING BEHAVIOR AS A FUNCTION OF TEMPERATURE

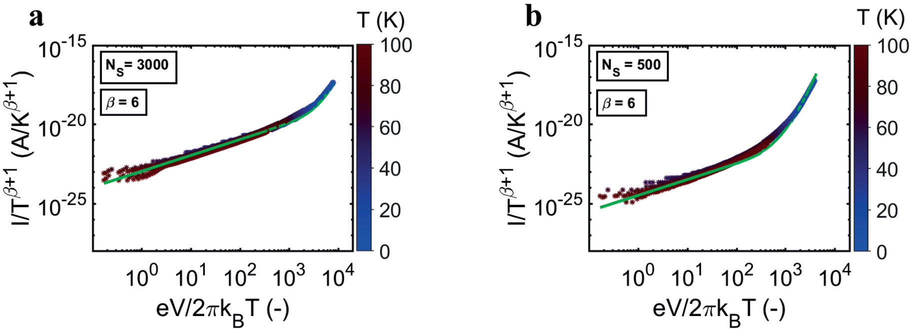

Figure S4: **Universal scaling behavior as a function of temperature.** Universal scaling curves for segment 1 (panel **(a)**) and 2 (panel **(b)**). The scaling curves for segments 3,4,5, are equivalent to Segments 8,12, and 13 in Chapter 2, which can be found there. Segments 6 - 8 were not measured as a function of temperature. The current-voltage curves in the temperature interval $T = [4, 100]$ K, are considered. On the vertical axis the current $I/T^{\beta+1}$, and on the horizontal axis the bias voltage scaled with temperature $eV/2\pi k_B T$. The green solid line gives a fit of the universal scaling relation to the data. The power law exponent β is visually calibrated to make the data fall onto the same curve the most (precision ±0.5) and is given in the inset of each panel. The transition from the low-bias, high-temperature regime to the high-bias, low-temperature regime occurs at a bias $eV \approx 2\pi N_S k_B T$. This transition point gives the parameter N_S, which gives the number of effective hopping steps.

4.6.5. TABLE WITH TEMPERATURE DEPENDENT PARAMETERS

Segment	L (μm)	L_E (μm)	G_0 (nS)	σ_0 (S/cm)	U_A (meV)	T_C (K)
#1	300	100	152	14	42.5 ± 0.7	80
#2	57	10	13.9	0.25	46.1 ± 1.8	90
#3	34.5	3, 10	6.20	0.066	41.8 ± 1.5	80
#4	4	3	2.72	0.0034	33.1 ± 0.7	70
#5	9	3	6.70	0.019	35.1 ± 1.5	70
#6	40	10	-	-	-	-
#7	40	10	-	-	-	-
#8	600	100	-	-	-	-

Table 1: **Table with parameters for segments 1 - 5.** Segments 6-8 were not measured as a function of temperature. In the first column, the measurement length, L. In the second column, the electrode width, L_E (if two different electrode widths were present, separated by a comma). In the third column, is the conductance at room temperature, G_0. In the fourth column, the corresponding conductivity, σ_0, calculated with the indicated length (L) and the effective conductive area, A, which is based on 60 parallel fibers with a 26 nm diameter [44] In the fifth column, is the activation energy, U_A, obtained from fitting an Arrhenius law to $G(1/T)$ curves for $T > 100$ K and $V < 0.5$ V. In the last column, is the cross-over temperature is given, defined as the temperature at which the conductance is 20% higher than expected from the Arrhenius relationship, with U_A from the previous column.

4.6.6. BEHAVIOUR OF THE TWO-CHAIN HOPPING MODEL FOR DIFFERENT PARAMETER SETS

In the two-state model, there are $i = 1, \ldots, N_S$ states with an energy t above the Fermi energy and there are $i = 1, \ldots, N_S$ states an energy t below the Fermi energy (N_S is the number of hopping sites). When a bias voltage, V, is applied, we assume it is equally divided between all hopping sites, meaning an electron looses an energy $\Delta = eV/N_S$ per hop. The implied assumption is that the voltage does not drop at the electrode-wire interface ($\alpha = 0$ in Chapter 3, see 'field-driven transport'). As put forward in the main text, when only nearest-neighbour transport is taken into account, the electrical current is:

$$I = e\Gamma_R p_i(1 - p_{i+1}) - e\Gamma_L p_{i+1}(1 - p_i),$$

where the ratio between the forward and backward hopping rate is determined by the detailed balance relation [56, 100]:

$$\frac{\Gamma_R}{\Gamma_L} = \exp\left(\frac{\Delta}{k_B T}\right).$$

In the two-state situation, the two states are off resonant with energy $\pm t$. For an off-resonant hopping chain, the current can be estimated as (Chapter 3):

$$I = e(\Gamma_R - \Gamma_L) p_1 (1 - p_1)$$

where p_1 is determined by the Fermi-Dirac distribution:

$$p_1 = \frac{1}{1 + \exp\left(\frac{\pm t - \gamma V_G}{k_B T}\right)}.$$

For $\Delta \ll k_B T$, the approximation $\exp\left(\frac{\Delta}{k_B T}\right) \approx 1 + \frac{\Delta}{k_B T}$ and the sum of the current in the chains can be written as:

$$I = e\Gamma_R \frac{eV}{4 N_S k_B T}\left[\frac{1}{1 + \cosh(\frac{t - \gamma V_G}{k_B T})} + \frac{1}{1 + \cosh(\frac{-t - \gamma V_G}{k_B T})}\right].$$

Here, it is assumed that the current in both hopping states ($\pm t$) is independent, which means there are no transitions between the the two states. We do not take into account that electrons could go from the state at $+t$ to the state at $-t$ within the same hopping site (thermalisation). If we were to assume thermalisation faster than the hopping rate, we would obtain the same result for the current, because we would get the same p_i at every hopping site as now stated for p_1, with an equilibrium at the (local) Fermi energy (the dashed black line in Fig. 5). We also assume that when hopping to a nearest neighbour, the electron remains in the same electronic state but at a different position (from a $+t$-state at $i = 1$ to a $+t$-state at $i = 2$, for example). In Fig. S5, the behaviour of the gate response in the model is shown for a range of parameters.

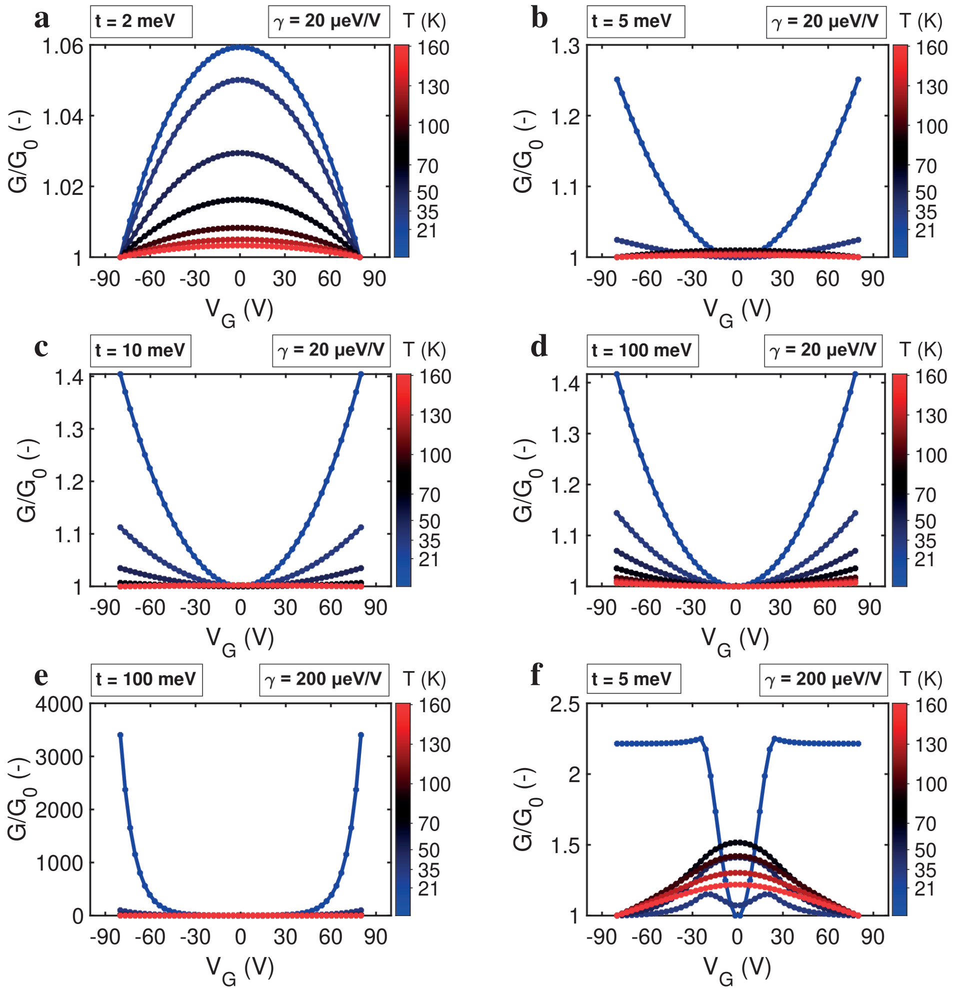

Figure S5: **Behaviour of the two-chain hopping model for different parameter sets.** Normalized conductance, G/G_0, plotted versus gate voltage, V_G, at multiple temperatures, T, given in the colour bar. Half the gap size, t, and the gate coupling, γ, are given in the plot. In panel (**a**), for a small gap size, the conductance is optimal near zero gate voltage, because the occupation probabilities of both chains were already high. In panels (**b**), (**c**), and (**d**), it can be seen that the gate response is always not sensitive to the gap size, but to the amount by which the gate shifts the energies, γV_G. In panels (**e**), and (**f**), saturation in the gate response occurs at lower gate voltage, V_G, for smaller gap size, $2t$.

4.6.7. BEHAVIOUR OF THE CONSTANT DENSITY OF STATES MODEL, WITH GAP, FOR DIFFERENT PARAMETER SETS.

In the many-state model, we assume that at each hopping site, there is a 'constant density of states', with a 0.4 meV level spacing, which is smaller than the experimental temperatures (4 K, $k_B T \approx 0.4$ meV), so the individual level is never visible in the gate response (as in Fig. S5). Besides the constant density of states, around zero, a gap energy,

U_g, was introduced, from which all states are removed. In this model, we assume that electrons more quickly thermalise between the different states at the same hopping site, i, than the hopping rate. At each site, i, there is a local potential at which the occupancy would be one-half (the dashed black line in Fig. 5b), which is the local equilibrium for the thermalisation process. Again, we assume that the hopping occurs via equivalent neighbouring electronic states (e.g., from the state at energy $+t$ and hopping site $i = 1$ to the state at energy $+t$ and hopping site $i = 2$). In this case, we can sum up contributions in a similar manner as before to obtain:

$$I = e\Gamma_\mathrm{R} \frac{eV}{4N_S k_\mathrm{B} T} \sum_j \frac{1}{1 + \cosh\left(\frac{\epsilon_j - \gamma V_\mathrm{G}}{k_\mathrm{B} T}\right)},$$

where ϵ_j is the electronic state energy at zero bias voltage and zero gate voltage. We do not include a bias voltage dependence of the occupation probabilities because we assume full field-driven transport ($\alpha = 0$, see 'Chapter 3'). That means that if there were to be a single hopping chain at $\epsilon = 0$, the occupation probabilities of all sites would be $p_i = 1/2$. In Fig. S6, the behaviour of the gate response in the model is shown for a range of parameters. A good match with the data of Fig. 3 is obtained for $U_\mathrm{g} = 0.5 - 2$ meV with $\gamma = 100$ μeV/V (Fig. S6a,b,c). For gap sizes smaller than 0.5 meV there is effectively no energy gap, because the thermal energy is greater than the gap size ($k_\mathrm{B}T(4\mathrm{K}) \approx 0.4$ meV) and so there is no gate effect. For higher gap size than a few meV, with the same coupling, the effect and its temperatures dependence becomes too large and no saturation will be visible (Fig. S6d). Upon increasing the gate coupling, the saturation is again visible, but the total effect is now too large (Fig. S6e). For a stronger gate coupling with 1 meV gap size, complete saturation would be reached earlier and the gate effect would be of the same magnitude as in the experiment (Fig. S6f). Thus, everything considered, $U_\mathrm{g} = 0.5 - 2$ meV with $\gamma = 100$ μeV/V is reasonable.

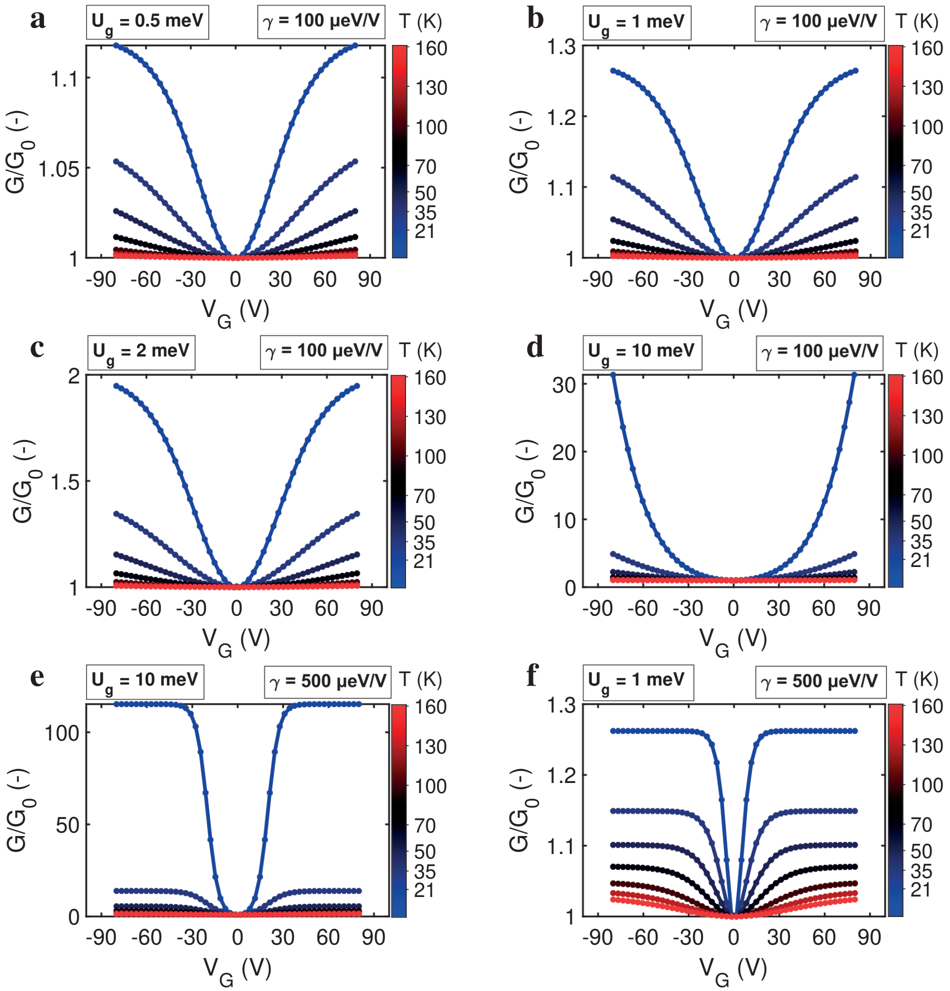

Figure S6: **Behaviour of the constant density of states model, with gap, for different parameter sets.** Normalized conductance, G/G_0, plotted versus gate voltage, V_G, at multiple temperatures, T, given in the colour bar. The gap size, U_g, and the gate coupling, γ, are given. The level spacing, inverse of the density of states, was 0.4 meV. In subfigures (**a**) to (**d**), only the gap size is increased. In subfigures (**e**) and (**f**), the coupling is higher than in the other subfigures, showing that the gate effect saturates at the same gate voltage, V_G, but the strength of the gate effect, G/G_0, differs greatly.

5

THE LOW-TEMPERATURE MAGNETO-RESISTANCE IN THE PROTEIN FIBERS OF CABLE BACTERIA

Jasper VAN DER VEEN, Silvia Hidalgo Martinez, Damian Bouwmeester, Filip J.R. Meysman and Herre S.J. van der Zant

ABSTRACT

Conductive protein fibers produced by bacteria form a novel class of electrical materials, but the mechanism of conduction in these biological wires remains poorly understood. Cable bacteria embed an extremely long type of these protein wires in their cell envelope, which they use to perform long-range electron transport over centimeter-scale distances. Previous work has shown that the conductivity of these fibers is high ($\geq$ 100 S cm^{-1}), has a low activation energy ($\sim$ 40 meV) and remains elevated at cryogenic temperatures. As such, the temperature dependence of the conductance resemble that of doped organic semiconducting nanowires. These latter materials display a magneto-resistance at low temperatures (< 10 K), which is attributed to wave function shrinkage. Here, we performed magneto-resistance measurements on the conductive fiber network in cable bacteria, which show a magneto-resistance of up to 50% at a temperature of $T = 1.8$ K and a magnetic field of $B = 8$ T. This magneto-resistance is compatible with a model based on wave function shrinkage. Crucially, this model implies that the distance

between hopping sites must be in excess of 10 nm. This distance is much higher than in other biological systems that exhibit electron transport.

5.1. INTRODUCTION

Conductive protein fibers form a class of promising materials at the interface between electronics and biology. Once their properties are properly understood and controlled, and if these properties prove to be sufficiently competitive, they could be integrated into novel type of green electronic devices [126]. Such bio-based electronic materials could be produced in a bioreactor, and being biodegradable, they would provide a promising prospect for reducing the problem of electronic waste [110]. Recently, it has been demonstrated that a variety of bacteria, including Shewanella [19, 20], Geobacter [29, 37, 127] and cable bacteria [2], naturally produce highly conductive protein fibers. However, the charge transport mechanism in these bio-wires remain elusive.

Conventionally, biological electron transport is depicted as a series of reduction-oxidation reactions, in which electrons are relayed between cofactors along a path through the protein structure. For example, in Shewanella nanowires, the interaction of multiheme cytochromes allows for electrons to be transported towards external solid electron acceptors [24]. In this process, hemes function as electron relay centres, in which a single iron centre changes its oxidation state from Fe(II) to Fe(III), as the electron transfers from one heme centre to the other [11]. This process of electron transfer is referred to as 'multi-step hopping'.

Cable bacteria stand out within the realm of bio-electricity, because the protein fibers that they produce are extremely long (> 1 cm) and highly conductive (> 100 S cm^{-1}). Moreover, cable bacteria do not appear to use iron-based cofactors (such as hemes or FeS clusters) like other electrogenic bacteria do. Spectroscopic evidence shows that there are no cytochromes or FeS clusters present in the conductive fibers of cable bacteria [44]. Instead, there appears to be Ni-containing cofactor present, whose molecular structure is yet unresolved [44]. Moreover, electric characterisation reveals markedly distinct properties. Measurement of the conductance as a function of temperature (Chapter 2), reveals an activation energy (~ 40 meV) that is ~ 5 times lower than for heme or FeS structures [48, 128, 129]. At low temperature, a transition from classical hopping to nuclear tunnelling is observed [91]. Moreover, if one fits a classical multi-step hopping model to the conductance data, one obtains the conclusion that distance between hopping sites must be in excess of 10 nm (Chapter 3). Together, these properties suggest that the conductance mechanism in cable bacteria is different from that in metal-reducing bacteria. Instead, the electrical properties resemble those seen in networks of graphene nanoribbons [62] and a variety of other organic semiconducting nanowires [57, 63, 130, 131].

In semiconducting nanowires made of polyacetylene or polyaniline, it has been shown that an external magnetic field can alter the electrical conductance, by a process that is known as wave function shrinkage [68, 132, 133]. In wave function shrinkage, the magnetic field reinforces the tendency of the electron to be spatially confined. In the most basic case, the electron is simply confined by the electrostatic attraction to a positive charged nucleus (hydrogen-like atom) [7]. In classical physics, when an electron is exposed to a uniform magnetic field (and neglecting electrostatic interactions), the electron will go into a cyclotron orbit, due to the Lorentz force. In quantum physics, if there is no confinement other than the magnetic one, only certain cyclotron radii are allowed, thus resulting in electronic states that are known as Landau levels. If both electrostatic and magnetic confinement are active, the electrostatic confinement is usually dominant, but a magnetic field can still alter the wave function. This process is termed the wave function shrinkage. When electron transport proceeds via a hopping mechanism, wave function shrinkage lowers the wave function overlap between neighbouring hopping sites, thus decreasing the hopping rate. This, in turn, gives rise to a magneto-resistance which should be proportional to the square of the magnetic field ($R \propto B^2$) [7]. This magneto-resistance effect has been demonstrated in a range of semiconducting materials, from networks of carbon nanotubes to nickel doped silicon [68, 132, 134–138]. Here, we examined whether such a magneto-resistance is also present in cable bacteria.

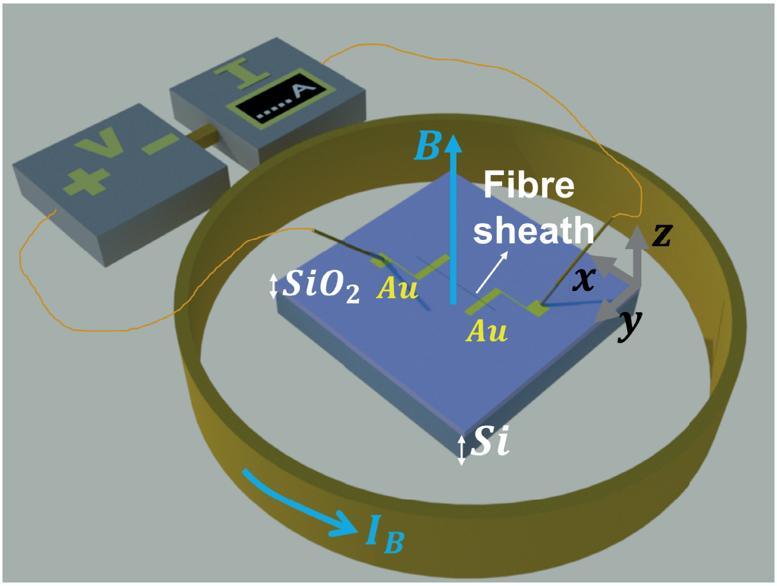

Figure 1: **Schematic representation of the experiment.** Gold patterned electrodes are created on top of a non-conductive SiO_2 substrate (light blue colour). A cable bacterium filament (fiber skeleton) is deposited in between the electrode contacts. A voltage bias, V, is applied across the electrodes using probe tips, and the current I through the fiber sheath is measured. A magnetic field, B, is created by applying an external current, I_B, to a superconducting electromagnet that encircles the setup. This surrounding magnet induces a magnetic field B, which is oriented in the vertical direction and attains positive values for an 'up' orientation of the field, minus for down.

5.2. RESULTS

To examine whether the conductance of cable bacteria depends on magnetic field, we deposited individual fiber skeletons onto a silicon/silicon-dioxide substrate with patterned gold electrodes (Fig. 1). Three separate segments were investigated with different conductive spacing (information is summarized in Table S2). We measured the current, I, as a function of applied bias voltage, V, for different temperatures T and range of magnetic fields B (from −8 T to 8 T and back again). The magneto-resistance effect is expressed as R/R_0, where the resistance $R = I/V$ with magnetization is compared to the reference value R_0 at zero magnetic field. The cryogenic measurement set-up allows a full temperature control between 300 K and 1.8 K.

The data for all segments at all temperatures is provided in Fig. S1. At a temperature of $T = 60$ K, the current-voltage characteristic $I(V)$s was found to be fairly linear (Fig. 2a)) and independent of the magnetic field (Fig. 2b). Accordingly, there was no magneto-resistance effect discernible.

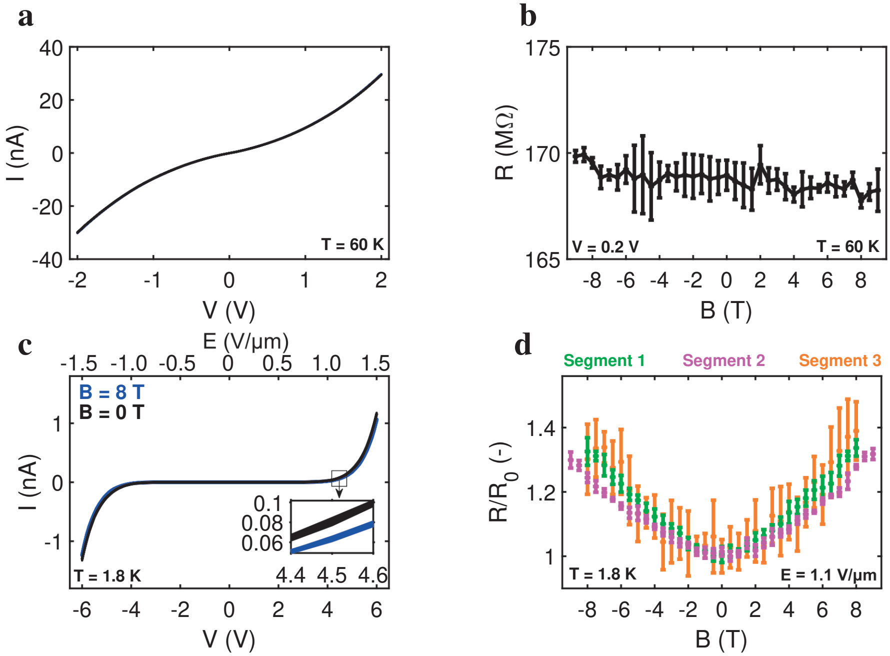

Figure 2: **Magneto-resistive effect in cable bacteria.** **a**, Current, I, versus the bias voltage, V, for segment 3, at a temperature $T = 60$ K. The $I(V)$ curve at $B = 8$ T (blue) and at $B = 0$ T (black), in the vertical z-direction (see Fig. 1). **b**, The resistance, R, versus magnetic field, B, determined at a bias voltage of $V = 0.2$ V, at temperature $T = 60$ K.**c**, Current, I, versus bias voltage, V, for no magnetic field ($B = 0$ T, black) and for high magnetic field ($B = 8$ T, blue). These $I(V)$-curves were taken at a temperature of $T = 1.8$ K. On the top axis, the bias voltage, V, is scaled by the measurement length ($L = 4$ μm), expressed as the electric field $E = V/L$. The inset shows the $I(V)$ in the region $V = 4.5 \pm 0.1$ V. The data are from segment 2. **d**, Resistance as a function of magnetic field, calculated as $R = I/V$, at an electric field of $E = 1.1$ V/μm. The resistance is normalized to the resistance at zero magnetic field, R_0. The temperature was $T = 1.8$ K. Each measured segment of cable bacteria has its own colour. For each magnetic field, several $I(V)$-curves were taken ($n = 4$). Using these curves, the average resistance and the standard deviation in the resistance are displayed.

When cooling down the sample close to absolute zero ($T = 1.8$ K), the current-voltage curve became more non-linear (Fig. 2c; see also 'Chapter 2'). When varying the magnetic field from $B = 0$ T to $B = 8$ T and comparing the current-voltage curves, $I(V)$, a magneto-resistance effect was noticeable that exceeds the current detection limit (inset Fig. 2c). This magneto-resistance effect was similar for all segments investigated when compared at the same value of the electric field, $E = V/L = 1.13$ V/μm (Fig. 2d). The magneto-resistance effect increased when the magnetic field increased, amounting to ∼ 30% at $B = 8$ T. For segment 2, the conductance was also determined at a lower electric field of $E = 0.75$ V/μm ($V = 3$ V), where the magneto-resistance at $B = 8$ T was 50% ($T = 1.8$ K). Furthermore, the curves were symmetric around $B = 0$, providing similar responses for positive and negative magnetic fields (Fig. 2d).

In the dilution fridge experiment, segment 1 was cooled down further to near absolute zero ($T \approx 100$ mK). During cooldown, the current decreased but eventually become constant below 2 K. The magneto-resistance increased to 76% at 100 mK (Fig. S1a).

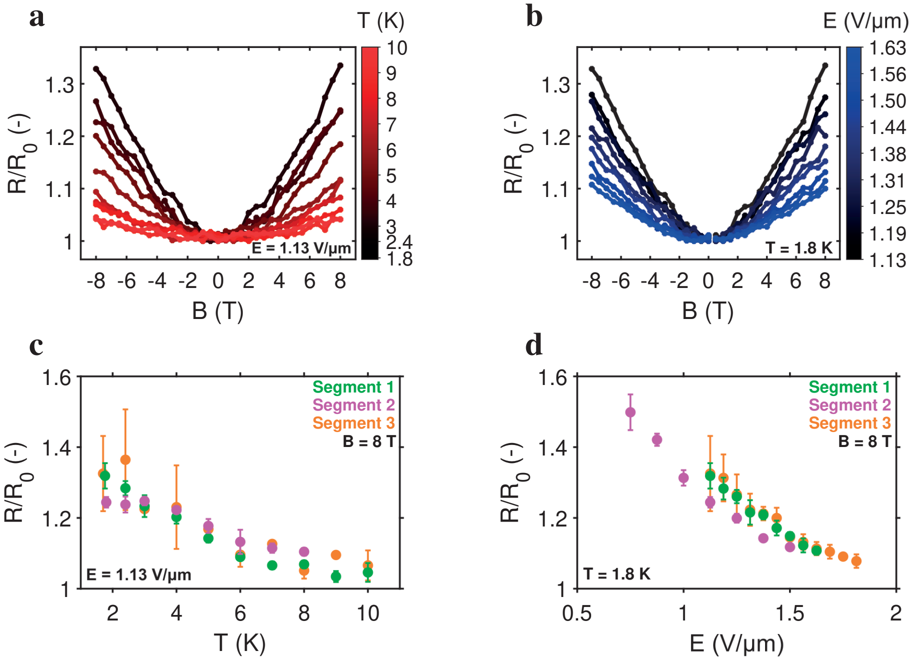

Figure 3: **Temperature and voltage dependence of the relative magneto-resistance.** **a**, Temperature dependence of the normalized resistance, R/R_0, calculated in the interval $V = 1.13 \pm 0.013$ V/μm, versus magnetic field, B (segment 1). The temperature is shown with a linear colour scale from black (1.8 K) to red (10 K), and each temperature value in the color bar represents a separate curve. **b**, Voltage bias dependence of the normalized resistance, R/R_0, measured at $T = 1.8$ K, versus magnetic field, B (segment 1). The voltage bias is shown with a linear colour scale from black (45 V) to red (65 V), and each voltage value in the colour bar represents a separate curve. **c**, Normalized resistance, R/R_0, versus temperature, T, shown at a high magnetic field ($B = 8$ T), for both segments measured (segment 1 is shown in (**a**) and (**b**)), determined at $E = 1.13$ V/μm. **d**, Normalized resistance, R/R_0, versus electric field, $E = V/L$ (bias voltage divided by the electrode separation) for both segments measured. The temperature was $T = 1.8$ K.

A magneto-resistance effect, $G(B)/G_0$, similar in size and shape to the effect in the z-direction, was found in the y-direction (the plane of the substrate, but perpendicular to the direction of the charge transport, Fig. S10a,b, y-direction in Fig. 1).

The magneto-resistance effect is both dependent on the temperature and the strength of the electrical field inside the cable bacterium wires (Fig. 3). When the temperature is step-wise increased from 1.8 K to 10 K, the magneto-resistance rapidly disappears. In segment 1, the effect dropped from 32% at $T = 1.8$ K to 4.2% at $T = 10$ K at the maximal value of $B = 8$ T (Fig. 3a). The other two segments showed a similar behaviour as a function of temperature (Fig. 3c), when compared at the same electrical field strength. The magneto-resistance also decreases when the electrical field increases. In segment 1, the R/R_0 dropped from 32% at $V = 1.13$ V/µm to 11% at $V = 1.63$ V/µm (Fig. 3b, Table S1). The shape of the magneto-resistance is symmetric for all measured temperatures and electric fields.

5.3. DISCUSSION

5.3.1. JOULE HEATING

When the bias voltage is increased, and more current is running through the filament, the magneto-resistance decreases (at a fixed temperature). A higher current through the filament could imply increased heat dissipation in the wire, so that the local temperature in the wire is higher than the mean temperature recorded in the setup. Therefore, it is worthwhile to question whether such Joule heating could play a role in the observed dependence of the magneto-resistance on the boas voltage.

To judge whether heat dissipation could raise the local wire temperature, we calculated the heat production $P = GV^2$ in all segments. In segment 1 ($L = 40$ µm), the dissipation level at 45 V and $T = 1.8$ K is $P \approx GV^2 \approx 7 \cdot 10^{-13} \cdot 45^2 \approx 1.4$ nW, while in segment 2 ($L = 4$ µm), the dissipation level at 4.5 V is $P \approx GV^2 \approx 2 \cdot 10^{-11} \cdot 4.5^2 \approx 0.4$ nW. In segment 3 ($L = 40$ µm), the heat dissipation is also $P \approx GV^2 \approx 2 \cdot 10^{-13} \cdot 45^2 \approx 0.4$ nW. The longer segments 1 and 3 have a lower heat production per unit length, so less local heating is expected, provided the heat transfer is radiative or occurs through conduction through the substrate (Table 1). If the heat transfer goes via the electrodes, more local heating is expected in the long segments, since their thermal resistance is higher. Nevertheless, the applied electric field has a similar effect on the magnetoresitance in all segments (Fig. 3d, Fig. S1 for all data). This indicates that Joule heating cannot play an important role.

Segment	L (µm)	P ($E = 1.13$ V/µm) (nW)	P/L (nW/ µm)
#1	40	1.4	0.03
#2	4	0.4	0.1
#3	40	0.4	0.01

Table 1: **Table with power dissipation values per segment**. In the first column, segment number. In the second column, segment length, L. In the third column, the total power dissipation in the fiber sheath, P, at $E = 1.13$ V/µm. In the fourth column, the power dissipation per unit length, P/L.

5.3.2. WAVE FUNCTION SHRINKAGE

In organic semiconducting nanowires with a similar low-temperature conduction behaviour as cable bacteria, such as doped polyacetylene and polyaniline, the wave function shrinkage model has been proposed to explain the magneto-resistance effect [68, 132, 133]. In this model, the magnetic field introduces an additional confinement next to the electrostatic force, thus reducing the charge carrier delocalisation (See appendix: 'wave function shrinkage model'). The more delocalised the charge carriers are, the greater is the relative effect of the magnetic field on the resistance [7]. Cable bacteria show a slightly stronger magnetic response than polyacetylene [132], suggesting that the charge carriers in the conductive fibers of cable bacteria are more extensively delocalized than in polyacetylene. On the other hand, when the magneto-resistance of our the fibers is compared to PANI (polyaniline) [132], the effect in cable bacteria is slightly weaker. This suggests that the characteristic length scale of transport in cable bacteria is quite similar to these organic conductive polymers, as is also seen from the temperature dependence of transport (Chapter 2).

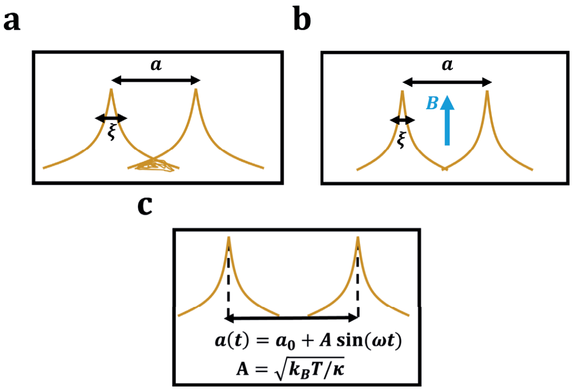

Figure 4: **Schematic representation of the wave function shrinkage model.** **a**, Two neighbouring hopping sites, with vertically in dark yellow the electron density, the wave function decay length, ξ and center-to-center distance, a. **b**, Same, but now with an external magnetic field in the vertical direction. The effective decay length is now smaller. **c**, The center-to-center distance, a, is fluctuating in time, t, with amplitude A, due to some vibrational mode with frequency ω and spring constant κ.

In the wave function shrinkage model proposed by Efros [7], an isolated hydrogen-like atom is analysed. Without the magnetic field, the wave function is spherically symmetric. When a magnetic field is imposed in the direction perpendicular to transport, the wave function is pulled towards the centre, decreasing the wave function overlap between neighbouring sites (Fig. 4a,b). The electron transfer rate between two sites is of the form:

$$\Gamma_R = \Gamma_0 \exp\left(-a/\xi\right), \tag{1}$$

where Γ_0 is an fixed pre-factor, ξ is the wave function decay length and a is the center-to-center distance between hopping sites. For magnetic lengths, $L_\mathrm{B} = (\frac{\hbar}{eB})^{1/2}$, larger than twice the wave function decay length, 2ξ (weak field regime), the magneto-resistance is [7]:

$$\frac{R}{R_0} = 1 + \frac{\xi a^3}{6}\left(\frac{eB}{\hbar}\right)^2 \tag{2}$$

Accordingly, a quadratic dependence of the magneto-resistance on the magnetic field is expected. Such a quadratic dependence is seen in the data (orange line in Fig. 5a). In this weak-field regime, the quadratic fit of the relative magneto-resistance directly gives the length scale: $(\xi a^3)^{1/4}$. This length scale, for all temperatures and applied electric fields for which the magneto-resistance was measured, gives $(\xi a^3)^{1/4} = 5 - 10$ nm (see Fig. S7). In a hopping model, the wave function overlap distance must of the same order or smaller than the hopping distance ($\xi \lesssim a$). This means the length, $(\xi a^3)^{1/4}$, is an approximate lower bound for the hopping distance. Accordingly, the distance between neighbouring sites must at least be $a \geq 5 - 10$ nm. This outcome supports the idea that electron transport in cable bacteria is delocalised. For example, if $\xi = 0.1a$, the number

$(\xi a^3)^{1/4} = 0.1^{1/4} a \approx 0.56a$, so $a \approx 1.8(\xi a^3)^{1/4}$ and the hopping length is than almost twice the derived length scale. For smaller ξ/a ratios the difference is even larger.

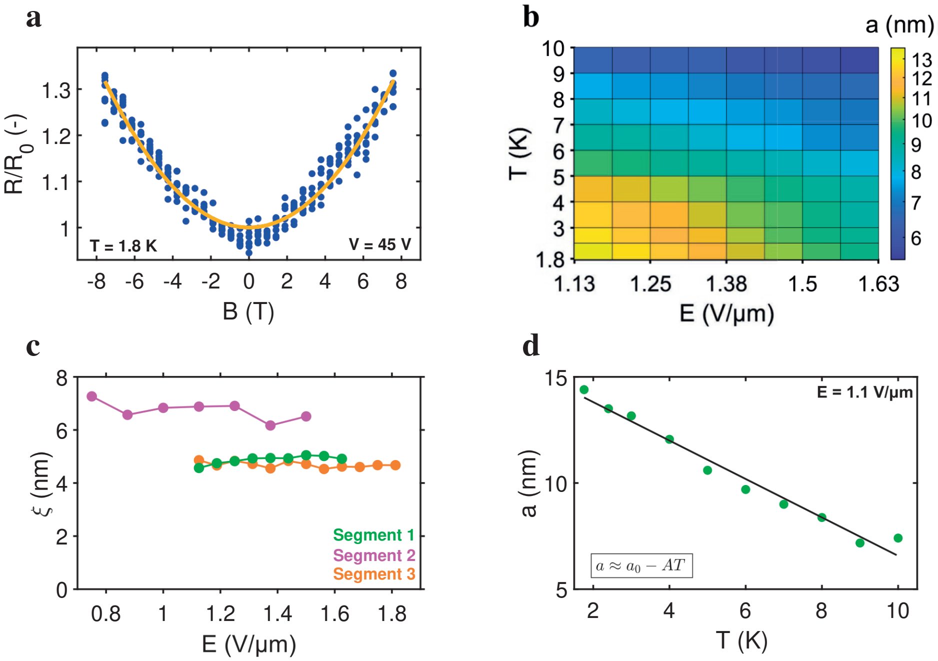

Figure 5: **Wave function shrinkage model.** **a**, Temperature dependence of the normalized resistance, R/R_0, calculated at $V = 45 \pm 0.6$ V, versus magnetic field, B (same segment as in Fig. 2), measured at $T = 1.8$ K. Each point represents a separate $I(V)$-curve. The dark yellow line is a quadratic fit to the resistance versus magnetic field data ($R/R_0 \propto B^2$). **b**, Colour map of the hopping distance, a, as deducted from the wave function shrinkage model. On the vertical axis temperature, T; on the horizontal axis the electric field, E. **c**, Decay length, ξ, as a function of electric field, E, for all segments. **d**, The hopping distance, a, at an electric field $E = 1.1$ V/μm, as a function of temperature (segment 1). The drawn black line is a fit to data with formula $a = a_0 - AT$, with $a_0 = 16$ nm and $A = 0.90$ nm/K.

With the additional assumption that, below $T = 10$ K, the temperature dependence of the hopping rate comes from the dynamics of the decay length, ξ, and the hopping distance, a, these lengths can be separated from the wave function shrinkage length scale, $d = (\xi a^3)^{1/4}$. We assume the pre-factor in the hopping rate Γ_R to be temperature independent (Eq. 1). The hopping rate in Chapter 2 had a different form, based on nuclear tunneling. To ensure compatibility between the two forms, it is required that vibrations involved in the reorganisation process, have already been frozen out ($k_B T < \hbar\omega_i$), which could be sensible given the very low temperature conditions ($T < 10$ K). In that case, a linear fit can be made per value of the electric field, E_i, as a function of temperature, T (Eq. 1 rewritten):

$$\ln(R(E_i, T)) = \ln(R_{\text{ref}}) + \frac{1}{\xi} a(E_i, T) \tag{3}$$

Here, R_{ref} is the fitted reference value of the resistance at zero hopping distance; this parameter is a consequence of that the used hopping rate, Eq. 1, is an approximation that it only depends on a and ξ. The fit can also be done in terms of the wave function shrinkage parameter, $d = (\xi a^3)^{1/4}$ (Fig. S7):

$$\ln(R(E_i,T)) = \ln(R_{\text{ref}}) + \frac{a^{1/4}}{\xi^{5/4}} d(E_i,T) = \ln(R_{\text{ref}}) + \frac{d(E_i,T)}{s}. \tag{4}$$

The parameter, $s = \frac{\xi^{5/4}}{a^{1/4}}$, is determined from the linear fit (Fig. S8), which gives the decay length and consequently the hopping length, through the relations $\xi = (ds^3)^{1/4}$ and $a = d^{4/3}/\xi^{1/3}$. The hopping distance is in the range, $a = 6-14$ nm, in all segments (Fig. 5b for segment 2, Fig. S9 for the other segments). It decreases for higher temperatures and electric fields (Fig. 5b,d). The decay length is approximately constant: $\xi \approx 5$ nm for the 40 µm sample and $\xi \approx 7$ nm for the 4 µm sample (Fig. 5c, shown for $T = 1.8$ K). The decrease for higher temperatures could be explained by vibrational modes (section 'Temperature dependence magneto-resistance'). For the electric field dependence we do no proposition here, and we would like to stress that there more potential ways to could describe the magnetic behaviour, such as a weak anti-localisation effect [139] or a energy splitting of electronic levels by the magnetic field.

With the decay length estimated from the experiment, it is now possible to test the weak-field assumption. When the magnetic length, L_B, is lower than 2ξ, the behaviour tends more to the strong-field regime [7], in which the magneto-resistance is linear ($R/R_0 \propto B$). The magnetic length is $L_\text{B} = (18,13,8)$ nm at $B = 2,4,8$ T and twice the decay length is $2\xi = (10,14,10)$ nm in the three segments, so at $B \sim 4$ T the magnetic length, L_B, and twice the decay length, 2ξ, are comparably large. Indeed, at higher magnetic fields ($B \gtrsim 4$ T), the magneto-resistance looks linear (Fig. 5a), so that at high magnetic fields the weak-field assumption is no longer valid. Furthermore, as expected, when R/R_0 is plotted vs B^2, it is visible that the curve is sub-parabolic (Fig. S6), which was also the case in magneto-resistance measurements in polyaniline nanowires [140]. Importantly, when applying the strong-field expression to the data, the conclusion that the hopping distance is ~ 10 nm remains intact (Fig. S5, see section 'Weak and strong-field limit' in 'Appendix: Wave function shrinkage model').

5.3.3. TEMPERATURE DEPENDENCE MAGNETO-RESISTANCE

Looking at a particular electric field along the temperature axis, we see the following behaviour in the hopping distance, a. It starts of at a base value, a_0, and decreases with temperature (Fig. 5d). As a simple, conceptual model, we propose a scenario where hopping centers periodically move closer to each other due to some slow, thermally activated vibrational mode (Fig. 4c). This makes the center-to-center distance fluctuate as $a = a_0 + A\sin(\omega t)$, with ω the angular frequency of the vibrational mode and t is the time. At some moments, the distances is smaller or larger than the equilibrium distance. This effectively increases the time-averaged hopping rate. Assuming tunneling through a rectangular barrier, the net effect is that the effective distance is reduced as [141]:

$$a = a_0 - \frac{2\sqrt{2m_e W} k_B T}{\hbar\kappa}, \tag{5}$$

where W is the energetic height of the tunneling barrier, m_e is the mass of the electron, and κ is the spring constant of the vibrational mode. The effective center-to-center distance as a function of temperature approximately decreases linearly as predicted by this equation ($a = a_0 - AT$; (Fig. 5d). This behaviour also persists to the smallest of temperatures ($T = 100$ mK, Fig. S11). Based on how quickly the hopping distance falls with temperature, we find: $A \approx 0.9$ nm/K (Table S2). The parameter A is related to the effective spring constant ($A = \frac{2\sqrt{2m_e W}k_B}{\hbar\kappa}$), which can be estimated by assuming that $W \sim 10$ eV (typical order of magnitude for atomic ground states and work functions), we can estimate the spring constant: $\kappa \approx 1$ pN/nm (values per segment listed in Table S2). This could be a sensible order of magnitude for a protein-based conductor, because nanometer displacements by piconewton forces are typical for protein-protein interactions, as experimentally observed in optical tweezer experiments, for example with actin and myosin [142]. To estimate whether the vibrational mode is thermally activated at low temperature ($\hbar\omega < k_B T$), we can estimate the frequency of motion, ω. For this, the effective mass of the vibration, m, is needed. In our conceptual model, we can assume that the vibrational mode moves a molecular structure with ~ 100 carbon atoms, which in one direction would stretch out to ~ 10 nm (bond length of ~ 0.1 nm), so the carbon atoms would have a effective mass of 1200 a.u. (neglecting hydrogen and possibility of other elements like nitrogen and oxygen, which have a similar mass). This gives a vibrational frequency $\hbar\omega \approx \hbar\sqrt{\frac{\kappa}{m}} \approx 10$ µeV, which only freeze out at $T \approx \hbar\omega/k_B \approx 0.1$ K. So, it could be a sensible proposition that the motion is still thermally activated in all measurements.

5.3.4. INTERPRETATION OF THE HOPPING LENGTH

The hopping distance results here (Fig. 5b), match the order of magnitude of those found through the temperature dependence and universal scaling curves (see Chapter 2). For segment 2, the universal scaling curve indicated that there are $N_S = 120$ hopping sites in $L = 4$ μm, so there is $a_{U.S.C} = L/N_S = 33$ nm of length available for each hopping site. From the wave function shrinkage model we find $a = 5-10$ nm. Given the many assumptions in the models, this is a good match. However, the modelling could be much improved. The idea of extended one-dimensional states presented in Chapter 2, with stretched wave functions in the direction of transport, is at odds with the model here, with an spherically symmetric electronic state in absence of magnetic field (Fig. 4a). Note, that the distances deducted from the universal scaling curve, $a_{U.S.C}$ and from the magneto-resistance, a, are different in origin, because the inferred the universal scaling curve looks at the number of energy dissipation (voltage division) events, while the magnetic effect is about how the magnetic field changes the wave function shape. Once structural inquiries reveals the molecular structures in the conductive protein fibers, the nano-scale features of electron transport could be modelled in detail.

5.4. CONCLUDING REMARKS

The magneto-resistance experiments confirm the length scale of transport already inferred from the temperature dependence measurements. The ~ 10 nm length scale is much larger than that in multi-step hopping in cytochromes (≤ 1 nm). The magneto-resistance measurements presented in this chapter form a second, independent line of evidence that electron transport in cable bacteria is more delocalised than in cytochromes, which is believed to be key for its higher conductivity.

5.5. METHODS

CABLE BACTERIA CULTIVATION

Natural marine sediment was collected from the creek bed in a salt marsh (51.4391°N, 4.1697°E; Rattekaai, the Netherlands) and used for enrichment incubations (procedure as described in [83]). Thick cable bacteria (ca. 4 μm diameter) developed within four weeks and were identified as Candidatus Electrothrix gigas based on size and morphology [42]. Cable bacterium filaments were harvested from the enrichment incubation and manipulated under a stereo-microscope with custom-made, small glass hooks. Individual filaments were washed repeatedly with MilliQ to remove sediment particles and salts. The resulting samples are referred to as “native cable bacteria”. In a subsequent step, the conductive fiber network was isolated from native cable bacterium filaments through a chemical extraction procedure that removes the membranes and the cytoplasmic cell content (procedure as described in [41]). After extraction, a so-called “fiber skeleton” is retained, in which the conductive fibers are embedded onto a carbohydrate sheath [41]. Notably, the fiber skeletons remain equally conductive as native cable bacteria, indicating that the extraction procedure does not affect the fiber structure [2].

FABRICATION

For fabrication of the electrode-patterned silicon substrate, see Chapter 2 and/or Chapter 4.

MAGNETIC SET-UPS

For the measurements in this paper, two different set-ups were used. Segments 1 and 3 were measured in a vessel with liquid helium (T = 4.2 K), in which a long cylindrical stick can be inserted. Inside the stick, there is a sample chamber which is pumped to vacuum conditions. Additional cooling power is achieved by pumping a tiny amount of liquid helium through a needle valve, which results in helium in the gas phase at a lower pressure and temperature than that of liquid helium. With this helium, the sample temperature can be cooled down to approximately T = 1.8 K. With a heater placed nearby the sample, the temperature can be controlled. Around the sample, there is a superconducting magnetic coil, with which magnetic fields of B = 9 T can be applied perpendicular to the substrate. The direction of the magnetic is fixed in the vertical direction, but can be changed from ’up’ to ’down’ by reversing the direction of the current through the coil. The set-up in which segment 2 was measured is the AttoDRY2100, which is a closed-cycle cyrostat (no liquid helium), which has a temperature range from T = 1.65 K to T = 300 K and magnetic control from -9 T to + 9 T. Additional measurements on segment 1 were done in a He-3/He-4 dilution refrigerator, which can reach temperatures down to 100 mK. In the dilution refrigerator there is a vector magnet with a magnetic field of B = 1 T, 3 T, and 8 T available in the x,y and z directions, where x is the direction of transport, y the in-plane perpendicular direction and z the vertical direction.

CURRENT-VOLTAGE CHARACTERISTICS

The magnetic field is swept from $B = -8$ T to $B = 8$ T and back again, in steps of $B = 0.5$ T. At each magnetic field, four current-voltage curves ($I(V)$) are taken. This means that in total there are eight $I(V)$s per magnetic field. The current at a particular voltage mentioned in the text, is calculated by averaging over all data points is a small interval. In the case of segment 1 and segment 3, all current points within ±0.5 V of the mentioned bias voltage, V, are used to calculate the resistance, $R = V/I$. In the case of segment 2, all points within ±0.1 V are used. The data points and error bars seen in the $R(B)/R_0$, refer to the average and standard deviation in the result over four $I(V)$'s. For calculating the resistance, for segment 1 and 3 data points with a current of below 5 pA were not analysed. This was approximately the offset in the $I(V)$, which was positive for one voltage sweep direction and negative for other. For segment 2, data points of below 0.5 pA were not analysed. This was roughly the detection limit in this case.

5.6. APPENDIX

5.6.1. RELATIVE MAGNETO-RESISTANCE FOR THE ENTIRE DATASET

This section of the appendix is dedicated to providing all magneto-resistive measurements that were used in this chapter, shown at bias voltages at which the current was above the detection limit. Data were taken at different temperatures which are indicated in the figures.

Segment 1

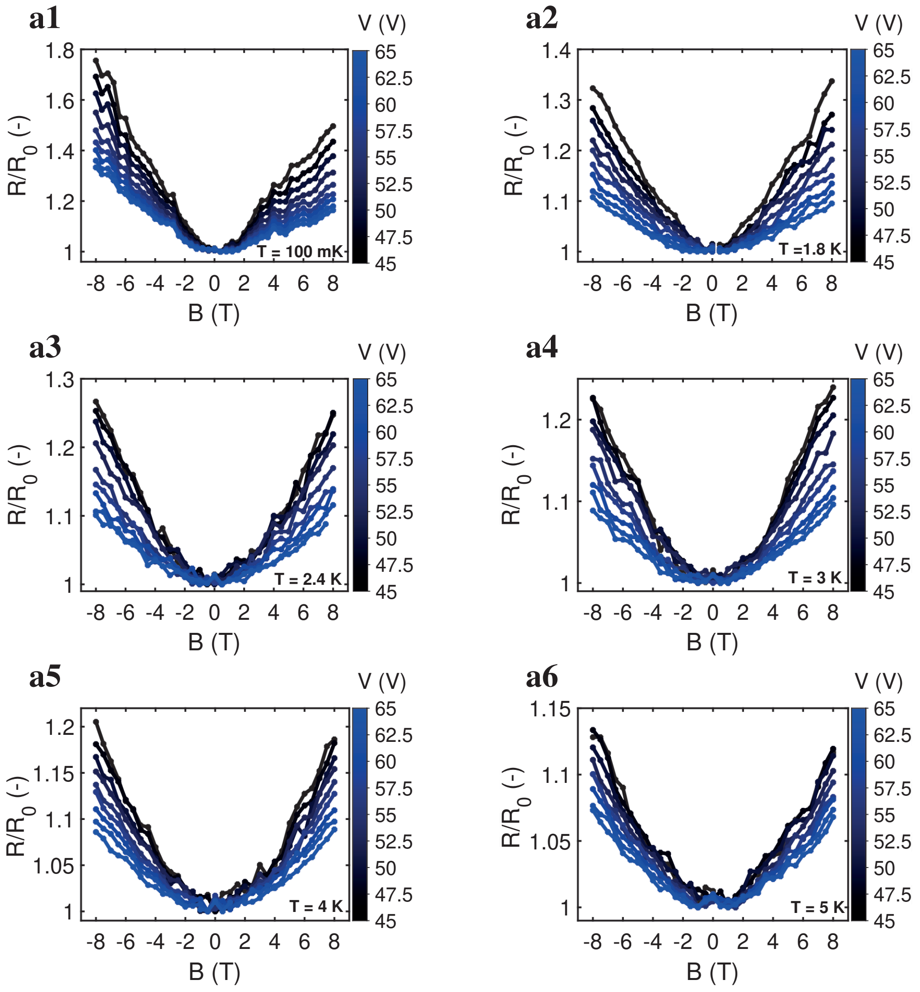

a7

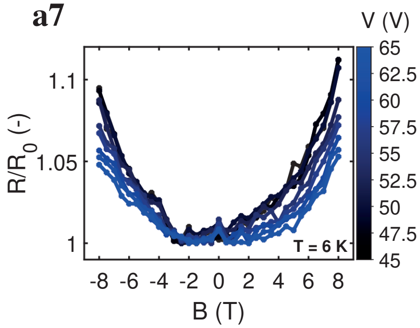

a8

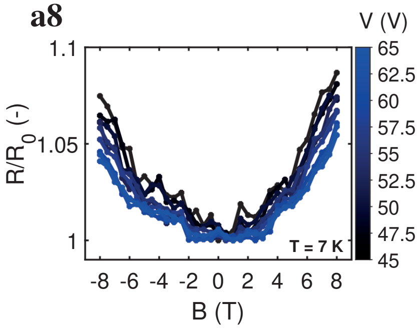

a9

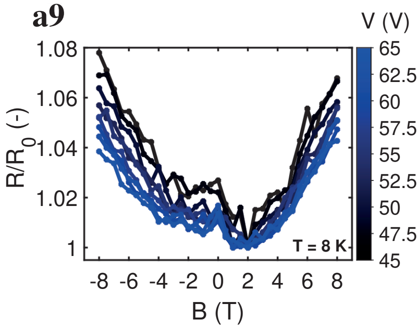

a10

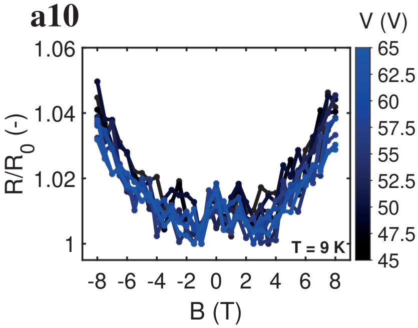

a11

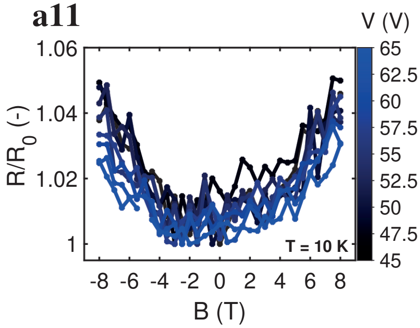

Segment 2

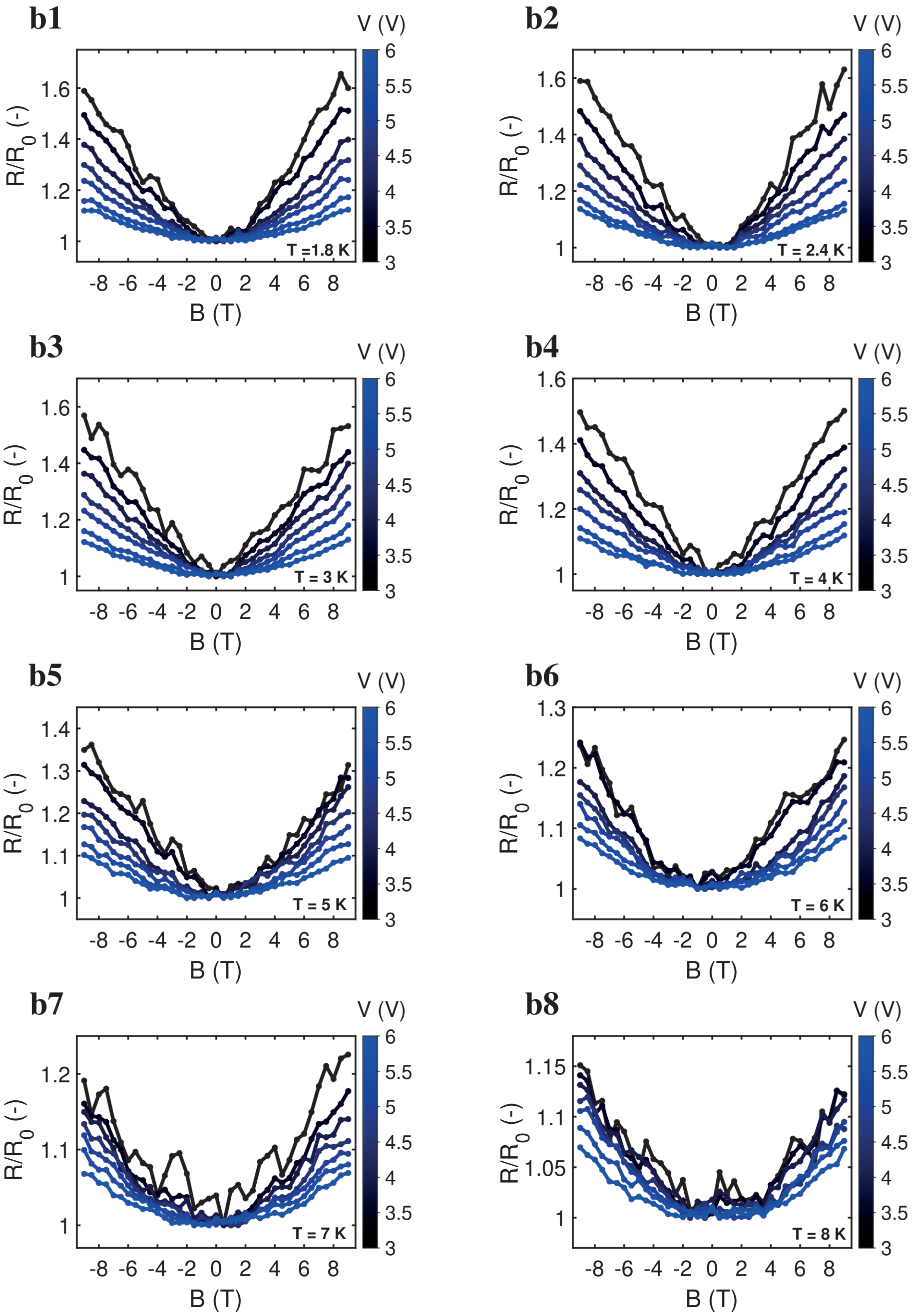
b1
V (V)
R/R0 (-)
1.6
1.4
1.2
1
-8 -6 -4 -2 0 2 4 6 8
B (T)
T =1.8 K
6
5.5
5
4.5
4
3.5
3
b2
V (V)
R/R0 (-)
1.6
1.4
1.2
1
-8 -6 -4 -2 0 2 4 6 8
B (T)
T = 2.4 K
b3
V (V)
R/R0 (-)
1.6
1.4
1.2
1
B (T)
T = 3 K
b4
V (V)
R/R0 (-)
1.6
1.4
1.2
1
B (T)
T = 4 K
b5
V (V)
R/R0 (-)
1.4
1.3
1.2
1.1
1
B (T)
T = 5 K
b6
V (V)
R/R0 (-)
1.3
1.2
1.1
1
B (T)
T = 6 K
b7
V (V)
R/R0 (-)
1.2
1.1
1
B (T)
T = 7 K
b8
V (V)
R/R0 (-)
1.15
1.1
1.05
1
B (T)
T = 8 K

Segment 3

c1

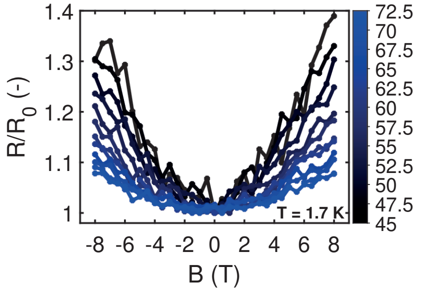

c2

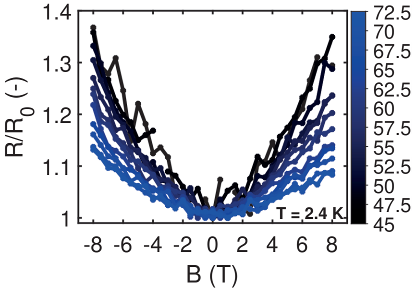

c3

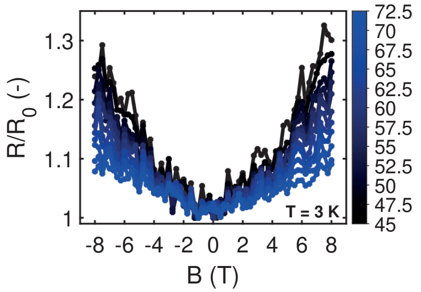

c4

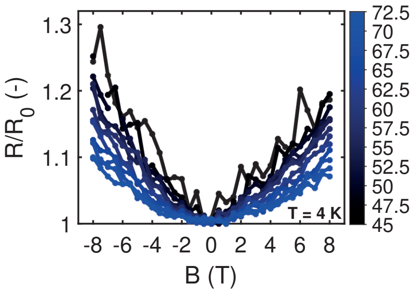

c6

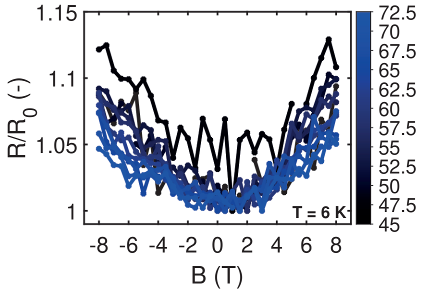

c7

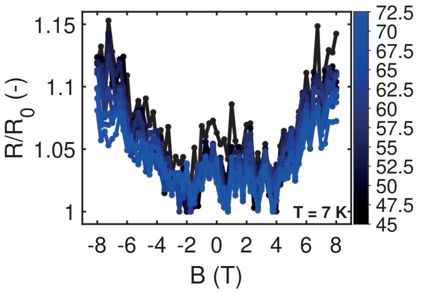

c8

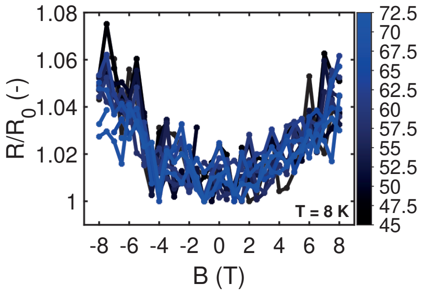

c9

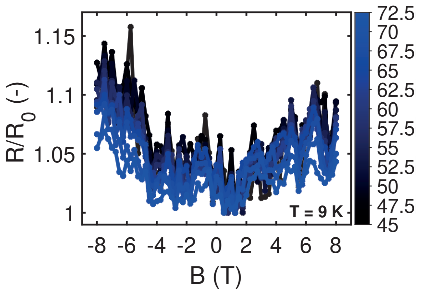

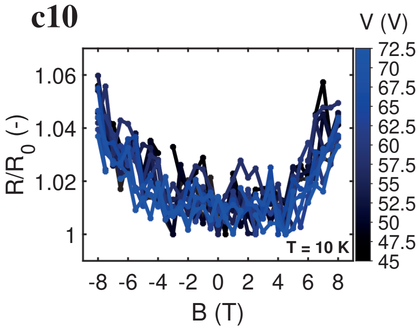

Figure S1: **Relative magneto-resistance for the entire dataset**. For the three segments and at all measured temperatures, the normalized resistance, R/R_0, versus magnetic field, B, is displayed. The letters **a.b** and c correspond to the segments 1,2 and 3, respectively.. In each subfigure, the magneto-resistance is shown at multiple applied bias voltages. Each bias voltage has its own colour, scaling linearly from black (45 V) to red (65 V), and each voltage value in the colour bar represents a separate curve. Note, that for segment 1, a dilution fridge measurement (T = 100 mK), is included.

5.6.2. TEMPERATURE DEPENDENT MEASUREMENTS

This appendix section is dedicated to showing that the measured segments showed the same characteristic temperature dependence as described in Chapter 2.

TEMPERATURE DEPENDENCE OF INVESTIGATED SEGMENTS.

Segment 1

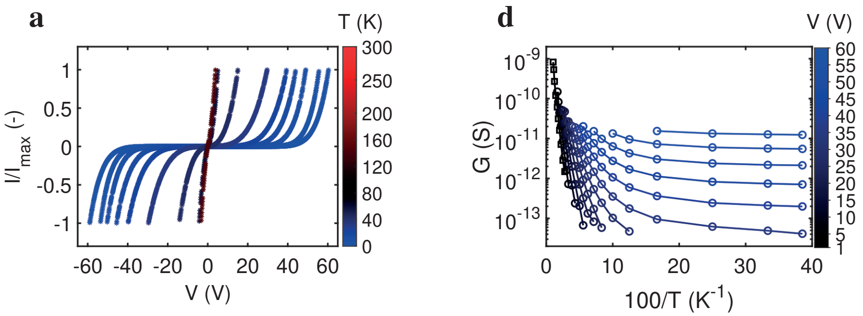

Segment 2

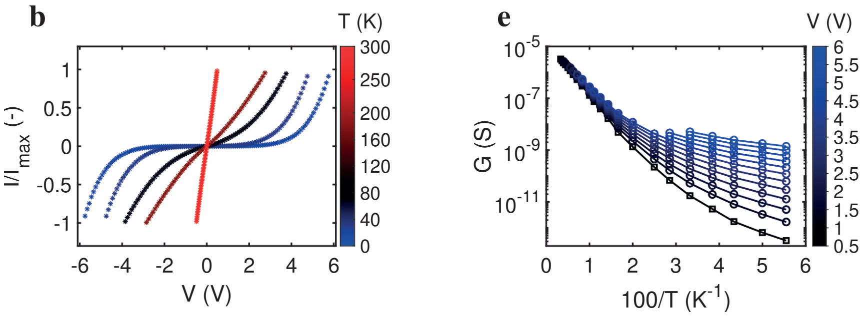

Segment 3

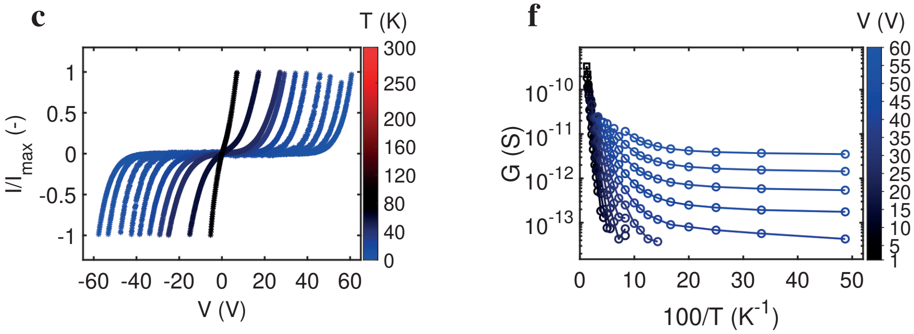

Figure S2: **Temperature dependence of investigated segments.** **a-c** Current-voltage ($I(V)$) characteristics recorded at different temperatures. To illustrate the change in shape of the $I(V)$ curve, the current is normalized to the maximum current obtained for each $I(V)$ trace. The color of the lines indicates the temperature, linearly changing from red to black in the range $100-80$ K and from black to blue in the range $80-4$ K, as shown in the colour bars next to the plots. **d-f** The data is plotted as $G = I/V$, as a function the inverse temperature, $100/T$, for different bias voltages, V. The colour scale linearly ranges from black (zero bias voltage) to blue (maximum bias voltage). The values in the colour bars next to the plot correspond to the lines plotted in the graph.

UNIVERSAL SCALING BEHAVIOR AS A FUNCTION OF TEMPERATURE

This appendix section is dedicated to the universal scaling behaviour of the three segments investigated.

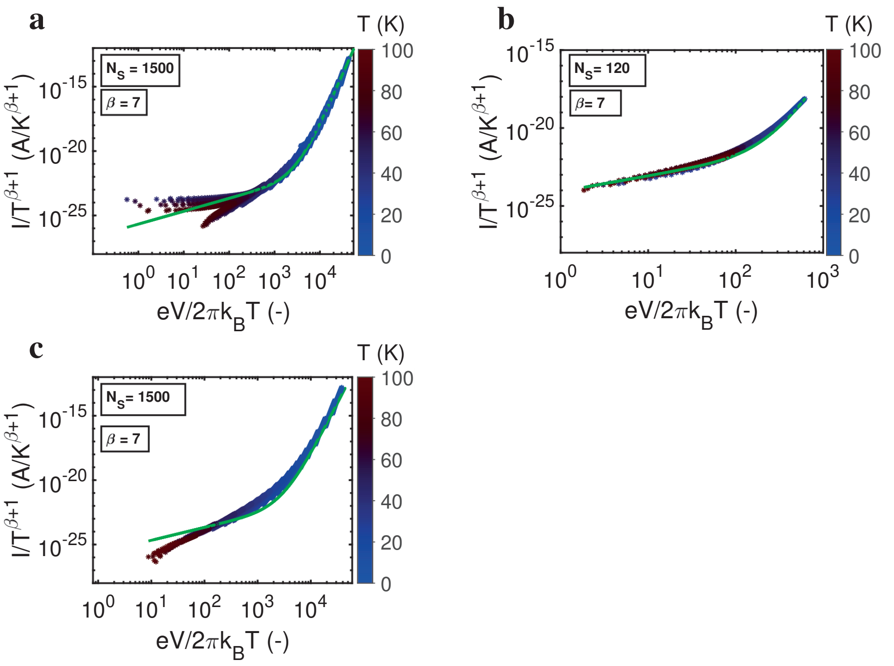

Figure S3: **Universal scaling behavior as a function of temperature.** Universal scaling curves for all three segments constructed using the current-voltage curves in the temperature interval $T = [4, 100]$ K. On the vertical axis the current $I/T^{\beta+1}$, and on the horizontal axis the bias voltage scaled with temperature, $eV/(2\pi k_B T)$. The green solid line gives a fit of the universal scaling relation to the data. The power law exponent β is visually calibrated to make the data fall onto the same curve the most (precision ±0.5) and is given in the inset. The transition from the low-bias, high-temperature regime to the high-bias, low-temperature regime occurs at a bias $eV \approx 2\pi N_S k_B T$. This transition point gives the parameter N_S (given in the insets), defined as the number of hopping sites.

5.6.3. COLOUR MAPS OF THE MAGNETO-RESISTIVE EFFECT IN TWO SEGMENTS

In this section, the relative magneto-resistance, R/R_0, is plotted for all electric fields, E, and temperatures, T, at which the magneto-resistance was determined.

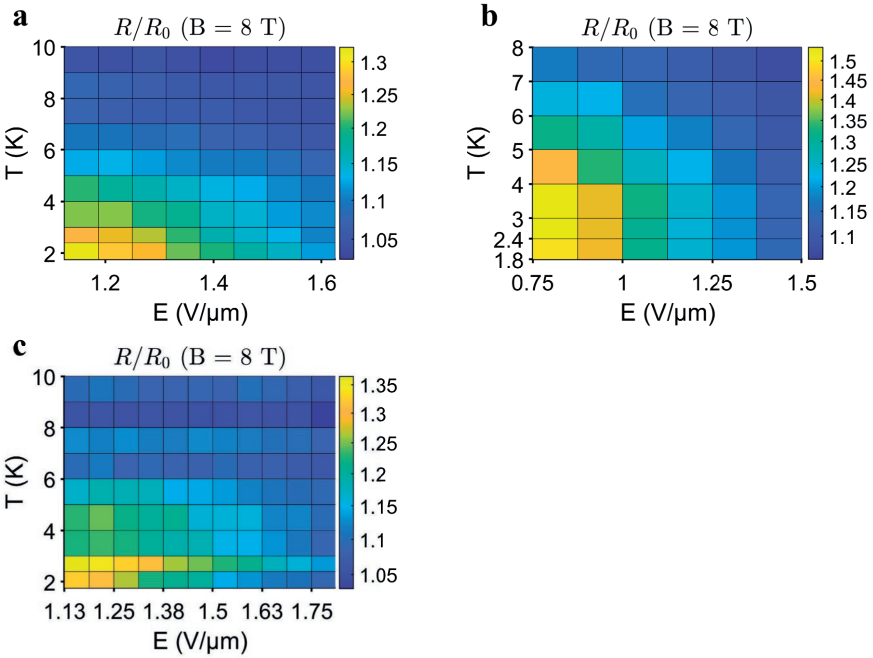

Figure S4: **Colour maps of the magneto-resistive effect for the three segments.** **a-c** correspond to the segments 1,2 and 3, respectively. The data plotted in Fig. S1 can be used to construct a colour map, with on the vertical axis the temperature, T. Each rectangle is coloured by the average of the four data points at its corners. On the horizontal axis, the electric field, E (voltage divided by segment length, see Table S2). The colour indicates the strength of the relative magneto-resistance, R/R_0 at high magnetic field ($B = 8$ T).

5.6.4. WAVE FUNCTION SHRINKAGE MODEL

The wave function shrinkage model used here, is laid out in 'Electronic Properties of Doped Semiconductors' by Shklovskii and Efros [7] in the chapter 'Hopping Conduction in a Magnetic Field'. A hydrogen-like atom is considered in a cylinderical coordinate system ($\mathbf{r} = \rho, \phi, z$), for which the Schrodinger equation is written as:

$$-\frac{\hbar^2}{2m_e}\left[\frac{1}{\rho}\frac{\delta}{\delta\rho}\left[\rho\frac{\delta\psi}{\delta\rho}\right]+\frac{\delta^2\psi}{\delta z^2}\right]+\frac{\hbar^2\rho^2}{8m_e\text{Ł}_{\mathrm{B}}^4}\psi-\frac{e^2}{4\pi\epsilon\mathbf{r}}\psi=E\psi, \tag{S1}$$

where m_e is the electron mass, $L_{\mathrm{B}} = (\frac{\hbar}{eB})^{1/2}$ is the magnetic length, ϵ is the electrical permittivity, $\mathbf{r}$ is the position vector of the electron with respect to the nucleus, ψ is the electron wave function and E are the energy levels (eigenvalues) of the solution to the Schrödinger equation. The penultimate and last term on the left hand side of the equation are the magnetic and electrostatic confinement terms.

WEAK- AND STRONG-FIELD LIMIT

In the weak field regime, where the magnetic length, L_{B}, is larger than twice the decay length, 2ξ, and the resistance has the dependence [7]:

$$R \propto \exp\left[\frac{|\mathbf{r}_{ij}|}{\xi}+\frac{(x_{ij}^2+y_{ij}^2)\xi|\mathbf{r}_{ij}|}{6L_{\mathrm{B}}^4}\right], \tag{S2}$$

where $|\mathbf{r}_{ij}|$ is the magnitude of the position vector from site i to site j. Assuming that all hopping sites are aligned on the x-axis, the expression simplifies to ($|\mathbf{r}_{ij}| = x_{ij} = a$, $y_{ij} = 0$):

$$R \propto \exp\left[\frac{a}{\xi}+\frac{a^3\xi}{6L_{\mathrm{B}}^4}\right]=\exp\left[\frac{a}{\xi}+\frac{a^3\xi}{6}\frac{eB^2}{\hbar^2}\right]\approx\exp\left(\frac{a}{\xi}\right)\left[1+\frac{a^3\xi}{6}\frac{eB^2}{\hbar^2}\right] \tag{S3}$$

In the whole data set the quantity $\frac{a^3\xi}{6}\frac{eB^2}{\hbar^2} \ll 1$, so that the linearization of the exponent can be done. Equation S3 only holds in the weak-field regime. The first requirement for this limit is that $2\xi \ll L_{\mathrm{B}}$. For $B = (2,4,8)$ T the magnetic length is $L_{\mathrm{B}} = (18,13,9)$ nm. Because the derived values for twice the decay length are $2\xi \approx 10-14$ nm (Fig. 5c, determined by Eq.4), for high magnetic fields ($B \gtrsim 4$ T), the measurement is not in the weak-field regime. The second requirement for the weak-field regime is that the hopping distance, a, should be much smaller than $\frac{L_{\mathrm{B}}^2}{2\xi}$. With the weak-field fitted values for the decay length, ξ, the ratio of interest can be evaluated (Fig. S5a; $B = 4$ T). It can be seen that for low electric field and low temperature, we reach ratios of more than unity. In this range, the measurement is not 'weak-field' at $B = 4$ T, more due to this second requirement. In any way, for the lowest temperature data and for fields above $B = 4$ T, the strong-field limit is the most appropriate, which gives [7]:

$$R \propto \exp\left[\frac{a^2}{2\lambda^2}\right]=\exp\left[a^2\frac{eB}{2\hbar}\right]\approx 1+a^2\frac{eB}{2\hbar}. \tag{S4}$$

It has been checked that the quantity $a^2\frac{eB}{2\hbar} \ll 1$, such that the linearization can be done (Table S1 for the values, β, in $R/R_0 = 1+\beta B^2$). For segment 2, the linear fit at lowest magnetic field and temperature are plotted in Fig. S5b, as well as the outcomes for the hopping distance, a (Fig. S5c). The conclusion that the hopping distance is $\sim 5-10$ nm (much larger than in multi-heme cytochromes), remains intact when the strong-field scenario is analysed.

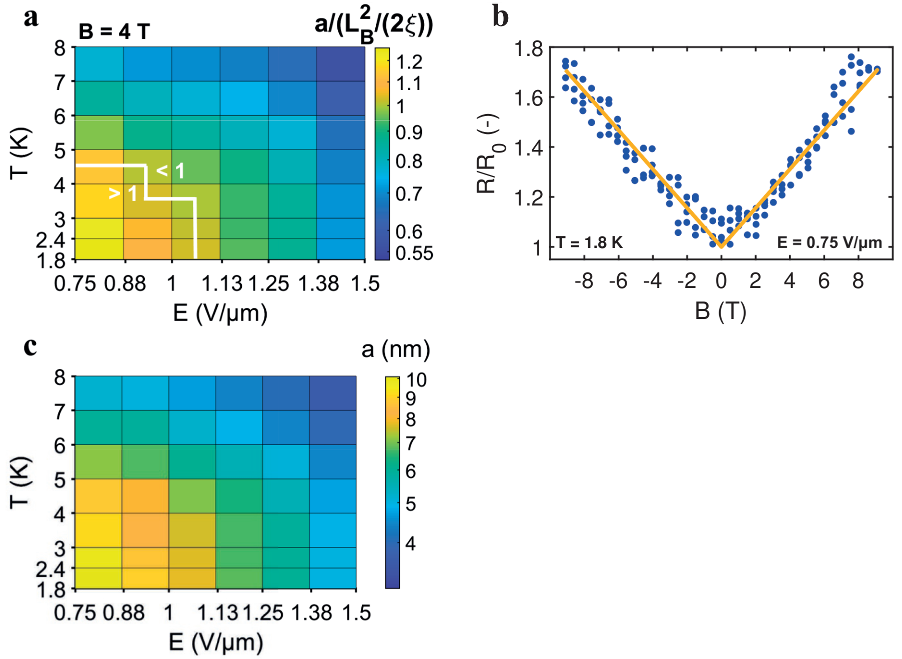

Figure S5: **Strong-field limit fit of wave function shrinkage.** **a** Test of the weak-field limit, by plotting the ratio between a and $\frac{L_B^2}{2\xi}$, as a function of temperature, T, and electric field, $E = V/L$, for segment 2 ($B = 4$ T). **b**, Relative magneto-resistance, R/R_0, versus magnetic field, B, on the data of segment 2, at the lowest temperature ($T = 1.8$ K) and lowest electric field ($E = 0.75$ V/μm). Each point represent a different current-voltage characteristic, $I(V)$. A linear fit through the data is plotted in dark yellow. **c**, For the same segment, Strong-field hopping distance, a, plotted versus temperature, T, and electric field, E. The strong-field hopping distance, a, is indicated by the colour bar to right and is determined from the linear fit and Eq. S4.

Given the fact that the measurement is in between the weak and strong-field limits, it should not be surprising that both the quadratic fit in the main text (Fig. 5a) and the linear fit here (Fig. S5) essentially capture the data. When plotting the magneto-resistance on the $B-$squared scale, it is clear that the data is sub-parabolic (Fig. S6). This was also the case in magneto-resistance measurements in polyaniline nanowires [140].

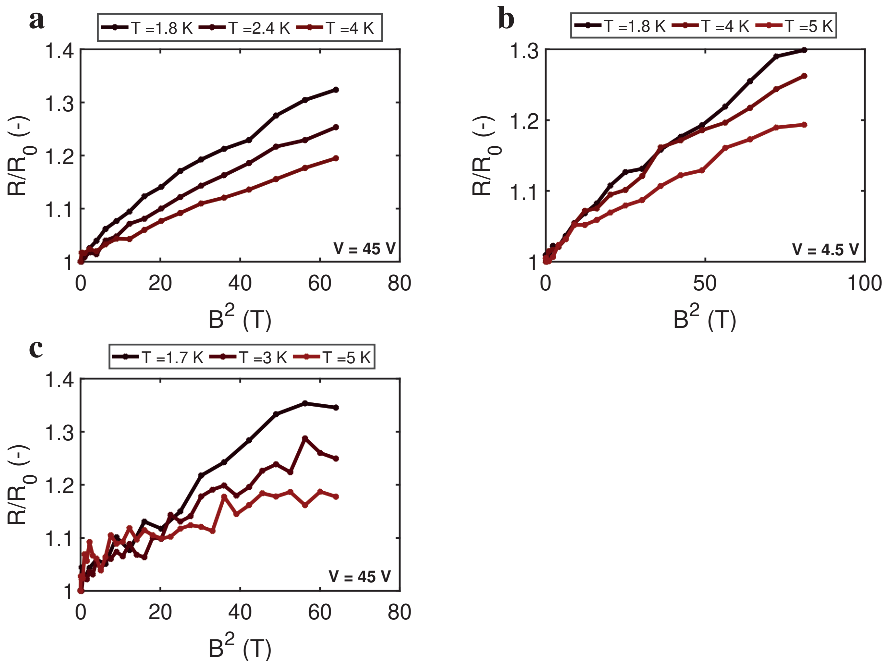

Figure S6: **Magneto-resistance as a function of B^2. a-c** correspond to the segments 1,2 and 3, respectively. The relative magneto-resistance, R/R_0, is plotted at three different temperatures, T, which are coloured from black to red on a linear scale between 0 K and 10 K. If the magneto-resistance scaled with B^2, a linear relationship should be there, but from the concave shape it can be seen the relation is sub-parabolic.

COLOUR MAPS OF THE CHARACTERISTIC LENGTH SCALE OF WAVE FUNCTION SHRINKAGE

The quadratic, weak-field wave fit in the magneto-resistance directly gives the length scale, $d = (a^3\xi)^{1/4}$:

$$\frac{R}{R_0} = 1 + \frac{\xi a^3}{6}\left(\frac{eB}{\hbar}\right)^2 .$$

In Fig. S7 this length scale is plotted for all electric fields, E, and temperatures, T. We find that $(a^3\xi)^{1/4}$ ranges from 6 to 12 nm for all segments, temperatures and electric fields considered. With the assumption that the temperature dependence of the conductance, $G(T < 10\text{ K})$, is due to a changing ratio between a and ξ ($G = G_0 \exp(-a/\xi)$), the length scales ξ and a can be separated (Fig. 5).

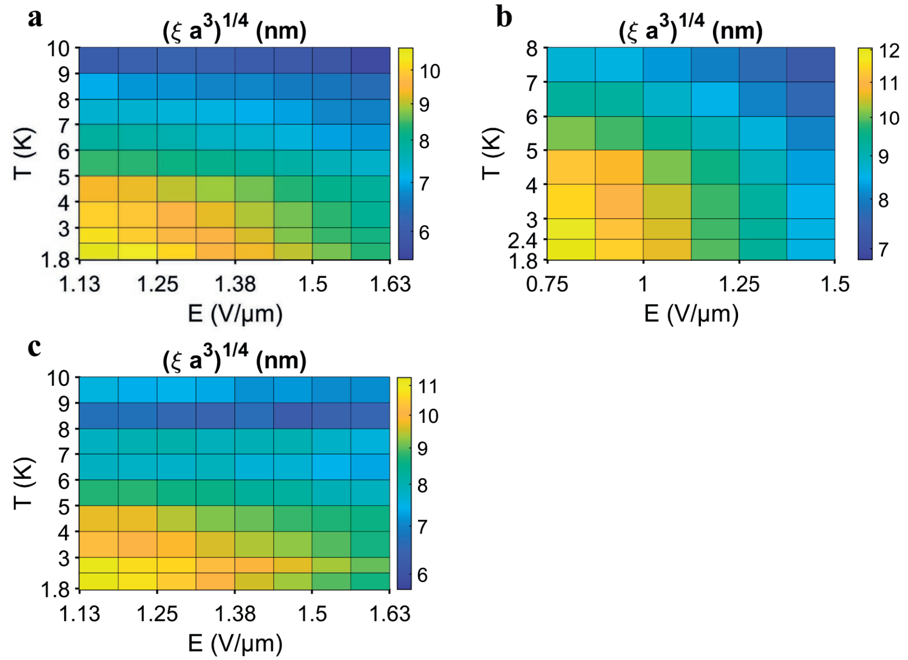

Figure S7: **Colour maps of the characteristic length scale of wave function shrinkage**. **a-c** correspond to the segments 1,2 and 3, respectively. The quadratic fit for the magneto-resistance. $R/R_0 = \beta B^2$, directly gives the parameter, $(\xi a^3)^{1/4}$, where ξ is the decay length and a is the hopping distance. Each rectangle is coloured by the average of the four data points at its corners.

Logarithmic resistance at zero magnetic field versus $d = (\xi a^3)^{1/4}$

As explained in the main text, All values for the magneto-resistance, are mapped to a length scale, d. Then the data is grouped per value of the electric field, E, such that the behaviour of d as a function of temperature at a fixed field can be determined. This temperature dependence is described by the ratio of the center-to-center distance, a, and the decay length, ξ, from Eq. 3 and Eq. 4 in the main text, expressing the relationship between $\ln(R)$, ξ and a). This allows to data to interpreted further in terms of the mentioned length scales.

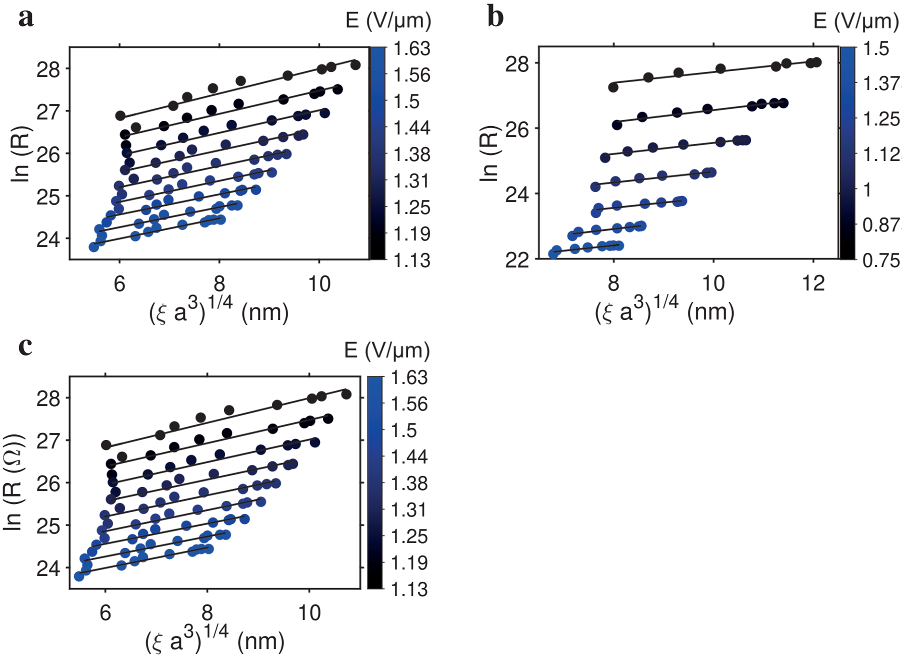

Figure S8: **Logarithmic resistance at zero magnetic field versus** $d = (\xi a^3)^{1/4}$**.** **a-c** correspond to the segments 1,2 and 3, respectively. On the vertical axis is the logarithm of the resistance, $\ln(R)$ and on the horizontal axis is the length scale, $d = (\xi a^3)^{1/4}$ All data points with a certain value of the electric field, E, are taken together, and a fit is done in of the logarithm of the resistance as function of temperature, $\ln(R(T))$, versus the length scale, $d(E,T)$ (black lines).

HOPPING DISTANCE FOR ALL SEGMENTS

Segment 1

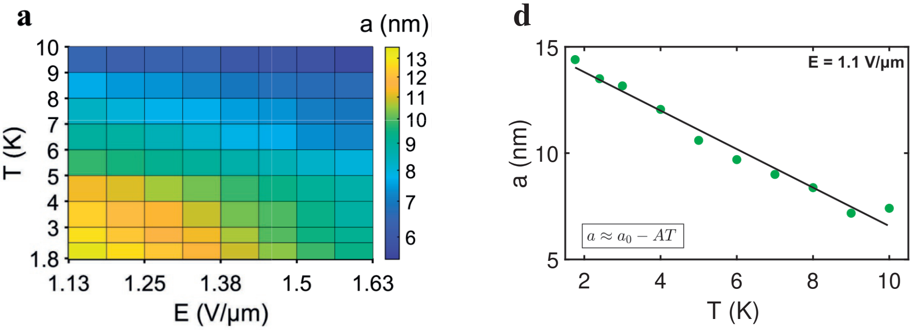

Segment 2

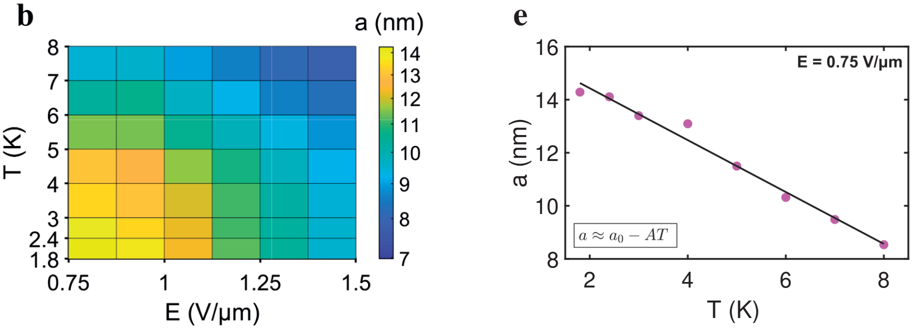

Segment 3

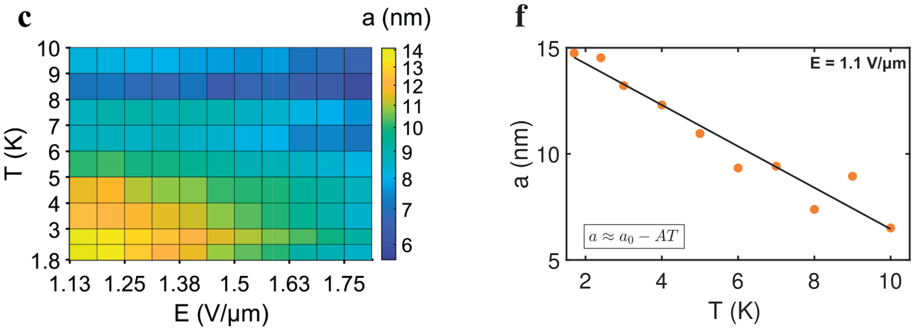

Figure S9: **Wave function shrinkage results for all segments** (weak-field regime). For segment 1, the figures are shown in the main text (Fig. 5b,d) **a-c**, Per segment, the colour map of the hopping distance, a, as determined from the wave function shrinkage model. On the vertical axis temperature, T; on the horizontal axis the electric field, E. Each rectangle is coloured by the average of the four data points at its corners. **d-f** Per segment, the hopping distance, a, at the lowest analysed electric field (E = 1.1 V/µm or E = 0.75 V/µm), as a function of temperature. The drawn black line is a fit to the data with formula $a = a_0 - AT$. For the three segments $a_0 = 16$ nm and $A = 0.9$ nm/K (see Table S2)

.

5.6.5. DILUTION FRIDGE MEASUREMENTS

DILUTION FRIDGE MEASUREMENTS IN THE PLANE OF THE SUBSTRATE

For segment 1, magneto-resistance measurements were done in a dilution refrigerator, where the temperature can be lowered to T = 100 mK. The relative magneto-resistance continued to increase, to a maximum value of 76%. The results of the relative magneto-resistive effect with the magnetic field in the vertical z-direction are shown elsewhere (Fig. S1a). The dilution fridge set-up also has a magnetic field available in the horizontal plane (see 'Methods: Magnetic set-ups'). In the horizontal y-direction (perpendicular to the direction of transport, Fig. 1), there was a magnetic field of B = 3 T available. This gave a magneto-resistance similar to the that in the vertical z-direction (Fig. S10a,b). In the x-direction (in the direction of transport), there was a magnetic field of B = 1 T available, allowing for full angle control in the xy-plane up to B = 1 T. As a function of angle at this field, there is no effect visible (Fig. S10c). This is inconclusive, because in the whole data set it is hard to see an effect at B = 1 T. Furthermore, during cooldown from T = 5 K to base temperature, the current was measurement at a fixed bias voltage of V = 60 V. It was observed that below T = 2 K the temperature dependence of the conductance at this bias voltage is flat as illustrated by Fig. S10d.

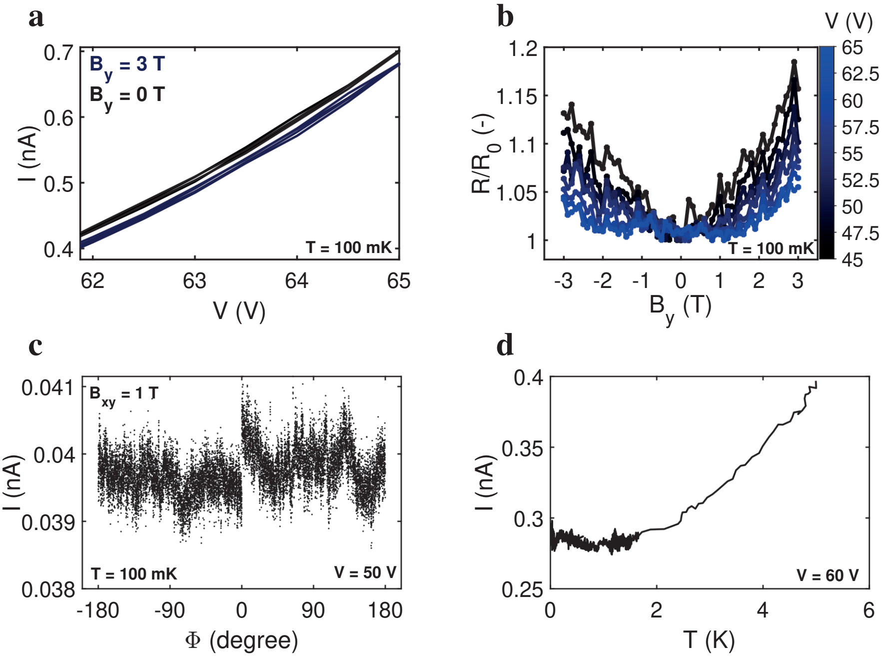

Figure S10: **Additional dilution fridge measurements.** Panels (a)-(c) are magneto-resistance measurements in the plane of the substrate, while panel (d) shows the current as a function of temperature during cooldown. **a**, Magneto-resistance in the plane of the substrate, roughly perpendicular to the direction of transport (see Fig. 1). Current, I, versus the bias voltage, V, at temperature $T = 100$ mK. The $I(V)$ was plotted at $B_y = 3$ T (dark blue) and at $B_y = 0$ T (black). **b**, Magneto-resistance in the plane of the substrate, roughly perpendicular to the direction of transport. The resistance, R, versus magnetic field, B. **c**, Electrical current, I, at $V = 50$ V in the xy-plane for all angles, ϕ, at magnitude $B = 1$ T. **d**, Current, I, as a function of temperature, T, during cooldown.

MAGNETO-RESISTIVE EFFECT, INCLUDING THE DILUTION FRIDGE MEASUREMENTS

The wave function shrinkage model has been applied to the data, excluding the dilution fridge measurements in segment 1. The magneto-resistance colour map has been extended with the dilution fridge data, which is dominated by the lowest temperature measurement (Fig. S11a). At T = 100 mK, the dependence of the relative magneto-resistance, R/R_0, on the electric field, $E = V/L$, is similar to that at other temperatures (Fig. 3, Fig. S11b). Including the measurements at the lowest temperature, the relative magneto-resistance increases to 76 % (Fig. S11c). When the wave function shrinkage model is applied to the results, we see that the effective center-to-center hopping distance continues to increase a the same pace (Fig. S11d). All in all, there is no trend deviation from the $T = 1.8 - 10$ K measurements to be observed in the dilution fridge.

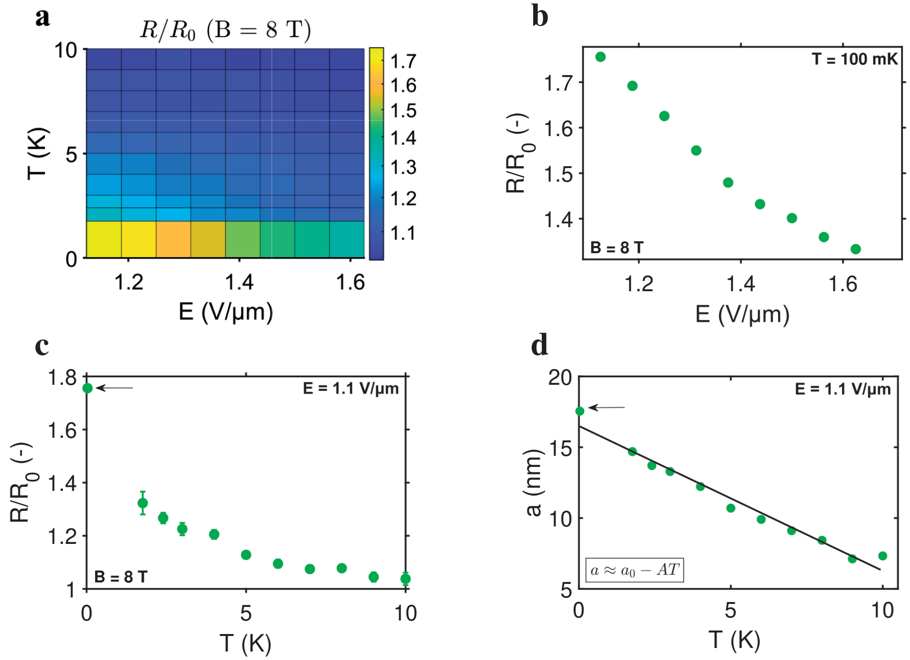

Figure S11: **Magneto-resistive effect, including the dilution fridge measurements**, on segment 1 (T = 100 mK). **a**, Colour maps of the magneto-resistive effect in segment 1. The data plotted in Fig. S1 is used to construct a colour map, with on the vertical axis the temperature, T. On the horizontal axis, there is the electric field, E (see Table S2 for the measurement length). the colour indicates the strength of the relative magneto-resistance, R/R_0 at high magnetic field (B = 8 T). **b**, Normalized resistance, R/R_0, versus electric field, E (bias voltage divided by the measurement length). The temperature was T = 100 mK. **c**, Normalized magneto-resistance, R/R_0, versus temperature, T. The magneto-resistance was determined at B = 8 T and at electric field E = 1.1 V/µm. All data but the lowest temperature point, indicated by the arrow, can also be found in Fig. 5. **d** The hopping distance, a, at lowest electric field and with the dilution fridge measurement added (T = 100 mK; E = 1.1 V/µm). The lowest temperature data point is highlighted by an arrow.

5.6.6. TABLES

TABLE WITH (MAGNETO-)RESISTANCE VALUES PER TEMPERATURE

Segment	T (K)	R_0 (TΩ)	R/R_0 (8 T)	B_0 (T)	β ($1/\mathrm{T}^2$)	a (nm)
#1	**0.1**	3.6	1.76	16	0.0096	17.7
	1.8	1.56	1.33	25	0.0051	14.3
	2.4	1.49	1.27	26	0.0043	13.5
	3	1.40	1.25	26	0.0040	13.1
	4	1.22	1.20	27	0.0030	12.0
	5	1.06	1.13	31	0.0020	10.5
	6	0.90	1.11	35	0.0015	9.7
	7	0.73	1.08	37	0.0011	8.9
	8	0.59	1.07	40	0.00098	8.5
	9	0.47	1.05	51	0.00051	7.2
	10	0.35	1.04	53	0.00062	7.4
#2	**1.8**	1.5	1.40	25	0.0050	14.3
	2.4	1.4	1.39	25	0.0049	14.1
	3	1.4	1.40	26	0.0047	13.4
	4	1.3	1.32	27	0.0041	13.1
	5	1.2	1.26	29	0.0030	11.5
	6	1.0	1.19	21	0.0023	10.3
	7	0.89	1.15	34	0.0018	9.5
	8	0.68	1.13	35	0.0015	8.5
#3	**1.8**	6.2	1.39	29	0.0063	14.9
	2.4	6.3	1.35	25	0.0060	14.8
	3	5.5	1.33	29	0.0043	13.3
	4	4.8	1.30	27	0.0035	12.4
	5	4.2	1.22	31	0.0023	10.9
	6	3.6	1.10	39	0.0015	9.5
	7	2.8	1.15	33	0.0015	9.5
	8	2.3	1.06	48	0.00047	7.8
	9	1.7	1.16	41	0.0013	9.0
	10	1.2	1.04	50	0.00047	6.7

Table S1: **Table with (magneto-)resistance values per temperature**. In the first column, is the segment number indicated. The second column gives the temperature, T. The third column gives the resistance, $R_0 = V/I$, averaged over the region $V = 45 \pm 0.5$ V for segments 1 and 3 and over the region $V = 3.0 \pm 0.1$ V for segment 2. The fourth column, gives the magneto-resistive effect at $B = 8$ T at $E = 1.1$ V/μm. The fifth column, gives the characteristic magnetic field of the quadratic magneto-resistance fit (wave function shrinkage, $\frac{R}{R_0} = (\frac{B}{B_0})^2$). The sixth column gives β in the relation $\frac{R}{R_0} = 1 + \beta B^2$. The last column gives the hopping distance, a, as implied from the wave function shrinkage model in the weak-field regime, at $E = 1.1$ V/μm.

TABLE WITH CHARACTERISTIC VALUES PER SEGMENT

Segment	L (µm)	$T_{\max}$ (K)	$G_{\max}$ (nS)	$\sigma_{\max}$ (S/cm)	U_A (meV)	A (nm K^{-1})	κ (pN/nm)
#1	40	110	0.83	0.014	43.1 ± 8	0.97	0.46
#2	4	300	3248	4.0	41.8 ± 0.4	0.91	0.50
#3	40	80	0.34	0.004	–	0.98	0.46

Table S2: **Table with characteristic values per segment**. In the first column, is the segment number. In the second, the distance in between electrodes covered by SiO_2 (the segment length, L). In the third, is the maximum temperature, $T_{\max}$ to which the temperature dependent measurement was extended. In the fourth, conductance, $G_{\max}$, at the maximum measured temperature. In the fifth, the is the corresponding conductivity, $\sigma_{\max}$, based on $G_{\max}$, the segment length, L and the conductive area, $A = N_F \cdot \pi (d_F)^2$, with $N_F = 60$ and $d_F = 25$ nm. In the sixth column, is the activation energy determined in the region $T > 70$ K (in the rest of this thesis, $T > 100$ K is used). For segment 3, there was not enough data to determine the activation energy. As a guide for translation to room temperature conductivity, given $U_A \approx 40$ meV, from 110 K to 300 K, note that an estimated factor 14 will be gained in conductivity for segment 1, and a factor 160 from 70 K for segment 3. In the sixth column, A, which is the reduction in effective hopping distance a, per Kelvin (Eq. 5). In the last column, is the stiffness/spring constant, κ, that is implied from A, assuming a classical harmonic oscillator model.

6

CONCLUDING REMARKS

Cable bacteria stand out in biology as they display an exceptional form of long-range conduction. The principal objective of this thesis was to achieve a better insight into the charge transport mechanism that sustains this long-range biological conduction over centimeter scale distances.

6.1. TEMPERATURE DEPENDENCE OF CONDUCTION

In Chapter 2, it was shown that the temperature dependence of the conductance in cable bacteria can be explained by a hopping mechanism, albeit not a conventional one. Analysis of an extensive current/voltage data set covering many fiber sheath samples ($n = 53$) revealed a thermally activated behaviour for high temperatures ($T > 75$ K), with an activation energy of ~ 40 meV. We verified that these properties are intrinsic to the protein fibre material and hence not arise from a contact effect with the electrodes. The corresponding reorganisation of $\lambda \approx 0.2$ eV is small compared to the reorganisation energy in multi-heme cytochromes [128, 129], which are responsible for the conductance in the nanowires of *Shewanella* and *Geobacter* bacteria [22, 32].

For lower temperatures ($T < 75$ K), the conductance flattens out as a function of the temperature, and hence, it remains relatively high at low temperatures. This flattening response is proposed to result from nuclear tunneling, in which, at low temperatures, quantum mechanical vibrations contribute more to the charge transport process than thermal motions. The mean energy of these vibrational modes was found to be $\hbar\langle\omega\rangle \approx 10$ meV (order of magnitude estimate). An electrical field arises in the conductive fibers as a result from the voltage bias applied between source and drain electrodes. At low temperatures, the conductance was found to be strongly dependent on this electric field. This behaviour is consistent with the scaling behaviour of nuclear tunneling: the field-dependent behaviour starts to come notable around $eV \approx N_S k_B T$, where N_S is the number of hopping sites.

While the charge transport in the periplasmic fibers of cable bacteria can be described as a hopping process, the apparent hopping distance (center-to-center distance between two charge carrier sites) strongly deviates from conventional electron transport in protein structures. The universal scaling curves indicate that there is only one hopping site over a length of 10 - 100 nm. This distance is 10-100 times larger than the packing distance of iron centres in multi-heme cytochromes [128]. This large hopping distance, combined with the low activation energy, suggests that the charge carriers in cable bacteria are substantially delocalised (Fig. 1).

6.2. NUCLEAR TUNNELING OR LUTTINGER LIQUID?

In Chapter 2, the conductance data were theoretically explained by a hopping mechanism in which the electron transport is assisted by nuclear tunneling at low temperature. In this model, the exponent determining the power law $G \propto T^{\beta}$ is determined by the ratio of reorganisation energy and vibrational frequency (see Eq. S19 in Chapter 2)

$$\beta = \lambda/(\hbar\omega_c) - 2 \tag{1}$$

However, other model explanations are possible. In the literature on carbon nanotubes (see for example Ref.[143]), a comparable low-temperature behaviour of the conductance is described by the Luttinger Liquid (LL) model. The Luttinger liquid describes a one-dimensional Fermi gas (1D metal) to which electron-electron interactions are added. As such, the Luttinger Liquid model leads to exactly the same mathematical expression for the universal scaling curve (Eq. S22 in Chapter 2). In a Luttinger Liquid, the number of tunnelling barriers equals the number of hopping sites (N_S) and the power law exponent is determined by the ratio between the charging energy, U_C, and the energy spacing Δ_C between electronic levels. In carbon nanotubes, if electrons tunnel between the ends of Luttinger liquid fragments, the exponent becomes [143]:

$$\beta = (\sqrt{1 + 2U_C/\Delta_C} - 1)/4. \tag{2}$$

The exponent values in carbon nanotubes ($\beta \approx 0.84$) are much smaller than in cable bacteria ($\beta \approx 6$). To obtain the values seen in cable bacteria, a high ratio between charging energy and level spacing is required: $U_C/\Delta_C = 312$. The charging energy is analogous to the reorganisation energy, because both quantities represent an energy difference upon loading an electron onto a given location. If the high temperature activation energy (50 meV) comes exclusively from the charging energy, the level spacing would be $\Delta_C = 50/312 = 0.13$ meV. In this model, many electronic levels are hence contributing to the charge transport. A similar conclusion is arrived upon in Chapter 4 when analysing the gate dependence of conduction in cable bacteria. Future theoretical assessments could examine the similarities and differences between the Luttinger liquid and the hopping/nuclear tunneling models, in particular for the conductance as a function of temperature.

Overall, the charge transport mechanism at the nanometer scale remains puzzling. The center-to-center distance between hopping sites a, as estimated in Chapter 2 ($a \sim 10$ -100 nm) is considerably larger than in conventional biological electron transport ($a \sim$ 1 nm). Note that a is possibly so large that it is experimentally reachable with electron beam lithography. Therefore, it could be worthwhile to try to extract a single protein fibre from a cable bacterium and connect this single protein fibre between electrodes that are only a few nanometers apart. This way, it might be possible to eliminate the hopping process within the protein fibres,and so the question: ’what is the charge transport mechanism on the nanometer scale?’, could be answered. Potentially, one might observe ballistic transport, in which the electron does not scatter or hop (dissipate energy) in the conductive fibre. If such a measurement could be done, it could give more insight into the charge injection mechanism at the electrodes as well as the conductive properties of the protein fibers.

6.3. CHARGE TRANSPORT IS RESONANT AND FIELD-DRIVEN

In Chapter 3, the one-dimensional hopping model, as proposed in Chapter 2, was analysed in more detail. An important goal was to understand if a classical Marcus-type one-dimensional hopping model could provide the high conductivity levels that are observed in cable bacteria (up to 100 S/cm) [2]. If charge injection and ejection at the electrodes is not rate limiting, different regimes of transport are theoretically possible: field-driven versus concentration-driven, resonant versus off-resonant. The experimental data collected allow to distinguish which regime is occurring in cable bacteria. In the concentration-driven regime, the current-voltage curves would quickly saturate beyond $V = 0.1$ V at room temperature. In the off-resonant regime, the $I(V)$ would be highly non-linear for low voltages, followed by a transition to a linear regime for high voltages. Neither features is seen in cable bacteria. Therefore, charge transport in cable bacteria can be viewed as resonant and field-driven. As it happens, this particular regime also enables the highest conductivity.

6.4. ARE LARGE HOPPING DISTANCES REALISTIC?

The model analysis shows that a conductivity on the order of 100 S/cm is only possible for large distances between hopping sites ($a > 10$ nm). This implies also that the conductance is solely dominated by the hopping process and that the hopping mobilities are high. As Chapter 3 shows, hopping mobilities are theoretically allowed to exceed those of metals (metals have mobilities of ~ 10 cm^2/Vs). At a one-to-ten ratio between the electronic coupling, H, and the reorganisation energy, $\lambda = 0.2$ eV ($H/\lambda = 0.1$), and with a large center-to-center hopping distance ($a = 10$ nm), the charge carrier mobility in a hopping system could reach 80 cm^2/Vs, and it could even rise above 300 cm ^{2}/Vs for $a > 20$ nm. Thus, the question can be asked whether such a large hopping distance (and associated high mobility) is reasonable.

In contrast to metals, in the one-dimensional hopping conductor model, it is assumed there is no mobility loss inside the hopping site, as it is described by a delocalised quantum-mechanical wave function. To test whether this is reasonable, the De Broglie wave length, $\lambda_\text{B} = h/p$ can be calculated, where h is Planck’s constant and p is the momentum of the electron. This concept was formulated more than a century ago, to estimate whether an object behaves like a particle or a wave. Over a distance smaller than the De Broglie wave length, matter can be expected to behave wave-like. Due to the hopping process, the electrons have a speed $p = mv = m\Gamma a$, where v is the speed of the electron, m the effective mass and Γ the hopping rate. Thus, the De Broglie wave length for hopping can be expressed as:

$$\lambda_\mathrm{B} = \frac{h}{m\Gamma a}. \tag{3}$$

For wave lengths smaller than the hopping site ($\lambda_B < a$), it looks reasonable to propose that electrons act as a standing wave within the hopping site. For a hopping rate of $\Gamma = 10^{12}$ s^{-1}, the point $\lambda_B = a$ is reached at $a = \sqrt{\frac{h}{m\Gamma}} = 26$ nm. Therefore, a wave behaviour over tens of nanometers is not unreasonable. For $a = 26$ nm, the electrons then have a hopping speed of $v = \Gamma a = 2.6 \cdot 10^4$ m/s, which is much lower than the Fermi velocity of electrons in a metal, 10^6 m/s. The latter gives a De Broglie wave length of only 0.1 nm, making electrons act as particles colliding with the metal lattice (e.g. gold atoms are placed 0.4 nm apart, which is larger than the De Broglie wave length). Perhaps, with a lower (hopping) speed of the electrons, they can retain the character of a standing wave within the hopping site, with a wave length much larger than the size of single atoms. As such, the electrons do not collide with them and the hopping mobility can reach levels that exceed those in metals.

Apart from the question whether the mobility is adequately described by the hopping process, it is also questionable whether charge carrier densities nearing that of metals can be realised. If that were the case, the conductivity of the one-dimensional hopping conductor would rival that of a metal. If we assume $a = 20$ nm and the hopping chain contains one tenth of charge carrier density in metals, one-dimensional hopping conductivities would rival those of metals. Electron-electron interactions could limit the charge carrier density, as in the Luttinger Liquid, but the reorganisation effect will screen electrons from each other's repulsive electric field. It would be interesting to investigate whether a (biological) one-dimensional hopping system can exist, whose conductivity rivals that of metals, both in theory and in practice.

6.5. CONDUCTANCE SHOWS A WEAK FIELD EFFECT

In Chapter 4, gate dependent measurements on fiber skeletons from cable bacteria are presented. These measurements show that there is little to no gate effect at room temperature (< % 2), with a slightly larger gate effect appearing at lower temperatures ($T <$ 150 K). Still, the gating effect remained small: the ratio between gated and ungated conductance was always less than 2. At low temperatures, the conductance increased for both sides of the gate voltage polarity, indicating that transport is not dominated by electron or hole mobilities in a band, as seen in semiconductors. Furthermore, the saturation of the conductance for high gate voltage indicates that the charge carrier density cannot be improved, even if the gate coupling would be more effective. To explain these data, a model was proposed in which a small energy gap (~ 1 meV) exists between conductive states on both sides of the Fermi energy. A single electron state (hopping state) on both the electron and hole side could not describe the observed gate response. Instead, the model only fits the experimental data when more electronic states are added. This proposition is at odds with the traditional view on electron transport in biology (e.g. multi-heme cytochrome hopping), in which there is only one available electronic state at a hopping site.

In future research, it could be worthwhile to make devices with more efficient gate coupling, for example by using hafnium oxide instead of silicon oxide, which has a much higher dielectric constant. Also, in many of the measurements, gold electrodes covered a large part of the cable bacteria filaments, which screens the gate effect and reduces the efficiency. Perhaps with a higher gate coupling and smaller electrodes, more features in the gate response would be visible. For example: the gate response may again begin to rise after saturation due to a peak in the density of states for higher energy values. More broadly speaking, the density of states, which determines the charge carrier density, remains unresolved in cable bacteria. This quantity could be calculated once the molecular/polymeric structure of the conductive protein fibres is known. This knowledge would clarify whether there is any prospect of increasing the conductivity by gating.

6.6. THE MAGNETO-RESISTANCE AT CRYOGENIC TEMPERATURES

In Chapter 5, low-temperature magneto-resistance measurements on cable bacteria are presented. At $T = 1.8$ K, an increase of the resistance of up to 50 % is observed at a magnetic field of $B = 8$ T. The magneto-resistance is reproducible among different samples with different spacing between the electrodes ($L = 4 to 40$ μm), and it disappears with increasing temperature and electric field. At a temperature of $T = 10$ K, only a few percent of magneto-resistance can be measured (4 %). The magnetic response follows that of the wave function shrinkage model and is very similar to the magnetic response in organic semiconductors such as polyacetylene and polyaniline [132, 133, 138].

Even though the temperature and field dependent behaviour of the magneto-resistance has been documented in other materials, its origin remains unclear. As documented in Chapter 5, the application of the wave function shrinkage model implies a reduction in the hopping distance with temperature and electric field. Therefore, it was proposed that a thermally activated vibrational mode is reducing the effective hopping distance with temperature, thus explaining the observed temperature response. However, no explanation for the field-dependent behaviour was given. A model that does capture this aspect, is the Variable Range Hopping model (VRH), in which the hopping distance decreases both with temperature and electric field. For organic polymers with a similar magnetoresistance, the proposed model was based on VRH [132]. Because this VRH model predicts a similar dependence of conductance on temperature as the nuclear tunneling model [144], it would be worthwhile to investigate the role of energetic disorder in hopping sites, in cable bacteria and other biological conductors. Only if the reorganisation effect plays a minor role in the charge transport, compared to energetic disorder, the VRH model is a more sensible choice. A combination of the two models (VRH and nuclear tunneling) could also capture the observed $G(E,T)$ behaviour (Chapter 2). At the moment, it is not excluded that beyond nearest neighbour hopping or energetic disorder play a role in charge transport.

6.7. CONCLUDING THOUGHTS

In summary, with the knowledge acquired in this thesis, the charge transport mechanism in cable bacteria can be described as follows. Cable bacteria have an extraordinarily low activation energy of transport, ~ 40 meV. The primary candidate for the origin of this activation energy is the reorganisation effect, because proteins are generally insulators

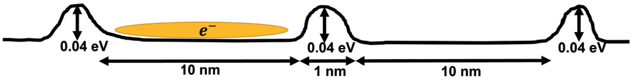

Figure 1: **Picture of charge transport in cable bacteria.** On the vertical axis, there is potential energy and on the horizontal axis, there is the position of the electron. To get to the next hopping site, the electron has to overcome a 0.04 eV barrier, which comes from the reorganisation effect. The electron is delocalised over the distance between barriers (yellow oval).

.

with large band gaps [12]. The reorganisation energy implied is $\lambda \approx 0.2$ eV, which is much lower than in other microbial conductors [22, 37]. When measuring the cable bacteria as a function of temperature, as treated in Chapter 2, the conductivity flattens out for temperatures below $T \approx 75$ K. This fits the nuclear tunneling model, in which vibrational modes freeze out, but retain their quantum vibrational energy, $\hbar\omega/2$, which makes more energy available to the hopping process than predicted in classical physics. The transition to nuclear tunneling was found to be dependent on the electric field, which is described in the universal scaling relation, which predicts a large distance between hopping centres ($a > 10$ nm, Fig. 1). The combination of low reorganisation energy and this large distance make it likely that electrons in cable bacteria are much more delocalised than on a heme cytochrome, which is key for the high conductivity in cable bacteria. Model analysis supports that the observed high conductivity in cable bacteria [2, 44] (~ 100 S/cm) is possible within a delocalised hopping model (Chapter 3). The gate dependence of conductivity supports that cable bacteria's charge carrier density cannot be tuned with a gate voltage, as in a band gap semiconductor (Chapter 4). Also, the shape of the gate voltage response suggests that the hopping chain with single, repeating electron state is a too simple picture for cable bacteria, because there seem to be more electronic states involved in charge transport. Lastly, the magnetic response supports that the hypothesis that the charge transport is governed by a delocalised hopping model (Chapter 5).

BIBLIOGRAPHY

1. Pfeffer, C. *et al.* Filamentous bacteria transport electrons over centimetre distances. *Nature* **491,** 218–221 (2012).
2. Meysman, F. J. *et al.* A highly conductive fibre network enables centimetre-scale electron transport in multicellular cable bacteria. *Nature Communications* **10,** 1–8 (2019).
3. Bjerg, J. T. *et al.* Long-distance electron transport in individual, living cable bacteria. *Proceedings of the National Academy of Sciences* **115,** 5786–5791 (2018).
4. Siu, C. in *Electronic Devices, Circuits, and Applications* 35–39 (Springer, 2022).
5. Van Zeghbroeck, B. *Principles of semiconductor devices* (2004).
6. Melissinos, A. C. & Napolitano, J. *Experiments in modern physics* (Gulf Professional Publishing, 2003).
7. Efros, A. L. & Shklovski, B. I. *Electronic Properties of Doped Semi-conductors* 202–241 (1984).
8. Yu, D., Wang, C., Wehrenberg, B. L. & Guyot-Sionnest, P. Variable range hopping conduction in semiconductor nanocrystal solids. *Physical review letters* **92,** 216802 (2004).
9. Backenstoss, G. Conductivity mobilities of electrons and holes in heavily doped silicon. *Physical Review* **108,** 1416 (1957).
10. Basescu, N *et al.* High electrical conductivity in doped polyacetylene. *Nature* **327,** 403–405 (1987).
11. Pirbadian, S. & El-Naggar, M. Y. Multistep hopping and extracellular charge transfer in microbial redox chains. *Physical Chemistry Chemical Physics* **14,** 13802–13808 (2012).
12. Herz, T., Otto, P. & Clark, T. On the band gap in peptide α-helices. *International Journal of Quantum Chemistry* **79,** 120–124 (2000).
13. Senevirathna, W., Daddario, C. M. & Sauvé, G. Density functional theory study predicts low reorganization energies for azadipyrromethene-based metal complexes. *The Journal of Physical Chemistry Letters* **5,** 935–941 (2014).
14. Oshi, R., Abdalla, S. & Springborg, M. Study of the influence of functionalization on the reorganization energy of naphthalene using DFT. *Computational and Theoretical Chemistry* **1099,** 209–215 (2017).
15. Marcus, R. A. & Sutin, N. Electron transfers in chemistry and biology. *Biochimica et Biophysica Acta* **811,** 265–322 (1985).

16. Rust, M., Lappe, J. & Cave, R. J. Multistate effects in calculations of the electronic coupling element for electron transfer using the generalized Mulliken- Hush method. *The Journal of Physical Chemistry A* **106,** 3930–3940 (2002).
17. Cave, R. J. & Newton, M. D. Generalization of the Mulliken-Hush treatment for the calculation of electron transfer matrix elements. *Chemical Physics Letters* **249,** 15–19 (1996).
18. Myers, C. R. & Nealson, K. H. Bacterial manganese reduction and growth with manganese oxide as the sole electron acceptor. *Science* **240,** 1319–1321 (1988).
19. Gorby, Y. A. *et al.* Electrically conductive bacterial nanowires produced by Shewanella oneidensis strain MR-1 and other microorganisms. *Proceedings of the National Academy of Sciences* **103,** 11358–11363 (2006).
20. El-Naggar, M. Y. *et al.* Electrical transport along bacterial nanowires from Shewanella oneidensis MR-1. *Proceedings of the National Academy of Sciences* **107,** 18127–18131 (2010).
21. El-Naggar, M. Y., Gorby, Y. A., Xia, W. & Nealson, K. H. The molecular density of states in bacterial nanowires. *Biophysical journal* **95,** L10–L12 (2008).
22. Xu, S., Barrozo, A., Tender, L. M., Krylov, A. I. & El-Naggar, M. Y. Multiheme cytochrome mediated redox conduction through Shewanella oneidensis MR-1 cells. *Journal of the American Chemical Society* **140,** 10085–10089 (2018).
23. Breuer, M., Rosso, K. M. & Blumberger, J. Electron flow in multiheme bacterial cytochromes is a balancing act between heme electronic interaction and redox potentials. *Proceedings of the National Academy of Sciences* **111,** 611–616 (2014).
24. Pirbadian, S. *et al.* Shewanella oneidensis MR-1 nanowires are outer membrane and periplasmic extensions of the extracellular electron transport components. *Proceedings of the National Academy of Sciences* **111,** 12883–12888 (2014).
25. Khan, F. S. T., Samanta, D., Chandel, D., Shah, S. J. & Rath, S. P. Heme–Heme Interactions in Diheme Cytochromes: Effect of Mixed-Axial Ligation on the Electronic Structure and Electrochemical Properties. *Inorganic Chemistry* **60,** 12870–12882 (2021).
26. Subramanian, P., Pirbadian, S., El-Naggar, M. Y. & Jensen, G. J. Ultrastructure of Shewanella oneidensis MR-1 nanowires revealed by electron cryotomography. *Proceedings of the National Academy of Sciences* **115,** E3246–E3255 (2018).
27. Lovley, D. R., Stolz, J. F., Nord Jr, G. L. & Phillips, E. J. Anaerobic production of magnetite by a dissimilatory iron-reducing microorganism. *Nature* **330,** 252–254 (1987).
28. Caccavo Jr, F. *et al.* Geobacter sulfurreducens sp. nov., a hydrogen-and acetate-oxidizing dissimilatory metal-reducing microorganism. *Applied and environmental microbiology* **60,** 3752–3759 (1994).
29. Reguera, G. *et al.* Extracellular electron transfer via microbial nanowires. *Nature* **435,** 1098–1101 (2005).

30. Lovley, D. R. Cleaning up with genomics: applying molecular biology to bioremediation. *Nature Reviews Microbiology* **1,** 35–44 (2003).
31. Wang, F. *et al.* Structure of microbial nanowires reveals stacked hemes that transport electrons over micrometers. *Cell* **177,** 361–369 (2019).
32. Yalcin, S. E. *et al.* Electric field stimulates production of highly conductive microbial OmcZ nanowires. *Nature chemical biology* **16,** 1136–1142 (2020).
33. Gu, Y. *et al.* Structure of Geobacter cytochrome OmcZ identifies mechanism of nanowire assembly and conductivity. *Nature microbiology* **8,** 284–298 (2023).
34. Lampa-Pastirk, S. *et al.* Thermally activated charge transport in microbial protein nanowires. *Scientific reports* **6,** 1–9 (2016).
35. Adhikari, R. Y., Malvankar, N. S., Tuominen, M. T. & Lovley, D. R. Conductivity of individual Geobacter pili. *Rsc Advances* **6,** 8354–8357 (2016).
36. Tan, Y. *et al.* Expressing the Geobacter metallireducens PilA in Geobacter sulfurreducens yields pili with exceptional conductivity. *MBio* **8,** 10–1128 (2017).
37. Malvankar, N. S. *et al.* Tunable metallic-like conductivity in microbial nanowire networks. *Nature Nanotechnology* **6,** 573–579 (2011).
38. Guberman-Pfeffer, M. J. Assessing Thermal Response of Redox Conduction for Anti-Arrhenius Kinetics in a Microbial Cytochrome Nanowire. *The Journal of Physical Chemistry B* **126,** 10083–10097 (2022).
39. Dahl, P. J. *et al.* A 300-fold conductivity increase in microbial cytochrome nanowires due to temperature-induced restructuring of hydrogen bonding networks. *Science advances* **8,** eabm7193 (2022).
40. Nielsen, L. P., Risgaard-Petersen, N., Fossing, H., Christensen, P. B. & Sayama, M. Electric currents couple spatially separated biogeochemical processes in marine sediment. *Nature* **463,** 1071–1074 (2010).
41. Cornelissen, R. *et al.* The cell envelope structure of cable bacteria. *Frontiers in Microbiology* **9,** 3044 (2018).
42. Geelhoed, J. S. *et al.* Indications for a genetic basis for big bacteria and description of the giant cable bacterium Candidatus Electrothrix gigas sp. nov. *Microbiology Spectrum,* e00538–23 (2023).
43. Thiruvallur Eachambadi, R. *et al.* An ordered and fail-safe electrical network in cable bacteria. *Advanced Biosystems* **4,** 2000006 (2020).
44. Boschker, H. T. *et al.* Efficient long-range conduction in cable bacteria through nickel protein wires. *Nature Communications* **12,** 1–12 (2021).
45. Bonné, R. *et al.* Intrinsic electrical properties of cable bacteria reveal an Arrhenius temperature dependence. *Scientific reports* **10,** 1–8 (2020).
46. Moser, C. C., Keske, J. M., Warncke, K., Farid, R. S. & Dutton, P. L. Nature of biological electron transfer. *Nature* **355,** 796–802 (1992).
47. Gray, H. B. & Winkler, J. R. Electron flow through metalloproteins. *Biochimica et Biophysica Acta (BBA)-Bioenergetics* **1797,** 1563–1572 (2010).

48. Blumberger, J. Recent advances in the theory and molecular simulation of biological electron transfer reactions. *Chemical Reviews* **115,** 11191–11238 (2015).

49. Meysman, F. J. Cable bacteria take a new breath using long-distance electricity. *Trends in microbiology* **26,** 411–422 (2018).

50. Jiang, Z. *et al.* In vitro single-cell dissection revealing the interior structure of cable bacteria. *Proceedings of the National Academy of Sciences* **115,** 8517–8522 (2018).

51. Schwarze, M. *et al.* Molecular parameters responsible for thermally activated transport in doped organic semiconductors. *Nature Materials* **18,** 242–248 (2019).

52. Liu, C. *et al.* A unified understanding of charge transport in organic semiconductors: the importance of attenuated delocalization for the carriers. *Materials horizons* **4,** 608–618 (2017).

53. De Vault, D. & Chance, B. Studies of photosynthesis using a pulsed laser: I. Temperature dependence of cytochrome oxidation rate in chromatium. Evidence for tunneling. *Biophysical journal* **6,** 825–847 (1966).

54. Devault, D., Parkes, J. H. & Chance, B. Electron tunnelling in cytochromes. *Nature* **215,** 642–644 (1967).

55. Moser, C. C., Anderson, J. R. & Dutton, P. L. Guidelines for tunneling in enzymes. *Biochimica et Biophysica Acta (BBA)-Bioenergetics* **1797,** 1573–1586 (2010).

56. Egger, R., Mak, C. & Weiss, U. Quantum rates for nonadiabatic electron transfer. *The Journal of chemical physics* **100,** 2651–2660 (1994).

57. Asadi, K. *et al.* Polaron hopping mediated by nuclear tunnelling in semiconducting polymers at high carrier density. *Nature Communications* **4,** 1710 (2013).

58. Hopfield, J. Electron transfer between biological molecules by thermally activated tunneling. *Proceedings of the National Academy of Sciences* **71,** 3640–3644 (1974).

59. Jortner, J. Temperature dependent activation energy for electron transfer between biological molecules. *Journal of Chemical Physics* **64,** 4860–4867 (1976).

60. Van Grondelle, R. & Novoderezhkin, V. I. Quantum effects in photosynthesis. *Procedia Chemistry* **3,** 198–210 (2011).

61. Jortner, J. Dynamics of electron transfer in bacterial photosynthesis. *Biochimica et Biophysica Acta (BBA)-Reviews on Bioenergetics* **594,** 193–230 (1980).

62. Richter, N. *et al.* Charge transport mechanism in networks of armchair graphene nanoribbons. *Scientific reports* **10,** 1–8 (2020).

63. Kim, K. H. *et al.* Apparent power law scaling of variable range hopping conduction in carbonized polymer nanofibers. *Scientific reports* **6,** 1–8 (2016).

64. Read, A. D., Bentley, R. E., Archer, S. L. & Dunham-Snary, K. J. Mitochondrial iron–sulfur clusters: Structure, function, and an emerging role in vascular biology. *Redox Biology* **47,** 102164 (2021).

65. Filman, D. J. *et al.* Cryo-EM reveals the structural basis of long-range electron transport in a cytochrome-based bacterial nanowire. *Communications biology* **2,** 1–6 (2019).

66. Liu, J. *et al.* Metalloproteins containing cytochrome, iron–sulfur, or copper redox centers. *Chemical Reviews* **114,** 4366–4469 (2014).

67. Myers, A. B. Resonance Raman intensities and charge-transfer reorganization energies. *Chemical Reviews* **96,** 911–926 (1996).

68. Choi, A *et al.* Probing spin-charge relation by magnetoconductance in one-dimensional polymer nanofibers. *Physical Review B* **86,** 155423 (2012).

69. Taylor, N. B. & Kassal, I. Generalised Marcus theory for multi-molecular delocalised charge transfer. *Chemical Science* **9,** 2942–2951 (2018).

70. Giannini, S. *et al.* Quantum localization and delocalization of charge carriers in organic semiconducting crystals. *Nature Communications* **10,** 1–12 (2019).

71. Polizzi, N. F., Skourtis, S. S. & Beratan, D. N. Physical constraints on charge transport through bacterial nanowires. *Faraday discussions* **155,** 43–61 (2012).

72. Binnig, G., Rohrer, H., Gerber, C. & Weibel, E. Vacuum tunneling. *Physica B+ C* **109,** 2075–2077 (1982).

73. Frisenda, R., Stefani, D. & Van Der Zant, H. S. Quantum transport through a single conjugated rigid molecule, a mechanical break junction study. *Accounts of Chemical Research* **51,** 1359–1367 (2018).

74. Mowat, C. G. & Chapman, S. K. Multi-heme cytochromes—new structures, new chemistry. *Dalton Transactions,* 3381–3389 (2005).

75. Jortner, J. & Ratner, M. A. *Molecular electronics* (Blackwell Science Oxford, 1997).

76. Blankenship, R. E. *et al.* Comparing photosynthetic and photovoltaic efficiencies and recognizing the potential for improvement. *Science* **332,** 805–809 (2011).

77. Balzani, V., Piotrowiak, P, Rodgers, M., Mattay, J, Astruc, D, *et al. Electron transfer in chemistry* (Wiley-VCH Weinheim, 2001).

78. Nazarov, Y. V. & Blanter, Y. M. *Quantum transport: introduction to nanoscience* (Cambridge University Press, 2009).

79. Kell, A., Feng, X., Reppert, M. & Jankowiak, R. On the shape of the phonon spectral density in photosynthetic complexes. *The journal of physical chemistry B* **117 24,** 7317–23 (2013).

80. Becker, D., Banerjee, R., Dickman, M., Gladyshev, V. & Ragsdale, S. *Redox biochemistry* (John Wiley & Sons, 2007).

81. Malkin, S. Y. *et al.* Natural occurrence of microbial sulphur oxidation by long-range electron transport in the seafloor. *The ISME journal* **8,** 1843–1854 (2014).

82. Risgaard-Petersen, N. *et al.* Cable bacteria in freshwater sediments. *Applied and environmental microbiology* **81,** 6003–6011 (2015).

83. Burdorf, L. D. *et al.* Long-distance electron transport occurs globally in marine sediments. *Biogeosciences* **14,** 683–701 (2017).

84. Scholz, V. V. *et al.* Cable bacteria at oxygen-releasing roots of aquatic plants: a widespread and diverse plant–microbe association. *New Phytologist* **232,** 2138–2151 (2021).

85. Geerlings, N. M. *et al.* Division of labor and growth during electrical cooperation in multicellular cable bacteria. *Proceedings of the National Academy of Sciences* **117,** 5478–5485 (2020).

86. Scilipoti, S., Koren, K., Risgaard-Petersen, N., Schramm, A. & Nielsen, L. P. Oxygen consumption of individual cable bacteria. *Science Advances* **7,** eabe1870 (2021).

87. Amdursky, N. *et al.* Electronic transport via proteins. *Advanced Materials* **26,** 7142–7161 (2014).

88. Valianti, S., Cuevas, J.-C. & Skourtis, S. S. Charge-Transport Mechanisms in Azurin-Based Monolayer Junctions. *The Journal of Physical Chemistry C* **123,** 5907–5922 (2019).

89. Amdursky, N. *et al.* Electron transfer proteins as electronic conductors: Significance of the metal and its binding site in the blue Cu protein, azurin. *Advanced Science* **2,** 1400026 (2015).

90. Strycharz-Glaven, S. M., Snider, R. M., Guiseppi-Elie, A. & Tender, L. M. On the electrical conductivity of microbial nanowires and biofilms. *Energy & Environmental Science* **4,** 4366–4379 (2011).

91. Van der Veen, J. R. *et al.* Quantum-assisted electron transport in microbial protein wires across macroscopic distances. *arXiv preprint arXiv:2308.09560* (2023).

92. Cottaar, J & Bobbert, P. Calculating charge-carrier mobilities in disordered semiconducting polymers: Mean field and beyond. *Physical Review B* **74,** 115204 (2006).

93. Berlin, Y. A., Burin, A. L. & Ratner, M. A. Charge hopping in DNA. *Journal of the American Chemical Society* **123,** 260–268 (2001).

94. Monroe, D. Hopping in exponential band tails. *Physical Review Letters* **54,** 146 (1985).

95. Lindsay, S. Ubiquitous electron transport in non-electron transfer proteins. *Life* **10,** 72 (2020).

96. Fratini, S., Mayou, D. & Ciuchi, S. The Transient Localization Scenario for Charge Transport in Crystalline Organic Materials. *Advanced Functional Materials* **26** (2015).

97. Jiang, X. *et al.* Cysteine linkages accelerate electron flow through tetra-heme protein STC. *Journal of the American Chemical Society* **139,** 17237–17240 (2017).

98. Van Wonderen, J. H. *et al.* Nanosecond heme-to-heme electron transfer rates in a multiheme cytochrome nanowire reported by a spectrally unique His/Met-ligated heme. *Proceedings of the National Academy of Sciences* **118,** e2107939118 (2021).

99. Troisi, A. The speed limit for sequential charge hopping in molecular materials. *Organic Electronics* **12,** 1988–1991 (2011).

100. Nazarov, Y. V. & Danon, J. *Advanced Quantum Mechanics: A Practical Guide* (Cambridge University Press, 2013).

101. Hwang, J., Wan, A. & Kahn, A. Energetics of metal–organic interfaces: New experiments and assessment of the field. *Materials Science and Engineering: R: Reports* **64,** 1–31 (2009).

102. Beebe, J. M., Engelkes, V. B., Miller, L. L. & Frisbie, C. D. Contact resistance in metal- molecule- metal junctions based on aliphatic SAMs: effects of surface linker and metal work function. *Journal of the American Chemical Society* **124,** 11268–11269 (2002).

103. Bolotin, K. I. *et al.* Ultrahigh electron mobility in suspended graphene. *Solid state communications* **146,** 351–355 (2008).

104. Evers, F. & Mirlin, A. D. Anderson transitions. *Reviews of Modern Physics* **80,** 1355 (2008).

105. Coropceanu, V. *et al.* Charge transport in organic semiconductors. *Chemical reviews* **107,** 926–952 (2007).

106. Brédas, J.-L., Calbert, J. P., da Silva Filho, D. & Cornil, J. Organic semiconductors: A theoretical characterization of the basic parameters governing charge transport. *Proceedings of the National Academy of Sciences* **99,** 5804–5809 (2002).

107. Grozema, F. C. & Siebbeles, L. D. Mechanism of charge transport in self-organizing organic materials. *International Reviews in Physical Chemistry* **27,** 87–138 (2008).

108. Haynes, W. M., Lide, D. R. & Bruno, T. J. *CRC handbook of chemistry and physics* (CRC press, 2016).

109. Zhu, G. Y. *et al.* Crossover between the adiabatic and nonadiabatic electron transfer limits in the Landau-Zener model. *Nature communications* **12,** 1–10 (2021).

110. Cenci, M. P. *et al.* Eco-Friendly Electronics—A Comprehensive Review. *Advanced Materials Technologies* **7,** 2001263 (2022).

111. Chiang, C. *et al.* Conducting polymers: Halogen doped polyacetylene. *The Journal of Chemical Physics* **69,** 5098–5104 (1978).

112. Chiang, C. K. *et al.* Electrical conductivity in doped polyacetylene. *Physical review letters* **39,** 1098 (1977).

113. Xu, J.-C., Liu, W.-M. & Li, H.-L. Titanium dioxide doped polyaniline. *Materials Science and Engineering: C* **25,** 444–447 (2005).

114. Holland, E., Pomfret, S., Adams, P. & Monkman, A. Conductivity studies of polyaniline doped with CSA. *Journal of Physics: Condensed Matter* **8,** 2991 (1996).

115. Wang, Z. *et al.* Kinetics of reduction of Fe (III) complexes by outer membrane cytochromes MtrC and OmcA of Shewanella oneidensis MR-1. *Applied and Environmental Microbiology* **74,** 6746–6755 (2008).

116. Myers, J. M. & Myers, C. R. Role for outer membrane cytochromes OmcA and OmcB of Shewanella putrefaciens MR-1 in reduction of manganese dioxide. *Applied and environmental microbiology* **67,** 260–269 (2001).

117. Burroughes, J., Friend, R. & Allen, P. Field-enhanced conductivity in polyacetylene-construction of a field-effect transistor. *Journal of Physics D: Applied Physics* **22,** 956 (1989).

118. Chen, D., Lei, S. & Chen, Y. A single polyaniline nanofiber field effect transistor and its gas sensing mechanisms. *Sensors* **11,** 6509–6516 (2011).

119. Katz, H., Dodabalapur, A & Bao, Z. *Oligo-and polythiophene field effect transistors* (Wiley-VCH Verlag GmbH: Weinheim, Germany, 1999).

120. Kunugi, Y. *et al.* Organic field-effect transistor using oligoselenophene as an active layer. *Chemistry of materials* **15,** 6–7 (2003).

121. Wu, H.-Y. *et al.* Influence of molecular weight on the organic electrochemical transistor performance of ladder-type conjugated polymers. *Advanced Materials* **34,** 2106235 (2022).

122. Liu, F. *et al.* Relating chemical structure to device performance via morphology control in diketopyrrolopyrrole-based low band gap polymers. *Journal of the American Chemical Society* **135,** 19248–19259 (2013).

123. Porath, D., Levi, Y., Tarabiah, M. & Millo, O. Tunneling spectroscopy of isolated C 60 molecules in the presence of charging effects. *Physical Review B* **56,** 9829 (1997).

124. Lu, X., Grobis, M, Khoo, K., Louie, S. G. & Crommie, M. Charge transfer and screening in individual C 60 molecules on metal substrates: A scanning tunneling spectroscopy and theoretical study. *Physical Review B* **70,** 115418 (2004).

125. Sau, J. D., Neaton, J., Choi, H. J., Louie, S. G. & Cohen, M. L. Electronic energy levels of weakly coupled nanostructures: C 60-metal interfaces. *Physical review letters* **101,** 026804 (2008).

126. Yan, H., Park, S. H., Finkelstein, G., Reif, J. H. & LaBean, T. H. DNA-templated self-assembly of protein arrays and highly conductive nanowires. *science* **301,** 1882–1884 (2003).

127. Lovley, D. R. & Walker, D. J. Geobacter protein nanowires. *Frontiers in microbiology* **10,** 2078 (2019).

128. Breuer, M., Rosso, K. M., Blumberger, J. & Butt, J. N. Multi-haem cytochromes in Shewanella oneidensis MR-1: structures, functions and opportunities. *Journal of The Royal Society Interface* **12,** 20141117 (2015).

129. Tipmanee, V., Oberhofer, H., Park, M., Kim, K. S. & Blumberger, J. Prediction of reorganization free energies for biological electron transfer: A comparative study of Ru-modified cytochromes and a 4-helix bundle protein. *Journal of the American Chemical Society* **132,** 17032–17040 (2010).

130. Aleshin, A., Lee, H., Park, Y. & Akagi, K. One-dimensional transport in polymer nanofibers. *Physical review letters* **93,** 196601 (2004).

131. Kronemeijer, A. *et al.* Universal scaling in highly doped conducting polymer films. *Physical review letters* **105,** 156604 (2010).

132. Kim, K. H. *et al.* Probing variable range hopping lengths by magneto conductance in carbonized polymer nanofibers. *Scientific Reports* **8,** 4948 (2018).

133. Park, Y. W. Magneto resistance of polyacetylene nanofibers. *Chemical Society Reviews* **39,** 2428–2438 (2010).

134. Gu, H. *et al.* Electrical transport and magnetoresistance in advanced polyaniline nanostructures and nanocomposites. *Polymer* **55,** 4405–4419 (2014).

135. Rosenbaum, R., Murphy, T., Palm, E., Hannahs, S. & Brandt, B. Magnetoresistance of insulating amorphous Ni x Si 1- x films exhibiting Mott variable-range hopping laws. *Physical Review B* **63,** 094426 (2001).

136. Tian, Y. *et al.* Origin of large positive magnetoresistance in the hard-gap regime of epitaxial Co-doped ZnO ferromagnetic semiconductors. *Physical Review B* **79,** 115209 (2009).

137. Jaiswal, M., Wang, W., Fernando, K. S., Sun, Y.-P. & Menon, R. Magnetotransport in transparent single-wall carbon nanotube networks. *Physical Review B* **76,** 113401 (2007).

138. Bozdag, K. D., Chiou, N.-R., Prigodin, V. & Epstein, A. J. Magnetic field, temperature and electric field dependence of magneto-transport for polyaniline nanofiber networks. *Synthetic metals* **160,** 271–274 (2010).

139. Bercioux, D. & Lucignano, P. Quantum transport in Rashba spin–orbit materials: a review. *Reports on Progress in Physics* **78,** 106001 (2015).

140. Ghosh, M, Barman, A, De, S. & Chatterjee, S. Transport properties of HCl doped polyaniline and polyaniline–methyl cellulose dispersion. *Journal of applied physics* **84,** 806–811 (1998).

141. Bruno, W. J. & Bialek, W. Vibrationally enhanced tunneling as a mechanism for enzymatic hydrogen transfer. *Biophysical journal* **63,** 689–699 (1992).

142. Finer, J. T., Simmons, R. M. & Spudich, J. A. Single myosin molecule mechanics: piconewton forces and nanometre steps. *Nature* **368,** 113–119 (1994).

143. Bockrath, M. *et al.* Luttinger-liquid behaviour in carbon nanotubes. *Nature* **397,** 598–601 (1999).

144. Liu, C. *et al.* A unified understanding of charge transport in organic semiconductors: the importance of attenuated delocalization for the carriers. *Materials Horizons* **4,** 608–618 (2017).

ACKNOWLEDGEMENTS

A little over four years ago, I was given the opportunity by my promotors **Filip** and **Herre**, to work on the subject of cable bacteria, to become a scientist. I did not have to think for long, as this was a childhood dream come true. Therefore, thank you for offering me this chance. I would also like to thank you for our cooperation in the broad sense: giving direction when required, feedback in writing, our discussions on the subject, and for always showing enthusiasm for the research. In particular, I would like to thank **Herre** for his daily supervision, for his interest in my measurements in the lab, and for giving me advice on guiding master students. I believe your critical view, honesty and clear communication style effectively helps people to grow professionally. It has certainly helped me. In a similar way, I would like to thank **Filip**, for always asking the next critical question about (gaps in) my work, for his interest in the modelling of cable bacteria conduction and his interest in pretty much everything that has to do with cable bacteria and the natural sciences, which bridges gaps between different fields of science that would otherwise be separated. Next, I would like to think **Yaroslav**. You were of great support, part of the my supervision team for my entire PhD period, and always joined our biweekly meetings to help me seeing right from wrong and you were always available for questions.

Through **Filip**'s research group, I have come into contact with some very friendly people. The foremost person to thank is (of course), **Silvia**. Perhaps I should have started with you? You woke up in Antwerpen at very insensible early hours from my perspective (6 a.m. or so), to bring cable bacteria samples to Delft. Without you, none of the research I have done would have been possible. It was always very 'gezellig' when you were in Delft, whether experiments worked out great or less so. The method by which you extract the cable bacteria's conductive structures is now published, but you remain just as irreplaceable. Next, I would like to thank **Diana**, Eric and **Jeanine**. Somehow, I remember many pleasant conversations with you in many different places (Delft, Antwerpen, Gent, Aarhus and Barcelona). I would also like to thank **Dmitri**, perhaps my 'closest relative' in research terms, **Bent**, with whom I almost co-authored an article and who knows a lot about beer, **Anwar**, who was born in the same city as I but got lost in Belgium somehow, **Jesper**, who even dared to change his nationality from Dutch to Belgian, **Ines**, **Jiji**, **Nicole** and **Philip**. Thank you all for your great company.

At **Herre**'s research group, I had the opportunity to guide some very friendly master students, who also greatly contributed to the work and to the joy of going to work. I would like to thank **Rick**, with whom I took a selfie in the cleanroom with face masks when it was new, **Albert**, who measured the temperature dependence on primary display in Chapter 2 and **Matteo**, who studied the length dependence of conductivity in more detail, which was vital to the finalising the Chapter. I would also like to thank **Katja**, who worked with Yaroslav and me on modelling the gate dependence, through capacitive coupling, of a one-dimensional hopping chain. Unfortunately I have not completed writing her work down.

Also, I would like to thank **Spiros**, who as a professor from the university of Cyprus visited Delft because he was interested in what I measured, and opened up a world of thinking to me that I previously could not (and still cannot really) grasp. Also thanks to **Stefani**, for bringing this knowledge to Delft, helping me with the theoretical work, for pushing it forward and for your company.

I also had the pleasure of working with some great colleagues in Delft. Particularly, it was an honor to be **Damian**'s colleague, who suggested the method for predicting the more complicated occupancy profiles in Chapter 3. The similarity between his and my data has lead to interesting discussions about different charge transport models. Besides thanking him, I would like also the other two PhD students that started around the same time as I: **Thomas** and **Jacqueline**. You have all been great company. I would also like to thank **Maria**, who supported me in the early phase of my PhD time. Thanks also to **Talieh** for her willingness to colloborate and also to her and **Josep** for their positive influence on the group. Thanks also to **Maurits** my fellow teaching assistent in modern physics, **Sergeii**, **Tristan**, **Sebastiaan**, **Luca** and **Chunwei** for their company and that of countless master students with whom they worked together.

I would also like to thank the Kavli cleanroom staff, in particular **Anja**, who taught me how to use the laserwriter, which was involved in all my samples. Also thanks to **Arnold** for computer support, **Marc** for evaporator training, **Charles**, for dry etching and wafer support and **Eugene** for wet bench area training and his general concern for safety. I would like to thank **Roald** and **Hosanna** for their help with the SEM and the FIB-SEM. Besides the cleanroom staff, I would like to thank **Nikos** for training me in the wet bench area. A special thanks ago goes out to **Tino**, for technical support in the lab, of course. He fixed many pumps and solved many problems in the (new) lab. Also, it is always interesting to talk about politics and the state of the world with him, as well as about daily matters.

Tot slot, zou ik graag een aantal belangrijke mensen in mijn leven willen bedanken voor hun steun de afgelopen jaren. Die steun lijkt vaak vanzelfsprekend en heeft meestal niets met mijn werk aan de universiteit te maken, maar soms gaat het er ook wel over. In veel gevallen gaat die steun al een leven lang terug, zoals die van **pap** en **mam**. Ook de afgelopen jaren was die steun er weer. Het was vaak goed eten en gezellig in Den Haag, ook met **Hubert** en **Anniek**. Dank daarvoor. Ook onze jaarlijks terugkerende kerstvakanties met gezin, **mammama** en anderen zijn van grote waarde geweest. Ook bedankt aan opa **Ruud** en oma **Mieke** voor het in stand houden van ons jaarlijkse diner bij ’de Chinees’ in Eindhoven en hun interesse in mijn tijd als promovendus. Ook aan de andere kant van land, in Burgum (Friesland), stonden er vaak twee mensen voor ons (mij en Elise) klaar, namelijk **Leo** en **Carla**. Tot slot, wil ik graag **Elise** bedanken voor mijn levensgeluk de afgelopen vier jaar.

CURRICULUM VITÆ

Jasper Ruud VAN DER VEEN

04-12-1994	Born in The Hague, the Netherlands.

EDUCATION

2007–2013	Secondary School Christelijk Gymnasium Sorghvliet The Hague, The Netherlands	
2013–2016	Bachelor of Science in Applied Physics Delft University of Technology Delft, The Netherlands	
2016–2019	Master of Science in Applied Physics Delft University of Technology Delft, The Netherlands	
	Thesis:	Phonon-mediated charge transport in cable bacteria
	Supervisor:	Prof. dr. ir. H.S.J. van der Zant
2019–2023	Ph.D. in Biotechnology Delft University of Technology Delft, The Netherlands	
	Thesis:	The charge transport mechanism in cable bacteria
	Promotors:	Prof. dr. ir. F.J.R. Meysman Prof. dr. ir. H.S.J. van der Zant

LIST OF PUBLICATIONS

2. **Jasper R. van der Veen**, Silvia Hidalgo Martinez, Albert Wieland, Matteo De Pellegrin, Rick Verweij, Yaroslav M. Blanter, Herre S.J. van der Zant and Filip J.R. Meysman. *Quantum-assisted electron transport in microbial protein wires across macroscopic distances*, Arxiv.org.

1. **Jasper R. van der Veen**, Stephanie Valianti, Herre S.J. van der Zant, Yaroslav M. Blanter and Filip J.R. Meysman. *A model analysis of long-distance electron transport in cable bacteria*, Physical Chemistry Chemical Physics.